On the variability of turbulent mixing within the upper layers of the Atlantic Cold Tongue region

Dissertation
zur Erlangung des Doktorgrades
der Mathematisch-Naturwissenschaftlichen Fakultät
der Christian-Albrechts-Universität
zu Kiel

vorgelegt von
Rebecca Marie Hummels

Kiel 2012

GEOMAR
Helmholtz-Zentrum für Ozeanforschung Kiel

Zusammenfassung

Die Variabilität der Meeresoberflächentemperatur (SST) im äquatorialen Atlantik ist von klimatischer Bedeutung für die angrenzenden Kontinente. Ein charakteristisches Merkmal dieser SST Variabilität ist das saisonale Auftreten der atlantischen Kaltwasserzunge (ACT). Die individuellen Beiträge zum Wärmebudget der Deckschicht, das den saisonalen Verlauf der SST bestimmt, konnten bis heute nicht vollständig geklärt werden. Speziell der Beitrag des diapyknischen Wärmeflusses aufgrund von Turbulenz ist noch immer umstritten.

Das Hauptziel dieser Arbeit ist die Bestimmung der regionalen und saisonalen Variabilität der turbulenten Vermischung und des resultierenden, diapyknischen Wärmeflusses in den oberen Schichten der ACT Region. Die Basis für diese Untersuchung bildet ein Datensatz von Mikrostrukturbeobachtungen gewonnen während diverser Schiffsreisen in verschiedene Regionen der ACT während unterschiedlicher Jahreszeiten. Die abgeschätze Variabilität des diapyknischen Wärmeflusses wird dann in das Wärmebudget der Deckschicht integriert. Die daraus bestimmte Variabilität der turbulenten Vermischung wird im Folgenden mit der Variabilität der groß-skaligen Zirkulation in Beziehung gesetzt.

Die Beobachtungen der Hintergrundbedingungen in Form der Parameter Scherung und Schichtung unterhalb der Deckschicht lässt fundamentale Unterschiede zwischen der westlichen und östlichen äquatorialen, sowie der südlichen ACT Region erkennen. Dies führt dazu, dass kritische Froude Zahlen (Fr), die ein Indikator für erhöhte Vermischungsintensität sind, am häufigsten in der westlichen äquatorialen ACT Region auftreten. Die Verteilung kritischer Fr Zahlen unterhalb der Deckschicht ist generell in guter Übereinstimmung mit der regionalen und saisonalen Variabilität turbulenter Vermischungsintensität. Dissipationsraten der turbulenten kinetischen Energie (ϵ) in der äquatorialen Region (2°S-2°N) sind deutlich erhöht verglichen mit polwärtigen Regionen. Außerdem ist ϵ in der westlichen, äquatorialen ACT Region von Mai bis November höher als im Osten. Die borealen Sommermonate, übereinstimmend mit dem Zeitpunkt des Auftretens der ACT, können als die Saison höchster Vermischungsaktivität innerhalb der gesamten äquatorialen Region identifiziert werden. Diapyknische Wärmeflüsse am Fuße der Deckschicht in der westlichen, äquatorialen ACT Region, abgeleitet aus Beobachtungen von ϵ und Schichtung, reichen von maximal 90 Wm^{-2} im borealen Sommer bis 40 zu Wm^{-2} im November. In der östlichen, äquatorialen Region wurden maximal 25 Wm^{-2} während des borealen Sommers beobachtet. Außerhalb der äquatorialen Region übersteigen die diapyknischen Wärmeflüsse niemals 10 Wm^{-2}. Einen wesentlichen Beitrag zu den hohen Wärmeflüssen in der westlichen, äquatorialen Region vor allem im borealen Sommer und Herbst liefert die meridionale Komponente der Geschwindigkeitsscherung. Es ist deshalb zu vermuten, dass tropische Instabilitätswellen (TIWs), die diese Geschwindigkeitskomponente wesentlich beeinflußen, einen wichtigen Beitrag zur turbulenten Vermischung in dieser Region liefern.

Die Integration des abgeschätzten diapyknischen Wärmeflusses in das Wärmebudget der Deckschicht hebt hervor, dass der diapyknische Wärmefluss den grössten Beitrag zur Abkühlung im borealen Sommer und Herbst in der gesamten, äquatorialen ACT liefert. Dies betont seine

Schlüsselrolle für die Abkühlung während der ACT Entstehung. In der südlichen ACT Region ist das Wärmebudget der Deckschicht hauptsächlich durch atmosphärische Terme bestimmt. Desweitern wird gezeigt, dass existierende Turbulenz-Parametrisierungen für die äquatoriale Region, die eine grobe Abschätzung der relevanten turbulenten Größen ohne kostspielige Messungen ermöglichen sollen, die Vermischungsintensität und die abgeleiteten diapyknischen Wärmeflüsse überschätzen.

Abstract

Sea surface temperature (SST) variability within the equatorial Atlantic is of climatic relevance for the surrounding continents. A striking feature of this SST variability is the annual appearance of the Atlantic cold tongue (ACT). The respective contributions to the ML heat budget forming the seasonal cycle of SSTs within the ACT could up to date not be clarified. Especially the role of the diapycnal heat flux due to turbulence in cooling SSTs is still controversially discussed.

The main focus of this study is to infer regional and seasonal variability of upper ocean turbulent mixing and the inferred diapycnal heat flux within the ACT region using a multi cruise data set of microstructure observations. The assessed varibility of the diapycnal heat flux is then intregrated into the ML heat budget within different regions and seasons of the ACT. In addition, the variability in mixing intensity is related to the variability in large scale background conditions, which were additionally observed during the cruises.

The observations indicate fundamental differences in background conditions in terms of shear and stratification below the mixed layer (ML) for the western and eastern equatorial as well as the southern ACT region. This leads to the occurence of critical Froude numbers (Fr), which points towards elevated mixing intensity, most frequently in the western equatorial ACT. The distribution of critical Fr below the ML reflects the regional and seasonal variability of mixing intensity. Turbulent dissipation rates (ϵ) at the equator (2°N-2°S) are strongly increased in the upper thermocline compared to off-equatorial locations. In addition, ϵ is elevated in the western equatorial ACT compared to the east from May to November, whereas boreal summer appears as the season of highest mixing intensities throughout the equatorial ACT region, coinciding with ACT development. Diapycnal heat fluxes at the base of the ML in the western equatorial ACT region inferred from ϵ and stratification range from a maximum of 90 Wm^{-2} in boreal summer to 40 Wm^{-2} in November. In the eastern equatorial ACT region maximum values of about 25 Wm^{-2} were estimated during boreal summer. Outside the equatorial region, inferred diapycnal heat fluxes are comparably low rarely exceeding 10 Wm^{-2}. Critical to the enhanced diapycnal heat flux in the western equatorial ACT region during boreal summer and autumn is elevated meridional velocity shear in the upper thermocline. It is thus suggested that TIWs are crucial contributors to mixing within this region during this timeperiod.

Integrating the obtained heat flux estimates in the ML heat budget accentuates the diapycnal heat flux as the largest ML cooling term during boreal summer and early autumn in the entire equatorial ACT region and crucial for decreasing SSTs for ACT development. Within the southern ACT region SST cooling is dominated by atmospheric forcing.

Additionally, it is shown that most of the existing parametrization schemes for the equatorial thermocline, which are supposed to estimate the general magnitude of mixing related parameters without cost-intensive observations, tend to overestimate turbulent mixing intensity and the inferred diapycnal heat fluxes within the equatorial ACT region.

Contents

Contents

Publications

This thesis contains the manuscript: Hummels, R., Dengler, M. and B. Bourlès (2012), *Seasonal and regional variability of upper ocean diapycnal heat flux in the Atlantic Cold Tongue*, which has been recently submitted to Progress in Oceanography. The submitted manuscript is attached in *Appendix B*.

Appendix C1: Wade, M., G. Caniaux, Y. DuPenhoat, M. Dengler, H. Giordani and R. Hummels (2011), *A one-dimensional modeling study of the diurnal cycle in the equatorial Atlantic at the PIRATA buoys during the EGEE-3 campaign*, Ocean Dynamics, 61:1-20

Appendix C2: Rhein, M. and M. Dengler and J. Sültenfuß, R. Hummels, S. Hüttl-Kabus and B. Bourlès (2010), *Upwelling and associated heat flux in the equatorial Atlantic inferred from helium isotope disequilibrium*, Journal of Geophysical Research, 115 (C08021)

1. Introduction

1.1. Motivation - why are small scale processes important?

In oceanography, science deals with processes on largely different scales in space and time covering the range between basin-wide and millennial to millimeter and seconds. This study is concerned with processes due to turbulence occupying the lowest end of scales. Turbulence serves as the final step within the cascade of kinetic energy: Energy fed into the oceans at large scales driving the circulation system is believed to cascade towards smaller scales via eddies and waves, which finally break transferring energy into turbulent motions. Once embedded in turbulent motions the energy is either used to mix water masses, describing the transfer of kinetic to potential energy or lost to dissipation meaning a conversion to heat. Hence, if the energy input at large scales should cease, the cascade would break down, after the entire kinetic energy is dissipated.

Within the framework of this thesis, mixing due to turbulent motions is further investigated. In general, mixing of water masses describing a property exchange across isopycnals can only be accomplished by molecular diffusion. However, small scale turbulent motions act to enlarge gradients of e.g. temperature and thereby accelerate the molecular mixing process. This accelerated property exchange due to turbulence is referred to as turbulent mixing or diapycnal mixing due to turbulence. In this study the regional as well as seasonal variability of turbulent mixing intensity within the eastern equatorial Atlantic is investigated. Furthermore, the role of the inferred heat flux due to this turbulent mixing in cooling sea surface temperatures (SSTs) will be discussed.

For a better understanding of the interest in processes shaping turbulent mixing intensity, which take place on smallest scales, the role of turbulent mixing for the global meridional overturning circulation (MOC) will be pointed out. The MOC is associated with an enormous equator-to-pole heat transport within the northern Atlantic, peaking at 1.3 PW (1PW=10^{15} W) in the subtropics [*Ganachaud and Wunsch*, 2000], providing a crucial feature to the mean climate state. It consists of an inter-basinwide circulation, driven by the wind as well as thermohaline processes, which is often associated with the simplified idea of the so called global conveyor belt: rather local deep convection sites in high latitudes e.g. the Labrador, Greenland and Weddel seas are connected with regions in lower latitudes, where waters are enlightened and thereby shifted to intermediate depths. Finally, waters are brought to the surface in upwelling regions and returned to the deep convection sites in high latitudes (fig.1.1). Hence, one of the previously postulated driving mechanisms of the MOC is the deep convection governed by air-sea interactions. The main part of this deep convection, at least within the Atlantic basin, is associated with shelf convection in the Southern Ocean and Nordic Seas and to a lesser extent by open ocean convection [*Lumpkin*

1. Introduction

In the absence of deep reaching diapycnal mixing, the deep ocean would simply fill up with cold dense water having a rather uniform density [*Sandström*, 1908]. As waters below the thermocline are stratified, processes must be at play that prevent the homogeneous ocean formulated by Sandström. *Munk* [1966] postulated an equilibrium between the upwards advection of cold waters and the downwards turbulent diffusion of heat, which results in the observed abyssal stratification. He used a simple one-dimensional advection/diffusion model:
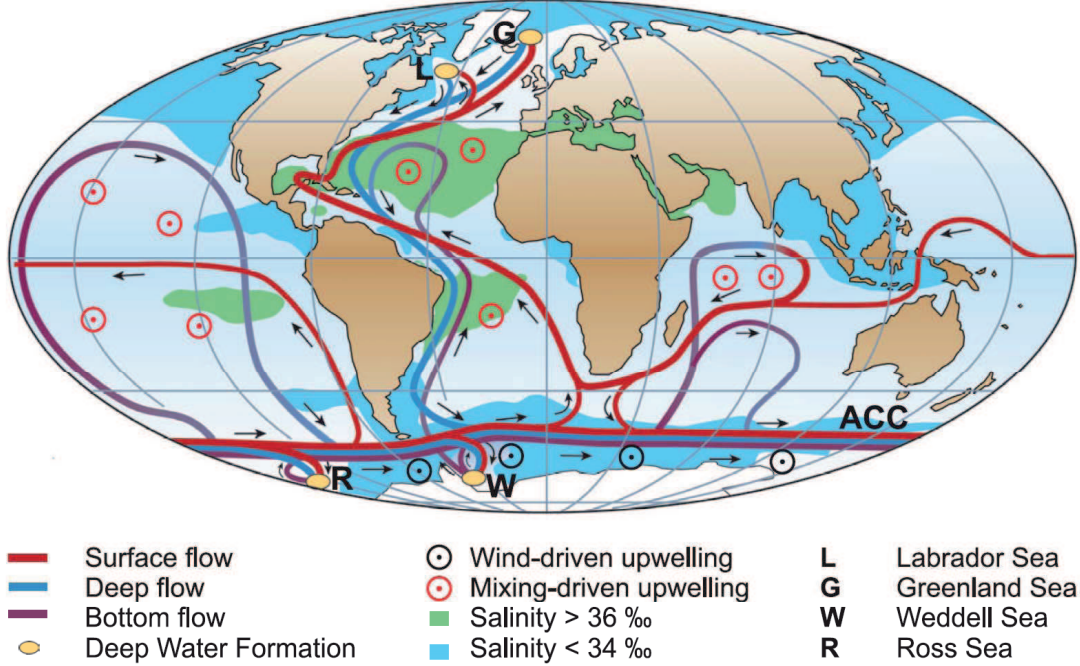

Figure 1.1.: Sketch of the global conveyor belt: Deep convection sites in high latitudes (marked as G,L and W) and the pathways of the formed deep waters (blue) are connected to various areas of deep reaching ocean mixing, where waters are enlightened and warmed. In addition, their surface return pathways (red) to the high latitudes are shown [*Rahmstorf*, 2002].

$$w\frac{\partial \rho}{\partial z} = \frac{\partial}{\partial z}(K_\rho \frac{\partial \rho}{\partial z}), \tag{1.1}$$

where w is the vertical velocity, K_ρ the eddy diffusivity, a measure of turbulent mixing intensity, z the vertical coordinate and ρ the density. Under the assumption that w and K_ρ are constant and ρ is horizontally homogeneous, the solution of equation 1.1 is $\rho = \rho_0 e^{\frac{z}{H}}$, with $H = K/w$. H can then be determined from the exponential form of the abyssal profiles. Evaluating abyssal profiles from the central Pacific of density and a tracer provided *Munk* [1966] with two equations of the form 1.1 for the two unknowns w and K. He thereby estimated the values of $w = 0.7 \cdot 10^{-7} ms^{-1}$ and $K = 1 \cdot 10^{-4} m^2 s^{-1}$. As a consequence of this simple model, and assuming that the vertical velocity w is constantly distributed over the entire area of the ocean, a compensating global bottom water formation rate of about $25 Sv = 25 \cdot 10^6 m^3 s^{-1}$ is required. As this value agrees with previous estimates for the rate of bottom water formation [see *Munk and Wunsch*, 1998] one can

interpret the strength of the MOC directly related to turbulent mixing intensity. Consequently one may describe the MOC driven by turbulent mixing in the ocean interior or moreover the available energy for turbulent mixing. Hence, there are two opposing concepts for the driving mechanism of the MOC, either being "pushed" by deep convection or "pulled" by turbulent mixing. The idea of the MOC being pulled by turbulent mixing lead to various investigations about turbulent mixing processes.

Direct estimates of K_ρ using microstructure probes revealed an open ocean value of $K_\rho = 1 \cdot 10^{-5} m^2 s^{-1}$ [e.g. *Osborn and Cox*, 1972; *Gregg*, 1989], which seemed to contradict the estimates of *Munk* [1966] obtained with the simple model. Only since these low open ocean values for K_ρ were confirmed by tracer release experiments [*Ledwell et al.*, 1993] the community started to accept that open ocean eddy diffusivities could be considerably lower than *Munk* [1966]'s estimate. On the other hand, greatly enhanced values of eddy diffusivities of up to $1 \cdot 10^{-1} m^2 s^{-1}$ have been observed in boundary regions and close to seamounts [*Polzin et al.*, 1995, 1997; *Lueck and Mudge*, 1997]. *Munk and Wunsch* [1998] revisited the theory of *Munk* [1966] and stated that the power required to uniformly mix with an eddy diffusivity of $1 \cdot 10^{-4} m^2 s^{-1}$ over the entire ocean, is equivalent to highly elevated mixing in a few concentrated regions. This idea is further referred to as the hot spot theory: Small regions in the oceans were suggested to exist, where mixing is clearly enhanced, the hot spots, whilst the vast rest of the ocean should mix at a considerable lower rate in agreement with the open ocean observations of $K = 1 \cdot 10^{-5} m^2 s^{-1}$. The mixed waters are then thought to be laterally advected along isopycnals from the hot spots into the ocean interior forming the observed abyssal stratification.

The quest for available energy sources for mechanical mixing led *Munk and Wunsch* [1998] to the proposal of certain hot spots: in their investigation tides and winds stand out as the main, nearly equally important energy sources. Tidal flow over topography, especially in shelf areas as well as tide-generated internal waves cause elevated levels of turbulent mixing intensity within shelf areas and regions of irregular topography [*Polzin et al.*, 1995, 1997; *Lueck and Mudge*, 1997; *MacKinnon and Gregg*, 2003]. Indirect wind induced mixing involves interaction of large-scale wind driven flow with bottom topography or wind-induced internal waves radiating from the surface into the ocean interior, where they are presumed to break. In addition, wind mixing can occur directly, where abyssal isopycnals outcrop as in the Southern Ocean. Within the Antarctic Divergence zone, a result of the Ekman-transports due to the prevailing wind patterns, strong upwelling lifts up isopycnals. *Toggweiler and Samuels* [1998] state that in their numerical model the ocean could mix primarily at these near-surface outcrops.

During the search for these deep mixing hot spots, another "hot spot" of turbulent mixing was discovered clearly detached from the deep hot spots associated with the strength of the MOC: within the upper layers of the equatorial oceans turbulent mixing intensity has been observed elevated from the mixed layer depth (MLD) reaching into the stratified ocean interior [e.g *Crawford and Osborn*, 1979; *Gregg et al.*, 1985; *Peters et al.*, 1988; *Lien et al.*, 1995]. Within this hot spot turbulent motions are suggested to be triggered by the highly energetic current system. The opposite flowing currents provide enhanced levels of vertical shear, which nudge the flow to instability and finally result in turbulent motions. The proximity of this mixing hot spot

to the surface facilitates observations of turbulent parameters compared to the deep mixing hot spots and hence offers the possibility to conduct process studies about turbulent mixing. In summary, three major hot spots for turbulent mixing could be identified:

- Irregular topography including shelf areas

- Outcropping isopycnals in the Southern Ocean

- The upper layers of the equatorial oceans

Within this investigation the latter hot spot, the upper layers of the equatorial oceans, is further investigated.

1.2. The equatorial oceans

The equatorial oceans are exposed to a large, positive net surface heat flux throughout the year [fig.1.2, e.g. *Josey et al.*, 1999]. Thus, large amounts of heat are available to be transported from the surface into the ocean interior via turbulent mixing. Historically, the interest of understanding the heat flux due to turbulence at low latitudes was motivated by the hypothesis of *Sandström* [1908]. He suggested that the deep source of heat required for the balance of *Munk* [1966] is the downward penetration of heat at low latitudes due to turbulent mixing [see *Rahmstorf*, 2003]. Controversially, *Gregg et al.* [2003] has found that deep reaching ocean mixing is
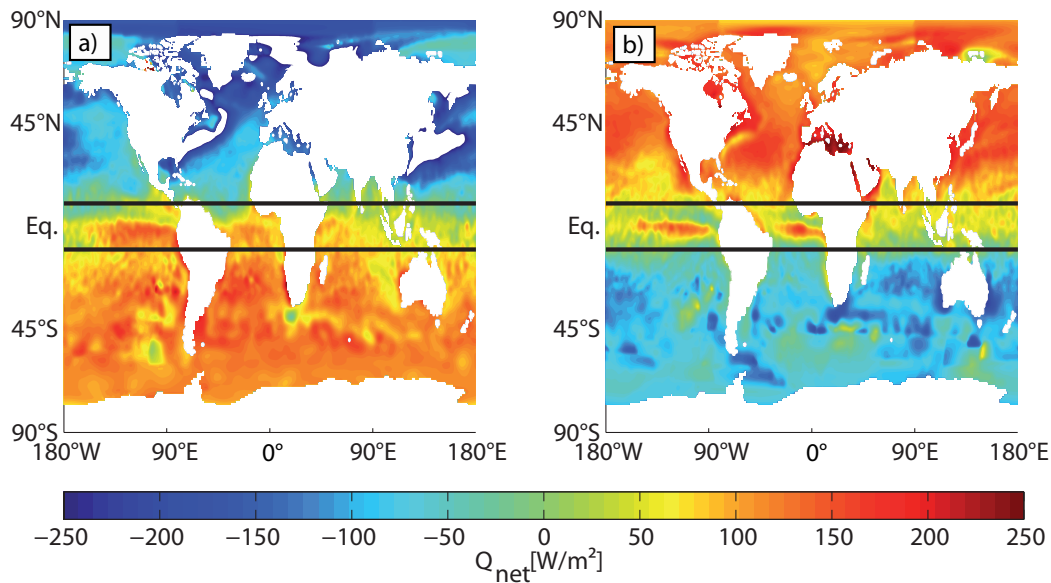
Figure 1.2.: Global net surface heat fluxes from the *da Silva et al.* [1994] marine Atlas for a) January and b) July. The black lines mark the 10°S and 10°N latitudes.

comparably low in the equatorial region, contradicting the idea of a direct connection between the diapycnal heat flux close to the surface and the deep turbulent mixing required in the balance of *Munk* [1966]. However, the upper layers of the equatorial region are identified as a mixing hot spot and thereby of scientific interest in understanding processes shaping turbulent mixing

intensity. In addition, the effect of the turbulent heat flux within this region on transporting heat from the surface into the ocean interior requires clarification.

Figure 1.3.: The dominant modes of ocean-atmosphere variability in the tropical Atlantic in boreal spring a) and boreal summer b). Gray contours describe the first EOF of regional precipitation anomalies in $[mm/day]$, coloured contours are the associated SST anomaly derived by regression in $[°C]$, arrows are the associated seasonal surface wind anomaly in $[m/s]$. Boreal spring includes the months March-April, boreal summer June-August [*Kushnir et al.*, 2006].

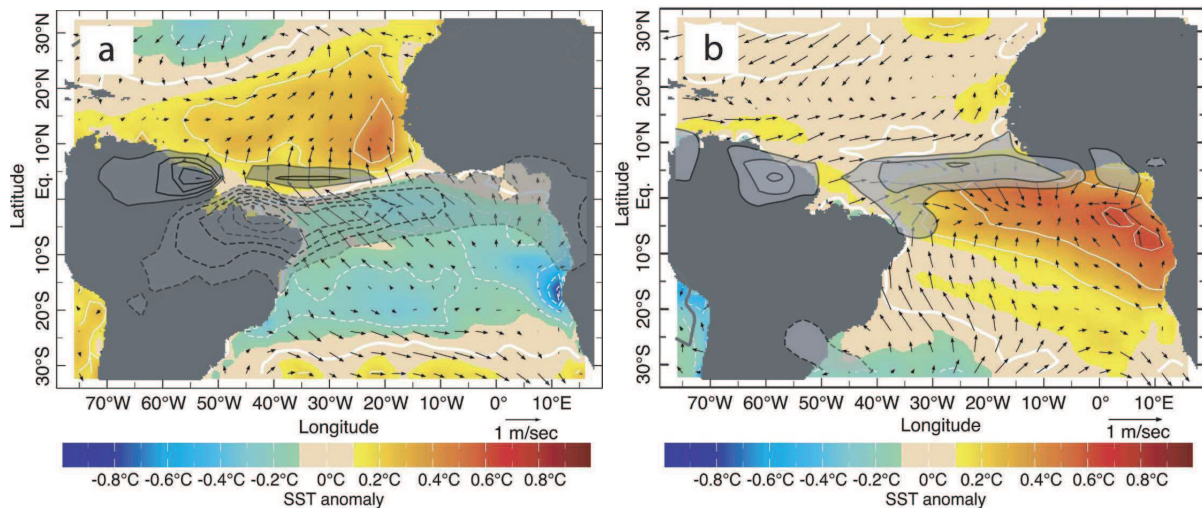Present-day knowledge about turbulent mixing in the equatorial oceans is based on studies from the central equatorial Pacific. Results from several extensive observational programs and model studies have shown the existence of strongly enhanced turbulence within this region and have greatly improved understanding of mixing processes, which are responsible for the strong turbulence occurring in the stratified upper water column of the equatorial thermocline [e.g. *Gregg et al.*, 1985; *Moum and Caldwell*, 1985; *Peters et al.*, 1988; *Moum et al.*, 1989; *Peters et al.*, 1994; *Skyllingstad and Denbo*, 1995; *Lien et al.*, 1995; *Wang and Müller*, 2002; *Lien et al.*, 2008; *Moum et al.*, 2009]. The consense of these studies is that the vertically sheared background, mainly formed by the Equatorial Undercurrent (EUC), but also due to the presence of the opposite flowing South Equatorial Current (SEC), provide the main energy source for turbulent motions. In addition, large-scale wave phenomena superimpose on the background current system and add additional vertical shear of horizontal velocity to the upper water column, enhancing the probability of shear instabilities to develop [*Peters et al.*, 1991; *Lien et al.*, 1995, 2008; *Moum et al.*, 2009].

Within these process studies in the central Pacific it was observed that turbulence within the zone of elevated shear levels occurs mainly concentrated in bursts. These bursts can extend from the base of the mixed layer (ML) several tens of meter into the stratified layers and last for a few hours. *Gregg et al.* [1985] were the first to report that the occurrence of these turbulent bursts is enhanced during night time, which was further referred to as the deep cycle turbulence. Average diapycnal heat fluxes over several days to weeks determined from microstructure observations

while this deep cycle turbulence was present were on the order of 40-100 Wm^{-2} [*Peters et al.*, 1988; *Moum et al.*, 1989; *Lien et al.*, 1995]. In the absence of deep cycle turbulence the average diapycnal heat flux reduced to 10-30 Wm^{-2} [*Peters et al.*, 1994; *Lien et al.*, 1995]. The observed variability in the strength of deep cycle turbulence, and hence the strength of the observed dissipation rates and diapycnal heat fluxes, was related to the variable background conditions, mainly shear and stratification, and to a lesser extent surface winds and net surface heat fluxes. Most recent turbulence observations from the central equatorial Pacific using microstructure probes [*Moum et al.*, 2009] and a Lagrangian float [*Lien et al.*, 2008] revealed a strongly pronounced deep diurnal cycle and associated highly elevated vigorous mixing in the upper thermocline during the presence of a tropical instability wave (TIW). TIWs result from instabilities of the equatorial current system [*Philander*, 1976]. Average diapycnal heat fluxes over the observational periods of 7 and 15 days respectively resulted in 200 and 400 Wm^{-2} in the presence of these waves. *Moum et al.* [2009] suggest the additional shear due to the meridional velocity of the TIW superimposed on the already sheared background (due to the EUC) and a near doubling of kinetic energy in the equatorial region due to the presence of the wave responsible for these elevated diapycnal heat fluxes.

Little is known about turbulent mixing within the equatorial Atlantic. The only observations of turbulent mixing intensity within this region have been obtained from the central equatorial Atlantic by *Crawford and Osborn* [1979]. Their results showed elevated turbulent mixing intensity from the ML into the stratified water column comparable to the findings from the equatorial Pacific. Their limited data set though could neither assess any variability of turbulent mixing intensity within this region, nor give much insight into the involved processes calling for further investigations.

The tropical Atlantic does not only gain attention as a hot spot of turbulent mixing, where large amounts of heat are available to be transported from the surface into the ocean interior. It additionally gains scientific interest due to its climatic relevance impacting sensitive regions of the surrounding continents. The annual as well as inter-annual climate variability of this region is determined by the variability of the Atlantic Marine Inter Tropical Convergence Zone (AMI) complex. This complex is comprised of the wind convergence zone, with its convective region and precipitation maximum as well as the surface low pressure trough and the maximum of the SST. The oceans influence on the variability of this complex and hence on climate variability is via SST.

On inter-annual timescales two distinct modes of coupled ocean-atmosphere variability associated with different phases in the seasonal cycle have been defined [*Kushnir et al.*, 2006] often referred to as tropical Atlantic variability (TAV). During boreal spring the conditions are favorable to develop the so called inter hemispheric gradient mode describing the correlation between rainfall patterns in the equatorial belt and the SST gradient between the northern and southern hemisphere (fig.1.3a). During boreal summer the conditions are likely to develop the zonal mode correlating rainfall patterns in the equatorial belt to SST variations along the equator dominated by the appearance of the Atlantic cold tongue (ACT), a characteristic feature of the eastern

tropical Atlantic (fig.1.3b). Several observational studies have confirmed the latter close relation of the variability in the position and intensity of the AMI complex, SSTs in the ACT region and rainfall patterns over northeastern Brazil and the African coast surrounding the Gulf of Guinea during boreal summer [*Giannini et al.*, 2003; *Kushnir et al.*, 2006; *Chang et al.*, 2006]. In addition, it was shown that inter-annual variability of SSTs in the ACT region impacts the onset and strength of the West African Monsoon [*Wagner and Silva*, 1994; *Brandt et al.*, 2011; *Caniaux et al.*, 2011]. Hence, the inter-annual variability of SSTs in the ACT region is tightly connected to rainfall anomalies over the adjacent continents.

This correlation suggests a possible predictability of rainfall variability in case of a predictability of SST. An improved forecast of rainfall anomalies would be of tremendous benefit for the sourrounding countries heavily relying on agriculture. Unfortunately, coupled climate models, that could be used for regional forecasts, have large SST biases in the ACT region [*Richter and Xie*, 2008] and in the Benguela upwelling region. In general the ocean responds on longer timescales than the atmosphere. Hence, as was suggested from model hindcast experiments, if inter-annual SST variability would mainly be driven by ocean dynamics, an improved forecast skill seems possible on timescales set by the involved oceanic processes. The role of long equatorial waves, e.g. Kelvin waves contributing to inter-annual SST variability within the ACT region is controversially discussed [*Moore et al.*, 1978; *Servain et al.*, 1982; *Hormann and Brandt*, 2009]. A recent study of *Brandt et al.* [2011a] suggests vertically alternating deep zonal jets significantly contributing to inter-annual SST variability within the eastern equatorial Atlantic. However, the individual contributions of different oceanic processes in shaping inter-annual SST variability within the ACT region are not clarified.

Besides the ambiguity about the contribution of oceanic processes on inter-annual SST variability, the respective contributions of oceanic processes on the seasonal variability of SSTs within the equatorial ACT region is not clear. The ACT region itself, reaching from the African coast until about 25°W at full cold tongue extent, exhibits a most striking seasonal SST cycle: from mid-May to mid-July SSTs decrease by about $6°C$ and stay on a cold level throughout September. In November SST gradually recovers to warm levels reached towards the end of the year (fig.1.4). The strongest imprint of the seasonal cycle as well as inter-annual variability is found at 10°W [*Jouanno et al.*, 2011], which is therefore often considered as the center of the ACT.
 Attempts to provide a complete description of the seasonal cycle of the ML heat balance from observations have yet been unsuccessful in closing the heat budget within this region: *Foltz et al.* [2003] obtained a residual heat gain of the ML on the order of 50 Wm^{-2} during boreal spring and early summer in the central tropical Atlantic (23°W), and on the order of 100 Wm^{-2} from late boreal spring to late autumn in the center of the ACT. The residual includes all unresolved processes such as the diapycnal heat flux, which could not be estimated from their data set, as well as errors. Similar residual heat gains in the ACT region were obtained in a recent study by *Wade et al.* [2011a] and have been previously reported for the eastern equatorial Pacific [*Wang and McPhaden*, 1999]. Note, that at other locations in the western equatorial Atlantic and in the southern ACT region the residuals determined by *Foltz et al.* [2003] were neglegible.
Numerical simulations with high-resolution general ocean circulation models have found the he-
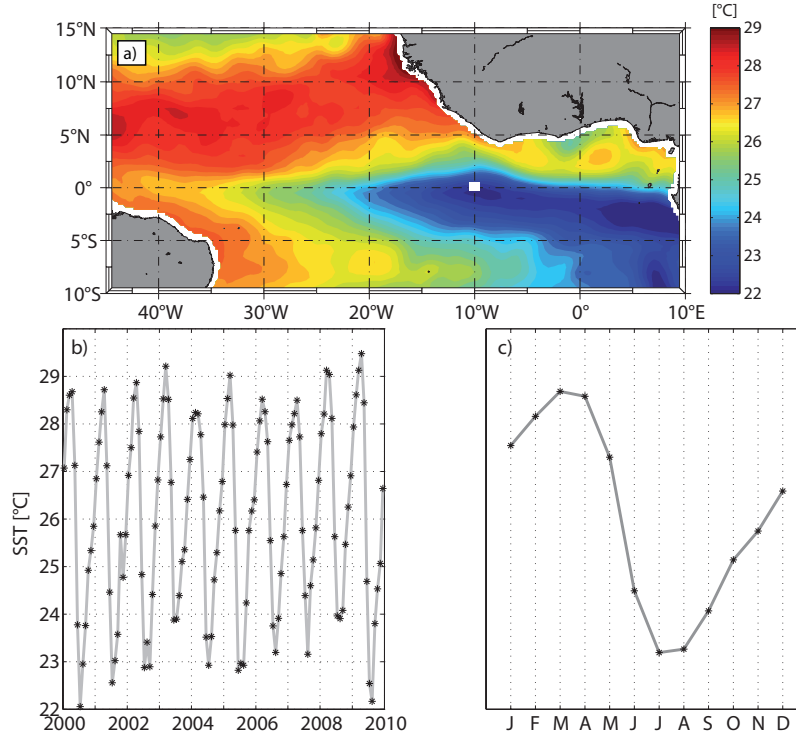
1. Introduction

Figure 1.4.: a) SST in the tropical Atlantic during July 2001 as observed with a satellite (white square marks area for figures b and c); b) inter-annual variability of SSTs at 10°W on the equator during years 2000-2009;c) average seasonal cycle (2000-2009) of SSTs at 10°W on the equator

at budget of the ML within the ACT region mainly controlled by air-sea interactions, vertical processes at the base of the ML and lateral advection of heat due to TIWs [*Peter et al.*, 2006; *Jouanno et al.*, 2011]. Of the different vertical processes, turbulent diapycnal heat flux due to mechanical mixing in the stratified vertically sheared equatorial current system was found to dominate mixed layer cooling [*Jouanno et al.*, 2011].

Could variations in turbulent mixing intensity be a suitable candidate for significantly affecting seasonal SST variability within the ACT region? It seems that a clarification of the role of diapycnal mixing on seasonal SST variability within the ACT region is pending. The process studies about turbulent mixing conducted within the equatorial Pacific were carried out at the western edge of the cold tongue. Additionally, they were devoted to individual processes shaping turbulent mixing intensity. A detailed study of the seasonal as well as regional variability of turbulent mixing intensity and the inferred diapycnal heat fluxes within the cold tongue region of either ocean has up to date not been performed. Hence, the contribution of the diapycnal heat flux to the ML heat budget during different stages of ACT development could not be clarified. Within the framework of this study an extensive observational microstructure data set consisting of repeated sections within the ACT region during different seasons is analyzed. The regional as well as seasonal variability of mixing intensity will be assessed and the contribution of the diapycnal heat flux to the ML heat budget investigated.

1.3. Turbulence in equations

To understand the setup of microstructure measurements, the meaning of the typically discussed parameters and their associated error sources, a brief introduction to theoretical concepts in the description of turbulence will be given. In addition, these theoretical concepts help to understand the design of parametrization schemes for various ocean regions.

Surprisingly, despite the enormous differences in scales, all motions in the oceans are included in a single set of deterministic equations, namely the Navier-Stokes-Equations on a rotating earth as part of the hydrodynamic equation system. As in many cases, scientists are interested in the mean state of the ocean and in addition, computational resources can not resolve the whole range of scales when numerically modelling the oceans, the so called Reynolds-averaging is introduced. Thereby all variables are split into an average and fluctuative part, the latter often being associated with the turbulent part of the motion, in the form $u = \overline{u} + u'$. The overbar denotes an average over time. Subsequently an average over time for the whole equation is performed. For example, a simple conservation equation for a variable ψ considering a local time derivative, an advection term and the divergence of the flux due to molecular diffusion has the form

$$\frac{\partial}{\partial t}\psi + \mathbf{u}\nabla\psi = \nabla\mathbf{k}\nabla\psi. \tag{1.2}$$

When performing Reynolds-averaging, the equation can be written as

$$\frac{\partial}{\partial t}\overline{\psi} + \overline{\mathbf{u}}\nabla\overline{\psi} = \nabla(\mathbf{k}\nabla\overline{\psi} - \overline{\mathbf{u'}\psi'}). \tag{1.3}$$

The derived equation describes the evolution of the average variable ψ $(\overline{\psi})$, nevertheless its form is highly similar to the initial equation. The difference is the appearance of an additional term associated with a turbulent flux: the averaged covariance of the fluctuative parts of u and ψ. Obviously, no statement about the average field is possible without knowledge of this turbulent flux, which is also referred to as Reynolds stress. Hence, in order to solve the equation, an expression for the turbulent flux is required. Speaking for the whole system of equations, several turbulent terms have to be reformulated in order to find solutions for the average fields. In fact, additional equations for turbulent fluxes can be formed, unfortunately they include further unknown terms only displacing the problems of closure to terms of higher order. This vicious circle is often referred to as the closure problem of turbulence. In order to escape this vicious circle and to find simple expressions for the required turbulent terms, the nature of these turbulent flux terms and its effects need to be investigated.

Turbulent motions are often referred to as chaotic, as it often appears that despite of apparently the same boundary conditions, turbulent motions progress very differently. This is due to the diffusive nature of turbulence, which will act to increase small deviations in the boundary conditions. Particles starting from close-by positions will in a statistical average tend to be departed from each other. The analogy to molecular diffusion, although highly less efficient, is often used to describe some statistical parameters of turbulent fluxes. As a descriptive example mixing milk into a cup of coffee is often used. One has to wait a long time until the milk is mixed with

1. Introduction

the coffee via molecular diffusion. By stirring the contents of the cup with the spoon, applying turbulent motion, accelerates this process tremendously. However, even if turbulent mixing is highly more effective than molecular diffusion, turbulent mixing does not exist without molecular diffusion: turbulent mixing can not exchange properties across isolines as does molecular diffusion. Instead the effect of turbulent mixing is to enlarge the gradients between e.g. milk and coffee increasing the effectiveness of molecular diffusion.

However, the analogy of the turbulent flux in its effect to the molecular diffusive flux, which can be expressed by the first law of Fick [*Fick*, 1855] via

$$J_i = -k \frac{\partial \psi}{\partial x_i}, \tag{1.4}$$

with a diffusivity coefficient k led to the proposal that turbulent fluxes can be reformulated in a similar way:

$$\overline{\mathbf{u}'\psi'} = -\mathbf{K}\nabla\overline{\psi}. \tag{1.5}$$

This expression is often referred to as the "Austauschansatz". Note, that in terms of diffusivities (k, K), the observed abyssal background value for the turbulent diffusivity K is two orders of magnitudes higher than the molecular thermal diffusivity of water (k), which is approximately $1.4 \cdot 10^{-7} m^2 s^{-1}$ reflecting the differences in effectiveness between the molecular and turbulent flux. It has to be kept in mind though, that the molecular diffusivity k is a physical property, while K is a statistical property defined to describe the effects of turbulence.

The subsequent question arising if the magnitude of these turbulent fluxes and hence its effect on the mean field is to be inferred, is how to get a handle on K. As the pure definition of a turbulent diffusivity K is rather an appliance than build on a physical principle - lacking a complete theory of turbulence - complicated constructs of assumptions and simplifications of equations are used to either infer the magnitude of K from direct observations or express its magnitude via known variables, so called parametrizations of K, which are required for numerical modelling.

Kinetic energy is believed to cascade from the large scale current systems to small, turbulent scales via eddies and waves. If these waves break, motions become turbulent and kinetic energy will be partly transferred to potential energy. The other part will be dissipated on the smallest scales meaning a conversion of kinetic energy to heat, describing the loss of kinetic energy of the system. Without continuous energy input by the wind and tides this cascade would break down, after the complete energy is dissipated. The fundamental equation describing the gain and loss of turbulent kinetic energy is the Turbulent Kinetic Energy (TKE) Equation. *Kolmogorov* [1942] was the first to propose the supplementation of the energy balance equations (for the mean kinetic energy (MKE) and the TKE) in an attempt to close the Reynolds equation system. At first this attempt seems hopeless, as it introduces new unknowns (again highlighting the closure problem). Nevertheless, these equations impose further constraints on the statistical character of turbulence. In addition, as the physical meaning of the additional terms in the energy balance equations is rather clear this helps in expressing them via simpler characteristics [*Monin and Yaglom*, 1965]. The TKE equation is derived by multiplying the non-hydrostatic Navier-Stokes-

Equations on a rotating earth by u'_j, summing over the indices j=1,2,3 and applying Reynolds-averaging resulting in:

$$\frac{\partial}{\partial t}\overline{E} + \overline{u_i}\frac{\partial}{\partial x_i}\overline{E} = -\frac{\partial}{\partial x_i}\overline{u'_i p'} - \overline{u'_i\frac{\partial}{\partial x_i}E} + \frac{\partial}{\partial x_i}\nu\frac{\partial}{\partial x_i}\overline{E} - \overline{u'_j u'_i}\frac{\partial}{\partial x_i}\overline{u_j} + \overline{w'b'} - \epsilon, \qquad (1.6)$$

where $\overline{E} = \frac{\overline{u'^2_1 + u'^2_2 + u'^2_3}}{2}$, is the turbulent kinetic energy, b is the buoyancy ($b = -g\frac{\rho}{\rho_0}$), $u_{i,j}$ are the velocity components and $x_{i,j}$ are the coordinates. The summation convention is invoked, implying summation over the index, which shows up twice in one term. The terms on the left hand side describe the local time derivative and the advection of TKE by the mean flow. On the right hand side terms represent from left to right the turbulent pressure work, the advection of TKE via the turbulent velocity, which is sometimes referred to as triple correlation, the molecular diffusion of TKE, the production or loss of TKE via the interaction of the shear of the mean flow with the turbulent flow, the production or loss of TKE via the turbulent buoyancy flux and finally the dissipation of TKE. If this equation is integrated over a closed volume, the first two terms on the right hand side as well as the advection term on the left hand side, would not contribute to the total TKE. These terms only act to redistribute TKE within the volume and are therefore often named the transport terms. The remaining terms are the production terms and the dissipation as well as the comparably small contribution of molecular diffusion. These remaining terms are often thought of as the physically more relevant ones.

In order to actually get a measure of the diffusivity K, *Osborn* [1980] suggested to simplify the TKE equation by assuming stationarity, horizontal homogeneity and neglecting the transport terms of TKE. Thereby, *Osborn* [1980] ended it up with a local balance of the production terms and the dissipation:

$$0 = -\overline{w'u'_j}\frac{\partial \overline{u_j}}{\partial z} + \overline{b'w'} - \epsilon = \overline{b'w'}(1 - \frac{1}{R_f}) - \epsilon, \qquad (1.7)$$

if defining the Flux Richardson number R_f as:

$$R_f = \frac{\overline{b'w'}}{\overline{w'u'_j}\frac{\partial \overline{u_j}}{\partial z}}, \qquad (1.8)$$

the ratio of the turbulent buoyancy flux to the production term of TKE via interaction with the mean flow. *Osborn* [1980] argues that for steady state energy arguments require this value less than 1. In fact, he states there are good arguments that the value is considerably less than 1. Furthermore, if the "turbulent mixing efficiency" γ is introduced as $\gamma = R_f/(1 - R_f)$ equation 1.7 can be simplified to

$$\overline{b'w'} = -\gamma\epsilon. \qquad (1.9)$$

As $R_f << 1$ is assumed, γ must also be considerable less than 1. As the term "turbulent mixing efficiency" suggests it describes the fraction of TKE, which is used to actually mix the water, meaning the fraction of TKE, which is converted to potential energy via the buoyancy flux. It is only a small fraction of the dissipation rate, implying that the vast amount of TKE is lost by dissipation. If now the Austauschansatz (equation 1.5) is invoked, the turbulent buoyancy flux

can be written as

$$\overline{b'w'} = -K_\rho \frac{\partial \overline{b}}{\partial z} = -K_\rho N^2 \qquad \text{with} \qquad N^2 = \frac{g}{\rho_0} \frac{\partial \rho}{\partial z}. \tag{1.10}$$

N^2 is termed the Brunt-Väisälä frequency and describes the stability of the water column. The resulting expression, if combing equation 1.9 and 1.10, for the turbulent eddy diffusivity of mass is

$$K_\rho = \gamma \frac{\epsilon}{N^2}. \tag{1.11}$$

Fortunately, the turbulent dissipation rate ϵ can be estimated from observations with high precision microstructure measurements (see chapter 2). Therefore equation 1.11 opens the possibility of inferring the magnitude of the turbulent eddy diffusivity from direct observations. It has to be kept in mind though, that this measure is build upon simplifications of the original equations and should therefore be treated with caution than being regarded as a direct, conclusive measure. Nevertheless, its use has been widely accepted and the obtained estimates of K_ρ have been confirmed by tracer release experiments [*Ledwell et al.*, 1993]. Together, these observations of K_ρ have opened the discussions on the hot spot theory as discussed above as they pointed out the discrepancy between the observed [*Osborn and Cox*, 1972; *Gregg*, 1989] and postulated [*Munk*, 1966] values for K_ρ for the open ocean. The expression for K_ρ (equation 1.11) can then further be used to determine a turbulent flux as proposed by equations 1.5 and 1.10.

In a similar procedure, *Osborn and Cox* [1972] determined the turbulent eddy diffusivity for heat (K_h) from the turbulent temperature variance equation:

$$K_h = \frac{\chi}{2(\partial \overline{T}/\partial z)^2}, \tag{1.12}$$

where χ is the turbulent dissipation rate of temperature, which can also be estimated from observations with microstructure instruments.

However, microstructure measurements are rather costly and can be applied only locally in space and time. Nevertheless, they have given enormous insight into the processes involved in shaping turbulent mixing intensity. The obtained knowledge and data sets have been used to infer parametrizations relating turbulent diffusivities to large scale parameters, such as e.g. shear and stratification. These parametrizations can then be implemented into numerical models to close the Reynolds equation system.

The inferred parametrization schemes used for numerical modelling are divided into schemes for boundary layers and the interior of the ocean, as the turbulence dynamics are found rather different. The boundary layers are highly active turbulent layers, as the direct influence of the wind at the surface leads to rigorous, continuous mixing, which is mainly not the case for the ocean interior.

For the surface boundary layers turbulent fluxes of a variable ψ (typically any tracer or one component of the velocity) are parametrized as

$$\overline{u_i' \psi'} = -c_\psi K \frac{\partial}{\partial x_i} \overline{\psi} \tag{1.13}$$

with $K = L\overline{E}^{0.5}$, whereas L is a length scale usually associated with eddies, and c_ψ is called the stability function, which can be a simple constant. With knowledge of $\overline{E}$, L and c_ψ the turbulent fluxes can be estimated, whereas $\overline{E}$ is calculated via the TKE equation, which is often further simplified by assuming horizontal homogeneity. As there are still unknown terms in the TKE equation and L is unknown, further assumptions are made resulting in different closures for the boundary layer models. E.g. *Gaspar et al.* [1990] closed the system by combining some of the unknown terms and finding algebraic expressions for L. Others form additional prognostic equations for either ϵ or $\overline{E}L$, which are used to derive an expression for L. The ones using an equation for ϵ are referred to as the k-ϵ closure schemes (k stands for TKE), the others using $\overline{E}L$ are named Mellor-Yamada models. In another approach equation 1.13 is extended by a non-local term γ_ψ, whereas this additional term can be dependant on e.g. the stratification and forcing, which was proposed by *Large et al.* [1994] and is named the KPP parametrization for boundary layers. In addition, another possibility in attempting to close the system is again forming equations for the turbulent fluxes theirselves, which will lead to a set of additional equations with unknowns of higher order (in need for parametrizations), which are referred to as closures of higher order. Some of the microstructure observations obtained within the framework of this study are used to validate the boundary layer model of *Gaspar et al.* [1990]. The collaboration with a french research group lead to the publication of *Wade et al.* [2011b], which is shortly summarized in Appendix C1.

For the interior of the ocean parametrization schemes are of a different form due to the generally different turbulence dynamics. As mentioned above, estimates of ϵ from microstructure observations and the use of equation 1.11 has shown that a homogeneous open ocean diffusivity of $1 \cdot 10^{-4} m^2 s^{-1}$ oversimplifies the situation. The availability of different data sets for different oceanic regimes lead to different parametrization schemes for characteristic regions of the ocean interior. For completeness, the principle ideas of parametrizations for the open ocean as well as shelf regions are pointed out, although they are not further discussed within this study.

For the open ocean case, in the absence of topographic features, background dissipation and diffusivity levels are assumed to be determined by the breaking of internal waves. For this case, parametrizations are often related to the energy level or shear level provided by the internal wave field. The internal wave field itself is often referred to as part of the finestructure acting on scales of 10-100m. The parametrizations mainly rely on the internal wave field being in a steady state described by the universal functional form of *Garrett and Munk* [1972] or its modified versions [*Garrett and Munk*, 1975, 1979]. The qualitative form of the vertical shear spectrum of horizontal velocities as a function of vertical wavenumber as proposed by *Garrett and Munk* [1972] was confirmed by the observations of *Gargett et al.* [1981] (fig.1.5): a white spectrum until some critical wave number k_0, followed by a k^{-1} roll-off. Beyond the roll-off, which points to a change in the physical processes involved, the turbulence spectrum follows up. Many parametrizations are build upon the principle, that an elevated spectral level at low wavenumbers associated with internal waves (which is then actually measured) is followed up by an elevated level of the turbulence spectrum and hence a higher dissipation rate, which is thereby
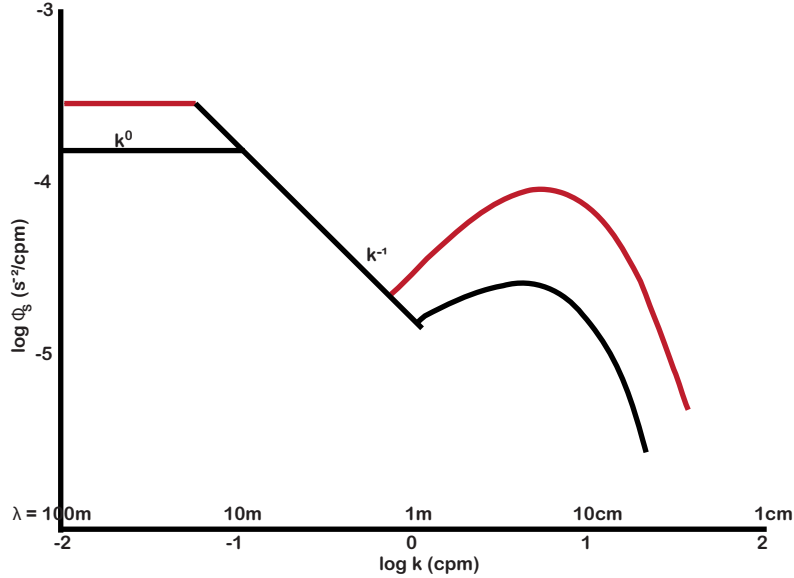
Figure 1.5.: Composite spectrum of vertical shear of horizontal velocities from vertical scales of 100m to a few centimeters based on a combination of observations from three profilers [*Gargett et al.*, 1981]; an additional assumed curve for elevated shear levels is shown (red).

parametrized (fig.1.5). *Henyey et al.* [1986] proposed a parametrization relating the dissipation rate ϵ to the energy flux through the wavenumber spectrum towards high vertical wavenumbers. Various parametrizations are modifications of this model relating the dissipation rate to the shear spectral level, shear variance or some related parameter, the Coriolis parameter f and N^2 [e.g. *Gregg*, 1989; *Polzin et al.*, 1995; *Fischer*, 2011].

Shelf regions, which are believed to be in a more rigorous state of mixing have modified parametrizations as proposed e.g. by *MacKinnon and Gregg* [2003] and investigated in *Schafstall* [2010], which are also based on the dynamical model of *Henyey et al.* [1986]. Here, the energy flux towards high wavenumbers is not inferred from the steady state spectrum proposed by *Garrett and Munk* [1972], but estimated via WKB scaling.

Within the context of this study the parametrization schemes for the ocean interior within the equatorial region are further considered (see chapter 7). For this region, the basic assumption is, that mixing intensity is mainly associated with shear instabilities triggered by the large scale background shear provided by the highly energetic equatorial current system. Therefore, parametrizations for this region relate mixing intensity (in terms of dissipation rates ϵ or eddy diffusivities K) to the gradient Richardson number (Ri), which is defined as

$$Ri = \frac{N^2}{S^2} \tag{1.14}$$

relating the shear variance (S^2) of the large scale current system to the stratification (N^2). (Note, that the gradient Richardson number is the resulting expression of the Flux Richarson

number (equation 1.8), if the Austauschansatz is invoked for both of the turbulent fluxes).

Hence, as for some parametrizations developed for the open ocean mentioned above, the shear variance has to be determined. For the open ocean case, where mixing intensity was associated with a background internal wave field in steady state over a considerable depth range of several hundred meters, determination of the shear spectral level or shear variances relies on the evaluation of shear spectra. For this purpose complete profiles are fed into the routines, resulting in one characteristic mixing value for ϵ or K_ρ. On the contrary, for the equatorial region, where mixing is associated with the large scale background shear provided by the equatorial current system, shear levels strongly vary with depth. Therefore, the determination of shear variances for the parametrization schemes of the equatorial region is based on simple first differencing of the velocity profiles, providing a vertical profile for shear variances. Hence, mixing intensity in terms of ϵ or K_ρ can thereby be parametrized as a depth varying function of shear and stratification. The simplicity of the first differencing method is in addition appealing for numerical modeling, where the resolution between layers is often too coarse for reliable estimations of the shear spectra.

However, based on a simple Ri dependence, with shear variances determined from first differencing, several parametrization schemes for the equatorial oceans have been proposed, which have been tuned to fit different data sets or models: The interior KPP [*Large et al.*, 1994], which is supposed to cover open ocean as well as equatorial conditions, consists of an internal wave contribution, assumed to be constant, as well as a contribution dependant on Ri. Other functional dependencies on Ri have been proposed by *Peters et al.* [1988] and *Pacanowski and Philander* [1981]. *Zaron and Moum* [2009] state that Ri dependant parametrizations are not adequate and extend their functional forms by additional parameters (see chapter 7 for details on the equatorial parametrization schemes).

However, a variety of parametrization schemes (not only for the equatorial region, but for all different oceanic regimes) are available and point towards the diversity of solutions, when trying to tackle the turbulent terms. Without a complete theory of turbulence at hand, the question arises, which solution is the least evil. Therefore, every additional data set of microstructure observations has to be used to understand the processes shaping mixing intensity and to validate and improve the existing parametrization schemes.

1.4. Aim and structure of this study

The role of the small scale process termed turbulent mixing for the mean climate state has been pointed out. Furthermore, the upper layers of the tropical Atlantic could be distinguished as an adequate "hot spot" for investigating turbulent mixing intensity and to gain insight in the involved processes. In addition, the need to clarify the contribution of the diapycnal heat flux to the heat budget of the ML within the equatorial ACT region could be emphasized. Principles and parameters for the estimation of turbulent fluxes were described.

1. Introduction

In chapter 2 the main circulation of the tropical Atlantic as well as its seasonal and intra-seasonal variability are described. In contrast to former process oriented studies in the equatorial Pacific, this study aims to provide integral estimates of mixing related parameters representative for different seasons and regions in the eastern tropical Atlantic. For this purpose a unique data set from the tropical eastern Atlantic ocean consisting of 8 cruises carried out between 2005 and 2008 is analyzed combining observations of microstructure shear and temperature as well as large scale velocity data and hydrography as described in chapter 3. In chapter 4, the observed seasonal and regional variability in background conditions for turbulent mixing in terms of shear and stratification resulting from the variability in large-scale conditions as described in chapter 2 is discussed. These varying background conditions are related to the variability of dissipation rates of turbulent kinetic energy (ϵ), eddy diffusivities (K_ρ) and diapycnal heat fluxes (J_h) in chapter 5. In chapter 6 the contribution of the assessed diapycnal heat fluxes to the mixed layer heat budget is discussed by estimating individual terms of the budget at different locations within the ACT. As numerical models depend heavily on parametrization schemes, chapter 7 investigates the adequacy of the different proposed equatorial parametrization schemes for the presented data set. A synthesis of the obtained results is given in chapter 8.

2. The tropical Atlantic

The mean upper-layer circulation of the tropical Atlantic is a superposition of different dynamical regimes. The main current features of the upper-layer circulation system are primarily wind-driven, such as the North and South Equatorial Currents (NEC, SEC) as part of the subtropical gyres, the EUC as well as the North Equatorial CounterCurrent (NECC) and their associated seasonal variability. Additional wind-driven features are the so-called Sub-Tropical Cells (STCs). The upper limb return path of the MOC transporting warm waters northward within the Atlantic modifies the wind-driven circulation patterns resulting in the observed mean circulation pattern for the upper layers in the equatorial Atlantic (fig.2.1).

To understand the wind-driven circulation pattern, the wind-induced Ekman transports (90° to the right of the wind direction on the northern hemisphere, 90° to the left on the southern hemisphere) have to be considered, which lead to convergences and divergences due to the meridionally varying wind pattern as shown schematically in fig. 2.2. The resulting average differences in sea level cause pressure gradients, which are balanced by geostrophic currents (for geostrophy, the pressure gradient force is balanced by the Coriolis force). The scheme observed in the tropical Atlantic is not symmetric about the equator as the ITCZ, characterized by the light wind belt of the Doldrums, is always positioned north of the equator, forcing the south-easterly trades to traverse the equator. The meridional migration of the ITCZ during the year imposes seasonal variability on the wind driven currents e.g. the NECC and nSEC [*Stramma and Schott*, 1999]. For the EUC the balance is modified due to the vanishing Coriolis force at the equator: The zonal component of the trades cause a pressure gradient along the equator due to a convergence of waters at the western boundary. A compensating flow within the subsurface layer is invoked, which is balanced by frictional forces providing the balance for the EUC.

Concerning the MOC, the strength of the northward return flow within the warm water sphere referred to as the upper limb was estimated by *Ganachaud and Wunsch* [2000] to be of about 16 Sv in the Atlantic passing the equator within the upper layer western boundary current, the North Brazil Current (NBC). *Schott et al.* [2004] state that this northward flow reaches the northern subtropics by 2 routes. The first route consists of the separation of rings from the retroflection of the NBC, which travel further northward into the Carribean. The second route is proposed as an eastward detours into the zonal equatorial currents, mainly the EUC, NEUC and NECC. Thus, changes in the strength of the return flow could possibly change the amount of water fed into these zonal currents causing additional variability. Nevertheless, variations in the strength of this return flow are presumed to act on timescales of inter-annual to decadal.

STCs are referred to as shallow overturning cells (confined to the upper 500m of the water column) connecting subduction regions in the subtropics of both hemispheres with upwelling areas in the eastern equatorial region. The existence and strength of the STCs is strongly influenced
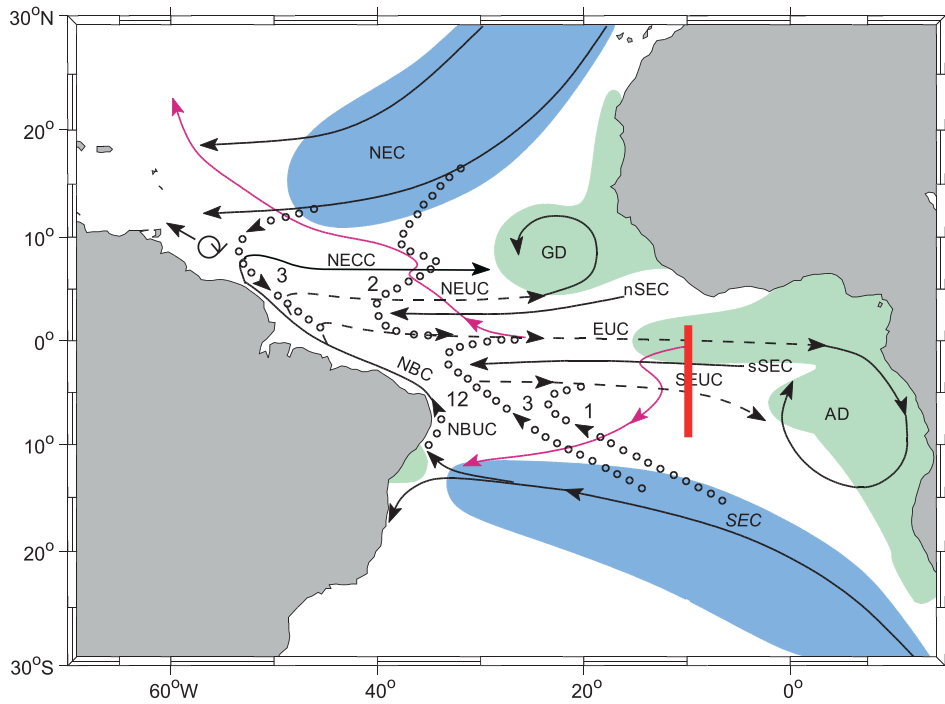
Figure 2.1.: Schematic representation of the upper layer equatorial Atlantic circulation system participating in the STC. Subduction (blue) and upwelling (green) zones are indicated. Surface currents are marked with solid lines, undercurrents with dashed lines. Interior equatorward thermocline pathways of the STCs are dotted, the numbers represent transport estimates for interior and western boundary pathways. Surface poleward pathways for the central basin are marked by thin magenta lines. Red line marks the 10°W section shown in fig.2.3. From *Schott et al.* [2004]
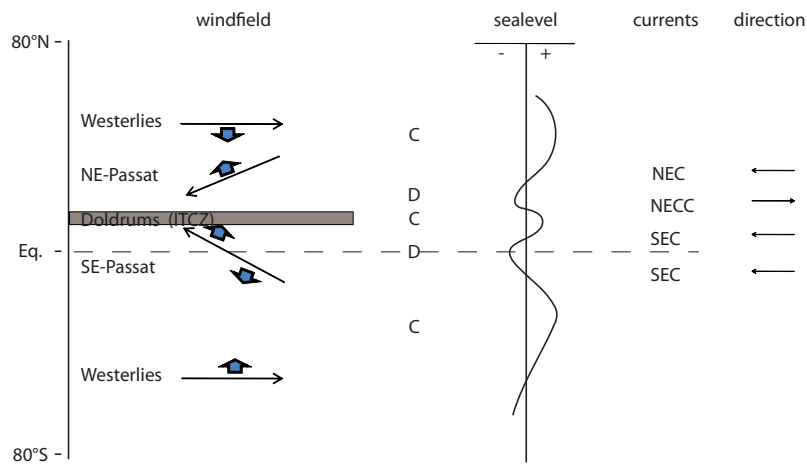

Figure 2.2.: Schematic of the wind driven surface circulation in the tropical Atlantic. The large-scale wind circulation is indicated with black arrows on the left and the resulting Ekman transports indicated by blue arrows. The resulting convergence (C) and divergence zones (D) are indicated with letters to the right and the resulting displacement of the sea level is indicated with the black curve in the middle of the sketch. The balancing geostrophic currents due to these pressure differences are indicated on the far right.

by winds at the tropical-subtropical border. These winds cause poleward Ekman-flow draining surface waters out of the tropical region, forcing a compensating return flow [*Schott et al.*, 2004; *McCreary and Lu*, 1994; *Malanotte-Rizzoli et al.*, 2000]. Subduction rates, where subduction is referred to as a flux across the base of the ML, are composed by vertical and lateral components [*Karstensen and Quadfasel*, 2002]. The vertical component is mainly due to Ekman pumping, a result of the negative windstress curl. The lateral component is due to horizontal advection through a tilted mixed layer base. The water subducted in the eastern subtropics in both hemispheres flows equatorward via interior pathways [*Liu*, 1994]. Within the equatorial region these thermocline waters also feed into the zonal current system. The primary equatorial branch of the STCs is associated with the EUC bringing waters eastward to the areas of strong Ekman divergences, where they are presumed to be upwelled. If purely wind-driven these cells would probably be of the same strength in both hemispheres as was found in model studies driven by winds only [*Frantantoni et al.*, 2000]. The asymmetry of the cells in the Atlantic is induced by the purely northward return flow of the MOC, leading to a stronger STC in the southern hemisphere compared to the northern one [*Zhang et al.*, 2003; *Frantantoni et al.*, 2000]. *Schott et al.* [2004] reported that mainly wind anomalies on the tropical-subtropical border influence the strength of the STCs circulation and thereby can impact the transport of the EUC on inter-annual to decadal timescales.
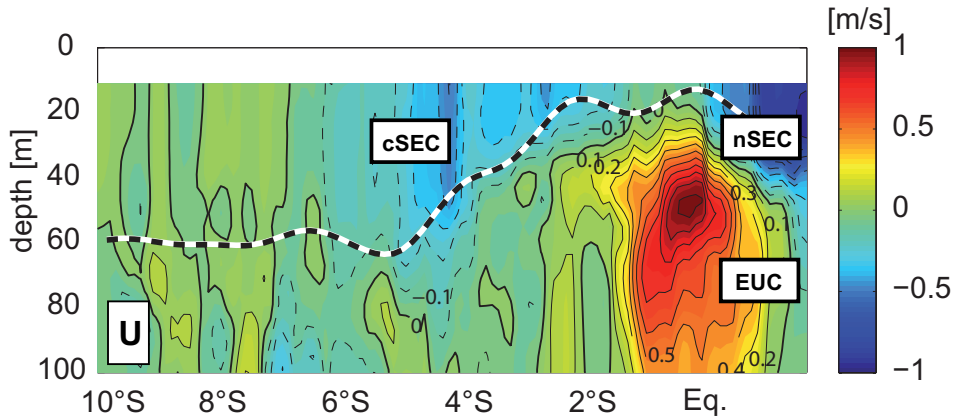

Figure 2.3.: Zonal velocity along 10°W during EGEE3 (June 2006) from 10°S to 1.5°N. The black and white line denotes the MLD. Location marked in fig.2.1 as red line.

Within the region of the ACT surface westward flow associated with the SEC occurs in two current branches. The northern nSEC is located between the equator and 4°N while the cSEC is situated between 6°S and 2°S [fig. 2.3, e.g. *Molinari*, 1982; *Kolodziejczyk et al.*, 2009; *Brandt et al.*, 2010]. Between the westward flows, the eastwards EUC can be found between 2°S and 2°N with maximum velocities of $1 ms^{-1}$ at a depth of 40m to 80m. In the southern ACT region zonal velocities are strongly reduced. *Stramma and Schott* [1999] mention the presence of the eastwards SECC at around 8°S within the upper 100m of the water column. However, they also refer to ambiguous observations of zonal velocities (eastwards as well as westwards) in the upper layers of the eastern South Atlantic. In the velocity data presented here, the SECC can not be clearly detected. This exemplary section suggests the equatorial ACT region being

dominated by strong surface as well as subsurface currents, while the southern ACT does not inhibit comparable strong current features. In addition, the section reveals mixed layer depths considerably lower in the southern ACT region than in the equatorial band.

In the following, the regional, seasonal and some of the intra-seasonal variability of large-scale features such as surface forcing, the current system and MLDs representative for the ACT region are discussed. As fig.2.3 suggests the equatorial (2°S-2°N) and southern (10°S-6°S) ACT region to be subject to rather different dynamics these regions will be distinguished.

2.1. Net surface heat flux

As was mentioned in the introduction, the equatorial Atlantic is characterized by positive net surface heat fluxes throughout the year. Within the equatorial ACT region (2°S-2°N) the net surface heat flux ranges from 20-150 Wm^{-2} (fig.1.2, 2.4a). The seasonal variability in the net surface heat flux is caused by variations in the incoming shortwave radiation and the latent heat flux, while sensible and outgoing long wave heat fluxes remain rather constant throughout the year. In the central basin (30°W-5°W) the net surface heat flux is dominated by a semi-annual cycle with a first peak in February/March and a second peak occurring from July to September. As previously discussed [*Marin et al.*, 2009], this second peak, caused by a reduction of the latent heat flux due to decreasing surface winds, acts against the development of the cold tongue by warming the upper ocean at a rate of 100-120 Wm^{-2}. In the eastern part of the equatorial ACT east of 5°W, net surface heat fluxes are reduced and between 20 and 90 Wm^{-2}, exhibiting a minimum from May to August. This minimum is due to reduced short wave radiation and increased latent heat flux.
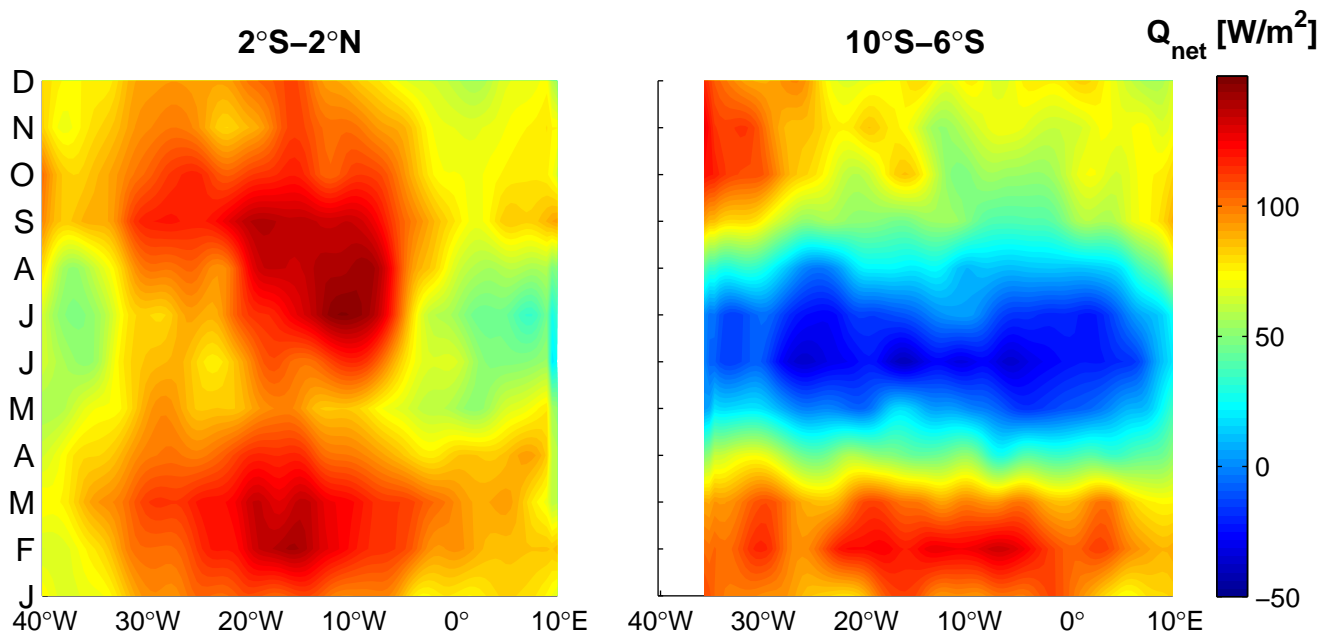

Figure 2.4.: Seasonal evolution of net surface heat flux [*da Silva et al.*, 1994] for the equatorial (left panel) and southern ACT region (right panel)

The southern ACT region between 10°S-6°S comprises negative as well as positive net surface he-
at fluxes ranging from -50-150 Wm^{-2} accordingly cooling or warming the upper ocean (fig.2.4b).
The entire basin within this latitudinal belt is dominated by an annual cycle reaching minimum
values of up to -50 Wm^{-2} from May to July cooling the upper ocean during cold tongue deve-
lopment. These negative net surface heat fluxes result from a reduction in the incoming solar
radiation during boreal summer and an increase of the latent heat flux from April to September,
which is caused by increasing surface winds. Maximum values are found in February when the
incoming solar radiation is strongest and the latent heat flux is at its minimum.

2.2. Winds

The main atmospheric circulation is dominated by the trade winds surrounding the ITCZ. The
migration of the ITCZ during the year shifts the prevailing wind pattern meridionally. The
ITCZ itself is associated with the zone of rather light winds referred to as the Doldrums, which
separate the large regions influenced by the trade winds. The largest differences in the wind
pattern is observed comparing the February/August monthly averages, as the ITCZ position is
closest/furthest to the equator (fig.2.5).
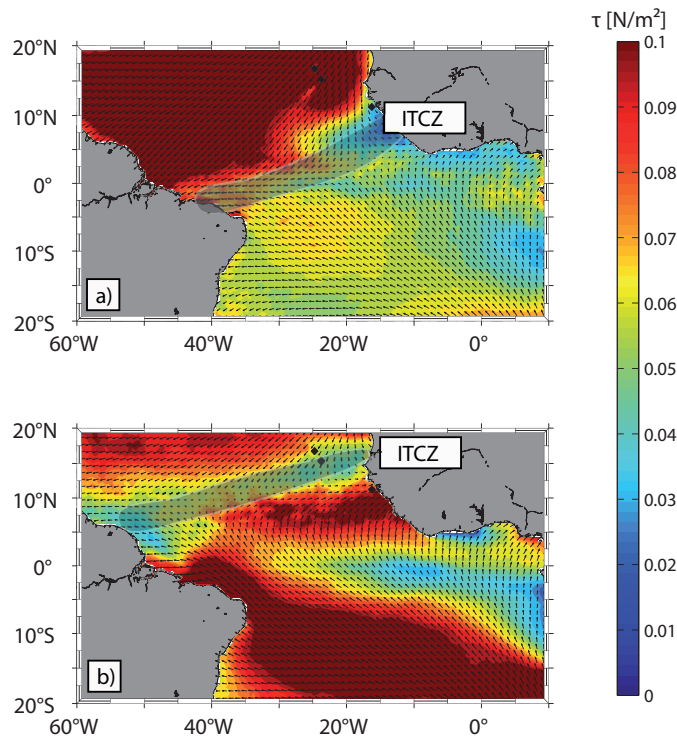
Figure 2.5.: Average monthly wind stress magnitude (2000-2009) in February (a) and August
(b) as observed by Quickscat. The light grey shaded area represents the light wind
belt associated with the ITCZ.

Related to this northward shift of the ITCZ and the huge temperature and humidity differences
between land and sea, is the seasonal appearance of the West African Monsoon (WAM) during
boreal summer. In general, a monsoon is associated with seasonal changes in the atmospheric

2. The tropical Atlantic

circulation (a characteristic is the reversal of the predominant winds) and related precipitation due to the asymmetric heating of land and sea. During boreal summer, when the ITCZ is at its northernmost position, the predominately dry north-easterly trades over West Africa get interrupted by humid southerly to south-westerlies associated with a strong increase in precipitation referred to as the WAM (fig. 2.5b).
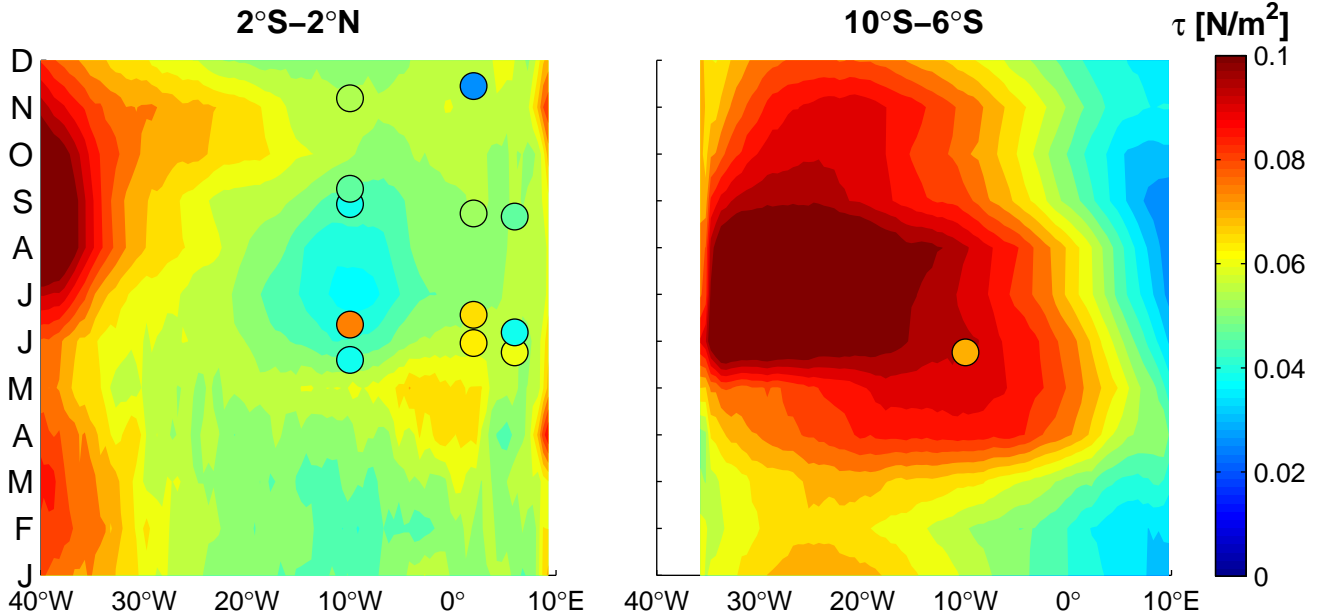

Figure 2.6.: Seasonal evolution of wind stress magnitude (from Quickscat winds) for the equatorial (left panel) and southern ACT region (right panel). Circles show observed values during the cruises.

Within the equatorial belt (2°S-2°N), the meridional shift of the ITCZ imprints a semi-annual cycle on the wind stress (fig.2.6a). Resulting magnitude and phase of this semi-annual cycle vary throughout the basin. In the central basin wind stress intensification are found in April/May and in October/November. The latter wind stress maximum has been reported to cause a second cooling of the ACT in late boreal autumn [*Okumura and Xie*, 2006, their fig.1b]. Superimposed on the seasonal variability are intra-seasonal wind bursts, which can elevate the wind stress locally and contribute to temporal variability of cold tongue development [*Marin et al.*, 2009]. *Yu et al.* [2011] find spectral peaks in zonal as well as meridional winds at intra-seasonal periods, among which the 40-60 day peak is evident across most of the equatorial basin. The southern ACT region (10°S-6°S) is dominated by an annual cycle in wind stress with maximum values during May to August, leading to the increased latent heat flux during this period.

2.3. Mixed layer depth

For the data used within the framework of this study the MLD was generally calculated with the temperature threshold criterion. The MLD is defined as the depth at which the temperature has reduced by $0.2°C$ compared to its surface value. Visual inspection of the individual profiles led
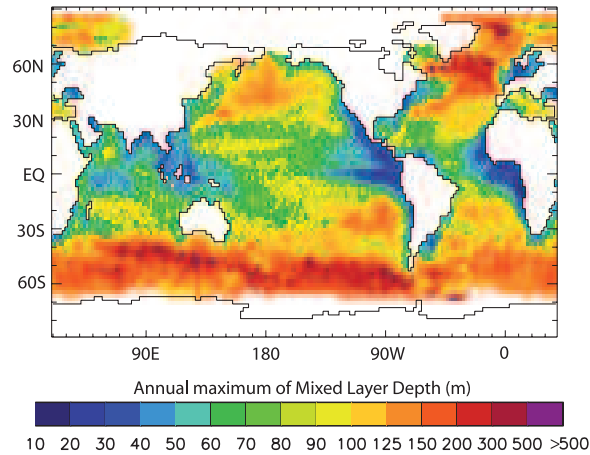
Figure 2.7.: Maximum annual MLD from the $\Delta T = 0.2°C$ criterion climatology. From *de Boyer Motegut et al.* [2004], their figure 14b.

to corrections in some cases. The threshold criterion of $0.2°C$ is also used in the ML climatology of *de Boyer Motegut et al.* [2004], which is further used in this study (chapter 6).

The eastern equatorial Atlantic is characterized by extremely shallow MLDs. East of 20°W from about 2°N to 4°S and within the Gulf of Guinea MLDs of only 10-30m are observed throughout most of the year [*de Boyer Motegut et al.*, 2004]. Within the equatorial belt (2°S-2°N) a seasonal cycle in the magnitude of the MLDs is observed with maximum values occurring in boreal autumn. During this period, mixed layers of 40m were reported for 10°W,0°N [*Foltz et al.*, 2003], while climatologies suggest mixed layers to be slightly shallower [fig.2.8a, *de Boyer Motegut et al.*, 2004]. In general MLDs are shallower in the eastern equatorial belt than in the west. This zonal MLD gradient is most pronounced between 40°W (70m) and 10°W (20m) during boreal summer and autumn. In fact the shoaling of MLDs can also be observed in the southern ACT region (10°S-6°S, fig.2.8b). Here MLDs are genereally deeper and reach their maximum during boreal summer.

2.4. Currents and variability

Surface The variability of zonal velocities in the equatorial belt (2°S-2°N) associated with the wind driven SEC is strongest in the central basin, extending until about 0°E into the Gulf of Guinea [*Lumpkin and Garaffo*, 2005] with maximum westwards velocities of up to $0.8ms^{-1}$. *Lumpkin and Garaffo* [2005] suggest that east of 0° possibly a joint, early SEC, as a combination of the nSEC and cSEC can be found. The seasonal variation [also shown in *Hormann and Brandt*, 2007] corresponds to the semi-annual variation in the wind stress: a strong SEC in boreal spring/summer accelerated shortly after the trade wind intensification in April/May and reduced in boreal autumn after the relaxation of the wind stress (fig.2.6a, 2.9a). The second increase in wind stress in late boreal autumn is weaker and accordingly, the second SEC maximum, as first reported by *Richardson and McKee* [1984] is reduced in comparison to the boreal summer maximum.
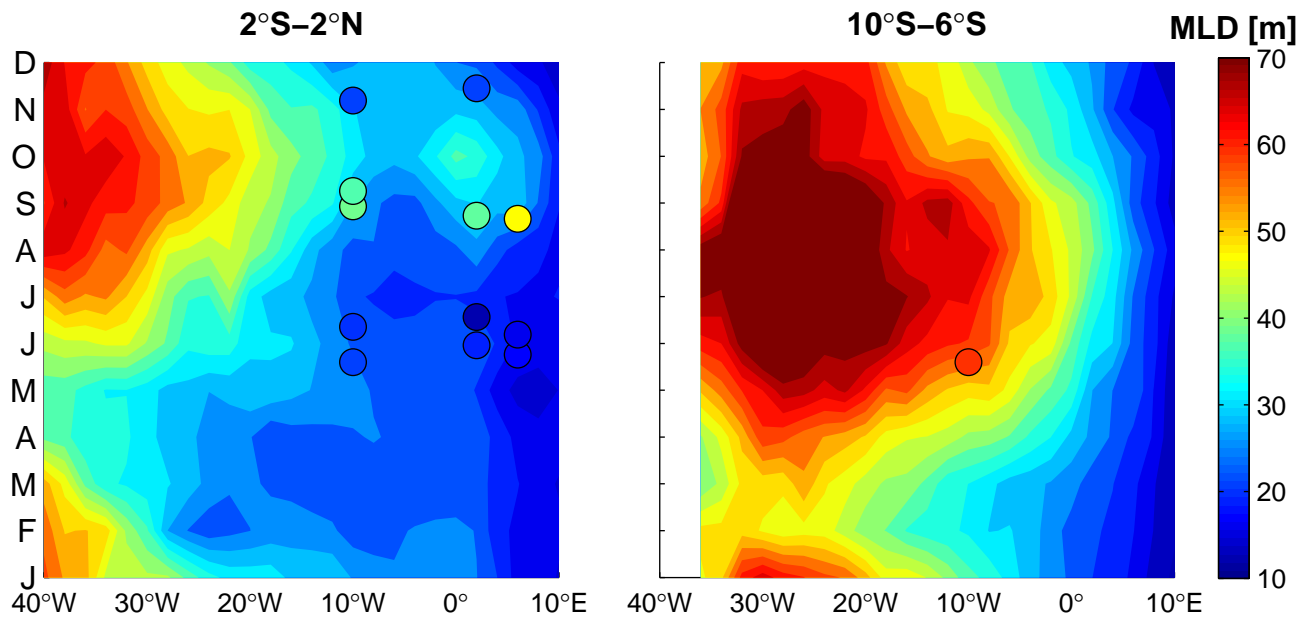
Figure 2.8.: Seasonal evolution of mixed layer depth [*de Boyer Motegut et al.*, 2004] for the equatorial (left panel) and southern ACT region (right panel). Circles show observed values during the cruises.
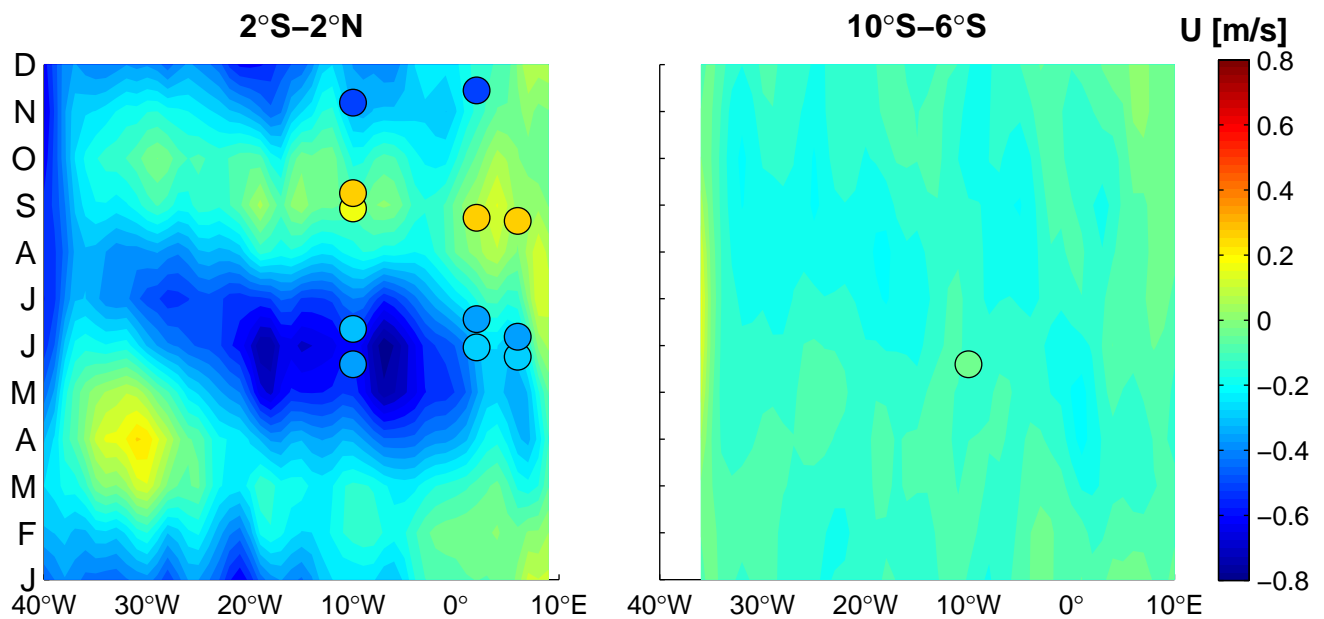

Figure 2.9.: Seasonal evolution of zonal surface velocities [*Lumpkin and Garaffo*, 2005] for the equatorial (left panel) and southern ACT region (right panel). Circles show observed values during the cruises.

In the southern ACT region (10°S-6°S) zonal surface velocities do not exceed 0.3 ms^{-1} and no clear seasonal variation is apparent (fig.2.9b).

Subsurface   A well-known feature of the subsurface flow in the equatorial belt (2°S-2°N) is the weakening and shoaling of the EUC from west to east [*Brandt et al.*, 2011; *Stramma and Schott*, 1999; *Bourlès et al.*, 2002; *Mercier et al.*, 2003; *Kolodziejczyk et al.*, 2009]. In the center of the basin at 23°W, the EUC is still rather strong and exhibits velocities above $0.8ms^{-1}$ at its core [*Brandt et al.*, 2011]. In the Gulf of Guinea, however, zonal velocities associated with the EUC are reduced and reach $0.6ms^{-1}$ at 10°W [fig.2.10a, *Kolodziejczyk et al.*, 2009; *Brandt et al.*, 2011]. Maximum eastward velocity of the EUC at 2°E (fig.2.10b) compiled from four EGEE cruises (3-6, tab.1), is only about $0.5ms^{-1}$ and its meridional extent is reduced being confined between 1°N and 1°S. In addition, the vertical extent of the EUC also diminishes towards the east (fig. 2.10). In the eastern Gulf of Guinea (6°E), the EUC appears to be a transient feature: during August 2000 an eastward subsurface current was not present between 2°S and 2°N [*Bourlès et al.*, 2002]. Additionally, the depth of the EUC core is modulated seasonally, deepening in boreal autumn in accordance with the MLD and thermocline movements as described by *Kolodziejczyk et al.* [2009] for 10° in agreement with observations at 23°W [*Provost et al.*, 2004; *Brandt et al.*, 2006, 2008]. However, the EUC strength in terms of maximum velocities does not seem to follow a distinct seasonal cycle [*Arhan et al.*, 2006; *Brandt et al.*, 2008; *Kolodziejczyk et al.*, 2009].
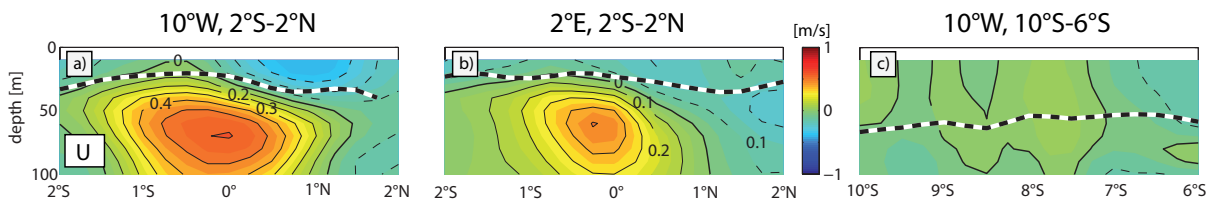

Figure 2.10.: Mean sections of zonal velocity in the equatorial region along 10°W (a) and 2°E (b) as well as along 10°W in the southern ACT region (c). The average sections at 10°W are compiled from 13 cruises, whereas the 2°E average was compiled from 4 cruises (tab.1) and the southern section includes 3 cruises: EGEE2, EGEE3 and EGEE5. The black and white line denotes average MLDs.

In the southern ACT region zonal velocities in the subsurface are strongly reduced (fig.2.10c). A current band of eastwards velocities, which could be associated with the SECC, can not be explicitly detected. The SEUC at 10°W was observed to be centered at around 5°S and below 100m depth [*Kolodziejczyk et al.*, 2009] outside the range considered in this study.

Intra-seasonal variations   In addition to variability of the current system, intra-seasonal equatorial waves are known to impact variability in the equatorial circulation. *Düing et al.* [1975] firstly report the tropical Atlantic Ocean to be traversed by baroclinic intra-seasonal waves, e.g. TIWs. On the equator, these waves have typical periods of 20-40 days and wave lengths of 600-1200 km. They are most active in boreal summer and autumn [e.g. *von Schuckmann et al.*, 2008] and have been observed in the western and central equatorial Atlantic [*Athie and Marin*, 2008]. However, it is not clarified how far east in the Gulf of Guinea they are excited. Nevertheless, at least the western part of the Atlantic cold tongue seems to be subject to intra-seasonal variability of the velocity field induced by TIWs. On the equator, TIWs are associated with
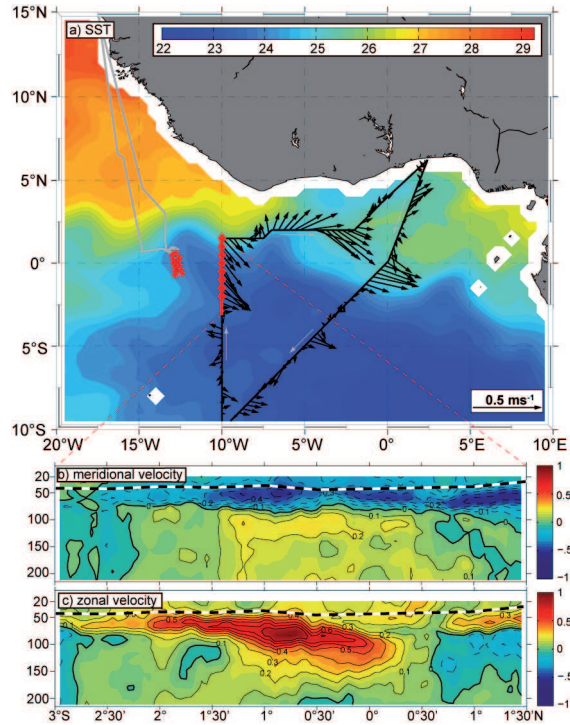
Figure 2.11.: Example of the impact of intra-seasonal fluctuations on a) SST, b) meridional velocity and c) zonal velocity as observed during EGEE2 (September 2005) along 10°W.
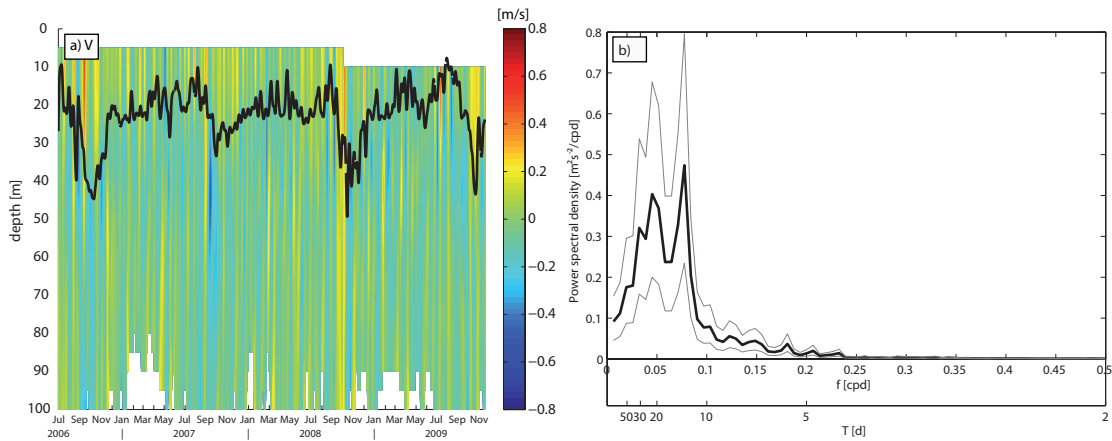
Figure 2.12.: a) Timeseries of meridional velocity observed by the PIRATA mooring at 10°W,0°N. Black line denotes MLD. b) Power spectral density of meridional velocity averaged between 15-30m depth at 10°W,0°N (see a)). The 95% confidence interval is based on the χ^2 distribution. Note that the power spectral density is shown in frequency space, the second xaxis therefore only translated the frequencies into periods, as they are more instructive.

elevated meridional velocities of up to $1ms^{-1}$ (fig.2.11, 2.12a) [e.g. *Weisberg and Weingartner*, 1988]). Shipboard ADCP sections from 10°W indicate that in the center of the cold tongue TIWs are present and that they are characterized by highly baroclinic velocity structures. Typically,
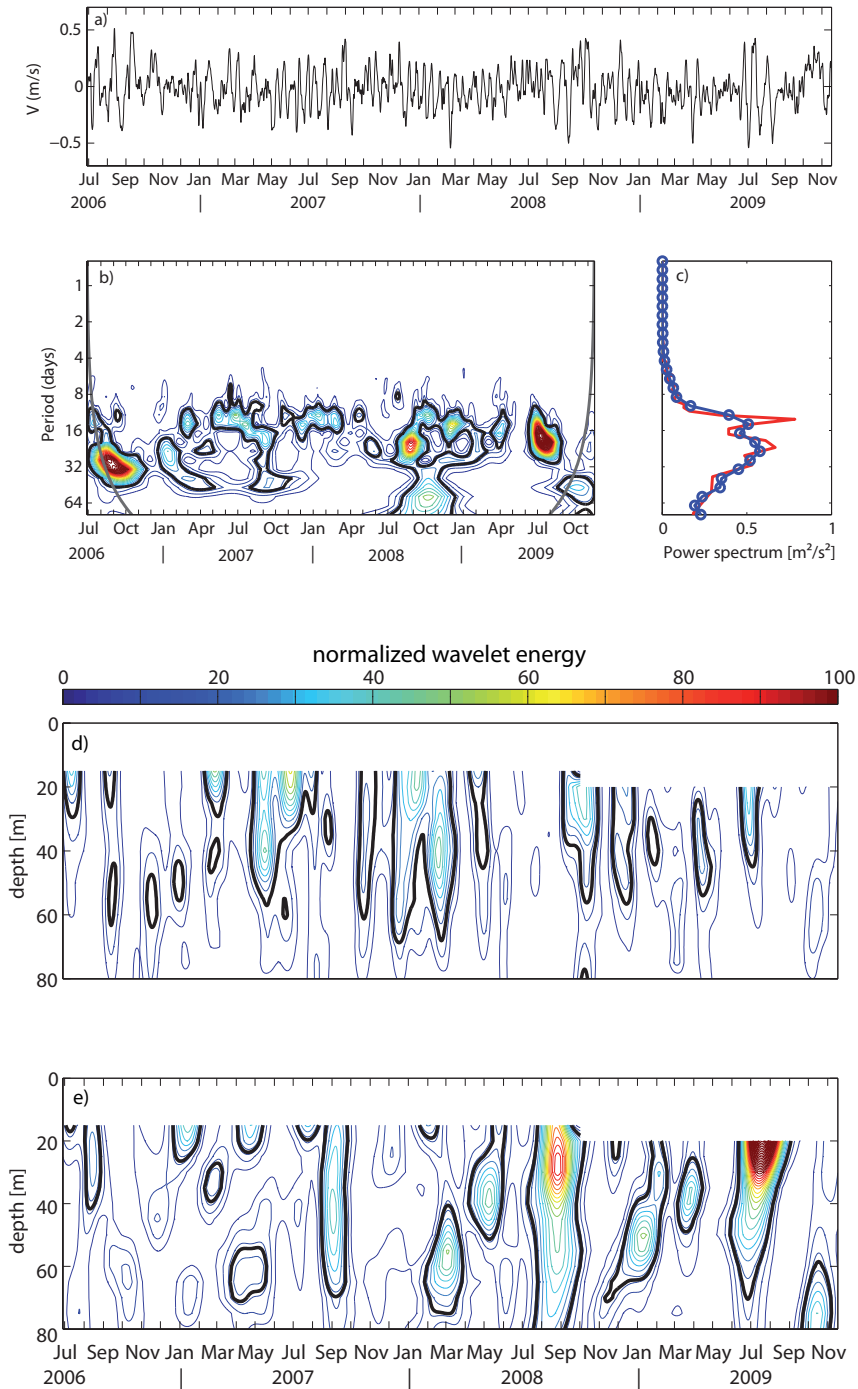
Figure 2.13.: a) Timeseries of average meridional velocity (15-30m) used for the wavelet analysis in b) and c); b) wavelet power spectrum in coloured contours, 95% significance level as solid black line and cone of influence (indicating the region, where edge effects due to the finite length timeseries get important) as solid grey line; c) global wavelet power spectrum (blue line and circles) with the power spectrum obtained via Fourier analysis (red line); wavelet power spectrum as in b), but for the complete section (all different depth layers, instead of one timeseries) for a period of 12 days (d) and 20 days (e).

meridional velocities are most pronounced just below the ML at 50-60m depth (fig.2.11, 2.12a), while below the EUC core meridional velocities change sign and weaken. Furthermore, moored ADCP observations at 10°W,0°N give further insight into the characteristics of these waves and their variability in the central ACT region: The power spectral density for average meridional velocities in the upper layer (15-30m) for the timeperiod from July 2006 until November 2009 shows two peaks in the 10-40 day period range (fig.2.12b). The peak at around 12-14 days is most pronounced, but rather narrow and contains about 9% of the total variance. The rather broad second peak centered at around 20-22 days however contains 23% of the total variance and falls into the period range associated with TIWs in the central and western basin.

Performing wavelet analysis does not only provide information about the dominant modes of variability in frequency space as the spectrum, but additionally delivers information about the temporal distribution of these modes within a timeseries. Due to the improvement towards the resolution in time, the resolution in frequency is reduced, nevertheless they are both reasonable. The wavelet analysis in this study was performed using the wavelet tools of *Torrence and Compo* [1998], hence the chosen parameters and methods can be further viewed in their publication. For the purpose of the analysis, a certain wavelet function is chosen, e.g. the Morlet wavelet, consisting of a plane wave with a certain frequency/period referred to as the wavelet scale modified by a Gaussian. Applying this wavelet on the timeseries provides a wavelet transform, which in principle is a localized Fourier transform, assessing the modes of variability in frequency space within a certain timeperiod of the timerseries. The amplitude of the wavelet power spectrum is then obtained by taking the square of the absolute value of the wavelet transform. By varying the wavelet scale assigned to the wavelet function, the wavelet power spectrum is obtained for a range of scales along the timeseries. Due to the finite length of the timeseries errors will occur at the beginning and the end of the timeseries. The timeperiod subject to these edge effects obviously depends on the considered scale and is marked by the "cone of influence". In addition, the size of the cone of influence at each scale gives a first measure about whether to consider a certain peak in the wavelet power spectrum as a data spike or a robust signal: a robust signal at a certain scale should have a width equal or greater than the cone of influence at this scale. For further assessment of the significance of peaks within the wavelet power spectrum, a significance test against a red noise process is performed. Therefore, for every local wavelet power spectrum, defined as a vertical slice through the wavelet power spectrum, a 95% confidence level is contructed. This confidence level is obtained by multiplying a red noise background spectrum by the 95th percentile value for χ_2^2. Only peaks passing this confidence level are considered as significant. Note, that for a significance test against white noise, a lot more peaks would pass the significance level. For a red noise process with a higher lag-1 coefficient of 0.9 the prominent peaks of the presented analysis for the lag-1 coefficient of 0.72 are still significant. Before performing the wavelet analysis the timeseries is normalized by its variance.

Performing wavelet analysis for the average upper layer timeseries of meridional velocity also accentuates enhanced variability in the 10-30 day period range exceeding the significance levels (fig.2.13b). The global wavelet spectrum defined as the average of the local wavelet power spectrum over time, is the smoothed expression of the power spectrum obtained via Fourier

analysis (fig.2.13c), emphasizing the close relation of these forms of timeseries analysis. Note, here the power spectrum is shown, whereas in fig.2.12b the power spectral density is displayed. Significant wavelet power within the 10-30 day range in the upper layer is evident from July to September/October for the years 2007-2009 coinciding with the seasons of highest TIW activity reported in *von Schuckmann et al.* [2008] for the central basin (fig.2.13). To further examine the depth distribution of wavelet energy, the complete section is analyzed and the periods of 20 days and 12 days respectively are extracted. As suggested from the power spectral density more energy is contained in the peak associated with a period of 20 days than for the one associate with a 12 day period, which is also evident for the depth distributed wavelet power spectrum (fig.2.13d,e). In addition, the seasonality of the 12 day wavelet power spectrum is not as clearly pronounced as for the 20 day wavelet power spectrum, where significant wavelet power is found from July to September/October in the upper 60m (fig.2.13e). In accordance to the weakening velocities associated with TIWs towards the EUC core from the ship section along 10°W (fig.2.11), the wavelet energy reduces towards the EUC core (fig.2.13e). These findings confirm intra-seasonal variability associated with TIW characteristics to be evident within the equatorial ACT region at least until 10°W with highest activity in boreal summer and autumn. Similar baroclinic structures of TIWs have also been observed in the equatorial Pacific [e.g. *Moum et al.*, 2009; *Kennan and Flament*, 2000]. Note, a hint for TIW presence can also be obtained with SST observations, where they induce wave-like undulations (fig.2.11a).

In the Gulf of Guinea east of 10°W *Athie and Marin* [2008] reported the dominance of intra-seasonal signs with periods of 10-20 days, which they interpreted as equatorially trapped mixed-Rossby-gravity waves having large zonal scales and no apparent zonal propagation.

This chapter summarized the mean features of the circulation within the tropical Atlantic. The focus on the ACT region revealed fundamental differences in atmospheric forcing, MLDs and the currents system with its associated variability for the western and eastern equatorial as well as southern ACT region. How the assessed variability of these parameters will affect background conditions for turbulent mixing in terms of shear and stratification will be further investigated in chapter 4. Previously, chapter 3 will describe the entire data sets used within the framework of this study.

3. Data and Methods

The entire data set of this study consists of a multi-cruise program, which can be considered as the core of the data set, combining observations of microstructure as well as large scale background observations, additional available cruise data, buoy data from the Pilot Research moored Array in the Tropical Atlantic [PIRATA, *Bourlès et al.*, 2008] network, satellite derived products as well as climatologies.
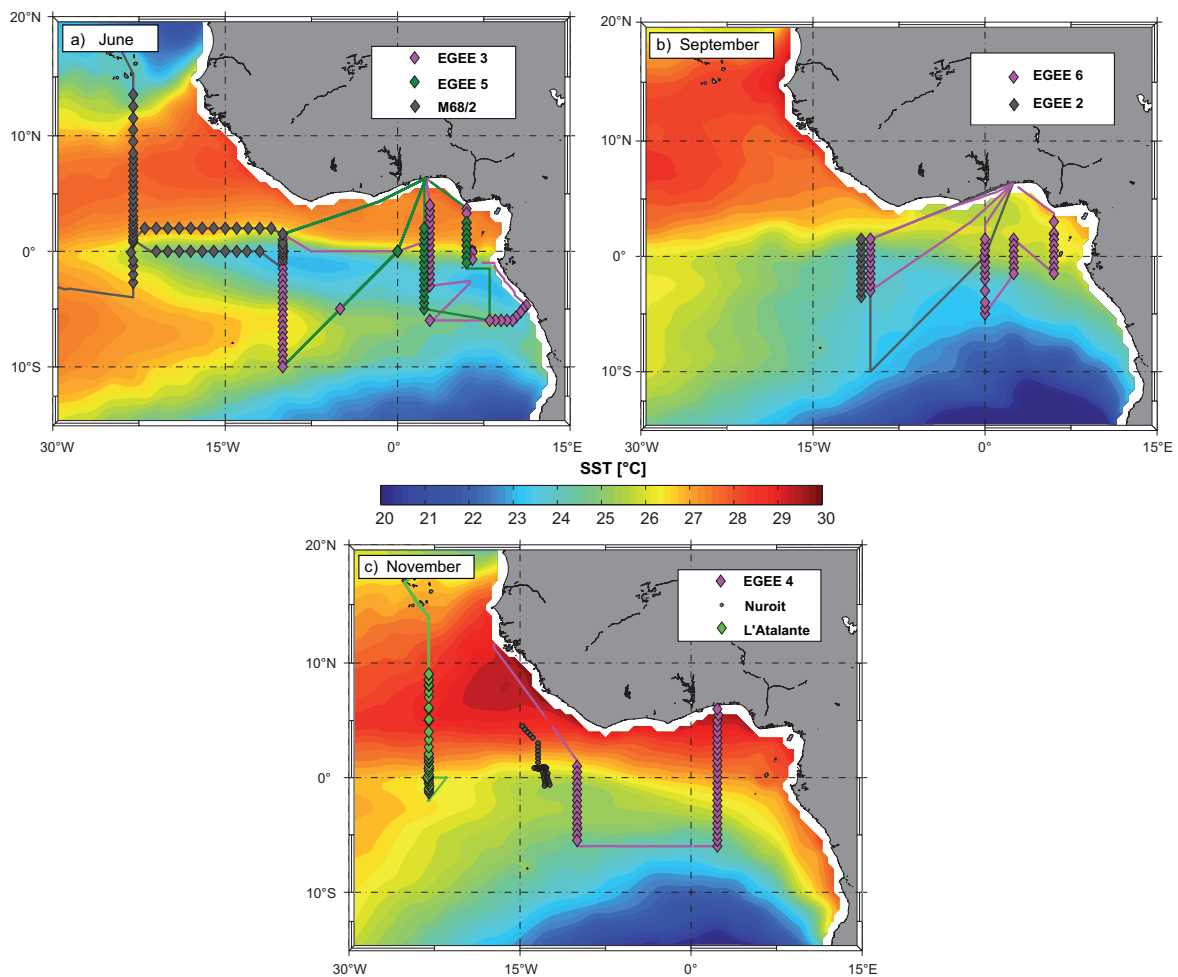
3.1. Direct shipboard observations

Figure 3.1.: Cruisetracks and observed SST during the different seasons. Monthly SSTs are averaged over years 2005-2007 and diamonds mark positions of microstructure stations. Colours are associated with the different cruises as pointed out in the legends.

The shipboard observations were collected on eight cruises mainly undertaken between 2005 and 2007 to the ACT region and the eastern equatorial Atlantic. Five of these cruises (EGEE2-EGEE6) were carried out in the scientific framework of the french EGEE-campaign [*Bourlès et al.*, 2007], the ocean observational part of the AMMA project [*Redelsperger et al.*, 2006] designed to investigate the oceanic and atmospheric variability in the eastern tropical Atlantic. This program aims to highlight the variability on different time scales from daily to inter-annual, thus several meridional sections have been frequently repeated. A special focus was given to the section along 10°W, which has also been occupied during other programs especially by the PIRATA service cruises. Two cruises (EGEE3 and EGEE5) were scheduled to coincide with the West African Monsoon onset and the development of the ACT in boreal spring and early summer (end of May to July), while another two cruises (EGEE2 and EGEE6) were carried out during the mature phase of the monsoon (September-October), when the cold tongue is still well developed. Finally, one cruise (EGEE4) was conducted in the second half of November, while the cold tongue was disintegrated.

In addition, data sets from two cruises to the western ACT region carried out in June 2006 (M68/2) and March 2008 (Atalante4) were available. These cruises were part of the Verbundprojekt "Nordatlantik" focusing on tropical climate variability. The measurement program in June 2006 was conducted on two meridional sections along 10°W and 23°W as well as two zonal sections along the equator and 2°N between 23°W and 10°W. In March 2008 solely the 23°W section was occupied. Finally, data from a cruise by N/O Le Nuroit (December 1994) was also analyzed, which was collected in the regions about and between the Romanche (RFZ) and Chain Fracture Zones close to 10°W. Specially, two cross equatorial sections from 1°N to 0.75°S at about 13°W were used (fig.3.1, tab. 3.1).

The cruise data presented here, highlighting conditions within the ACT region between 23°W and 6°E as well as between 2°N and 10°S, is a subset of the above observational programs and consists of microstructure shear and temperature profiles using loosely tethered or free fall instruments, conductivity-temperature-depth (CTD) profiles and near-continuously sampled profiles of upper-ocean horizontal velocity recorded with vessel-mounted acoustic Doppler current profilers (vmADCP).

3.1.1. CTD data

Information on the hydrographic background (temperature and salinity fields) was routinely acquired with a Seabird 911 system of Seabord Electronics attached to a rosette of 12 (N/O L'Antea) or 24 (on all other vessels) Niskin bottles. Temperature and conductivity are recorded at a sampling rate of 24 Hz, while lowered through the water column. Water samples taken underway were used for calibration purposes as well as for analysis of biogeochemical parameters including nutrients. Water samples for calibration of the Seabird conductivity sensors were analyzed on board using Guideline salinometers. Profiles were interpolated on a regular 1dbar grid and final accuracy for salinity derived from the CTD measurements was in genereal 0.003, for temperature 0.002°C.

3. Data and Methods

Cruise ID	Ship	Schedule	Sections	MSS profiler	MSS	CTD
	N/O Le Nuroit	20.11.-6.12.1994	13°W	HRP	15	-
Ata4	N/O L'Atalante	26.2.-10.3.2008	23°W	MSS032	180	51
EGEE2	N/O Le Suroit	2.-19.9.2005	10°W	MSS028	48	62
EGEE3	N/O L'Atalante	29.5.-22.6.2006	23°W,10°W,2°E,6°E	MSS026	386	73
EGEE4	N/O L'Antea	2.11.-1.12.2006	10°W,2°E	MSS026	117	42
EGEE5	N/O L'Antea	7.6.-14.6.2007	2°E,6°E	MSS032	68	31
EGEE6	N/O L'Antea	3.9.-24.9.2007	10°W,0°,2°E,6°E	MSS032	119	41
M68/2	FS Meteor	9.6.-8.7.2006	23°W,10°W,0°N,2°N	MSS028	200	115
					$\sum$ 1133	$\sum$415

Table 3.1.: Table of cruises indicating the used ship, duration time, the occupied microstructure(MSS) sections, the microstructure profiler in use, the amount of MSS profiles and the amount of CTD stations.

3.1.2. vmADCP data

Information on the velocity field is obtained with vessel-mounted ADCPs, which differed in systems and configurations during the individual cruises.

An ADCP sends acoustic pulses and gains information on the velocity of the water column evaluating the returned signal in terms of the doppler shift: An acoustic pulse, a so-called ping, is transmitted, which is back-scattered by small particles in the water column like e.g. plankton moving with the flow. If the back-scattered signal shows a shift in frequency, the sender and the scattering particles do not move at the same speed. Using the doppler principle and assuming that the scattering particles are moving solely with the underlying flow the velocity in the depth of the scattering particles can be determined. The time delay between sent and received signal gives via the sound speed of the sea water information about the depth of the scattering particles. As ADCPs are able to listen to the backscattered signal in different time windows a vertical profile of the velocity field can be obtained. ADCPs are available working with different frequencies, which limits their operating distance: e.g. a 300kHz instrument can sample mainly the upper 150m, whereas a 75kHz instrument can reach until about 700m. The frequency of the ADCPs used on the cruises of this study was either 150kHz (N/O Le Suroit) or 75 kHz on all other vessels. N/O L'Atalante was additionally equipped with a 300kHz ADCP and FS Meteor had an additional 38 kHz ADCP installed that were simultaneously collecting data on both vessels. Bin sizes varied between 4m (300kHz, L'Atalante) and 8m for all other cruises. Data processing is e.g. complicated by ship movements, nevertheless standard processing techniques [e.g. *Fischer et al.*, 2003] were used. *Fischer et al.* [2003] reported their accuracy estimates for hourly averaged data to result in errors of 1 cms^{-1} for on-station data and 2-4 $cms-1$ for underway measurements for a 75 kHz ocean surveyor. Velocity sections shown in this study heavily rely on the underway data, whereas calculation of Froude numbers is mostly limited to the less defective on-station data. Note, that the upper 10-20 meters are usually lost due to a blank ping and a water column disturbed by the ships movement. All vmADCP data sets have been interpolated on a regular depth grid depending on the bin size and provided as one-hour

Serial number	MSS026	MSS028	MSS032
Type	MSS90D	MSS90L	MSS90D
Noiselevel [W/kg]	$5 \cdot 10^{-10}$	$1 \cdot 10^{-9}$	$5 \cdot 10^{-10}$
Sensors			
CTD (24Hz)	yes	yes	yes
Shear (2 x)	yes	yes	yes
Acceleration	yes	yes	yes
FP07	yes	yes	yes
Fast conductivity	no	yes	no
Oxygen	no	yes	yes
Turbidity	no	no	yes
Tilt	yes	no	no

Table 3.2.: Overview of the microstructure profiler setups

or 10-minute averages after post-processing.

3.1.3. Microstructure data

Microstructure profiling on most cruises was conducted with three different loosely tethered MSS profilers (MSS90L and MSS90D) manufactured by Sea& Sun Technology (Trappenkamp, Germany) in collaboration with ISW Wassertechnik. The profilers were operated with an electrical winch aboard the ship supplying the Kevlar cable sufficiently fast to minimize disturbing vibrations, which could be caused by a cable strumming behind the instrument. Data acquisition was performed in real time via the Kevlar cable. All profilers transmit data to the deck unit via 16 channels with a high data transmission rate of 1024 Hz. This high data transmission rate is sufficient to resolve small scale gradients of velocity and temperature [*Osborn and Cox*, 1972]. The small or in better words micro scales wished to be resolved here are way below one meter. All profilers are of similar setup, all equipped with 2 shear sensors (airfoil, 4ms response), a fast-responding temperature sensor (Thermistor FP07), an acceleration sensor and the standard CTD sensors, whereas the latter sample at a lower frequency of 24 Hz. For a detailed description of the instruments the reader is referred to *Prandke and Stips* [1998]. Some of the profilers had additional sensors mounted as summarized in tab. 3.2, which are not further used in this study. All sensors are installed on the front tip of the profiler protected by a metal frame, whereas the fast velocity and temperature sensors are fixed ahead of the other sensors in order to ensure their measurements to be acquired of the undisturbed water column. The profilers are optimized by individual ballasting to sink at a rate of 0.5-0.6 ms^{-1}. Especially at the equator this led to additionally ballasting as the strong EUC tends to capture the profiler decelerating its vertical descent. The high profiler descent speeds of 0.5-0.6 ms^{-1} minimize uncertainties in microstructure shear measurements, as the probe sensitivity increases with increasing probe speed. Unfortunately, it challenges measurements with the fast thermistors due to their response time (see section 3.4.3). Noise levels of turbulent dissipation rates are better than $1 \cdot 10^{-9} Wkg^{-1}$ for the MSS90L and better than $5 \cdot 10^{-10} Wkg^{-1}$ for MSS90D [*Prandke and Stips*, 1998; *Schafstall et al.*, 2010]. During the cruise in December 1994, microstructure data was acquired with the

High Resolution Profiler [HRP, *Schmitt et al.*, 1988], a free falling internally recording instrument. The HRP samples velocity shear with two airfoil probes and temperature microstructure, as well measuring finescale temperature, conductivity and horizontal velocity. Dissipation noise levels for this instrument are on the order of $1 \cdot 10^{-11} W kg^{-1}$ [see *Polzin and Montgomery*, 1996].
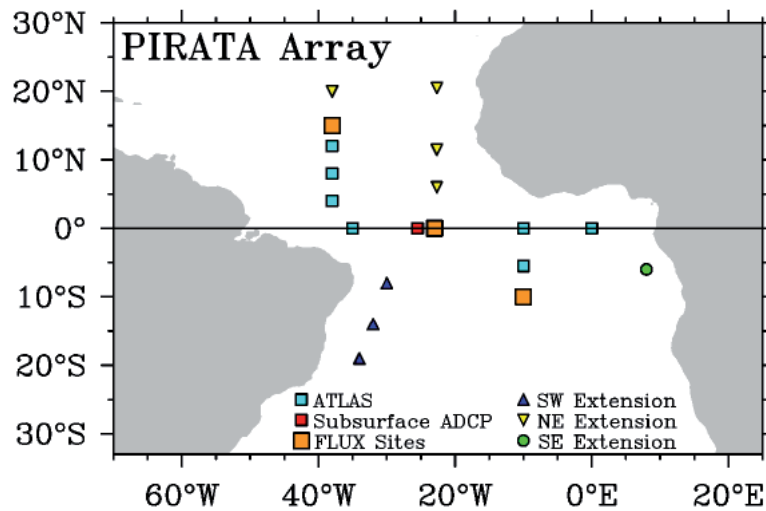
3.2. Other data sets

3.2.1. PIRATA moorings

Figure 3.2.: Design of the PIRATA Array with its different stations from http://www.pmel.noaa.gov/pirata/pir_implement.html

The PIRATA (PIlot Research moored Array in the Tropical Atlantic) array was designed in order to study air-sea interactions affecting climate variability on seasonal, inter-annual and longer time scales in the tropical Atlantic ocean as a joint program in the 1990's. It consists of several ATLAS moorings and some additional stations (fig.3.2) observing surface as well as subsurface parameters. The top buoys of the ATLAS moorings record short and long wave ration, rain, windspeed and direction, relative humidity, air temperature and sea level pressure, while in the subsurface, temperature (at the depths: [1:20:140 180 300 500]m) and salinity (at depths of [1 20 40 120]m) observations are available. At some sites ADCPs observe the subsurface velocity field (e.g. 23°W,0°N and 10°W,0°N) providing velocities on a regular 5m depth grid with a bi-daily resolution at 0 and 12 UTC. The data is generally available in real-time and can be accessed via http://www.pmel.noaa.gov/tao/data_deliv/. In the framework of this study data from the PIRATA buoys is used to calculate the individual terms of the mixed layer heat budget at 23°W,0°N, 10°W,0°N, 10°W,10°S and 0°E,0°N. Data sets between 1997 and 2009 were used for the calculations as further described in section 6.1.

3.2.2. PIRATA cruises

Servicing of the PIRATA buoys requires frequent cruises to the mooring locations. In order to gain more information on the seasonal variability of the background hydrographic and velocity fields additional CTD and vmADCP data of seven PIRATA service cruises along 10°W is used. These data have been collected between 10°S and 1.5°N from 1999 and 2009 during different seasons of the year. These data sets can be freely accessed via the PIRATA web site at http://www.ifremer.fr/ird/pirata/pirata_cruises.php. The velocity and hydrographic sections are described and analyzed in detail by *Kolodziejczyk et al.* [2009].

3.2.3. Satellite products

Satellite products of surface winds and sea surface temperatures are used in this study.

The wind data are collected on-board the Quickscat satellite launched by the NASA in 1999 with a SeaWinds rotating scatterometer. It has a higher resolution and a wider sampling pattern as former satellites. The windfields are available (www.cersat.ifremer.fr) as daily or monthly global fields at a 1/2° x 1/2° horizontal resolution from the Centre de Recherche et d'Exploitation Satellaire (CERSAT), at IFREMER, Plouzane (France), where statistical interpolation using an objective method was performed in order to construct average synoptical fields, without data gaps from the discrete measurements.

The sea surface temperatures in use are measured on-board the TRMM (Tropical Rainfall Measuring Mission) satellite launched in 1997 with the TMI (TRMM Microwave Imager). Global fields are available on a 0.25° x 0.25° grid for different temporal resolutions of 1day, 3days, 1 week and 1 month. The average fields are again derived using an optimum interpolation scheme and available via http://www.ssmi.com/tmi/.

3.2.4. Climatologies

Surface velocities

Climatological information on the surface velocity field in this study is taken from several different analysis: the drifter-derived climatology of *Lumpkin and Garaffo* [2005], the YoMaHa'07 (further referred to as YoMaHa) data set based on ARGO float measurements [www.apdrc.soest.hawaii.edu/projects/yomaha/, *Lebedev et al.*, 2007] and the OSCAR program [www.oscar.noaa.gov, *Bonjean and Lagerloef*, 2002] combining information of sea level anomalies and surface winds.

Climatological surface velocities of *Lumpkin and Garaffo* [2005] are based on drifter data. A drifter consists of a surface buoy, equipped with a temperature sensor and a transmitter to sent the data and its position to a satellite, and a drogue, which is centered at a depth of 15m below the sea surface in order to ensure, that the drifter really drifts with the surface current and is not solely displaced by the surface winds. As the drifters are subject to displacements by the currents, observations are distributed highly irregular. In order to provide an improved monthly mean surface velocity climatology *Lumpkin and Garaffo* [2005] spatially binned the Lagrangian observations of the total velocity and treated them as a timeseries

composed of a time-mean, annual and semiannual components as well as an eddy residual. Decomposing the signal in this way before averaging is supposed to suppress biases due to the uneven distribution of measurements especially in regions dominated by a strong seasonal cycle. Results were smoothed via optimum interpolation and are available on a 1° x 1° global grid via http://www.aoml.noaa.gov/phod/dac/drifter_climatology.html. *Lumpkin and Garaffo* [2005] find their methodology producing significantly improved estimates compared to simple bin averaging as tested against an eddy resolving model of the Atlantic ocean.

The YoMaHa data set relies on ARGO float surface trajectories obtained from the satellite fixes during the data transmission phase of the floats at the surface. ARGO floats are designed to drift at a depth level of about 1000m for a cycle of about 10 days. At the end of every cycle the floats further descend to 2000m depth and then rise to the surface, measuring a complete profile of temperature and salinity. During their surfacing time, they connect to a satellite transmitting their data, while their displacements at the surface are being tracked. After completing the data transmission they begin their next cycle. A monthly surface velocity climatology is constructed by simple bin averaging and provided on a 1° x 1° global grid.

The OSCAR surface velocities are derived by combining the computation of the geostrophic component of the surface velocity from satellite altimetry and the Ekman component from satellite derived surface winds and can therefore be referred to as an indirect method. The climatological surface velocities are available on a 1° x 1° global grid.

SST

Calculation of different terms of the mixed layer heat budget requires the use of climatological SST values. Two different data sets are used in this study, whereas the first one comes along with the surface drifter velocities of *Lumpkin and Garaffo* [2005], obtained with the same processing procedures as described above. The second set is provided by *Reynolds and Smith* [1994] and is based on a combination of satellite and in-situ data, which are mapped using optimum interpolation techniques. The resulting SST climatology was since then updated with an extended data base and is available on a 1° x 1° global grid via
http://iridl.ldeo.columbia.edu/SOURCES/.IGOSS/.nmc/.Reyn_SmithOIv1/.climatology/sst/.

Mixed layer Depth

The climatology of mixed layer depths used in this study was established by *de Boyer Motegut et al.* [2004] based on millions of available profiles from the World Ocean Circulation Experiment (WOCE) and the ARGO program. Individual mixed layer depths are estimated from individual profiles by the threshold criteria of 0.02°C for temperature and 0.03 kgm^{-3} for density, which have been found to deliver optimum results. The reference depth is set to 10m to avoid influence of the diurnal variation of temperature and density. The individual MLDs are then averaged in bins, whereas the median is calculated. A slight smoothing is applied, before using an ordinary kriging method to optimally predict missing data. In this study the climatology for the temperature criterion is used, which is available on a 2° x 2° global grid via http://www.lodyc.jussieuc.fr/ cdblod/mld.html

3.3. **Sampling Strategy**

In this study the regional and seasonal variability of turbulent mixing in the ACT region is investigated. Thus, in contrast to previous microstructure measurement programs, designed to gain insight to the different local processes shaping mixing activity, that often sampled at a single location for a period of several days to weeks [e.g. *Peters et al.*, 1988; *Moum et al.*, 1989; *Lien et al.*, 1995; *Moum et al.*, 2009], the sampling strategy pursued here was to profile at several locations during a single cruise. This new sampling strategy could be accomplished by integrating microstructure profiling into the CTD program during all cruises except for the 1994 cruise. On each single microstructure station at least 3 but up to 20 profiles were collected from the surface to between 150m and 300m depth in order to enlarge the statistical significance of individual signals. In addition, several stations were occupied for 24 hours or longer, while microstructure data was collected continuously, in particular during boreal summer 2006, which are discussed in *Wade et al.* [2011b] (see Appendix C1). In total, a subset of the entire data set summarized in tab. 3.1 consisting of 785 microstructure profiles on 224 stations within the ACT region from the surface to 150 and 250m depth are used in this study.

3.4. **Microstructure data processing**

3.4.1. **Inferring eddy diffusivities**

Microstructure profilers are designed to measure small scale shear of velocity and/or temperature, which can be used to estimate the dissipation rates of turbulent kinetic energy (ϵ, section 3.4.2) and the dissipation rate of temperature (χ, section 3.4.3). As pointed out in section 1.3, ϵ can then be used according to *Osborn* [1980] to derive an expression for the eddy diffusivity of mass in the form of

$$K_\rho = \gamma \frac{\epsilon}{N^2} \tag{3.1}$$

Note, that the magnitude of the mixing efficiency γ is still under discussion. Energy arguments require $\gamma \leq 0.2$ [*Osborn*, 1980]. *Oakey* [1982] found a median value of $\gamma = 0.2$ for ocean turbulence for independent measurements in active turbulent regions. Ever since, $\gamma = 0.2$ is commonly used in the oceanographic community [e.g. *Moum and Caldwell*, 1985; *Gregg et al.*, 1985; *Peters et al.*, 1988; *Lien et al.*, 2008; *Moum et al.*, 2009, etc.]. Nevertheless, the universality of this parameter was challenged by several numerical and experimental studies [e.g. *Yamazaki and Osborn*, 1993; *Ruddick and Walsh*, 1997; *Fringer and Street*, 2003]. More recent numerical simulations [*Smyth et al.*, 2001] showed that γ can sometimes exceed 0.2 dependant on the evolutionary stage of a turbulent overturn. *Shih et al.* [2005] found in their numerical study a dependence of γ on the turbulent activity parameter [also referred to as isotropy index *Gargett et al.*, 1984a] $I = \epsilon/(\nu N^2)$. For an intermediate turbulent regime characterized by $7 < I < 100$, they find $\gamma = 0.2$ the best estimate, which holds for more than 65% of the data set of this study (see fig.3.3). Thus, here γ is set to the constant value of 0.2, which additionally facilitates comparison of the results to previous studies [e.g. *Moum et al.*, 1989; *Lien et al.*, 2008; *Moum et al.*, 2009]. The third term in equation 3.1 is the buoyancy frequency N^2. In order to derive a measure for
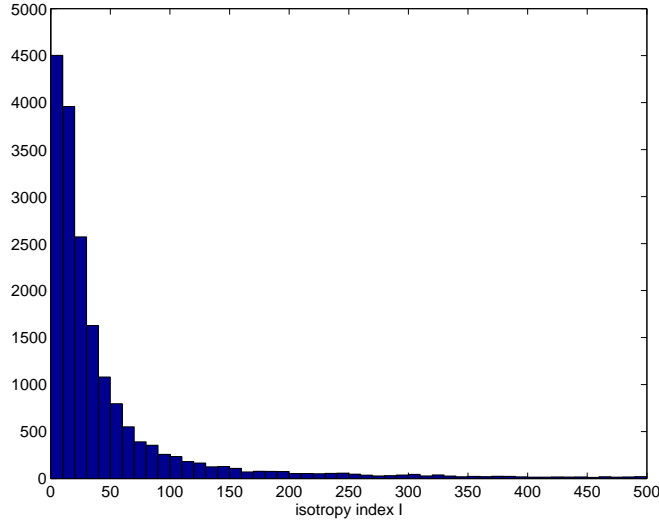
Figure 3.3.: Histogram of the activity parameter (isotropy index) I for all measurements used in this study.

the background stratification, N^2 has to be smoothed. *Peters et al.* [1988] suggest that mean gradients or filtered data should be matched in resolution to the resolution of the large-scale background shear data. In this study N^2 is calculated from least squared fits to salinity and temperature using a depth interval of 30m in the deeper water column or less in the region close to the mixed layer to avoid biases in stratification.

In accordance to the eddy diffusivity for mass, the eddy diffusivity for heat can be estimated by simplifying the temperature variance equation according to *Osborn and Cox* [1972] resulting in:

$$K_h = \frac{\chi}{2(\partial \overline{T}/\partial z)^2}. \tag{3.2}$$

The temperature gradient for the latter equation is calculated over the same depth intervals as the stratification for the eddy diffusivity of mass.

3.4.2. Estimating ϵ

The procedures of estimating the turbulent kinetic energy dissipation from microstructure measurements for the profilers in use was already described in *Schafstall* [2010]. Some of the processing procedures and obstacles, which have also occupied other scientific groups working with different instrument setups [e.g. *Moum et al.*, 1995; *Gregg*, 1999; *Luketina and Imberger*, 2001] are already pointed out there. Nevertheless, the main facts will be lined up in the following.

In order to estimate spatial gradients of small scale velocity shear from a measured time series of small scale velocity fluctuations the frozen field assumption or Taylor hypothesis has to be valid. It allows for the conversion of the time derivative of velocity (as measured) into the spatial derivative (needed for further calculations) in direction of the profiler movement: $\frac{\partial u}{\partial z} = \frac{1}{V}\frac{\partial u}{\partial t}$, where V is the mean sinking velocity of the profiler. In general, this hypothesis is valid, if the measured field evolves slowly compared to the time during which it is measured or in other

words if the fluctuating velocities are small compared to the profiler speed V [*Townsend*, 1976, p.67]. This can be assumed to be valid for the observations of this study. This also allows for the conversion of the frequency to the vertical wavenumber spectrum.

As mentioned in the introduction, the equation of turbulent kinetic energy (TKE) provides a term for the turbulent dissipation rate (ϵ). The most general form for ϵ is given by

$$\epsilon = \nu(T)\overline{\frac{\partial u'_i}{\partial x_j}(\frac{\partial u'_i}{\partial x_j} + \frac{\partial u'_j}{\partial x_i})} \qquad (\text{e.g.}\textit{Moum et al.} [1995]), \qquad (3.3)$$

where ν is the molecular viscosity of sea water, mainly a function of temperature. The indices indicate the standard tensor notation with summation over all three components. Under the assumption of isotropy the 12 terms of equation 3.3 are simply related, leaving only one independent term to be estimated following *Hinze* [1975]:

$$\epsilon = 7.5\nu\overline{[\frac{\partial u'}{\partial z}]^2} \qquad (3.4)$$

the mean of the variance of the the small scale vertical velocity shear. Ideally "the mean" denoted by the overbar represents an ensemble average over a large number of representations of the turbulence, which can not be obtained with a vertical profile. Therefore here the mean is rather a mean over a finite depth interval.

As mentioned this simplification only applies under the assumption of isotropy, an assumption not necessarily applicable in a stratified ocean. The concerns formulated by *Gargett et al.* [1984a] are, that stratification could possibly suppress motions in the vertical, leading to an overestimation of ϵ, if estimated only via one of the horizontal velocity components. *Kolmogorov* [1941] was the first to substantiate the intuitive idea of an energy cascade from large, anisotropic, energy containing scales to small scales, which are assumed isotropic, homogeneous and statistically stationary. The mathematical quantity considered to embody the concept of energy is the three dimensional kinetic energy spectral density $E(k)$ (defined as $\int_0^\infty E(k)dk = 1/2\overline{(u_1^2 + u_2^2 + u_3^2)}$). *Kolmogorov* [1941]'s second hypothesis implies that for isotropic turbulence a range of wavenumbers exist (termed inertial subrange), between energy containing and dissipative scales, within which the spectrum only depends on the wavenumber k and ϵ and shows a characteristic $k^{-5/3}$ roll-off. Accordingly, expressions for the one dimensional spectral functions, which can be actually measured, also inhibit this characteristic roll-off in the inertial subrange, which has been confirmed for observations. Hence, *Gargett et al.* [1984a] examined the validity of the isotropic assumption by investigating the changing shape of the roll-off in the inertial subrange for varying magnitude of I. They found that for $I > 200$ no substantial errors arise, when assuming isotropy and thus estimating ϵ via equation 3.4. *Yamazaki and Osborn* [1990] find under the alternative approach of assuming axisymmetric turbulence and measuring 2 independent velocity stains, that the isotropic formula (equation 3.4) provides identical dissipation estimates for $I > 20$ to their approach and that the error for lower I is limited to a maximum of 35%. They state, that dissipation estimates from the isotropic formula for $I > 20$ are a good estimate as long as one uses a horizontal velocity component. *Rehmann and Hwang* [2005] state that in a sheared

stratified flow, shear will disrupt the axisymmetry assumed by *Yamazaki and Osborn* [1990] and cause even larger errors in dissipation estimates via the isotropic formula.

However, as *Moum et al.* [1995] state, for anisotropy to become more evident ϵ has to diminish relative to the stratification. In this study the vast amount of data was acquired in the equatorial region, where dissipation rates are known to be rather high in comparison to other regions in the ocean. This is in favor of I to be large. On the other hand, the thermocline of the tropics is known to be a region of high stratification reducing I and hence enlarging the possibility of anisotropy to become an issue.

For only 9% of the data used in this study $I > 200$, whereas 55% are associated with $I > 20$ (fig.3.3). The bulk of data not crossing the threshold of $I = 20$ is in the ϵ range of $1 \cdot 10^{-9} W kg^{-1}$
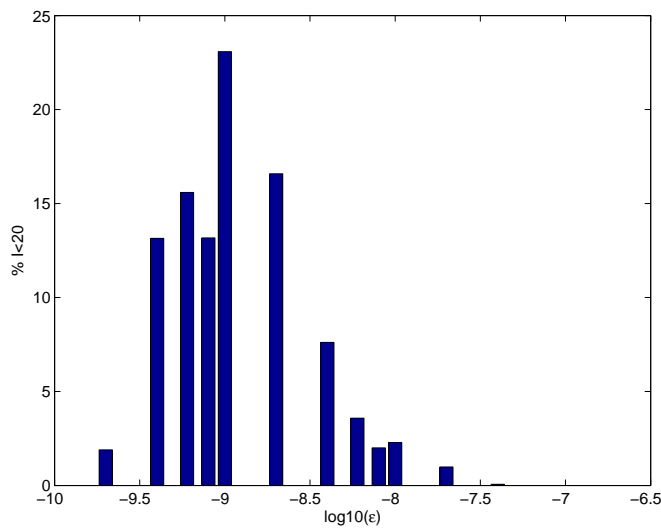

Figure 3.4.: Percentages of dissipation rates with $I < 20$

(see fig.3.4). In addition, data with $I < 20$ is predominantly found at depths greater than 60m. The main interest of this study lies on the evaluation of mixing intensity immediately below the mixed layer, which is rather shallow in the tropics (see section 2.3). Hence, the isotropic assumption will not significantly affect the results of this study and will be used in the following in the estimations of ϵ. In addition, most of the data with $I < 20$, which have potentially be corrected, are attributed with ϵ values slightly above the noise level of the used instruments (tab. 3.2).

One possibility for the spectral description of a timeseries, is displaying the power spectral density. In this case the power spectral densities are normalized such as that the integral over all frequencies equals the variance of the timeseries. Hence, as the Taylor hypothesis is valid permitting the transformation of the frequency spectrum to the wavenumber spectrum, ϵ can be estimated via the evaluation of shear spectral densities (Φ_v) in the form of:

$$\epsilon = 7.5\nu \overline{[\frac{\partial u'}{\partial z}]^2} = 7.5\nu \int_0^\infty \Phi_v dk_z. \tag{3.5}$$

This is referred to as the variance method for estimating ϵ [*Gregg*, 1998]. In practice, it is not possible to integrate over all wavenumbers, as the complete spectrum can not be resolved by airfoil sensors. This establishes the need for an adequate definition of integration limits as well as corrections for the variance loss due to this limited wavenumber range. Fortunately, *Nasmyth* [1970] proposed a universal shape for the spectral density for full developed turbulence. Hence, the information about the variance distribution as a function of wavenumber can be used for variance loss corrections: 97% (90%) of the variance is contained in the integral of the spectral density until k_v ($0.5k_v$), the Kolmogorov wavenumber, defined as

$$k_v = \frac{1}{2\pi}(\frac{\epsilon}{\nu^3})^{\frac{1}{4}} \quad \text{in cpm (cycles per meter).} \tag{3.6}$$

Obviously, for the measurements of this study, k_v can fall in the wavenumber band already affected by noise and can therefore not be used as the upper integration limit (fig.3.5). In general, finding the adequate integration limits is always a compromise between excluding noise, but containing most of the resolved variance.

Processing The lower integration limit (k_{min}) is set to 2 cpm as this is the highest wavenumber associated with internal waves and the lowest wavenumber, which can be resolved with the used instruments. The upper integration limit (k_{max}) is found by an iterative procedure similar to the one described in *Moum et al.* [1995]. A first guess of the dissipation rate is obtained by integrating the individual spectra between 2 and 30 cpm. According to this first guess, k_{max} is iteratively adjusted dependant on the derived k_v (equation 3.6), but never allowed to exceed 30 cpm. Subsequently, the dissipation rate estimates are corrected for the response function of the airfoil sensors, which are assumed to respond as a single-pole low pass filter according to *Oakey* [1977]

$$H^2_{Oakey}(k) = \frac{1}{1 + (\frac{k}{k_s})^2}. \tag{3.7}$$

Prandke et al. [2000] found $k_s = 100\,cpm$ for the used sensors. Afterwards the variance loss due to the integration limits is corrected with the universal form of the Nasmyth spectrum (comp.fig.3.5) in the formulation provided by *Wolk et al.* [2002].

To enlarge the statistical significance of individual events, two individual airfoil sensors are used and the signals are individually processed. If one estimate of ϵ exceeds the other by a factor of 8, only the smaller one is used. In addition, visual inspection of the individual profiles was performed in order to exclude outliers. The remaining ϵ estimates are then averaged logarithmically in bins of 2 dbar.

3.4.3. Estimating χ

In analogy to the general formulation of ϵ (equation 3.3) provided by the TKE equation, the general form of the turbulent dissipation rate of temperature is derived when examining the equation for temperature variance:

$$\chi = 2D[\overline{\frac{\partial T'}{\partial x_j}}]^2, \tag{3.8}$$
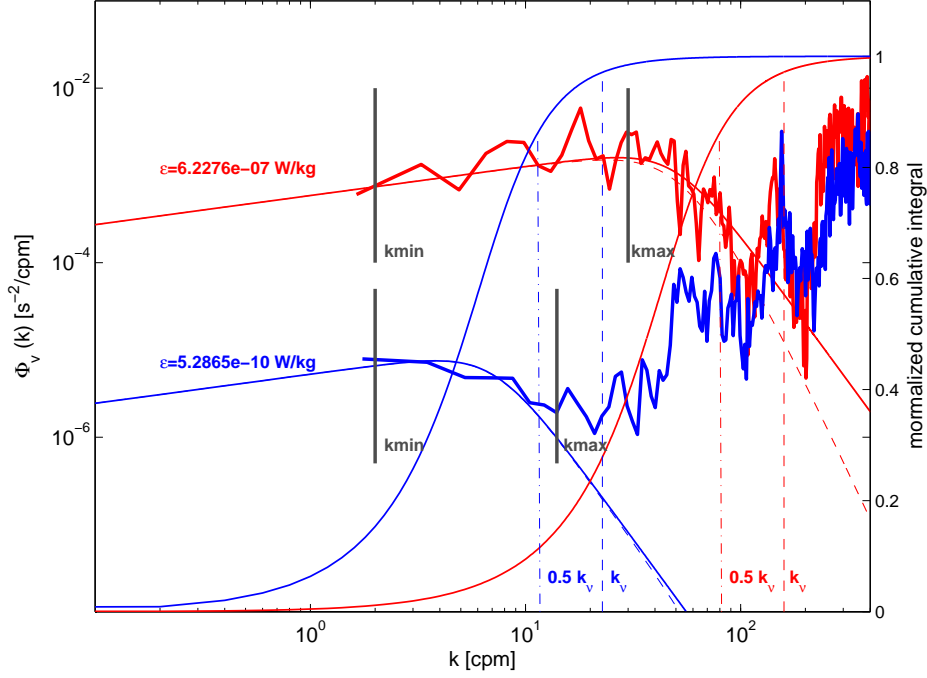
3. Data and Methods

Figure 3.5.: Observed shear spectra for different levels of the turbulent dissipation rate as measured in September 2006 in colour. Solid colored lines mark the associated universal forms of the Nasmyth spectra together with the response correction (as dashed lines) and their cumulative integral respectively. The appropriate k_v are shown as well as the assessed integration limits.

where D is the molecular diffusivity of heat. Here, the isotropic assumption and conversion to a spectral estimate of the variance leads to

$$\chi = 6D\overline{[\frac{\partial T'}{\partial z}]^2} = 6D \int_0^\infty \Phi_T(k)dk_z, \tag{3.9}$$

where $\Phi_T(k)$ is the temperature gradient spectral density. Two different analytical forms for the temperature gradient spectrum have been proposed by *Batchelor* [1959] and *Kraichnan* [1968]. In this study the universal form of the Batchelor spectrum in the formulation given in *Luketina and Imberger* [2001] is adopted. As for the universal form of the Nasmyth spectrum, a certain value of ϵ or in case for the Batchelor spectrum of χ fixes the exact spectral shape of the analytical form. For the Batchelor spectrum, the analytical form is not only related to χ, but also to ϵ via the Batchelor wavenumber (k_b) defined as

$$k_b = \frac{1}{2\pi} \left(\frac{\epsilon}{\nu D^2} \right)^{\frac{1}{4}}. \tag{3.10}$$

Note, that this relation is also used to estimate ϵ via Batchelor curve fitting of temperature gradient spectra [*Luketina and Imberger*, 2001]. The universal functional form assesses the variance content in certain wavenumber bands: 97% of the variance is contained in the wave number band until k_b, about 90% until $0.6k_b$. Despite the similar setup of the problem to the estimations of ϵ,

the approach of estimating χ differs. Whilst the estimation of ϵ is build on the direct integration of the observed spectral density and the analytical form of the Nasmyth spectrum is mainly used for variance loss correction, the main principle of estimating χ is to best fit the variance of the observed spectral density integrated over a certain wavenumber range to theoretical Batchelor curves with varying values of χ. Hence, the closest match of variance in the chosen wavenumber band between observations and analytical curves, assesses the estimate of χ. As was discussed for the estimation of ϵ a crucial point in the estimation process is assessing the adequate integration limits, a compromise between excluding noise, but resolving most of the observed variance. The
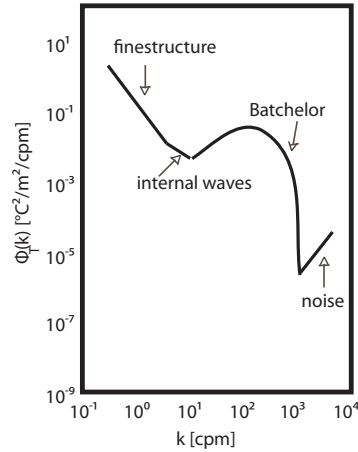

Figure 3.6.: The functional form of Batchelor for the temperature gradient spectral density together with its contaminating sources internal waves and noise [after *Luketina and Imberger*, 2001]

temperature gradient spectra are, as the small scale velocity shear spectra, shaped by different processes in the different wave number bands such as e.g. finestructure, internal waves and instrument noise. Inspection of the observed temperature gradient spectral densities used in this study revealed that deviations from the functional form of the Batchelor curve are mainly due to internal waves at the low wavenumbers and instrumental noise at high wavenumbers (fig.3.6). This has to be accounted for when assessing the integration limits.

Processing For the instrument setup used here, three different output signals for the fast temperature sensor are available: the original signal as well as two further frequency amplified signals designed to improve the resolution at higher frequencies. The amplified signals pass through a serial connection, providing the original, a simply amplified signal and a double or combined amplified signal. Note, that the amplifications can be easily accounted for in the spectral domain. Noise levels can be identified more distinctly for the double amplified signal, which is further used in this study (fig.3.7).

To find adequate integration limits, a first guess on the magnitude of χ is obtained by best fitting the variance of the observed temperature gradient spectral density in a narrow wavenumber band between 19 and 43 cpm to the variance of various Batchelor curves in the same wavenumber band. The various Batchelor curves are provided by varying values of χ between $\epsilon/1000 -$
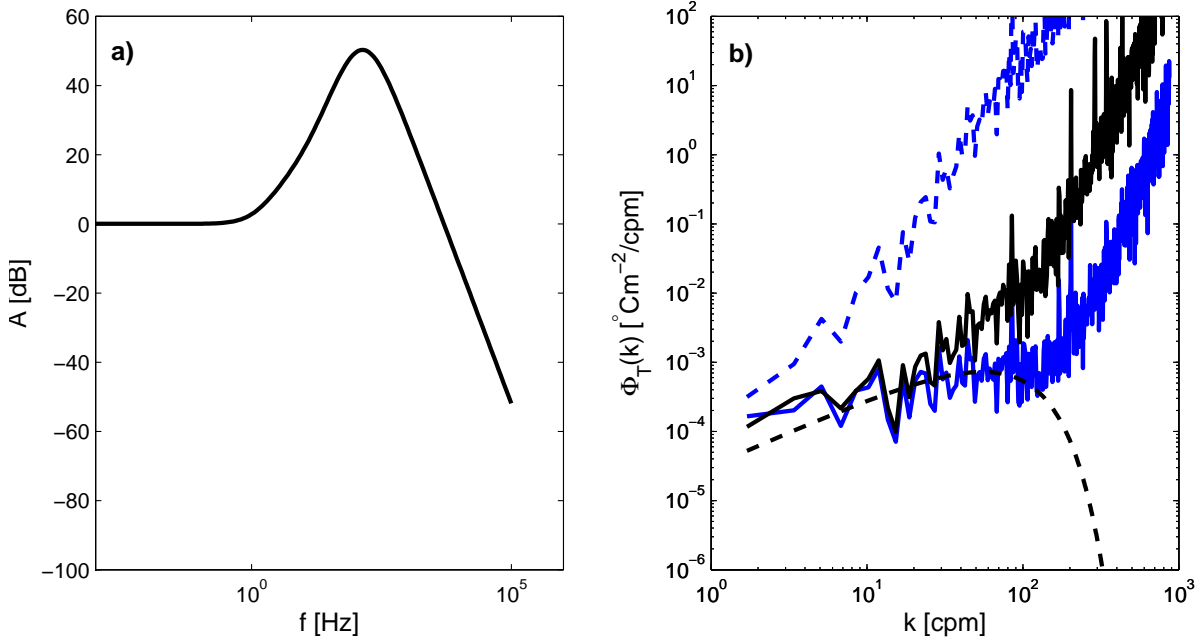
3. Data and Methods

Figure 3.7.: a) combined frequency amplification b) original signal output (black solid line), amplified signal (dashed blue line), the amplified signal corrected for the frequency amplification (solid blue line) and an adequate normalized Batchelor curve (dashed black line).

$\epsilon \cdot 1000$. This first guess on the magnitude of χ is fed into an empirical formula relating the appropriate integration limits to the first guess on χ. The empirical formula has been defined by choosing integration limits by hand for all temperature gradient spectra obtained on EGEE2. To further exclude noise introduced by internal waves at the low wavenumber end, the slope of the temperature gradient spectral density at the lowest resolved wavenumbers is checked and k_{min} adjusted if necessary. Batchelor curve fitting is repeated as described above for the variance between k_{min} and k_{max} (fig.3.8).

Before Batchelor curve fitting as described above can be applied, the temperature gradient spectral densities have to be corrected for the response function of the thermistor sensors [*Luketina and Imberger*, 2001], which is not as straight forward as described for airfoil sensors. Several attempts of determining the response function of the thermistors resulted in ambiguous results, proposing either a single [*Lueck and Mudge*, 1997] or double pole [*Gregg and Meagher*, 1980] filter. Both of these filters require a response time, which has been found to depend on the profiler velocity [e.g. *Gregg and Meagher*, 1980] and the individual glass coating of the sensor [*Nash et al.*, 1999; *Nash and Moum*, 2002]. Here, the formulation for the thermistor response function (H_{FP07}^2) resembling a double pole filter and the response time (τ) as proposed by *Gregg* [1999] are adopted:

$$H_{FP07}^2 = \frac{1}{[(1 + (2\pi\tau f)^2)])^2}, \qquad \tau = tu_{profiler}^{-0.32}. \qquad (3.11)$$

τ is dependant on profiler speed ($u_{profiler}$) and the individual constant t, which is unique to every individual sensor, mainly due to the individual glass coating [*Nash et al.*, 1999; *Gregg*, 1999].
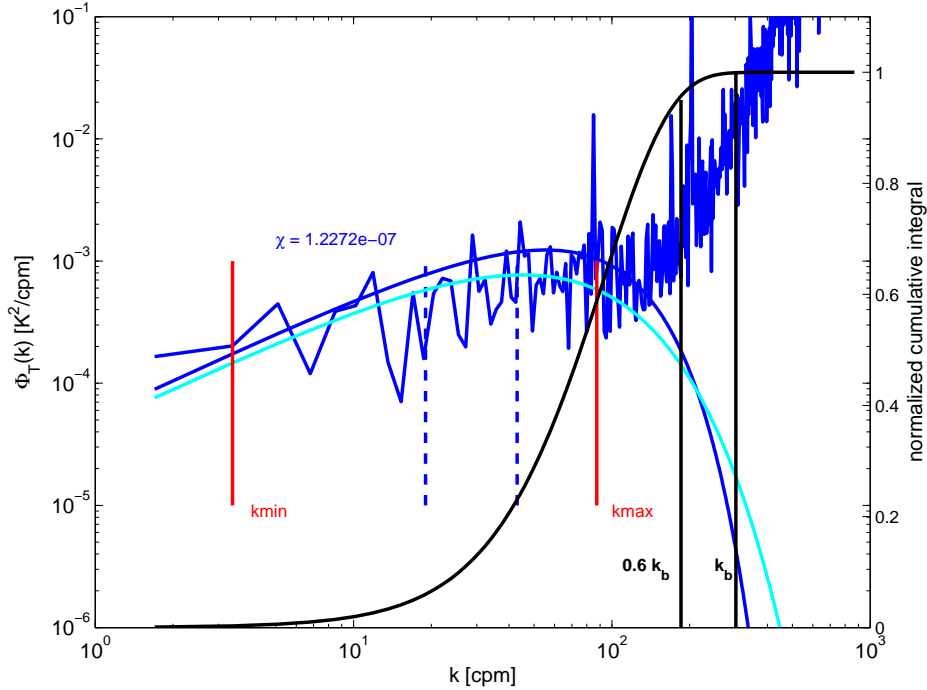
Figure 3.8.: Observed temperature shear spectra as measured in September 2006 in blue. The smooth blue(cyan) line marks the associated universal form of the Batchelor(Kraichnan) spectra. The smooth black line represents the cumulative integral of the normalized Batchelor spectrum. The appropriate k_b(black) are shown as well as the assessed integration limits(red) and the lines of 19 and 43 cpm (dashed blue).

As the profiler speed is adjusted to be fairly constant, assessing the correct value for t remains the challenge. The effect of differing values of t on the response function H^2_{FP07}, the resulting corrections of the spectral density and the associated different estimations of χ are depicted in fig.3.9. For high values of t, the response function causes a strong reduction of variances at high frequencies/wavenumbers (fig.3.9a), which leads to an overcorrection of the temperature gradient spectral density (fig.3.9b) and hence to large estimates of χ by the fitting procedure. The proposed range of t leads to an unacceptable uncertainty in χ on the order of 10. *Nash et al.* [1999] as well as *Gregg* [1999] call for costly tank calibrations of individual thermistors to rule out the uncertainties in the response function, especially the response times, and hence t to improve estimates of χ. In the framework of this study an algorithm was implemented trying to estimate the appropriate individual constant t for the individual sensors, which will be described in the following.

Obviously, the effect of the response function correction on the temperature gradient spectrum is most significant for $k > 30 cpm$ (fig.3.9b). For low wavenumbers ($k < 20 cpm$) the correction of the temperature gradient spectrum for the thermistor response has a neglegible effect. Therefore, as a first step of the algorithm the normalized Batchelor curve is best fitted to the variance in a low wavenumber band around k_{min}, where the thermistor response correction has a minor effect, assessing the estimate of χ. In the second step the variance in a high wavenumber band of the Batchelor curve for the previously assessed χ is compared to the variance in the same high
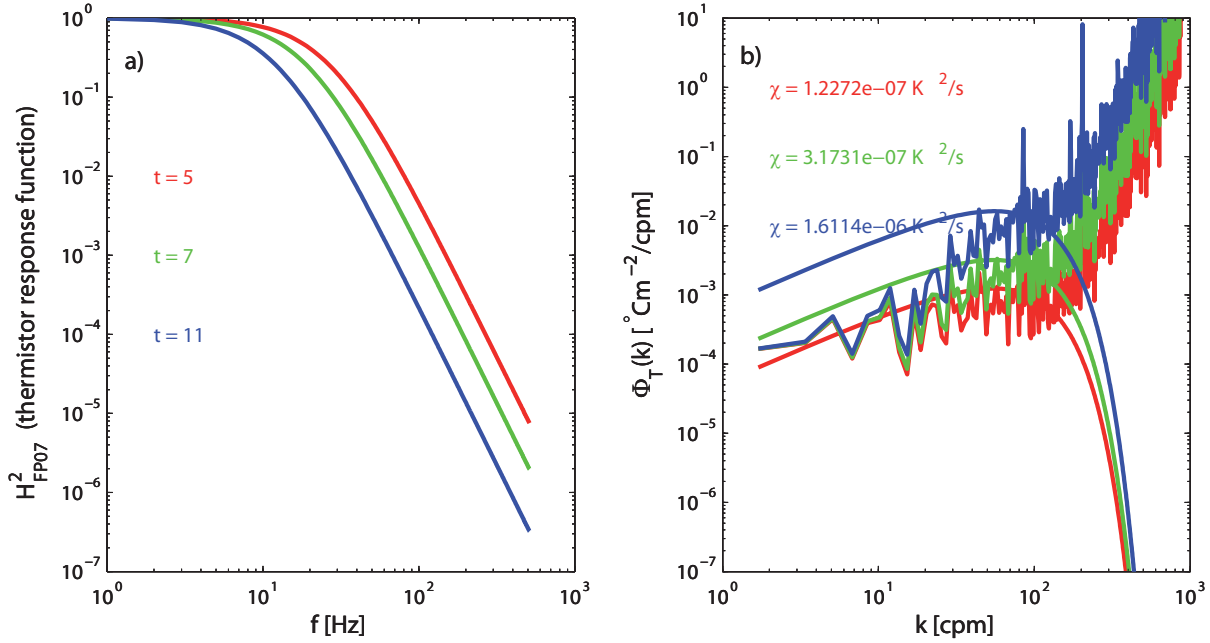
Figure 3.9.: a) shape of the H_{FP07} for varying values of t, which correspond for a constant profiler speed of 0.6 m/s to response times of τ=5.8, 8.25 and 13ms. (Note, for fixed t of 5, the different response times τ correspond to variations in profiler speed of 0.6, 0.21 and 0.05 m/s respectively.) b) effect of correcting the temperature gradient spectrum for the differing response functions and the resulting estimations of χ.

wavenumber band of the observed temperature gradient spectral density corrected for varying values of t. The idea is that for an appropriate value of t the ratio of the observed corrected variance to the variance of the fitted Batchelor curve in this high wavenumber band should equal 1. To exclude the additional effect of $u_{profiler}$ on τ only spectra with $0.57 < u_{profiler} < 0.63 ms^{-1}$ were included in the algorithm.

The resulting averaged ratios of the observed to fitted variances in the high wavenumber band for values of t varying between 4 and 9 for the thermistor used on EGEE6 in September 2007 are shown in fig.3.10. The ratio equals 1 for $t = 5$, a value also chosen in *Gregg* [1999].

So far, the result for the individual constant t seems clear without ambiguity. However, the implemented algorithm heavily relies on the fact that the chosen functional form of the normalized Batchelor spectrum is correct and adequate. Unfortunately, this is questioned when viewing the literature: the universal constant q contained in the functional form of the Batchelor spectrum, which according to *Nash et al.* [1999] has a dramatic effect on the estimate of χ, has been assessed between 2 [*Batchelor*, 1959] and 12 [*Gargett et al.*, 1984b] spanning a wide range. In addition, as mentioned previously another universal form of the temperature gradient spectrum was proposed by *Kraichnan* [1968], where in addition to q another universal constant of questionable magnitude q_{Kr} is introduced. Application of the algorithm for various values of q and the different forms of the universal spectrum leads to ambiguous results concerning t for an individual thermistor (tab. 3.3), which result in an uncertainty of χ of a factor 3.

The uncertainty of a factor of 3 would further be reflected in the estimates of eddy diffusivities
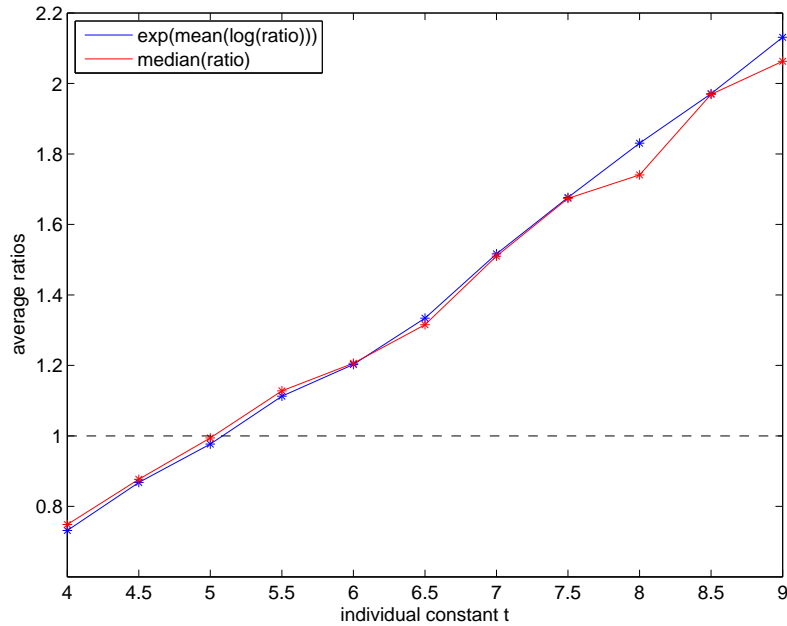
Figure 3.10.: Average ratios of the variance in the high wavenumber band for the observed temperature spectral density to the fitted Batchelor curve for varying values of the individual constant t. Median ratios in red and exponentially averaged ratios in blue.

universal spectrum	B	B	B	K
q/q_{Kr}	$3^{\frac{1}{2}}$/-	$2(3^{\frac{1}{2}})$/-	5.6/-	5.6/7.5
constant t	7	6.25	5	4.8

Table 3.3.: Different estimates for the individual constant t obtained via the algorithm for different choices of the functional form of the spectrum: Batchelor (B) or Kraichnan (K) and the corresponding constants g, q_{Kr}.

of heat (K_h) as well as the resulting turbulent heat flux J_h.

In addition to the outlined uncertainties previous studies reported that estimates of χ at profiler speeds above $0.5ms^{-1}$ are only based on the resolution of the low wavenumber band, which typically only accounts for 2-50% of the variance [*Gregg*, 1998, 1999; *Nash et al.*, 1999]. Hence, the estimate of χ heavily relies on extrapolated values. For the data set used in this study, at profiler speeds of around $0.6ms^{-1}$, only about 10% of the variance of the temperature gradient can be actually resolved for values of $\chi > 1 \cdot 10^{-6}K^2s^{-1}$. The sum of all these uncertanties challenges the belief in reliable estimates of χ in this configuration.

In regions, where stratification is dominated by temperature, which is highly accurate within the equatorial thermocline, $K_h = K_\rho$ should be expected [e.g. *Peters et al.*, 1988]. For the average equatorial profiles (between 2°S and 2°N) observed during September 2006 stratification does seem to be dominated by temperature at least until about 80m depth (3.11a). Thus, at least in the upper 80m K_h and K_ρ should be expected similar. For the average K_h calculated with
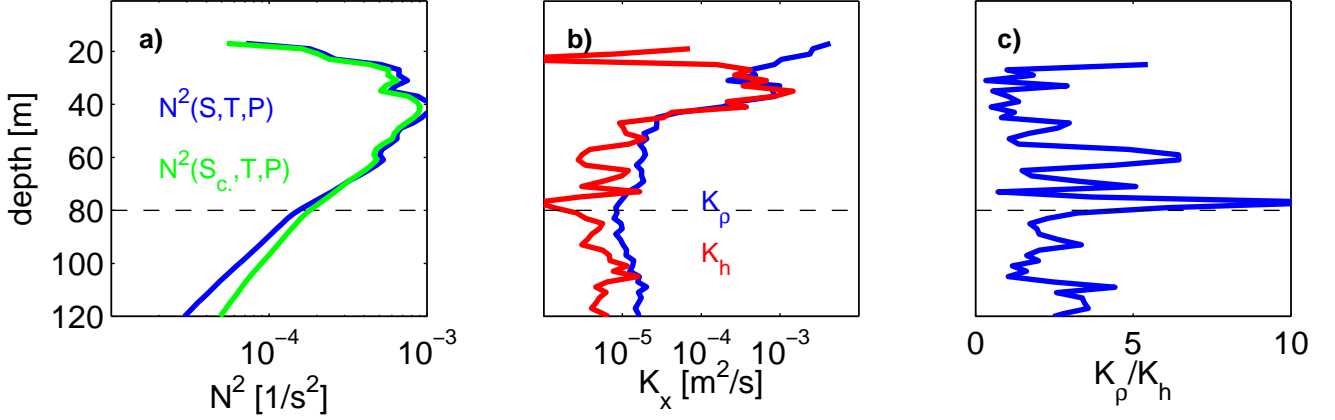
Figure 3.11.: a) Average equatorial profiles (2°S-2°N) of N^2, calculated with observed salinity (blue) and a constant salinity of 35 (green) as observed on EGEE6; b) corresponding profiles of average K_ρ (blue) and K_h (red); c) the ratio of K_ρ and K_h

an individual constant t of about 5, this expection can not be met, the ratio of K_h and K_ρ frequently reaching a factor of 5 (3.11b,c). In addition, estimates of K_h are more affected by noise, especially on single stations (not shown), which increases the differences found between K_h and K_ρ. This supplementary information confirms estimates of χ to be too uncertain for reliable estimates of eddy diffusivities and turbulent heat fluxes. Instead, as estimates of ϵ are clearly more reliable, and the focus of this study lies on the assessment of variability of turbulent parameters in the main thermocline of the tropics, where $K_h = K_\rho$ is expected, the diapycnal heat flux will be in the following calculated via

$$J_h = -\rho c_p K_\rho \frac{dT}{dz}. \tag{3.12}$$

In addition, this facilitates the comparison of the results with other recent studies [e.g. *Moum et al.*, 2009; *Lien et al.*, 2008], where the same expression for J_h is used.

Individual profiles for turbulent dissipation rates ϵ are arithmetically combined to provide station averages, which are the base for further calculations of eddy diffusivities for mass (K_ρ) and diapycnal heat fluxes (J_h).

4. Background conditions for turbulent mixing

As pointed out in the introduction, the aim of this study is to assess regional and seasonal variability of turbulent mixing intensity within the ACT and determine the role of the diapycnal heat flux on the heat budget of the ML. Chapter 2 revealed fundamental differences in the mean circulation in terms of atmospheric forcing, MLDs as well as the currents system and its associated variability for the western and eastern equatorial as well as the southern ACT. Within this chapter the regional and seasonal variability of background conditions for turbulent mixing in terms of shear and stratification resulting from the described large scale forcing will be investigated. Shear and stratification are the chosen background parameters to investigate due to their influence on turbulent mixing intensity. Elevated shear levels are believed to trigger the development of instabilities, while elevated stratification is thought to act against the development of instabilities.

To understand the special focus on shear and stratification variability directly below the ML one has to consider the vertical profile of the diapycnal heat flux. Profiles of the diapycnal heat flux from the equatorial Pacific are reported highly divergent in the vertical, showing maximum values at the base of the ML, rapidly decreasing below [e.g. *Lien et al.*, 2008]. The amount of heat being extracted from the mixed layer into the ocean interior is characterized by the diapycnal heat flux in a rather narrow layer below the ML, which is further explained in chapter 5. Therefore in the following, when the variability of background conditions for turbulent mixing will be described, a special focus will be laid on the layer right below the ML (MLD+5m to MLD+15m).

4.1. Shear

As was described in chapter 2 the circulation pattern in the tropical Atlantic exhibits regional, seasonal as well as intra-seasonal variability. The equatorial ACT region is mainly dominated by the energetic current bands associated with the EUC, nSEC and cSEC, whereas the southern ACT region showed strongly reduced zonal velocities. Due to these fundamental differences in the circulation, resulting levels of shear variance $\overline{S^2} = \overline{(\partial U/\partial z)}^2 + \overline{(\partial V/\partial z)}^2$ are clearly elevated in the equatorial ACT region compared to the south. Enhanced vertical shear is observed in the upper stratified ocean between 4°S and about 2°N (fig.4.1b). Exemplarily, it is shown that these enhanced shear levels sustain elevated mixing levels below the ML (fig.4.1c). Hence, elevated shear levels and enhanced mixing levels in the ACT region below the ML seem not only confined to the equator itself, which was already pointed out by *Peters et al.* [1994] for the equatorial Pacific, but are pronounced within a wider latitudinal extent ranging from about 4°S to 2°N.

4. Background conditions for turbulent mixing
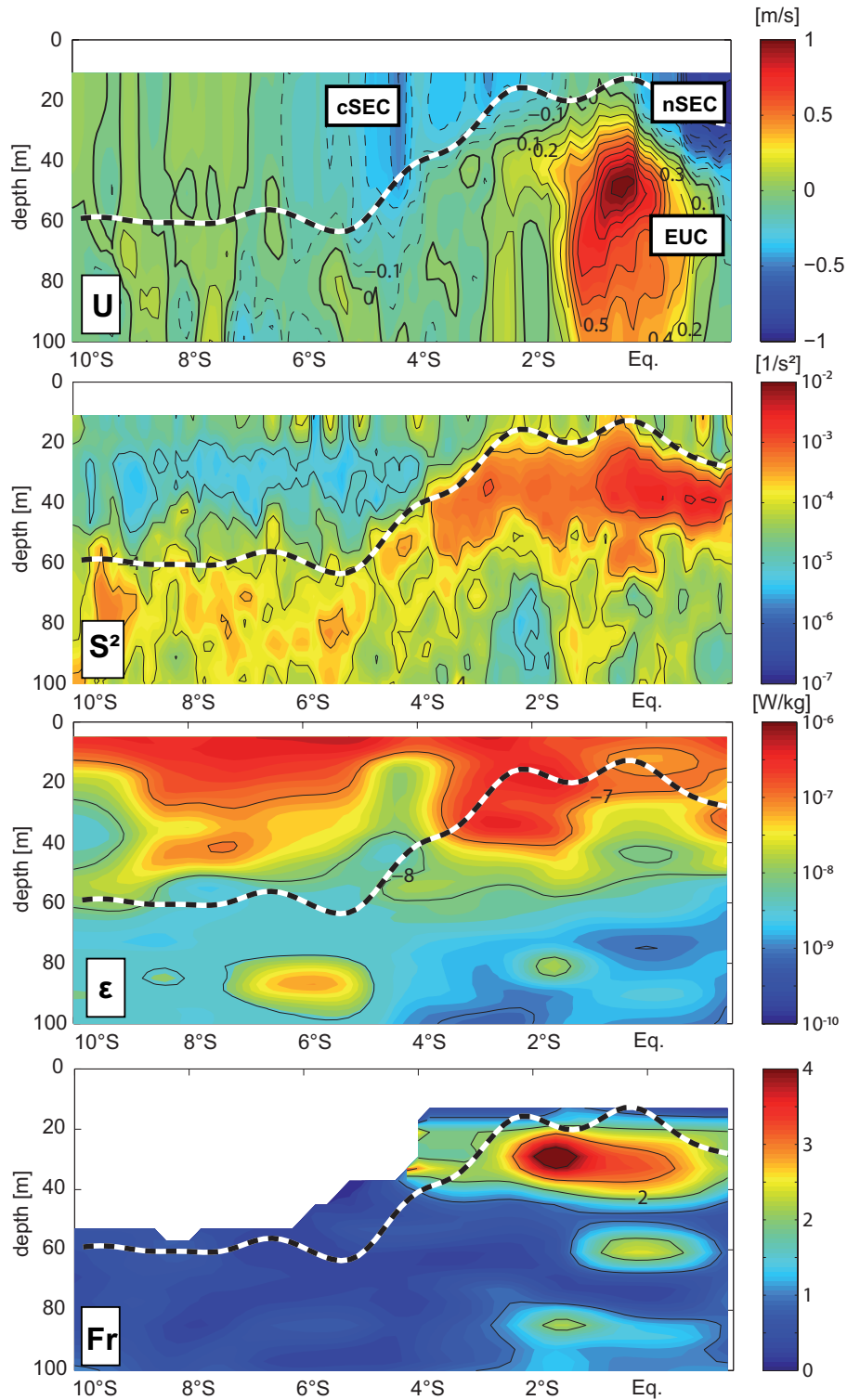

Figure 4.1.: a) Zonal velocity, b) shear, c) turbulent dissipation rate (ϵ) and d) Fr numbers along 10°W during EGEE3 (June 2006) from 10°S to 1.5°N. The black and white line denotes the MLD.

Note, that especially the opposing currents nSEC and EUC lead to increased vertical shear of horizontal velocities. In the southern ACT region (10°S-6°S), where zonal velocities are strongly

reduced, shear levels are accordingly lower as are observed mixing levels below the ML (fig.4.1a-c).
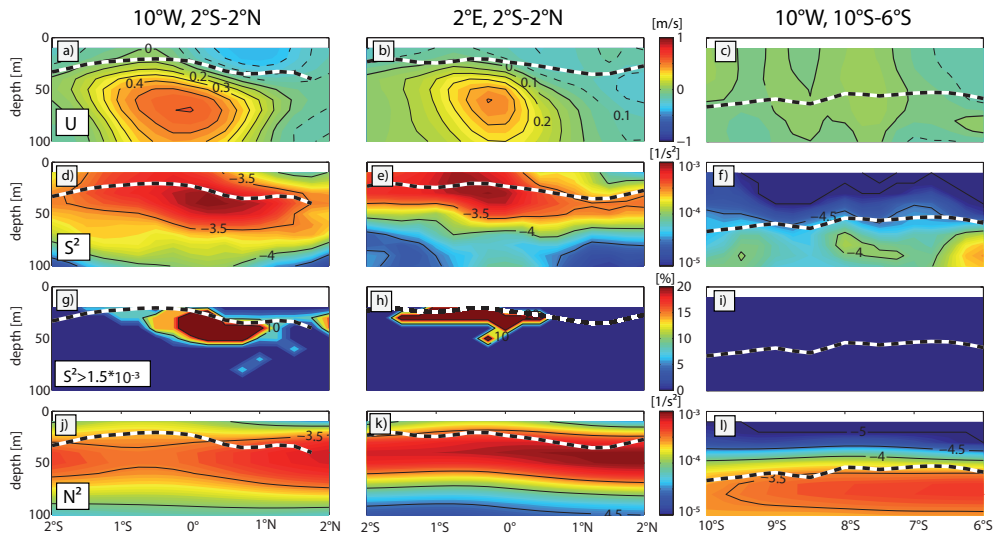

Figure 4.2.: Mean sections of zonal velocity (a,b,c), shear (d,e,f), percentage of shear values exceeding $1.5 \cdot 10^{-3} s^{-2}$ (g,h,i) and stratification (j,k,l) in the equatorial region along 10°W (1st column) and 2°E (2nd column) as well as along 10°W in the southern ACT region (3rd column). The average sections at 10°W are compiled from 13 cruises, whereas the 2°E average was compiled from 4 cruises (Tab.1) and the southern section includes 3 cruises: EGEE2, EGEE3 and EGEE5. The black and white line denotes average MLDs.

The general findings from the exemplary section along 10°W during June 2006 can be confirmed, when combining several ship sections. Combined shipboard ADCP sections indicate average shear variance to be elevated in the equatorial region from 2°N to 2°S (fig.4.2d,e). Highest shear levels are found between the surface mixed layer and the core of the EUC, which is located at 80m at 10°W and 23°W and at about 60m at 2°E. Thus, due to the shoaling of the EUC from west to east, elevated shear levels diminish in depth extent accordingly (fig.4.2d,e). Regardless of the reduction of EUC strength and the simultaneous weakening of the westward surface flow towards the east, average shear levels are of similar magnitude at 10°W and 2°E and elevated levels of shear variance ($\overline{S^2} > 1.5 \cdot 10^{-3} s-2$) are frequently observed at both locations. However, upper ocean shear levels observed with ADCPs moored at 23°W,0°N and 10°W,0°N show higher shear levels above the EUC core at 10°W than at 23°W [Jouanno et al., 2011, see also chapter 7]. It can be speculated that this could be due to the reduced depth range over which velocities vary towards the east due to the shoaling EUC. This would also explain the still elevated levels of shear at 2°E, where the EUC is slightly reduced in strength compared to 10°W, but its core is located about 20m shallower.

In addition to spatial variability, there is pronounced seasonal variability of shear in the upper
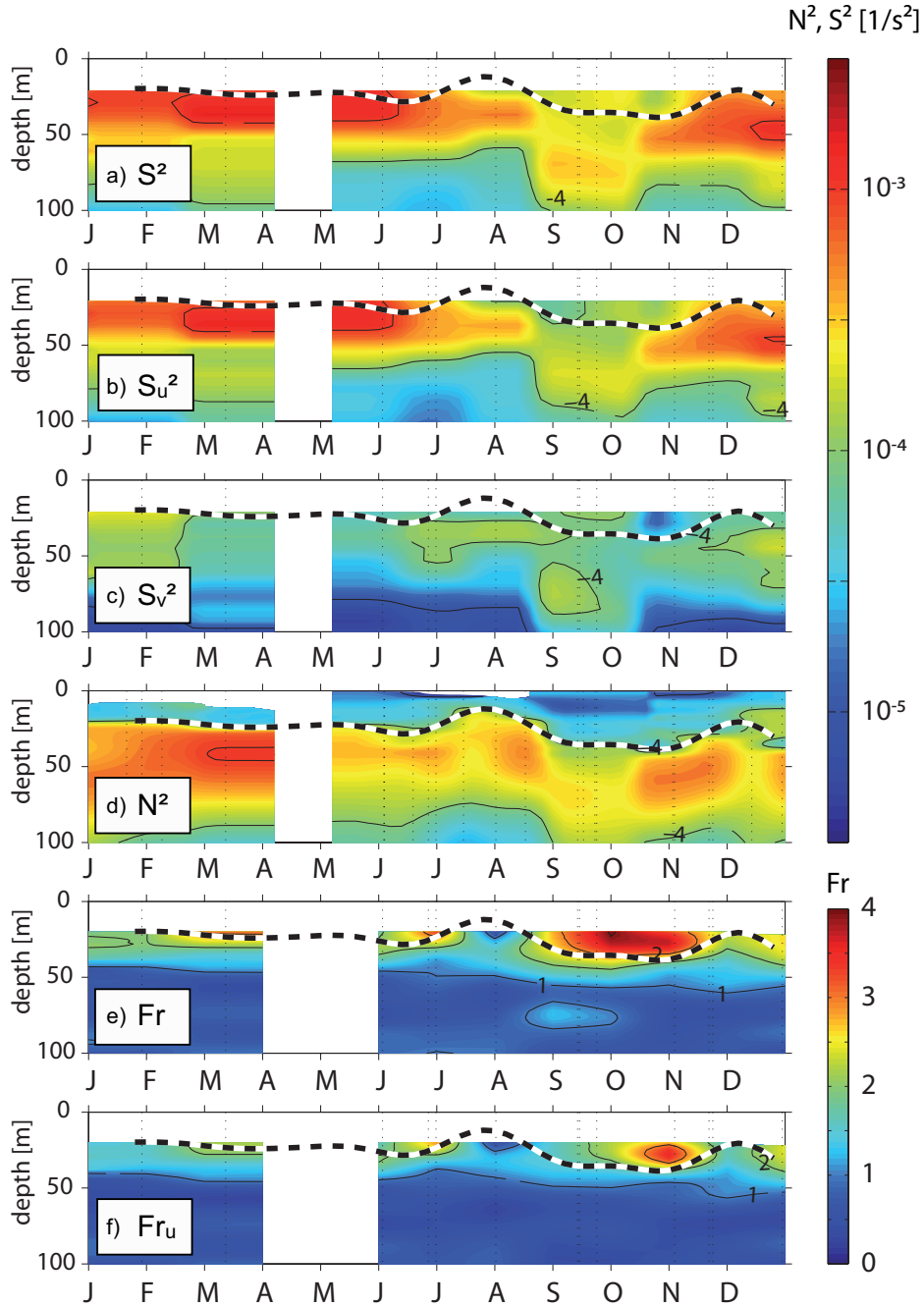
Figure 4.3.: Seasonal evolution of section averaged stratification (a), shear (b,c) and Froude numbers (d,e) constructed from available PIRATA cruise data along 10°W between 2°S and 2°N. The different shear sections arise from $S^2 = (du/dz)^2 + (dv/dz)^2$ and $S_u^2 = (du/dz)^2$ as well as accordingly $Fr = S^2/N^2$ and $Fr_u = S_u^2/N^2$.

water column. A climatological seasonal cycle of shear variance averaged from 2°N to 2°S along 10°W was constructed from 13 shipboard ADCP sections (fig.4.3a). Here, only ADCP data recorded with 8m bin sizes were used and shear variances were calculated from vertical derivatives of hourly-averaged velocities. Shear is highest in boreal spring and early summer, reducing in September during the ceasing of the westward surface velocities and whilst the EUC core is
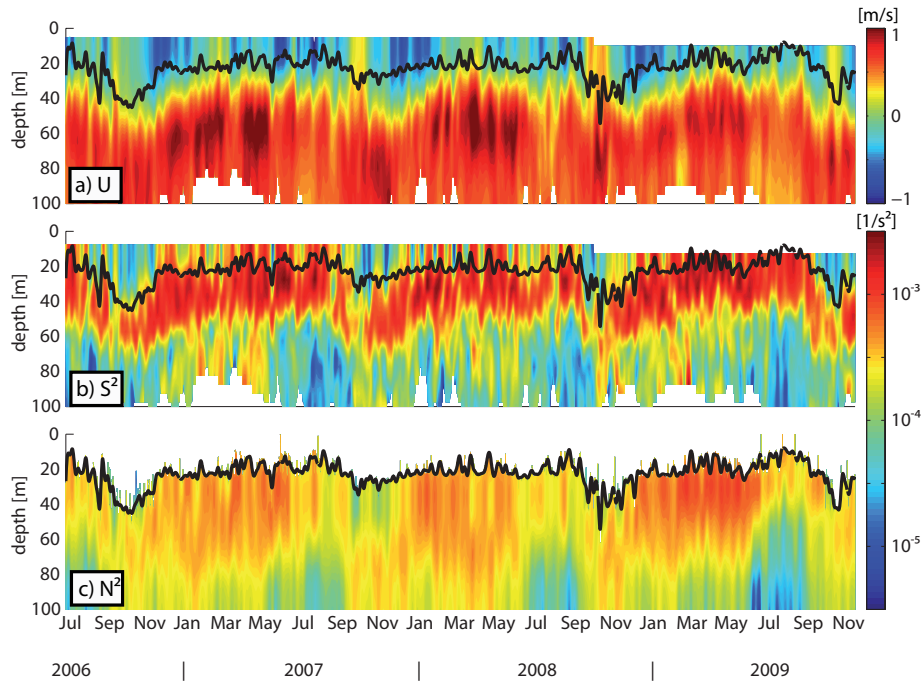
Figure 4.4.: Time-depth series between July 2006 and November 2009 of a) velocity, b) shear and c) stratification in the upper water column measured by the PIRATA buoy at 10°W,0°N. The black line denotes the MLD.
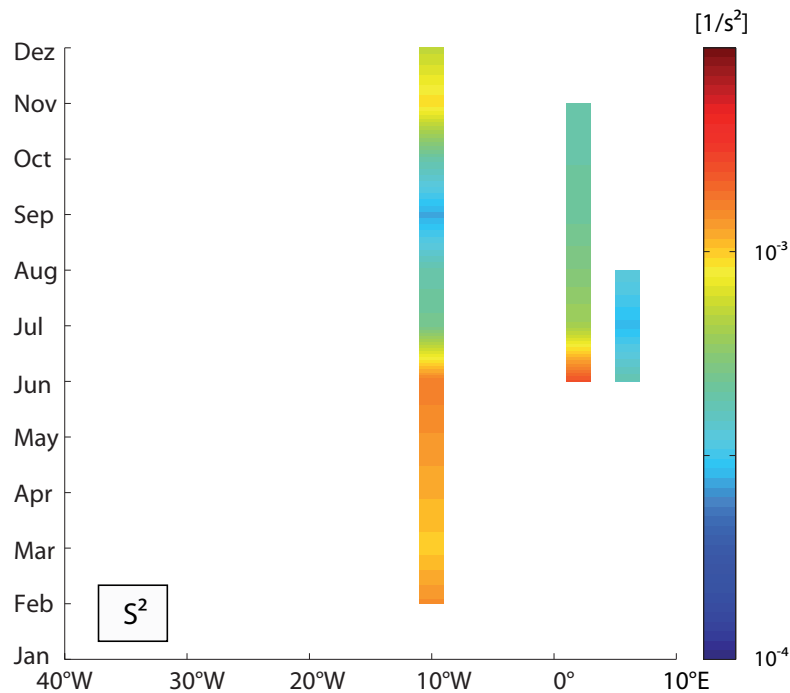
Figure 4.5.: Seasonal evolution of shear below the ML constructed from available cruise data.

deepening. In November shear levels again intensify. A similar seasonal evolution is observed for shear levels obtained from the ADCP moored at the PIRATA buoy. At this mooring site, ADCP measurements twice a day (0 and 12 UTC) for the timeperiod between July 2006 and
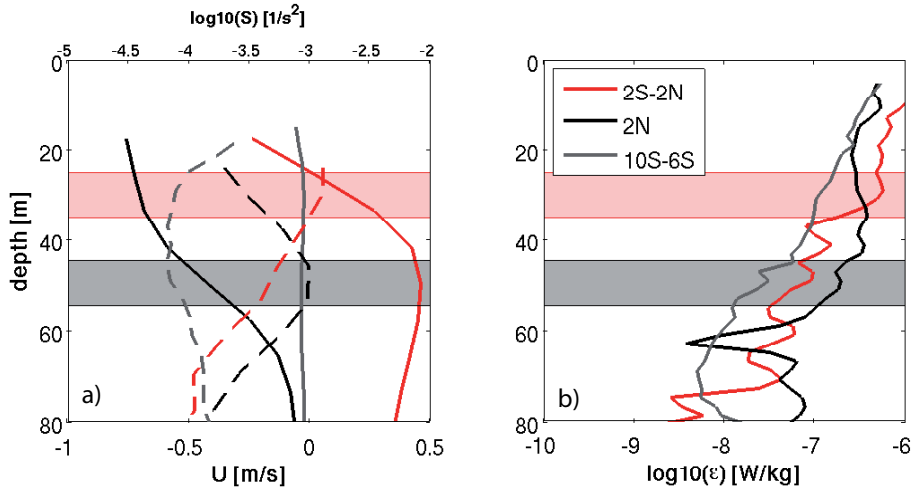
Figure 4.6.: a) Average zonal velocity (U, solid lines) and shear (S, dashed lines) profiles at 10°W for the entire equatorial belt (red), the northern edge of the cold tongue (black) and the southern ACT region (grey); b) the associated average profiles of dissipation rates of turbulent kinetic energy (ϵ). Average depth ranges of MLD+5 until MLD+15 are shaded for the equatorial region in red and for the poleward regions in grey.

November 2009 are available (see fig.4.4b). This ADCP record also shows the influence of the seasonal variability in nSEC strength as well as the vertical migration of the EUC core on the magnitude and vertical position of the shear maximum. Separating contributions of zonal and meridional shear for the ship sections provides information about the causes of the observed variability in shear levels.

Zonal shear is strongest during March to August (fig.4.3b), when the SEC shows its maximum velocities. The second SEC intensification in November/December is also reflected in a re-enhancement of zonal shear. Meridional shear shows maximum values in boreal summer and autumn (fig.4.3c). During this time period, TIWs are pronounced in the equatorial band (fig.2.13e) and inspection of the individual velocity sections (e.g. fig.2.11) indicates that meridional velocity shear is dominated by contributions of these waves. In autumn and between 2°N and 2°S, meridional shear variance contributes about 33% to total shear while in boreal summer it contributes about 25%. However, profile velocity time series from directly on the equator (not shown) suggest lower contributions of meridional shear: about 20% during boreal autumn and 12% during boreal summer. This implies that TIWs enhance shear levels throughout the region between 2°S and 2°N, but their relative contributions to S^2 directly at the equator is reduced.

Regional and seasonal variability of shear variance in the layer right below the surface ML is more pronounced than in deeper regions. Shear levels at 10°W and 2°E are of similar magnitude and reduced in boreal autumn compared to boreal summer. At 6°E the vessel mounted velocity data from 3 cruises indicates strongly reduced shear levels (fig.4.5).

It should be noted that enhanced shear variance below the ML is not only associated with the

EUC but that elevated levels are also found poleward of the EUC region in particular north of the equator in the vicinity of the nSEC (fig.4.1b, fig.4.6a). The shear provided by the nSEC itself results in average shear levels at 2°N to be of similar magnitude ($1 \cdot 10^{-3} s^{-2}$) below the ML than in the vicinity of the EUC. On the contrary, at the southern edge of the ACT (10°S-6°S), where no strong currents could be detected neither in the surface nor in the subsurface layer, average shear levels below the ML are considerable lower only of about $6 \cdot 10^{-5} s^{-2}$ (fig.4.2f, fig.4.6a), never exceeding $1.5 \cdot 10^{-3} s^{-2}$ on the considered cruise (fig.4.2i).

4.2. Stratification

Stratification, often characterized by the Brunt-Väisälä-Frequency N^2, is determined by the density gradient. Hence, the typical vertical distribution of N^2 shows low values within the rather homogeneous surface mixed layer of only around $5 \cdot 10^{-5} s^{-2}$ on average, increasing to maximum values of up to $1 \cdot 10^{-3} s^{-2}$ within the main thermocline associated with a depth range of 40-70m in the eastern tropical Atlantic.
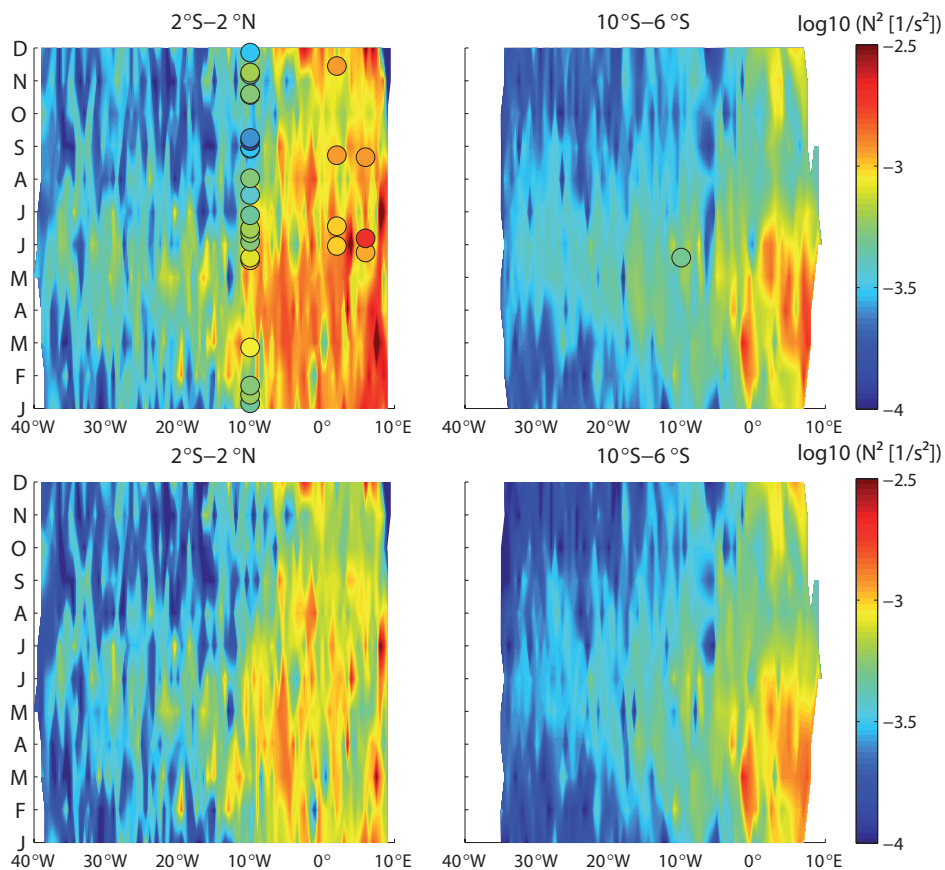

Figure 4.7.: Seasonal evolution of stratification constructed from ARGO float data in the equatorial (left panel) and southern ACT region (right panel). The climatology was constructed for observed salinity profiles (top panels) and a constant salinity of 35.5 (lower panels)
.

In contrast to shear, stratification within the ACT region below the ML increases from west to

4. Background conditions for turbulent mixing

east (fig.4.2j,k, fig.4.7a). A likely explanation for this behavior is associated with the large scale salinity distribution [e.g. *Jouanno et al.*, 2011]. East of 10°W surface waters are fresher due to enhanced precipitation in the Gulf of Guinea and fresh water discharges from the Niger and Congo rivers. The stronger stratification in the upper ocean is thus due to the strong increase of salinity of up to 3 in the upper 20-30m of the thermocline. *Jouanno et al.* [2011] find for their modeling study a strong reduction (50%) of stratification east of 0°E in the upper 30m, when omitting the influence of salinity on the stratification. For the climatology of stratification below the ML constructed from ARGO profiles the effect of salinity on the stratification, especially in the Gulf of Guinea, is also obvious. On average the reduction in stratification omitting salinity variations between 20°W-10°W is 15%, whereas further east between 0°-10°E it is about 35%. Thus, the influence of salinity on the strong stratification in the Gulf of Guinea also seems to hold for observations. However, the depth extent of elevated stratification diminishes towards the east due to the shoaling and narrowing thermocline (fig.4.2).

At 10°W, the seasonal variability of stratification between 2°S and 2°N constructed from the ship sections (fig.4.3d)) shows a similar temporal evolution as compared to shear variance. Stratification is strongest from January to April, while lowest values are observed in autumn, which is also observed for the climatology based on ARGO profiles (fig.4.7a). Similar to shear, stratification is strongest between the surface mixed layer and the EUC core. Stratification calculated from subsurface profiles of temperature and salinity measured by the PIRATA buoy shows similar characteristics. Temperature profiles are available at 10-minute resolution and are averaged over one hour including the ADCP observations. Unfortunately, salinity is available at hourly resolution only until the middle of September 2008, afterwards salinity is only available at daily resolution. As salinity is presumed to show less diurnal variation than temperature the daily averages are taken as day and night observations after mid September 2008. The resulting temperature and salinity fields are used to calculate N^2. Stratification is not well resolved by the measurements of the PIRATA buoy due to the coarse vertical resolution of salinity at only 1m, 20m, 40m and 120m. Nevertheless, the seasonal variability of stratification in terms of the reduction towards autumn as observed with the vertically high resolved ship sections (1m resolution for temperature and salinity) is captured (fig.4.4c). Note that in the western equatorial ACT (2°N-2°S) ship sections as well as moored observations indicate that stratification is in general lower than shear, indicating an average Richardson number of less than unity. However, stratification exceeds shear in the eastern equatorial ACT.

In the southern ACT region (10°S-6°S) stratification below the ML at 10°W is of similar magnitude compared to the equatorial region below the ML (fig.4.2j-l, 4.7). Note though that due to the deeper ML, the vertical distribution of stratification is shifted to greater depths (fig.4.2j-l). The increase in stratification towards the east is weaker than in the equatorial region, and the influence of salinity is lower (8% within 20°W-10°W and only 3% within 0°-10°E). Similar as described for the eastern equatorial ACT stratification exceeds shear levels in the southern ACT.

4.3. Froude numbers

Although energy transfer from the background flow to turbulence may also occur at higher gradient Richardson numbers $Ri = N^2/S^2$ [e.g. *Canuto et al.*, 2008], vigorous mixing in the equatorial thermocline is usually associated with Ri numbers smaller than 0.25 [e.g. *Peters et al.*, 1988], or gradient Froude numbers ($Fr = 1/Ri$) larger than 4 respectively. As suggested by the meridional distributions of shear variance, the occurrence of elevated Fr numbers are not only restricted to the equator, but are found in the region between 2°N and 2°S (fig.4.1d).
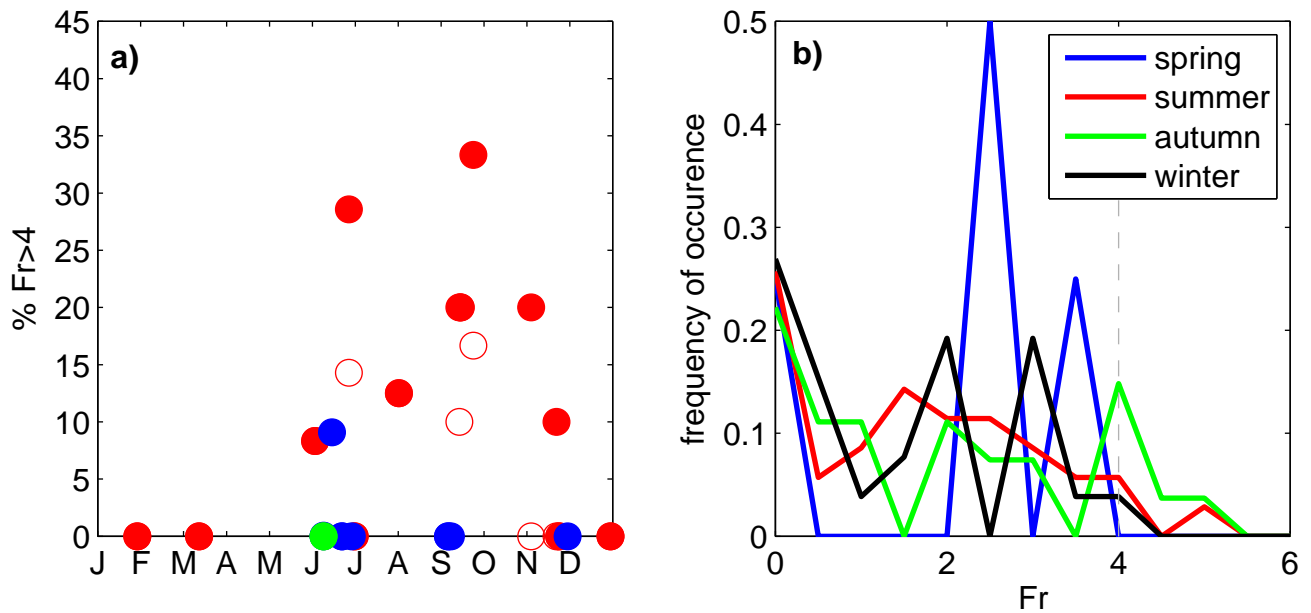
Figure 4.8.: a) Percentages of Fr numbers crossing the critical threshold of 4 for the equatorial region at 10°W (filled red circles), at 2&6°E (filled blue circles) and the southern ACT region (filled green circle). The empty circles are percentages of Fr numbers crossing the threshold calculated only with zonal shear. b) Seasonal distribution of Fr numbers in the equatorial region at 10°W.

Average Fr numbers determined from the seasonal distributions of shear and stratification levels from 10°W averaged between 2°S and 2°N, show values above one in the upper 50m of the water column throughout most of the year (fig.4.3e). However, higher average Fr numbers of above 2 below the ML are evident during the second half of the year. This suggests that Kelvin-Helmholtz instability and thus elevated mixing is more likely to occur in the upper stratified ocean from late boreal summer to early winter. As shear variance reduces from below the ML towards the EUC core while stratification increases, Fr numbers rapidly decrease below 50m depth. Average meridional velocity shear significantly contributes to the seasonal Fr distribution, particularly during the second half of the year. Fr numbers determined from zonal shear only hardly exceed values greater than 1 during this period (fig.4.3f).

Focusing on the layer just below the ML and extracting Fr numbers separately for every station below the individual ML strikes three main facts:

4. Background conditions for turbulent mixing

1. *Fr* numbers pass the critical threshold of 4 rather frequently in the western equatorial ACT region (10°W) between 2°S and 2°N (up to 35%), while in the eastern equatorial and southern ACT the critical threshold is only rarely exceeded.

2. The threshold of 4 in the western equatorial ACT is reached frequently from July to November (10-35%), whereas in the beginning of the year, low *Fr* numbers are observed (fig.4.8).

3. In the western equatorial ACT the percentage of *Fr* numbers exceeding the threshold of 4 is significantly reduced (by up to a factor of about 2), when meridional shear contributions are omitted from the calculations, highlighting the importance of meridional shear for instabilities to develop.

From the combined data of satellite SSTs, ship velocity sections as well as the moored velocity observations at 10°W,0°N it is suggested that TIWs significantly contribute to elevated meridional shear in the upper 60m of the water column from June to October (e.g. fig.2.11, fig.2.13). As has been shown for the equatorial Pacific [*Moum et al.*, 2009], it seems that the enhanced meridional velocities associated with TIWs contribute to the elevated frequency of occurrence of critical *Fr* numbers in the central ACT region including 10°W.

4.4. Summary and discussion

Inspection of the background settings for turbulent mixing in terms of shear and stratification within the ACT region suggests turbulent mixing intensity most likely to be elevated within the western equatorial ACT region during boreal summer and autumn.

The energetic currents observed within the equatorial ACT region elevate shear levels between the ML and the core of the EUC. Towards the eastern equatorial ACT the strength of the combined current system diminishes. The depth extent over which velocities vary also diminishes towards the east due to the shoaling of the EUC. Hence, shear levels at 2°E are still elevated and only clearly reduce as far east as 6°E, where the EUC was reported a transient feature. In the southern ACT region, however, shear levels are strongly reduced compared to the entire equatorial region due to strongly reduced horizontal velocities.

Seasonally shear levels in the western equatorial ACT region reduce towards autumn, re-intensifying towards the end of the year. In addition, the depth layer of highest shear levels is at its maximum depth in autumn. The meridional component of shear is rather constant from boreal summer through autumn and probably associated with the presence of elevated meridional velocities due to the presence of TIWs as described in chapter 2. The zonal shear component is dominated by the seasonal variation of the nSEC strength as well as the deepening of the EUC core during autumn. The deepening of the EUC core is in accordance with the deepening of the MLD and the thermocline during this period (chapter 2).

The mechanism driving the seasonal migration of the EUC core is presumably associated with the zonal pressure gradient [*Provost et al.*, 2004], probably also causing the deepening of MLDs and thermocline during autumn. In general, the shoaling thermocline and EUC in the equatorial

region are an adjustment to the zonal pressure gradient at the surface set up by the wind forcing. This pressure gradient is largest at the western boundary reducing towards the east. As the zonal pressure gradient relaxes during boreal summer, due to the reduction of the zonal winds at the equator in the central basin (fig.2.6), the zonal shoaling of the EUC and the thermocline probably relaxes accordingly during autumn as a lagged response.

Stratification below the ML in the equatorial region increases from west to east, which is associated with the presence of fresh waters in the upper layers in the Gulf of Guinea increasing the density gradient below the ML. Towards autumn, stratification reduces in the western equatorial region (until 10°W). This can probably be associated with the described relaxation of the zonal thermocline slope due to the relaxed surface wind stress as was assumed responsible for the deepening of the ML and the EUC core. For stratification, the widening of the isotherms (due to the relaxation of the zonal thermocline shoaling) during this season reduces the vertical density gradient and results in lower stratification. In the southern ACT region stratification is in general of similar magnitude below the ML. Nevertheless the increase towards the east can also be observed.

High Fr numbers crossing the critical threshold of 4, indicative of elevated mixing intensity, are frequently found in the western equatorial ACT region. In the eastern ACT region the critical threshold is reached less frequently. At 2°E shear levels are still of similar magnitude, but stratification has increased, reducing the occurrence of high Fr. As far east as 6°E in addition to the increased stratification, shear levels have strongly reduced, further decreasing the inferred Fr numbers. Seasonally, high Fr numbers are observed more frequently during boreal summer in the entire equatorial ACT region. It has been additionally observed that in the western equatorial ACT region meridional shear, which is presumed to be associated with TIWs, contributes nearly equally to the occurrence of critical Fr numbers especially during boreal summer and autumn. Note, that *Moum et al.* [2009] find for the equatorial Pacific during the presence of a TIW a fourfold decrease (from 12 to 3%) of Ri numbers crossing the critical threshold, if the meridional shear contribution is omitted from the calculations. The generally lower percentages in their study are probably due to the consideration of a deeper layer in comparison to the choice in this study. However, the findings of this study support the assumption that TIWs influence shear conditions favorable for mixing activity in the central equatorial oceans. Therefore, it is suggested that they crucially contribute to elevated mixing levels within the western equatorial ACT during boreal summer and autumn. In the southern ACT region Fr numbers are not observed to cross the critical threshold.

5. Mixing parameters

Within the following chapter, the microstructure data collected on the 8 cruises to the equatorial ACT region (tab.3.1) is discussed. The background conditions encountered during those cruises agree generally well with the climatological background conditions described in chapter 2 and 4. The only significant discrepancy between climatological background and observations was encountered during the Meteor cruise from June 25 to July 5 2006, which was due to the occurrence of an intra seasonal wind burst causing westerly wind stress above climatology [*Marin et al.*, 2009]. Nevertheless, the overall agreement of climatological background and background conditions observed during the cruises suggests that microstructure observations represent realisations under typical background forcing conditions in the sampled regions and seasons.

5.1. Dissipation rates

To date and except for the analysis presented below, results from microstructure measurements in the equatorial Atlantic were solely reported by *Crawford and Osborn* [1979]. Their data, consisting of 8 profiles obtained from different locations in the central equatorial Atlantic during July 1974, showed elevated turbulence levels in the upper shear layer of the EUC between the surface mixed layer and the main thermocline. Typical values of turbulent dissipation rates below the ML in their study were on the order of $3 \cdot 10^{-7} W kg^{-1}$.

As described in chapter 2, the 785 microstructure profiles available for this study were predominantly collected during repeated surveys along 4 meridional sections: $10°$W, $2°$E, $6°$E and $23°$W (tab.3.1). In general, turbulent dissipation rate profiles calculated from microstructure shear data collected outside the equatorial band (latitudes$> 3°$) rarely exhibit elevated turbulence levels in the upper thermocline (e.g. fig.4.1c). In fact, (arithmetically) averaged profiles of dissipation rates for the off-equatorial regions rapidly decrease below the ML within a few meters by an order of magnitude until indistinguishable from instrument noise ($< 1 \cdot 10^{-9} W kg^{-1}$) at 80m below the ML (fig.5.1). Note that for the following figures, the vertical coordinate is the vertical distance to the ML for better comparison of turbulence parameters. It has to be kept in mind though that MLDs get larger with distance from the equator (chapter 4). An entirely different depth distribution of dissipation rates compared to the off-equatorial regions is observed within the equatorial band ($\pm 2°$ latitude). Here patches of elevated dissipation rates are frequently observed way below the ML (fig.4.1d, 5.1a, 5.2). The average equatorial dissipation rate immediately below the ML is $4 \cdot 10^{-7} W kg^{-1}$ (with 95% confidence limits of $3.2 \cdot 10^{-7} W kg^{-1}$ and $4.4 \cdot 10^{-7} W kg^{-1}$ respectively and denoted by [] in the following. Note that these confidence limits are only based on statistical evaluations as explained in Appendix A.) and gradually decrease to $1 \cdot 10^{-9} W kg^{-1}$ at a depth of 130m below the ML. Above this depth, average dissipation rates are
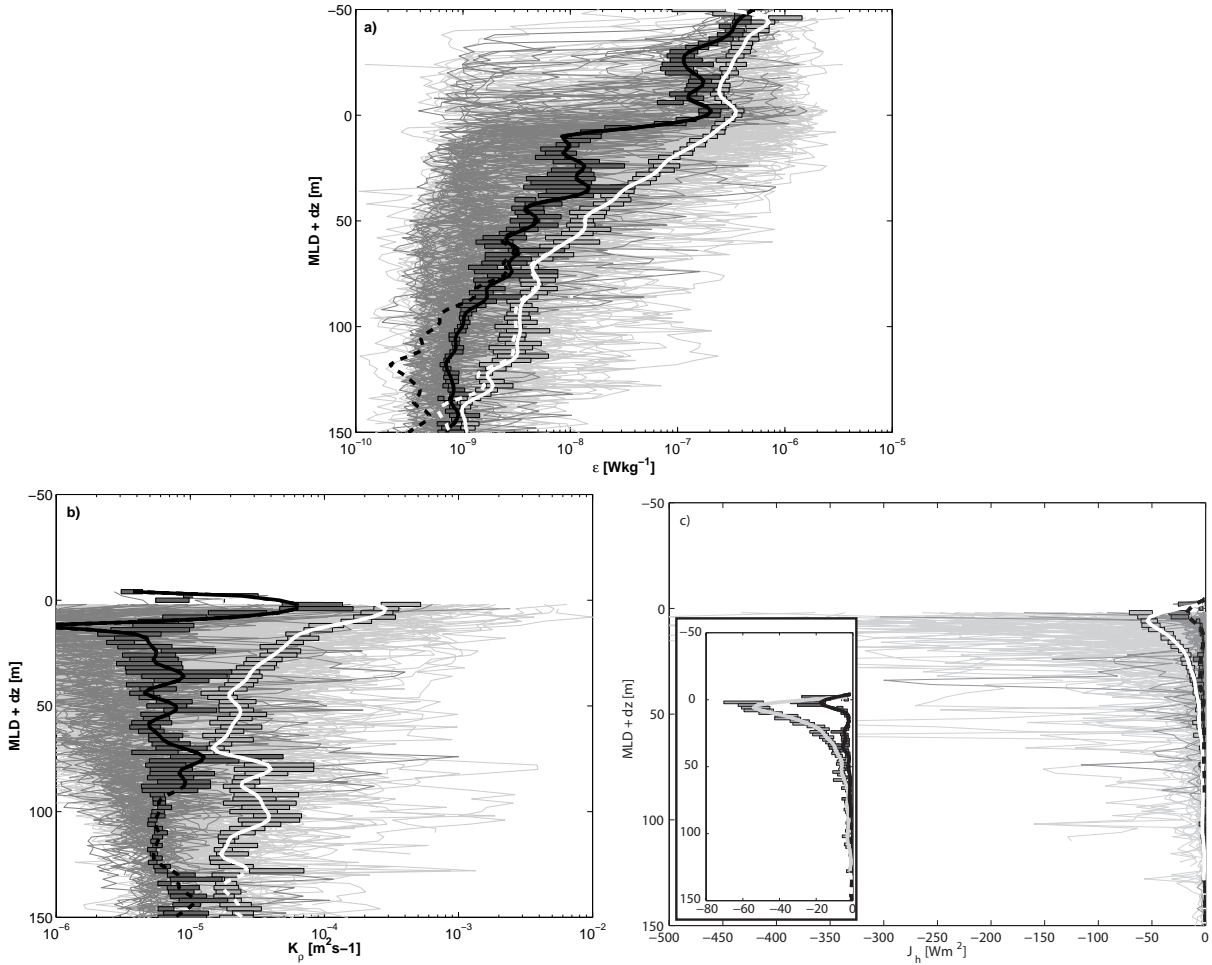
Figure 5.1.: a) Individual turbulent dissipation rate profiles from the off-equatorial (thin dark grey lines) and equatorial (thin light grey lines) regions together with their arithmetical averages (heavy black, heavy white). The vertical coordinate is adjusted to MLD+dz. 95% condidence limits are indicated as horizontal bars and are obtained using the bootstrap method as explained in Appendix A. Dashed lines indicate the effect of the noise level of the instrument as also explained in Appendix A; b) same as a) but for eddy diffusivities K_ρ; c) same as a) but for the diapycnal heat flux J_h.

hardly affected by the instrument noise level (fig.5.1a). In the layer from the ML to 30m below, turbulent dissipation rates in the equatorial region are elevated by an order of magnitude compared to the off-equatorial dissipation rates. Dividing the off-equatorial region into the northern edge of the ACT (2°N) and the southern edge (10°S) reveals rather different profiles of mixing intensity. At the northern edge, where the nSEC still provides significant shear to the upper water column, average dissipation rates below the ML in boreal summer are still elevated up to $4 \cdot 10^{-7} W kg^{-1}$. This is a reduction of about 2.5 compared to the average equatorial dissipation rates at 10°W during the same cruise (fig.4.6b). On the other hand, at the southern edge of the ACT, where velocities were strongly reduced and shear levels lower, average dissipation rates below the ML are of only about $3 \cdot 10^{-8} W kg^{-1}$ below the ML, reduced by a factor of about 10 compared to the equatorial rates. In the following, the discussion will focus on the data collected

5. *Mixing parameters*

within the equatorial band.

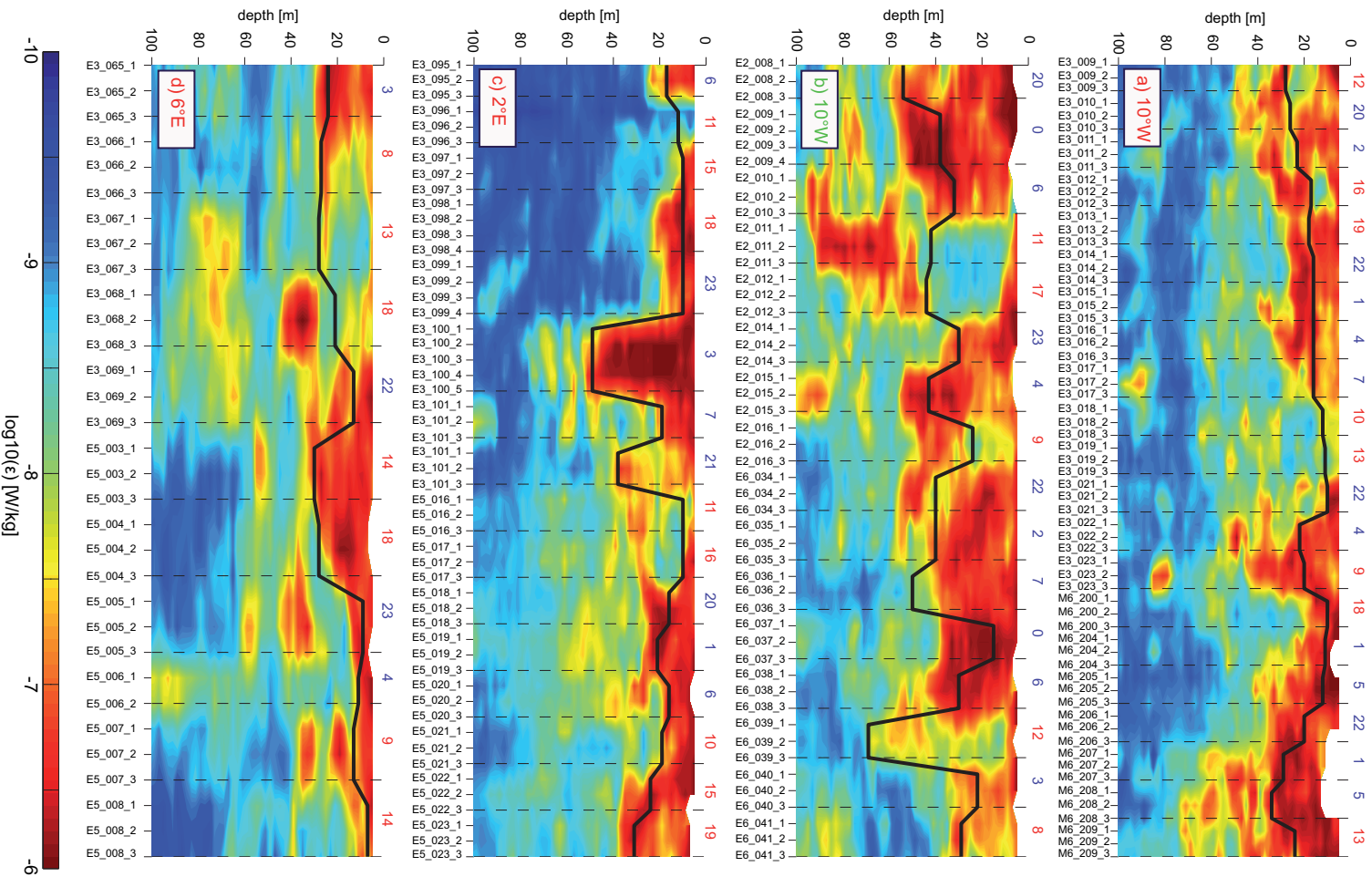Figure 5.2.: Contoured profiles of dissipation rates within 2° of the equator for different longitudes and seasons: a) June/July 10°W, b) September 10°W, c) June 2°E and d) June 6°E. Vertical dashed lines mark the change of sampling position. Profiles at single positions were usually repeated after about 20 minutes. Red and blue numbers above the plots indicate local sampling time.

Particularly notable at the equator at 10°W and to a lesser extent at 2°E were extensive dissipation rate maxima of $0.5 - 3 \cdot 10^{-6} W kg^{-1}$ that reached from the mixed layer 50m down into the thermocline (fig.5.2a-c). These maxima usually persisted during the entire sampling period of one to two hours at an individual station, indicating the considerably slow decay time of such vertical coherent turbulent structures. They were most common in boreal summer at 10°W, where they reached at least 20-30m into the stratified water column. At 2°E and 6°E, depth penetration of the coherent maxima into the thermocline is significantly reduced to 5 to 10m of the stratified waters.

The vertical and temporal distributions of turbulent dissipation rates from the central ACT region at 10°W agree well with previous observations from the equatorial Pacific at 140°W [e.g. *Gregg et al.*, 1985; *Moum et al.*, 1989; *Peters et al.*, 1994; *Lien et al.*, 1995]. There, similar strong bursts of turbulence extending from the mixed layer into the Pacific thermocline were frequently observed. However, many of the Pacific microstructure data sets indicate that the strong coherent bursts of turbulence predominantly occur during night time. This process, termed deep-cycle turbulence, involves night time convection in the mixed layer, elevated vertical shear of horizontal velocity in and below the mixed layer and internal waves and is confined to the upper 20 to 30m of the thermocline [e.g. *Moum et al.*, 1992; *Peters et al.*, 1994; *Wang and Müller*, 2002]. When active, night time dissipation rates in that layer are on average an order of magnitude larger than their day time counterparts. Although the depth penetration of the coherent bursts in the western ACT region is similar to the observations in the central Pacific, night time dissipation rates in a 20 m layer below the ML, between 23°W and 10°W, are on average only elevated by a factor of 3 compared to day time values. Moreover, in the eastern ACT region, east of 2°E, differences in day and night time dissipation rates are not detectable. Nevertheless, on average dissipation rates from the equatorial Atlantic are of similar magnitude compared to the observations from the equatorial Pacific [*Peters et al.*, 1988; *Moum et al.*, 1992; *Lien et al.*, 1995]. This is due to the fact that in contrary to the Pacific, elevated coherent bursts of turbulence in the Atlantic also occur during day time (fig.5.2) elevating the average dissipation rates below the ML towards the Pacific values.

At 10°W, two deeper maxima of turbulent dissipation rates $(0.5 - 1 \cdot 10^{-6} W kg^{-1})$ were observed that did not connect with mixed layer turbulence and extended up to 80m depth (fig.5.2a,b). Both occurrences were observed just above the EUC core in the region close to the equator. During both September cruises, a TIW was present at the sampling site contributing additional vertical shear to the upper water column (fig.4.8). It is thus likely that the enhanced dissipation rates below the mixed layer (fig.5.2b) and in particular the deeper maximum, are related to the presence of the instability waves. In the 10°W boreal summer data, the region of low mixing between 60 and 80m depth (fig.5.2a) reflects the core depth of the EUC, while below this region, i.e. in the lower shear zone of the EUC, occasional mixing events were observed. Within those events, however, dissipation rates rarely exceeded $1 \cdot 10^{-7} W kg^{-1}$. Similar deeper turbulent patches were also observed in the eastern ACT region (fig.5.2c,d). At 6°E in particular, these patches cannot be due to shear instability of the background EUC/SEC system as those currents are particularly weak in the eastern Gulf of Guinea.

5. Mixing parameters
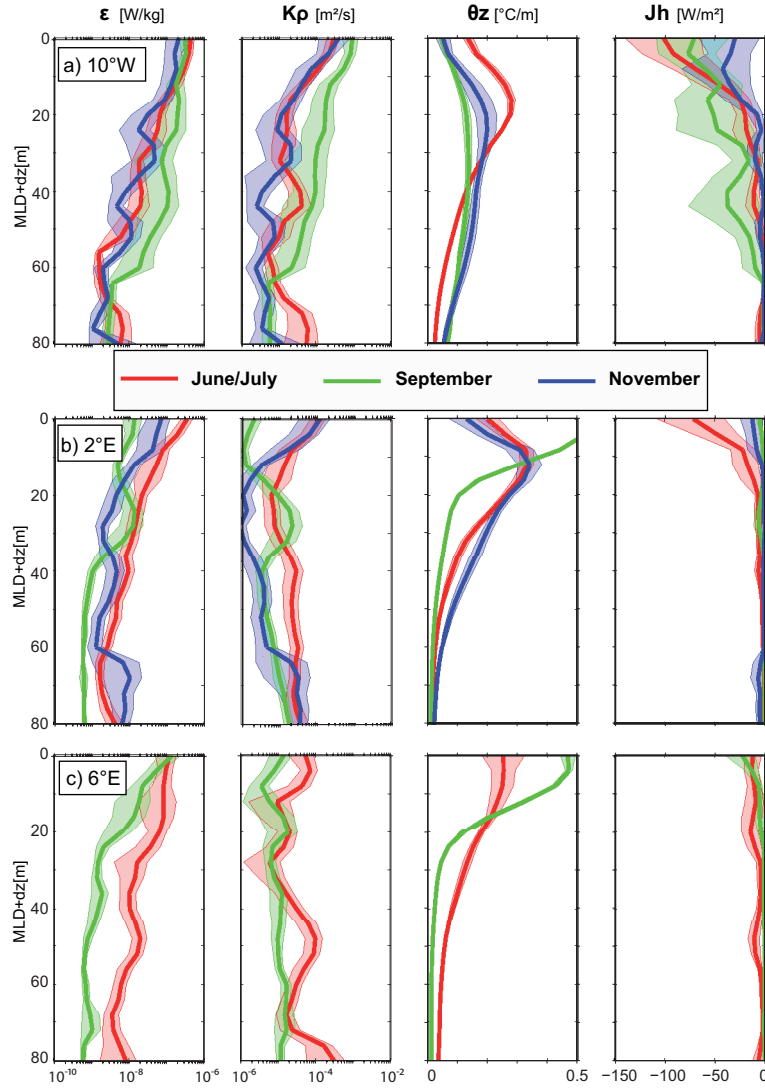
Figure 5.3.: Average seasonal profiles of dissipation rates (ϵ), eddy diffusivities (K_ρ), temperature gradient ($\partial T/\partial z$) and diapycnal heat fluxes (J_h) on sections 10°W (a), 2°E (b) and 6°E (c) in June/July (red), September (green) and November (blue). Coloured shadings are 95% confidence limits in vertical coordinates of MLD+dz.

To quantify the variability of mixing levels in the equatorial ACT region during the different phases of cold tongue development, average dissipation profiles and uncertainties were calculated for those ship sections, which have been sampled most frequently (fig.5.3). To avoid bias due to possible diurnal variations, dissipation rates were averaged separately for day and night before final averaging. Maximum average dissipation rates just below the mixed layer are about $4 \cdot 10^{-7} W kg^{-1} [8.4 \cdot 10^{-8}; 5.6 \cdot 10^{-7} W kg^{-1}]$ at 10°W in June, September and November. At this location, dissipation rates decrease by two orders of magnitude from below the base of the ML to the EUC core at 80m depth. In the September average, that includes data from two cruises (Sep. 2005 and Sep. 2007), dissipation rates stay on a rather uniform level until about 60m depth, abruptly decaying towards the EUC core. As suggested previously, the enhanced dissipation rates between 20 and 60m below the ML are associated with the presence of the

Figure 5.4.: Profiles of dissipation rates from the western (thin light grey line) and eastern (thin dark grey line) equatorial ACT region for a) June/July, b) September and c) November, together with their average profiles (west= heavy green line, east= heavy blue line) and the 95% confidence limits in vertical coordinates of MLD+dz.

TIWs at the sampling site, contributing additional vertical shear of horizontal velocities to the upper thermocline. This deeper pene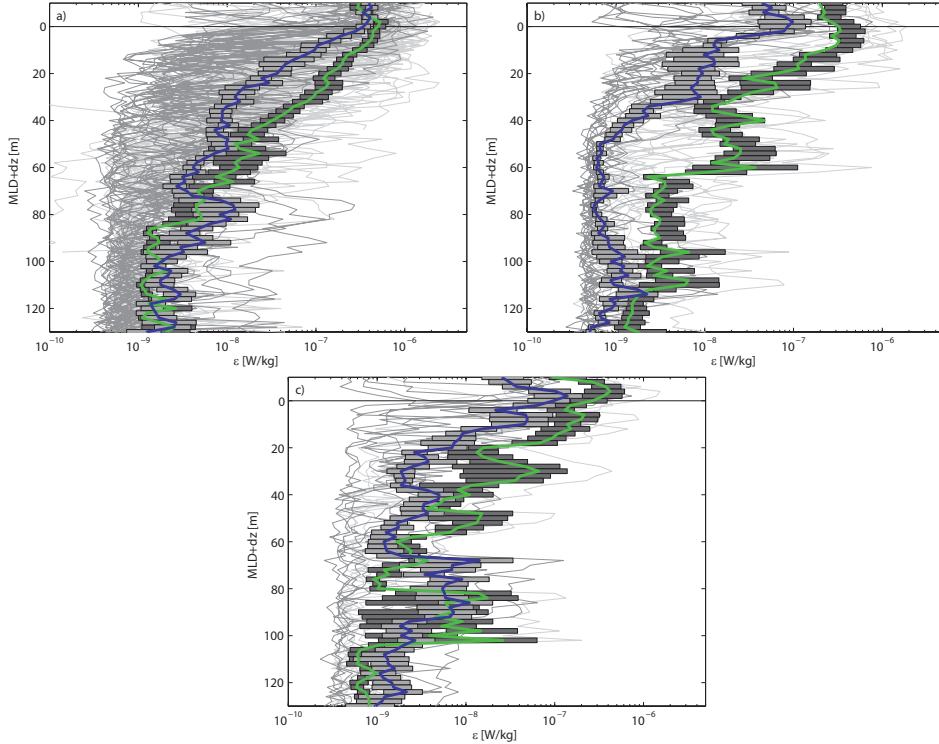tration of elevated dissipation rates during the presence of a TIW was also observed in the equatorial Pacific [*Moum et al.*, 2009]. In the eastern ACT region at 2°E, highest dissipation rates below the ML are found in June, significantly reducing in September and November. In general, the depth decay of average dissipation rates at 2°E and 6°E below the ML occurs more rapidly than at 10°W. At 2°E average dissipation rates below the ML are two orders of magnitude lower in September below the ML compared to June.

The discussed section averaged dissipation rate profiles point towards general differences between the western and eastern equatorial ACT region. To quantify zonal variability of dissipation rates in the equatorial ACT region, dissipation rate profiles were hence divided into the western (23°W-10°W) and eastern (2°-6°E) equatorial region. Higher dissipation rates in the western compared to the eastern equatorial ACT region below the ML can be found during all observed cold tongue stages (fig.5.4). Largest west-east differences in dissipation rates were found in September, of nearly two orders of magnitude. During this time, elevated dissipation rates associated with TIWs penetrate deep into the stratified layers in the western equatorial ACT, whereas lowest dissipation rates were observed in the east. During June/July and November, the average dissipation rates for the western and eastern equatorial ACT region differ by a factor of about 10. The western ACT region shows elevated dissipation rates directly below the ML of clo-

se $1 \cdot 10^{-7} W kg^{-1}$ during all observed seasons slightly reducing towards the end of the year, while in the eastern equatorial ACT region the decrease from boreal summer to September/November is more pronounced.

5.2. Eddy diffusivities

Another measure describing diapycnal mixing is turbulent eddy diffusivity. As explained in the introduction these diffusivities are used to describe turbulent fluxes in analogy to molecular diffusive fluxes (see section 1.3). Thus obtained turbulent fluxes can be integrated into the equation system one wished to solve. It was also pointed out, that numerical models crucially depend on the parametrization of diapycnal eddy diffusivity in order to estimate the turbulent fluxes and close their equation system. Hence, the magnitude and distribution of this parameter is of fundamental interest for the oceanographic research community. As previously discussed, *Osborn* [1980] described a method to estimate eddy diffusivities from dissipation rates derived from microstructure observations as well as stratification (equation 3.1).
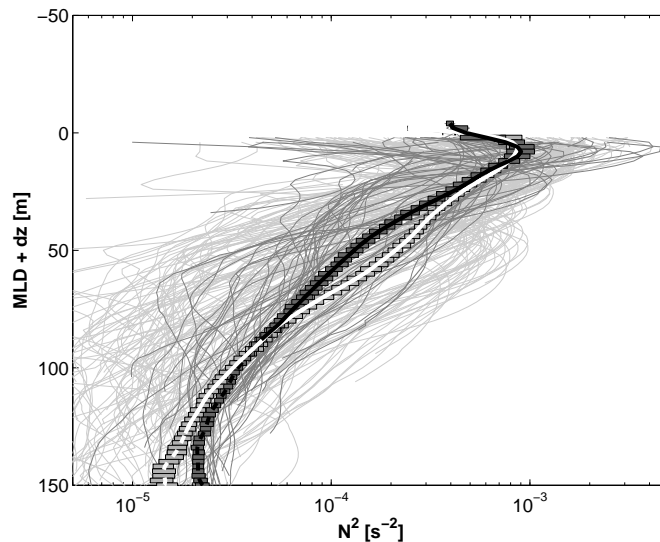
Figure 5.5.: Individual profiles of N^2 from the off-equatorial (thin dark grey lines) and equatorial (thin light grey lines) regions together with their arithmetical averages (heavy black, heavy white). The vertical coordinate is adjusted to MLD+dz. 95% condidence limits are indicated as horizontal bars and are obtained using the bootstrap method as explained in Appendix A.

Turbulent eddy diffusivities (K_ρ) increase with increasing dissipation rates and decreasing stratification. Within this study station averaged eddy diffusivity profiles are obtained from station averaged dissipation rate profiles and averaged buoyancy frequency profiles. The observed variability of these parameters in the upper equatorial thermocline results in a range of eddy diffusivities between 10^{-6} and $10^{-3} m^2 s^{-1}$ (fig.5.1b, 5.3). Equatorial dissipation rates were observed elevated by an order of magnitude compared to the off-equatorial region (fig.5.1a). Stratification in the off-equatorial region has a similar vertical distribution to the equatorial regions (fig.5.5).
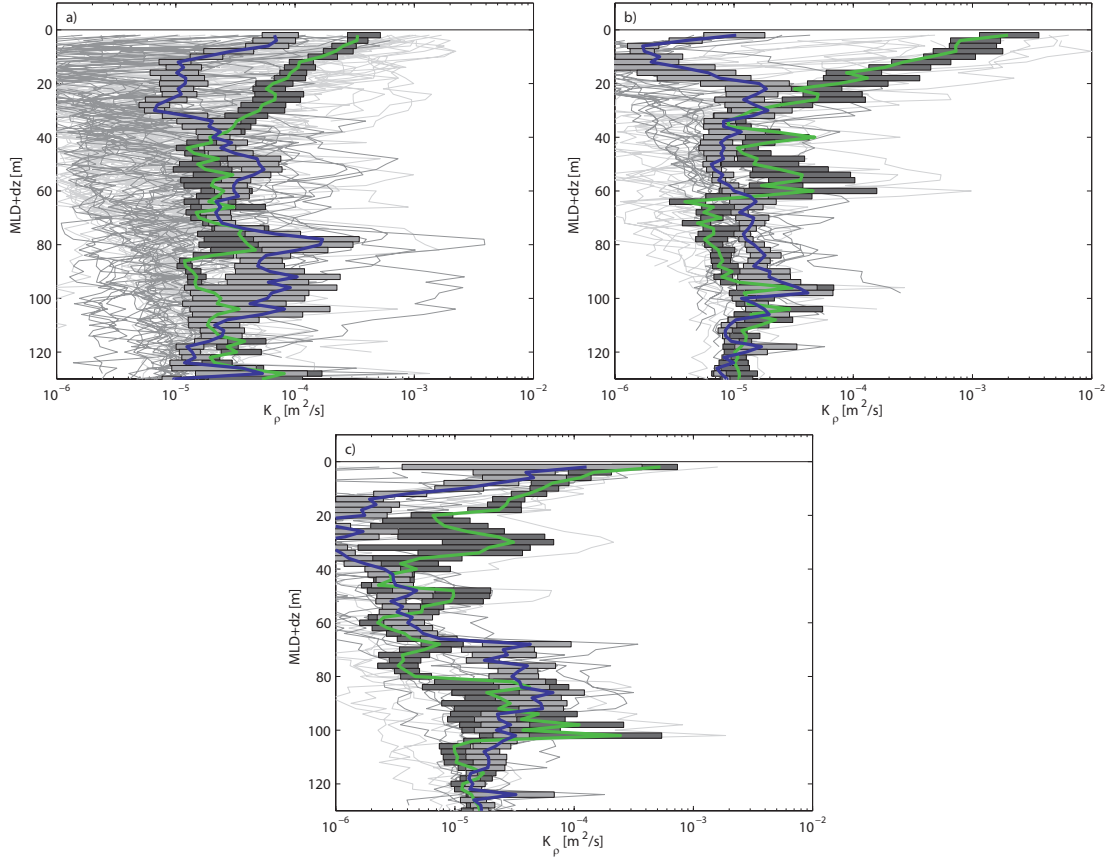
Figure 5.6.: Profiles of eddy diffusivity K_ρ from the western (thin light grey line) and eastern (thin dark grey line) equatorial ACT region for a) June/July, b) September and c) November, together with their average profiles (west= heavy green line, east= heavy blue line) and the 95% confidence limits in vertical coordinates of MLD+dz.

Again the depth coordinate is adjusted and the ML in the off-equatorial region is considerably deeper (chapter 2). Nevertheless, due to the reduced dissipation rates and the similar levels in stratification, average profiles of eddy diffusivities from the off-equatorial regions below the ML are reduced by an order of magnitude compared to the equatorial averages (fig.5.1b).

Average equatorial eddy diffusivities reduce from about $2.5 \cdot 10^{-4} m^2 s^{-1}$ (with 95% confidence limits of $2 \cdot 10^{-4} m^2 s^{-1}$ and $5 \cdot 10^{-4} m^2 s^{-1}$ respectively, obtained as explained in Appendix A and in the following denoted as []) just below the ML by over an order of magnitude towards the core of the EUC, caused by the reduction in dissipation rates and increasing stratification. Below MLD+50, average eddy diffusivities in the equatorial region stay at a rather constant level of about $2 \cdot 10^{-5} m^2 s^{-1} [1.4 \cdot 10^{-5}; 2.3 \cdot 10^{-5} m^2 s^{-1}]$. This corresponds to the range of eddy diffusivities reported from the equatorial Pacific [*Gregg et al.*, 1985; *Moum et al.*, 1989; *Peters et al.*, 1988; *Lien et al.*, 1995]. Note that within the ML, eddy diffusivities are not calculated due to the marginal stability of the water column. On the contrary, the average off-equatorial eddy diffusivities decrease from about $6 \cdot 10^{-5} m^2 s^{-1} [5 \cdot 10^{-5}; 1.3 \cdot 10^{-4} m^2 s^{-1}]$ directly below the ML to about $5 \cdot 10^{-6} m^2 s^{-1} [4 \cdot 10^{-6}; 8.3 \cdot 10^{-6} m^2 s^{-1}]$ at MLD+10m, where they stay at this level until about MLD+80. Below MLD+80 the estimations of eddy diffusivities are affected by

instrument noise in the estimates of ϵ.

Maximum eddy diffusivities in the equatorial ACT region are found at 10°W in September (fig.5.3), when dissipation rates are elevated until MLD+60. These elevated dissipation rates penetrating far into the stratified layers were associated with the presence of TIWs. During the same time, minimum levels of stratification were observed within the annual cycle (chapter 4). Hence, the elevated levels of dissipation rates in combination with low stratification result in these high eddy diffusivities. During the presence of a TIW eddy diffusivities were observed to be elevated up to $1 \cdot 10^{-2} m^2 s^{-1}$ below the ML in the equatorial Pacific [*Moum et al.*, 2009]. The presented data from the equatorial Atlantic exhibits maximum eddy diffusivities on the order of $1 \cdot 10^{-3} m^2 s^{-1}$ during the presence of TIWs (fig.5.3, 5.6). In June and November average eddy diffusivities at 10°W are reduced compared to September. The average June profile of eddy diffusivities from the entire western equatorial ACT (23°W-10°W), however, shows elevated values in June compared to November (fig.5.6a,c).

Further east in the Gulf of Guinea eddy diffusivities are in general reduced compared to the western equatorial ACT region during all observed cold tongue stages. This is due to the generally reduced dissipation rates within this region (fig.5.4) in combination with higher levels in stratification (chapter 4). In addition, the depth decay of eddy diffusivities in the eastern ACT occurs faster compared to the west. In the east, lowest eddy diffusivities are observed directly below the ML in September compared to the other months reduced by nearly two orders of magnitude. During this time dissipation rates were observed lowest and stratification was still comparably high. Note, that the autumn reduction of stratification could not be detected east of 5°W (chapter 3). Highest eddy diffusivities on the eastern longitudes are observed during boreal summer.

5.3. Diapycnal heat fluxes

As mentioned previously, eddy diffusivities can be used to describe turbulent fluxes (see section 1.3). This study aims to determine the downward heat loss of the ML due to turbulent mixing, hence the turbulent heat flux will be investigated within this section. To understand how heat should be extracted from the ML due to turbulent mixing one has to consider the vertical distribution of the diapycnal turbulent heat flux. Profiles of the diapycnal heat flux (J_h) from the equatorial Pacific were reported only negative and highly divergent in the vertical with a change between negative and positive divergence. Maximum values of J_h were observed at the base of the ML beyond which J_h decreased and vanished towards the core of the EUC [e.g. *Gregg et al.*, 1985; *Peters et al.*, 1988; *Lien et al.*, 1995]. A similar depth distribution is on average observed for the diapycnal heat flux from the ACT region (e.g. fig. 5.7). The vertical increase in magnitude of J_h within the ML describes that heat is transported out of this layer, cooling the ML and hence the SST. At the base of the ML the diapycnal heat flux reaches its 10-15m broad maximum. Below, J_h decreases, thus more heat is transported into this layer than taken out via turbulent mixing. Consequently this layer must be heated concerning the diapycnal heat flux. Hence, due to turbulence heat is redistributed from the ML to about the upper 100m of

the thermocline. The heat loss of the ML due to turbulence is accordingly characterized by the peak in magnitude of the diapycnal heat flux, which is concentrated in a rather narrow layer of about 10m at the base of the ML (fig. 5.7).
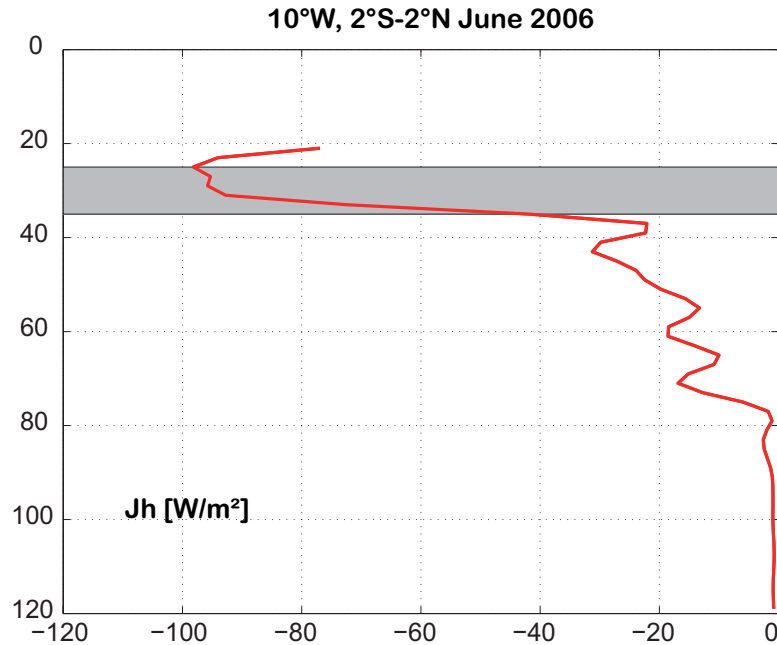
Figure 5.7.: Avergage profile of J_h observed in the equatorial region (2°S-2°N) at 10°W in June 2006. Negative values describe the downward transport of heat. The grey shading marks the average layer of MLD+5-MLD+15m

Former studies from the equatorial Pacific at 140°W on the equator have estimated the heat loss of the ML in a range of 10-100 Wm^{-2} dependent on varying background conditions [*Gregg et al.*, 1985; *Peters et al.*, 1991, 1988; *Lien et al.*, 1995]. Recent observations at this location showed diapycnal heat flux out of the ML of up to 400 Wm^{-2} during the presence of a TIW [*Moum et al.*, 2009].

Diapycnal heat fluxes inferred from microstructure observations in the equatorial Atlantic show in general a similar depth distribution as reported from the equatorial Pacific being always negative, but highly divergent in the vertical with a maximum in magnitude at the base of the ML. However, considerable regional as well as seasonal variability within the ACT region is evident concerning the maximum magnitude of J_h as well as the depth interval over which it decays.

Diapycnal heat fluxes in the off-equatorial ACT region are observed significantly lower compared to the equatorial ACT by at least a factor of 2 on average. This is in accordance with the strongly reduced dissipation rates and eddy diffusivities observed in the off-equatorial region compared to the equatorial belt. The average equatorial diapycnal heat flux reduces from about $55Wm^{-2}$ (with lower and upper 95% confidence limits of 44 and 60 Wm^{-2} respectively, see Appendix A, and are indicated by [] in the following) just below the ML to below $5Wm^{-2}$ at MLD+60 just above the EUC core. Below this depth, the diaypcnal heat flux ranges on a constant level

5. Mixing parameters
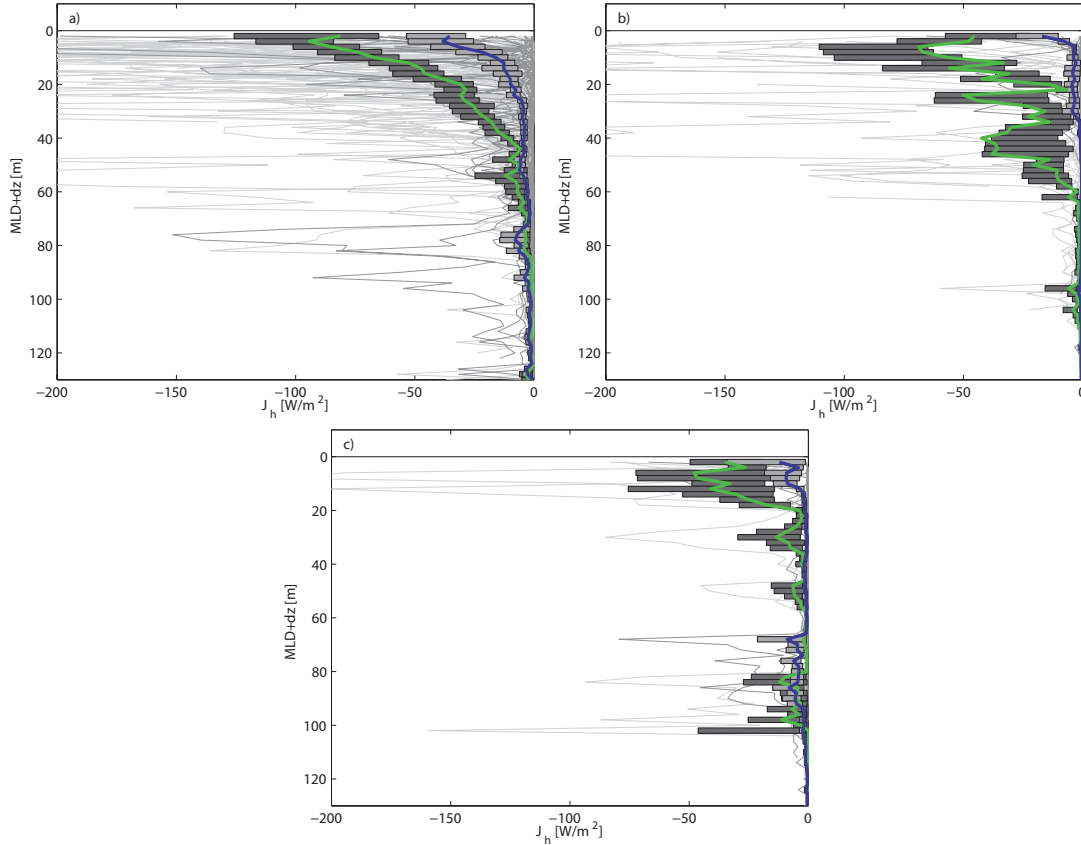
Figure 5.8.: Profiles of diapycnal heat flux J_h from the western (thin light grey line) and eastern (thin dark grey line) equatorial ACT region for a) June/July, b) September and c) November, together with their average profiles (west= heavy green line, east= heavy blue line) and the 95% confidence limits in vertical coordinates of MLD+dz.

of $0 - 5 Wm^{-2}$ in agreement with previous Pacific studies [e.g. *Peters et al.*, 1988; *Lien et al.*, 1995]. The average heat flux profile from off-equatorial regions indicates maximum values of only $17\ Wm^{-2}$ [15;33 Wm^{-2}] just below the ML, decaying more rapidly to below $5\ Wm^{-2}$ at MLD+10m.

Within the equatorial cold tongue region - in accordance with larger dissipation rates and eddy diffusivities - the western equatorial ACT region shows significantly larger diapycnal heat fluxes from the ML to the EUC core during all sampled cold tongue stages (fig.5.3, 5.8). In the western ACT region at 10°W in June/July the diapycnal heat flux right below the ML reaches maximum values of $90\ Wm^{-2}$ [62;124 Wm^{-2}] in June/July reducing to $7\ Wm^{-2}$ [4;10 Wm^{-2}] 30m below the ML. The decay with depth is more pronounced in June and November compared to September, when elevated dissipation rates and eddy diffusivities associated with the presence of a TIW penetrate until about MLD+60. Despite the highest observed eddy diffusivities in September, the comparably low temperature gradient - responsible for the low stratification - results in lower diapycnal heat fluxes than inferred for boreal summer (75 Wm^{-2} [50; 100 Wm^{-2}] directly below the ML). In November lowest values in the western equatorial ACT region of about 40 Wm^{-2} directly below the ML were observed.
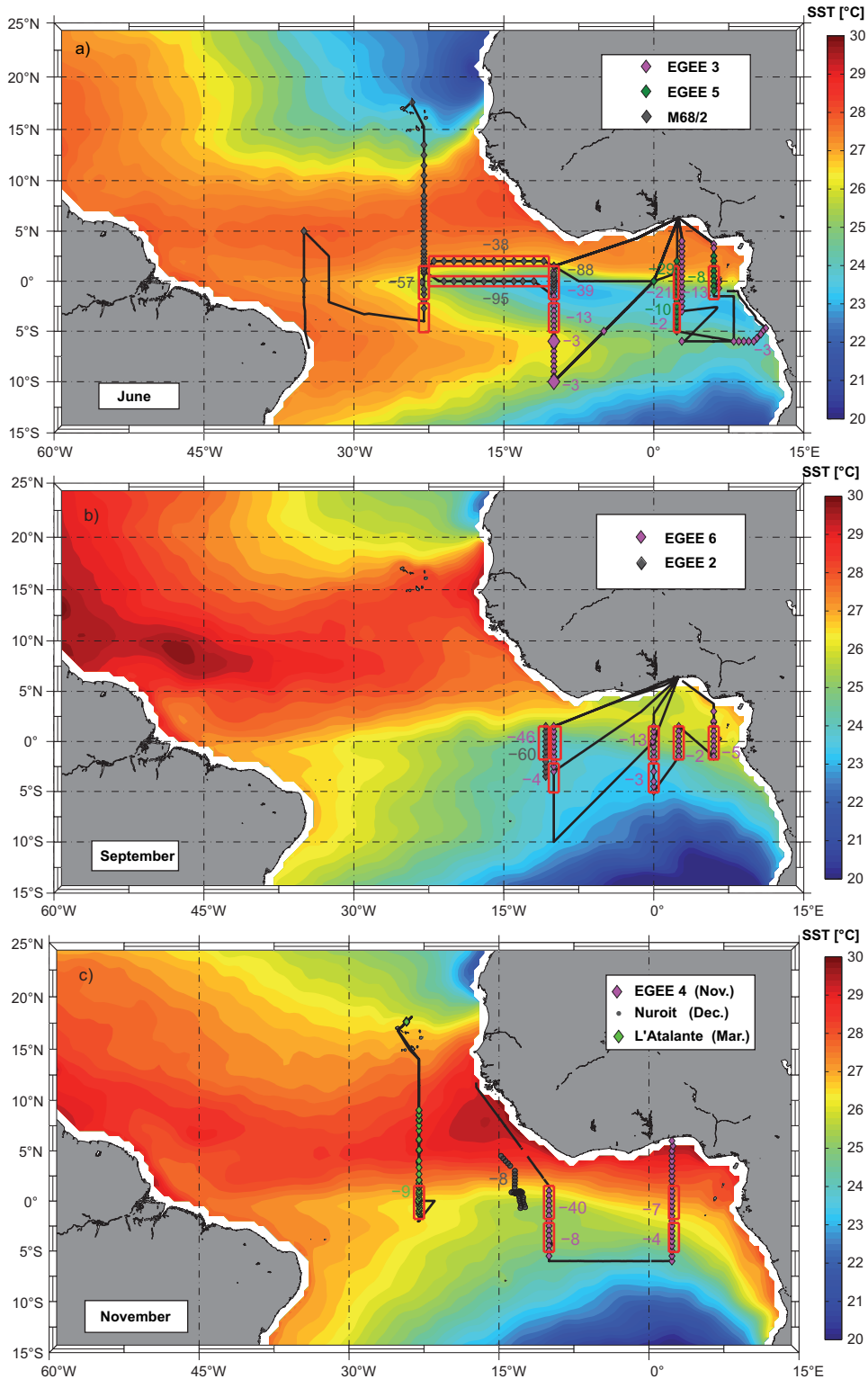
Figure 5.9.: Spatial and temporal variability of the section averaged downward diapycnal he-
at flux out of the ML indicated by negative numbers, $[Wm^{-2}]$. Maps show SST
averaged for the indicated months over years 2005-2007.

In the eastern ACT region at 2°E, diapycnal heat fluxes below the ML range between maximum

values of about 50 Wm^{-2} [30; 70 Wm^{-2}] in boreal summer, 5 Wm^{-2} [3;10 Wm^{-2}] in September and 13 Wm^{-2} [2; 23 Wm^{-2}] in November. Despite the high values observed directly below the ML in boreal summer, the decrease with depth is rather strong (a flux near zero already at about MLD+20m), a feature which was already found for the dissipation rates. At 6°E J_h is never observed to exceed 10 Wm^{-2}. The regional as well as seasonal variability of the diapycnal heat flux confirms the general findings for dissipation rates below the ML: higher J_h in the equatorial compared to the off-equatorial regions (fig.5.1c), elevated values in the western equatorial region compared to the east throughout the different observed cold tongue stages (fig.5.8). Maximum values are inferred for boreal summer within the entire equatorial ACT region, whereas the decrease from boreal summer to September and November is more pronounced in the east.

To further emphasize these general findings and to quantify the heat loss of the ML due to turbulence for every occupied section of this data set, the diapycnal heat flux was averaged below the ML range (MLD+5 to MLD+15) individually for every station. For the equatorial sections, heat losses were ensemble averaged for stations between 2°S and 2°N, while in the off-equatorial regions stations were combined as indicated in fig.5.9. Day and night averages were computed separately prior to ensemble averaging to avoid possible bias due to diurnal variability. It should also be stated that due to the rapidly decaying diapycnal heat flux profiles especially in the eastern equatorial and southern ACT region, the average between MLD+5 and MLD+15m can be considerably lower than the maximum value obtained directly below the ML. However, the results of this approach lead to a relatively coherent picture, which was already suggested from the evaluation of the average profiles. Highest ML heat losses are estimated for the western equatorial ACT (23°W-10°W) during boreal summer of 89 Wm^{-2} at 10°W in July and 95 Wm^{-2} for the section along the equator. Values for 23°W at the western edge of the ACT are slightly lower at 57 Wm^{-2}. About a month earlier in boreal summer (during May on EGEE3) only 39 Wm^{-2} were observed. It could be speculated that the boreal summer peak in ML heat loss as suggested from the other observations during boreal summer was not fully developed at this time. Towards September the western equatorial ACT shows ML heat losses of 48 Wm^{-2} and 60 Wm^{-2}, further reducing towards November (40 Wm^{-2}). Within the eastern equatorial ACT highest ML heat losses at 2°E (6 °E) of around 25 Wm^{-2} (13 Wm^{-2}) are observed in June/July reducing to 13 Wm^{-2} (5 Wm^{-2}) in September and 17 Wm^{-2} (-) in November. At the northern edge of the cold tongue (2°N) in the vicinity of the nSEC, ML heat losses are still of considerable magnitude reaching 38 Wm^{-2} during boreal summer. Towards the southern edge of the cold tongue, clearly separated from the equator, ML heat losses do not exceed 15 Wm^{-2} and in addition do not show any seasonal or regional variability. Note that the assessed ML heat losses obtained during this latter approach (average diapycnal heat fluxes within the layer MLD+5 to MLD+15) are further used as the contribution of the diapycnal heat flux to the ML heat budget in chapter 6.

5.4. **Summary and discussion**

Evaluation of the microstructure data used within the framework of this study revealed average dissipation rates, eddy diffusivities and diapycnal heat fluxes , that differed strongly between the equatorial ($\pm 2°$) and off-equatorial regions. Average dissipation rates and eddy diffusivities in the off-equatorial regions below the ML are reduced by an order of magnitude compared to the equatorial values, while the corresponding diapycnal heat fluxes are reduced by a factor of 2.

The regional and seasonal variability of mixing levels within the equatorial ACT region led in terms of dissipation rates to three major findings:

1. In the eastern equatorial ACT region dissipation rates below the ML are up to one order of magnitude reduced compared to the west during all observed cold tongue stages.

2. Seasonally, the boreal summer months June and July, coinciding with strong cooling of SSTs, exhibit highest dissipation rates throughout the entire equatorial ACT region compared to September and November. Nevertheless, a reduction of dissipation rates towards September and November is more pronounced in the eastern Gulf of Guinea.

3. In the western equatorial ACT region dissipation rates are elevated during boreal summer and autumn, in particular when TIWs are present.
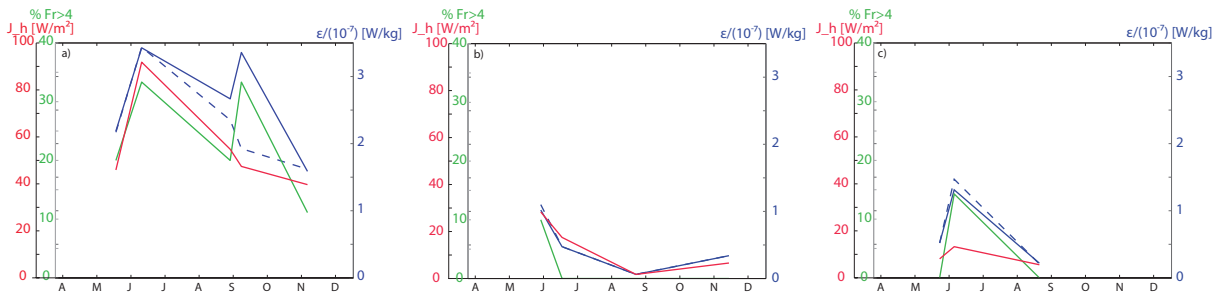
Figure 5.10.: Comparison of section averaged (2°S-2°N) fraction of Fr numbers crossing the critical threshold of 4 (green line), section averaged dissipation rates (blue line) and section averaged diapycnal heat fluxes (red line) in the layer MLD+5 to MLD+15. The dashed blue line of dissipation rates is an average over separate day and night averages, whereas the solid line does not take this into account. For the diapycnal heat fluxes previous day and night averaging was also taken into account. Note, that diapycnal heat fluxes are plotted as absolute values to compare variability and the x-axis denotes the month during which the section is occupied from April to December.a) 10°W, b) 2°E, c) 6°E.

In the entire equatorial ACT region diapycnal heat flux in the upper thermocline is elevated. In the western, equatorial ACT, where diapycnal heat flux at the base of the ML is found to peak, its magnitude ranges from 90 Wm^{-2} in boreal summer, reducing to 60 Wm^{-2} in September and 40Wm^{-2} in November. In the eastern equatorial ACT diapycnal heat flux during boreal summer of only 25 Wm^{-2} is inferred, further reducing towards the end of the year to about 5 Wm^{-2}.

5. Mixing parameters

Within the western equatorial ACT region the vertical and temporal distribution of dissipation rates are in good agreement with previous findings from the equatorial Pacific: The frequent occurrence of coherent bursts of turbulence penetrating from the ML into the stratified ocean is observed. In addition the ranges of average dissipation rates, eddy diffusivities and diapycnal heat fluxes are similar. Differences to the Pacific observations include the strength of the deep diurnal cycle. While in the data sets from the Pacific night time dissipation rates below the ML can be elevated by an order of magnitude, average night time enhancement in the western equatorial Atlantic is maximum a factor of 3. Moreover in the eastern equatorial ACT region no night time enhancement of dissipation rates can be detected. Observations from the equatorial Pacific indicate that night time enhancement of dissipation rates is associated with elevated internal wave activity. These internal waves are characterized by frequencies near the local buoyancy frequency and short horizontal wavelengths of about 200m. Up to date, the connection between the turbulent bursts and these waves are not fully clarified. A possible explanation for the night time enhancement was that these internal waves are generated by convectively driven eddies within the ML [*Gregg et al.*, 1985]. These waves are then thought to radiate into the stratified water column, where they cause local shear instabilities. However, recent observations [*Moum et al.*, 2011] and linear stability analysis [*Smyth et al.*, 2011] suggest that the properties of these internal waves are consistent with shear instabilities formed by the mean structure of currents and stratification, which has been suggested previously [*Mack and Hebert*, 1997; *Sun et al.*, 1998; *Smyth and Moum*, 2002; *Lien et al.*, 2002]. The observations presented here for the western equatorial ACT region show that these turbulent patches also occur during day time, ruling out the possibility that they are solely driven by night time convection in the ML.

In addition to the coherent bursts of thermocline turbulence connected to the ML, two deeper patches of turbulence were observed during boreal summer and autumn. During these periods elevated meridional shear associated with TIWs was observed, increasing the occurrence of critical Fr numbers (chapter 3). Hence, it seems plausible that TIWs elevate mixing intensity during these seasons. Similar deep penetration of turbulence in the presence of a TIW was also observed in the central equatorial Pacific [*Moum et al.*, 2009]. Their analysis showed elevated diapycnal heat fluxes of 400 Wm^{-2} on average below the ML over the sampling period of 14 days during the presence of this wave. The ensemble averages presented here do not indicate similar high diapycnal heat fluxes out of the ML (maximum 90 Wm^{-2}). Note that in light of the estimations of the ML heat budget at 10°W [*Foltz et al.*, 2003] 400 Wm^{-2} would lead to a severe imbalance of the budget, excessively cooling SSTs: 400 Wm^{-2} would cool a mixed layer of 20m by 12.8 K over one month. However, it appears that TIWs contribute to the elevated dissipation rates and hence diapycnal heat fluxes below the ML during boreal summer and autumn within the western equatorial ACT region.

Apart from TIWs, other large scale features such as inertio gravity waves [*Peters et al.*, 1991] and equatorial Kelvin waves [*Lien et al.*, 1995] were reported to contribute to the variability of mixing intensities and diapycnal heat flux in the equatorial region. Although these waves are frequently observed in the equatorial ACT [*Polo et al.*, 2008; *Hormann and Brandt*, 2009], they could not be distinguished from other variability in this data set. However, as shown in

chapter 6, including the obtained diapycnal ML heat losses into the ML heat balance leads to a good agreement between the observed heat storage and the sum of contributing terms. This fact suggests that the mixing processes observed during the different cruises are to some degree representative for the respective regions and seasons.

The general magnitude as well as the regional distribution of diapycnal heat flux, especially the reduction of maximum diapycnal heat fluxes towards the east in the equatorial ACT region, agree well with the results from a recent modelling study of *Jouanno et al.* [2011]. However, *Jouanno et al.* [2011] find, in addition to the boreal summer maximum for the diapycnal heat flux in the central equatorial ACT, a second maximum of similar magnitude in November and December. The existence of such a second maximum of similar magnitude to the boreal summer one can not be detected in the observations presented here.

In the central equatorial Pacific the depth distribution of dissipation rates between the ML and the EUC core could be related to the vertical distribution of the gradient Richardson number (as inferred from the large scale parameters shear and stratification). Low Ri numbers were predominantly observed in the upper shear region of the EUC coinciding with high dissipation rates. Towards the EUC core, Ri numbers increased and dissipation rates reduced [e.g. *Gregg et al.*, 1985; *Peters et al.*, 1988; *Lien et al.*, 1995]. *Crawford and Osborn* [1979] found that the same relation for profiles from the central equatorial Atlantic. In general, the observed depth distribution of Froude numbers ($1/Ri$) for this data set (section 4.3) corresponds to these studies. In addition, however, regional and seasonal variability of the frequency of Fr numbers crossing the critical threshold of 4 could be assessed (fig.4.8). The comparison of average dissipation rates as well as diapycnal heat fluxes below the ML with the fraction of critical Fr suggests a close relation of the variability of mixing parameters and the variability in large scale conditions in terms of shear and stratification (fig.5.10). Note, that due to the availability of ADCP velocities at 10-minute resolution for the presented cruises, Fr were recalculated with 10-minute resolved shear averaged over the corresponding 1 hour CTD stations were occupied, which were used to obtain N^2. For fig.4.8 hourly averages are taken to match the ADCP resolution of the additional PIRATA cruise data. To show the importance of the bias correction due to the acquisition time of the profiles at least for some of the cruises, average dissipation rates were calculated with and without the correction. However, the close relation of turbulent parameters and large scale forcing (shear and stratification) below the ML within the different regions and seasons of the equatorial ACT establishes the possibility of parametrizing turbulent parameters via observations of the background state. This will be further investigated in chapter 7.

6. Mixed layer heat budget

As pointed out in the introduction a complete understanding of the mixed layer heat budget is fundamental for understanding, quantifying and forecasting SST variability. SST variability within the ACT region has been found to crucially influence climate variability in sensitive regions of the surrounding continents. Model results for the ACT as well as the Pacific cold tongue have suggested diapycnal mixing as an important contributor to the ML heat budget [*Chang*, 1994]. The observational study of *Gouriou and Reverdin* [1992] already proposed the seasonal variability of diapycnal mixing within the ACT and the important contribution of the diapycnal heat flux to the ML heat budget within this region. Recent estimates of the ML heat budget within the ACT region did not include the diapycnal heat flux due to the lack of an adequate data base for the estimation of its magnitude and in particular its seasonal variability [*Foltz et al.*, 2003; *Wade et al.*, 2011a]. They have assessed this term as a residual, which also combined all error sources. In the previous chapter the variability of diapycnal heat fluxes below the ML, characterizing the heat loss of the ML, within the ACT region was inferred from microstructure observations. It was found that especially within the western, equatorial ACT the heat loss to the ML due to turbulence is of considerable magnitude ranging between 40-90 Wm^{-2} suggesting its important contribution to the ML heat budget. Within this chapter all terms contributing to the ML heat budget will be estimated for different regions of the ACT.

For the observations presented in this study, the seasonal variability of the diapycnal heat flux is best resolved at 10°W on the equator. Nevertheless, information about magnitude and some of the variability of the diapycnal heat fluxes could also be gained for other locations in the eastern equatorial ACT (0°E, 2°E, 6°E) region as well as the southern ACT region along 10°W (fig. 5.9). Therefore, in the following chapter the individual contributions of atmosphere and ocean to the ML heat budget will be investigated at the PIRATA buoy locations at 23°W,0°N; 10°W,0°N; 10°W,10°S; 0°N,0°E. At the buoy locations several atmospheric and oceanic variables are available for a timeperiod of several years, which can be used in the estimation of the individual terms of the budget. Procedures of estimating the individual terms are summarized in the next section.

6.1. Heat budget calculations

The heat balance equation for the ML can be expressed as

$$h\frac{\partial T}{\partial t} + h(\mathbf{v} \cdot \nabla T + \overline{\mathbf{v}' \cdot \nabla T'}) + (T - T_{-h})w_{entrain} = \frac{(q_{net} - q_{-h})}{\rho c_p}, \qquad (6.1)$$

where h represents the MLD, $\mathbf{v}$ and T are the velocity and temperature averaged from the surface until the depth -h, whereas $\mathbf{v}$' and T' are the deviations from the time mean, q_{net} stands for the net surface heat flux and q_{-h} for the net heat loss of the mixed layer. Here, q_{-h} is determined from the combination of the penetrative shortwave radiation and the diapycnal heat flux at the base of the ML (according to *Foltz et al.* [2003]). The terms represent from left to right local heat storage, horizontal advection (divided into a mean and eddy term), entrainment and the combination of net atmospheric heating and vertical turbulent diffusion at the base of the ML. Note that within this study the term "entrainment" is associated with vertical advection of heat, whereas "diapycnal mixing" describes the vertical diffusion of heat. Advective contributions due to baroclinic currents and temperature gradient in the mixed layer (the vertical temperature/velocity covariance) were neglected as they were found to be small [*Swenson and Hansen*, 1999]. The evaluation of the individual terms closely follows the procedures by *Foltz et al.* [2003]. Seasonal cycles of different variables are obtained from daily PIRATA data, averaged on every given day of the year and subsequently formed to a monthly average. The penetrative fraction of the shortwave radiation dependant on the MLD and the optical transparency of water is calculated via a simple e-folding decay following *Wang and McPhaden* [1999], leaving the shortwave radiation absorbed in the ML to be estimated as $Q_{abs} = (1 - 0.45e^{-h/25m})$. Latent and sensible heat fluxes are obtained with the COARE algorithm [*Fairall et al.*, 2003]. The horizontal advection is derived by multiplying the monthly surface velocities from climatology with climatological long term SST gradients [*Reynolds and Smith*, 1994]. The eddy term of the horizontal advection is estimated indirectly via the residual between the horizontal advection as described previously and the horizontal advection estimated as $h(\mathbf{v}\cdot\nabla T) = h(\frac{dT}{dt} - \frac{\partial T}{\partial t})$, following *Swenson and Hansen* [1999]. The total time derivative is obtained with SSTs provided from the drifter-climatology of *Lumpkin and Garaffo* [2005], whereas the local derivative is estimated with the climatological SSTs from *Reynolds and Smith* [1994]. The entrainment velocity can be expressed as $w_{entrain} = \frac{\partial h}{\partial t} + \nabla \cdot h\mathbf{v}$ [*Stevenson and Niiler*, 1983] estimating the local time derivative of the MLD from PIRATA temperatures and the divergence term by combining the mixed layer climatology with the climatological surface velocities. The monthly averages of the individual terms are then fitted to annual and semiannual harmonics and their derivation from the fit is used as an error estimate for the individual terms.

In order to correctly interpret the heat advection terms and compare the results to other studies, it has to be clarified, which processes are included in these terms - mean and/or eddy components. As pointed out, in this investigation the mean heat advection is separated into its zonal and meridional component and the eddy heat advection is estimated separately as in *Foltz et al.* [2003]. In addition, *Wang and McPhaden* [1999] point out the dependence of the eddy component of the meridional heat advection on the latitudinal averaging interval (dy). This is referred to as scale dependence and they associate it with the different dynamics dominating the equatorial (±2; influenced by TIWs) and off-equatorial regions (influenced by the Ekman-driven divergence regime). *Wang and McPhaden* [1999] claim that averaging over a narrow latitudinal extent will lead to a warming via the meridional eddy advection in association with TIWs, while a large averaging interval will be dominated by the Ekman driven divergence cooling the ML. The

6. Mixed layer heat budget

averaging interval in this study is set to $\pm 1°$ latitude and therefore the eddy advection term is expected to be dominated by a warming trend due to TIWs for the equatorial stations of the western ACT as was suggested by modelling studies by *Peter et al.* [2006] and *Jochum and Murtugudde* [2006].
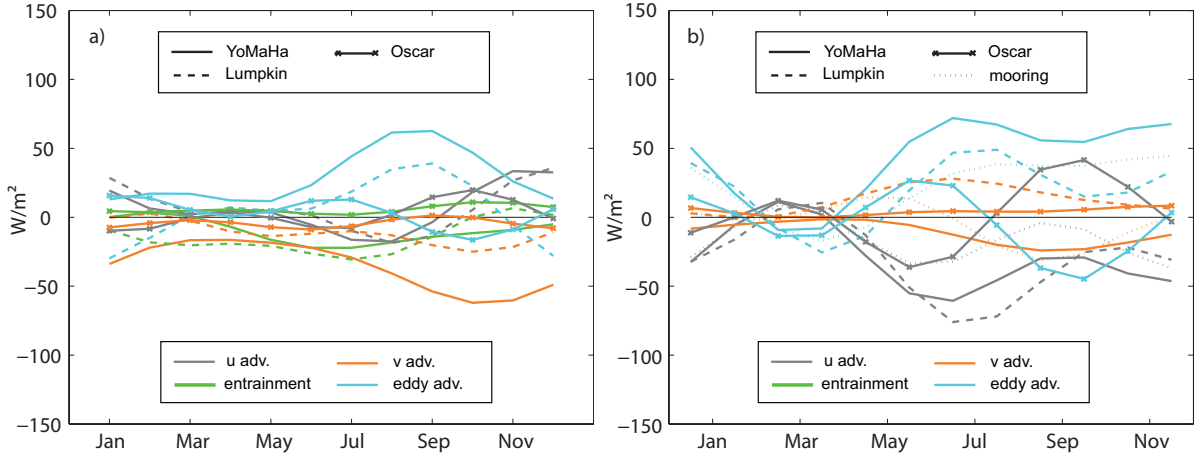

Figure 6.1.: Advection terms as well as entrainment estimated for different velocity products at a) 10°W,0°N and b) 23°W,0°N (YoMaHa'07 data: solid lines, drifter climatology of *Lumpkin and Garaffo* [2005]: dashed lines, OSCAR surface velocities: solid lines with crosses, mooring: dotted lines).

To estimate the heat advection terms (mean and eddy component) as well as the entrainment term information on surface velocities are required. Several surface velocity products are available (described in chapter 3) leading to inconclusive results concerning magnitude and sign of the affected terms (see fig.6.1). More important, different surface velocity products generate a warming or cooling of the ML. Some systematics can be seen: First, the spread of the different estimates of the affected terms is larger at 23°W, than at 10°W. Second, individual terms differ stronger within the second half of the year at both locations, reaching maximum discrepancies in the order of 100 Wm^{-2} at 23°W (eddy advection), whereas in the beginning of the year the spread is at maximum 50 Wm^{-2} or less.

In general, estimates of the terms in question based on *Lumpkin and Garaffo* [2005] and YoMaHa surface velocities agree well in terms of warming/cooling (e.g. zonal heat and eddy advection during most of the year, entrainment at 10°W). OSCAR velocities yield a warming via entrainment during the entire year at 10°W and a cooling via eddy advection in autumn at both locations in contrast to the other products (fig.6.1a). The warming, via entrainment, and cooling, via eddy advection, also contradicts the results of *Foltz et al.* [2003] at both locations.

Given the uncertainties in the gridded climatological products, advection terms at 23°W based on velocity observations from a moored ADCP are calculated to gain information on sign and magnitude for these terms. To obtain monthly ML velocities from the mooring over the timeperiod from 2002-2011, velocities available on a 5 dbar grid are averaged over the upper 20m on each given day of the year and subsequently averaged over a month. The advection terms based on the direct observation are lower in magnitude compared to the other velocity products (fig.6.1b).

One reason is probably that the first reliable bin of the ADCP is between 10-20m depth (see section 7.3.2), whereas the other products are based on surface observations, where velocities are expected to be stronger. On the other hand, climatological products are also attributed with errors, e.g. an unevenly sampled data base. The signs of the zonal heat and eddy advection during autumn based on moored velocities agree with the estimates of YoMaHa and *Lumpkin and Garaffo* [2005] and further challenge the belief in the estimates based on OSCAR velocities. Despite, the overall agreement between estimates based on *Lumpkin and Garaffo* [2005] and YoMaHa, discrepancies in sign and magnitude between these estimates can be seen. Largest discrepancies between these two estimates are observed for the eddy advection and in the order of $50\ Wm^{-2}$ during the second half of the year at both locations, eventually even differing in sign at 10°W. For the meridional advection, maximum differences are of similar magnitude but with opposite signs at 23 °W during boreal summer and autumn. As the YoMaHa based estimates agree best with the estimates based on the moored velocities as well as the former estimates of *Foltz et al.* [2003], they will be used in the following calculations.

As mentioned previously at 10°W on the equator, at the center of the cold tongue, the largest residual between the sum of the individual terms and observed heat storage was found [*Foltz et al.*, 2003]. In addition, the seasonal variability of the diapycnal heat flux as estimated within the framework of this study, is best resolved at this location and therefore we concentrate on the ML heat budget at 10°W, 0°N.

6.2. 10°W,0°N

The ML at 10°W on the equator is characterized by atmospheric heating, and heating through the advection by eddies. The ML is cooled by subsurface processes (diapycnal mixing and entrainment) and the meridional heat advection (fig.6.2a). For clarity fig. 6.2a does not include the contributions from sensible heat flux and from outgoing longwave radiation, as they both remain rather constant throughout the year and cool the ML at a rate of $5\ Wm^{-2}$ and about $50\ Wm^{-2}$, respectively. Oceanic subsurface processes as well as meridional heat advection cool the ML at different rates with strong variations within the seasonal cycle. Three distinct periods within the seasonal cycle of the heat storage, and associated with different stages of the cold tongue, can be identified (compare fig. 1.4 and fig.6.2b). From January until about April the cold tongue is absent and SSTs exhibit a slight warming. In May the cooling of the ML begins reducing temperatures by about 6°C until July. This will be further referred to as the development phase of the ACT. During the mature phase of the ACT, from August towards the end of the year, the ML is steadily warmed. Note, that the cooling occurs more rapid than the warming. In the following, the respective contributions of atmosphere and ocean warming and cooling the ML during the absence, development and mature phase of the ACT will be discussed.

During the **absence of the ACT** (January to April) the ML heat budget at 10°W is dominated by atmospheric forcing. The estimated oceanic contributions mostly do not exceed $20\ Wm^{-2}$. The maximum of $40\ Wm^{-2}$ is observed for the meridional heat advection, but balancing the other oceanic contributions. Due to the vanishing Coriolis parameter at the equator, meridional
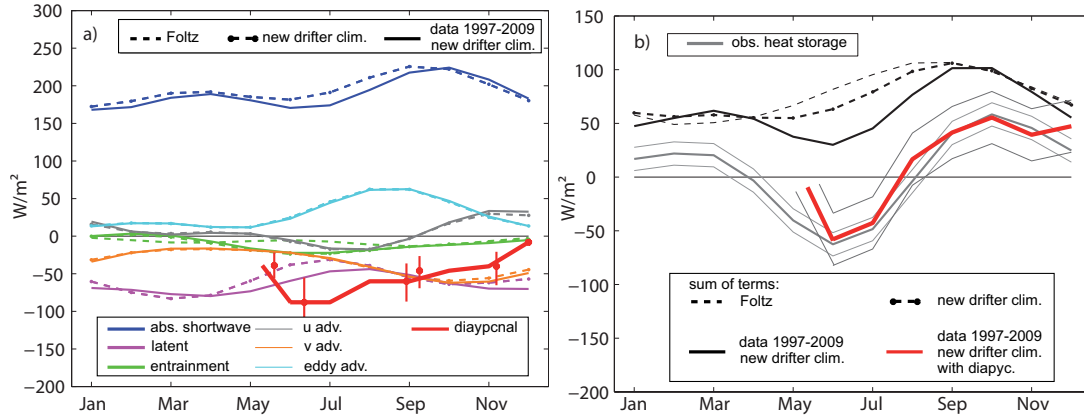
6. Mixed layer heat budget

Figure 6.2.: a) Seasonal variability of individual terms contributing to the ML heat budget at 10°W,0°N. Not shown in this figure are the rather constant contributions of the sensible heat flux (assessed with the COARE algorithm) and the outgoing longwave radiation (from *da Silva et al.* [1994]), which though have been included in the sum of all contributing terms in b). In b) the sum of all contributing terms of the ML heat budget are compared to the observed heat storage. The individual contributions are displayed as indicated in the legend.

velocities on the equator at 10° are a direct response to wind forcing. As wind is predominantly from the south to southeasterly at the equator (fig. 2.5) these winds induce a surface current in the same direction [*Rhein et al.*, 2010].

Within the **development phase of the ACT** (May to August), the wind decreases and the net heat flux from the atmosphere increases due to the reduction in latent heat flux (section 2). However, the strong increase in subsurface cooling (diapycnal heat flux and entrainment) during this phase leads, despite the warming of the atmosphere, to the cooling of the ML. A moderating effect on the increase in subsurface cooling is provided by the eddy advection. The dominant contribution of the different subsurface processes is the diapycnal heat flux at the mixed layer base reaching 90 Wm^{-2} in July. Other oceanic contributions are at maximum on the order of 50 Wm^{-2}. Although westwards surface velocities associated with the nSEC are intensified, the low temperature gradient and the shallow MLDs, lead to only a slight cooling via zonal heat advection. The warming effect via eddy advection was previously associated with TIWs from observations [*Wang and McPhaden*, 1999] and modelling studies [*Peter et al.*, 2006; *Jochum and Murtugudde*, 2006]. Wavelet analysis of moored velocities at 10°W on the equator have shown that TIWs are most active from June to October at this location (chapter 2). Hence, it seems likely that the eddy advection term reducing towards October and November is associated with these features. In addition, it was found that these waves contribute to elevated meridional velocity shear, which triggers elevated turbulent mixing at this location (chapter 4 and 5). *Jochum and Murtugudde* [2006] suggested a compensating effect of TIWs, warming the ML by lateral advection and cooling it simultaneously by increasing the diapycnal heat flux. The observations of this study seem to support these findings. However, the moderating effect of TIWs by warming the ML, is not strong enough to counteract the strong subsurface cooling dominated by the diapycnal heat flux and resulting in a decrease of SSTs.

During the **mature phase of the ACT** (August towards the end of the year) atmospheric forcing slightly increases due to the re-enhancement of the incoming solar radiation. The cooling, due to the diapycnal heat flux, is still of considerable magnitude, but decreasing. The same can be stated for the warming effect of the eddy advection. The dominance of the diapycnal heat flux reduces in favor of the meridional heat advection, which reaches 50 Wm^{-2} towards the end of the year. The increase in meridional heat advection is due to enhanced meridional temperature gradients and deeper MLDs. The cause of the increase in the meridional temperature gradient is not clear. The warming effect of the eddy advection during the development of the ACT reduces within the mature phase in favor of the zonal heat advection. By December zonal heat advection balances the meridional heat advection. Zonal heat advection at the beginning of the mature phase is rather weak due to the reduced surface velocities associated with the nSEC during August and September. With the re-enhancement of surface velocities in October/November (chapter 2) this term increases again. The gradual reduction in the subsurface cooling terms lead to a gradually increase in SSTs during this phase. Entrainment, as part of the subsurface cooling, generally cools the ML in agreement with *Rhein et al.* [2010] at a rather moderate rate of about 5 Wm^{-2} and throughout the year.

Comparison of the sum of the individual terms of the ML heat budget to the observed heat storage reveals a large residual of up to 90 Wm^{-2} when omitting the contribution of the diapycnal heat flux during boreal summer and autumn (black solid line in fig.6.2b). This was already reported by *Foltz et al.* [2003], who performed a similar study at this location. Considering now the diapycnal heat flux as a contributing term yields in a closure of the budget, within the uncertainties.

Foltz et al. [2003] attributed the large residual of up to 100 Wm^{-2} during summer within their study at 10°W,0°N to three main error sources:

1. underestimation of the meridional velocity-divergence-induced entrainment presumably due to the coarse resolution of the drifter climatology (2° latitude, 4° longitude)

2. underestimation of the latent heat flux due to bad data coverage (only one full year of measurements of the relative humidity in the timeseries between 1997 and 2002, within which the relative humidity was anomalously high, resulting in low latent heat fluxes)

3. neglection of the diapycnal heat flux due to the lack of information on the turbulent eddy diffusivity

Addressing error source 1): the effect of a different resolution of the drifter climatology on the entrainment term is indicated in fig.6.2a. It only accounts for an average increase of the entrainment term by 10 Wm^{-2}. Addressing error source 2): extending the timeperiod of the data base from 1997-2002 to 1997-2009 does affect the estimate of the latent heat flux by about 17 Wm^{-2} between May and July. In addition, the absorbed shortwave radiation is estimated lower, which has not been anticipated by *Foltz et al.* [2003]. These estimates strike the fact, that the main contribution to the required residual cooling during summer and autumn at this location must be provided by the diapycnal heat flux at the base of the ML.

6. Mixed layer heat budget

In conclusion, the large cooling generated by the diapycnal heat flux during summer and early autumn dominates the subsurface cooling terms and plays a crucial role for the ML heat budget. It is of crucial importance for the decrease in SSTs and hence the development of the ACT at this location.

6.3. 0°E,0°N

Moving out of the center of the ACT, the individual terms of the ML heat budget at the other PIRATA buoy locations will be accomplished with surface velocities at a 1° x 1° resolution as well as the time record of PIRATA observations between 1997-2009. In addition, the individual terms contributing to the ML heat budget, will be discussed again in the three already identified cold tongue phases (absence, development and mature).
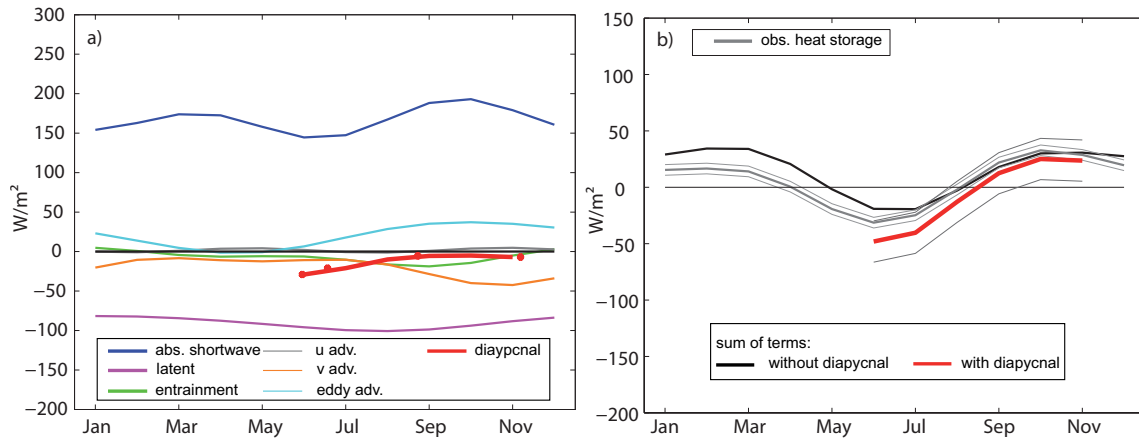
Figure 6.3.: a) Seasonal variability of individual terms contributing to the ML heat budget at 0°E,0°N. Not displayed in this figure are the rather constant contributions of the sensible heat flux (assessed with the COARE algorithm) and the outgoing longwave radiation (from *da Silva et al.* [1994]), which though have been included in the sum of all contributing terms in b) In b) the sum of all contributing terms of the ML heat budget are compared to the observed heat storage. The individual contributions are displayed as indicated in the legend.

As identified for the ML heat budget at 10°W, the ML heat budget at 0°E on the equator is warmed by atmospheric forcing and eddy advection and cooled by subsurface processes and meridional advection. However, as discussed in chapter 2, the seasonal cycle of the net surface heat flux strongly differs in the eastern, equatorial ACT region compared to the west. Within the eastern, equatorial ACT net surface heat fluxes strongly reduce during the development of the ACT. Accordingly, less subsurface cooling is required to decrease SSTs within this period. During the **absence of the ACT** (January to April) in the beginning of the year the ML heat budget is balanced by atmospheric forcing. Subsurface contributions do not exceed 20 Wm^{-2}. Incoming solar radiation reduces during **ACT development** (May to August), leading to the reduction in net surface heat fluxes during this time. Concurrently, the diapycnal heat flux as inferred from microstructure observations increases to its maximum value of about 25 Wm^{-2}.

Note, that at this location the seasonal variability of the diapycnal heat was composed from available estimations at 0°E,0°N as well as 2°E,0°N (fig. 5.9). The magnitude of the diapycnal heat flux at this location is clearly reduced compared to the western, equatorial ACT region. Nevertheless, it is the dominant subsurface cooling term. In addition, as MLDs are observed extremely shallow during this time (chapter 2) this additional subsurface cooling, which superimposes on the reduced net surface heat flux, is probably sufficient to decrease SSTs. As reported for 10°W during the development phase of the ACT the eddy advection term increases during this phase acting to warm the ML. The moderating effect of the eddy advection on the subsurface cooling is also observed for 0°E. However, at this location TIWs have not been observed. *Athie and Marin* [2008] suggest intra-seasonal variability in the Gulf of Guinea dominated by Yanai waves having long zonal wavelengths and a period between 10-20 days. These waves may be responsible for intra-seasonal velocity fluctuations causing an increase in the eddy advection term. Despite this moderating warming effect by eddy advection, the subsurface cooling dominated by the diapycnal heat flux exceeds, resulting in a cooling of SSTs and hence the development of the ACT.

During the **mature phase of the ACT** (August to the end of the year), a similar evolution towards the end of the year is observed as at 10°W. Net surface heat fluxes increase due to the increase in the incoming solar radiation. The cooling via subsurface processes dominated by the diapycnal heat flux reduces in favor of the meridional heat advection. As for the western equatorial region the meridional surface velocities are predominantly northward due to the predominantly southerly winds on the equator. Slightly different is the development of the eddy advection, which stays on a rather constant level towards the end of the year. The zonal heat advection at this location is neglegible throughout the year due to the strongly reduced zonal velocities. The cooling is overcome by the combined warming effects, which leads to the retraction of the cold tongue towards the end of the year. Entrainment acts to slightly cool the ML throughout the year, similar to what has been observed at 10°W.

Comparison of the the sum of individual terms to the ML heat budget and the observed heat storage reveals no large residual (fig.6.3b). As for 10°W,0°N integrating the diapycnal heat flux yields in a closure of the budget, within uncertainties. As was described above, even if reduced in magnitude compared to 10°W, the diapycnal heat flux provides the largest subsurface cooling term within the development phase of the cold tongue and hence seems to supply the essential contribution to cool SSTs.

No detailed study of the ML heat budget as far east as 0°E,0°N, in the Gulf of Guinea, has been published. *Wade et al.* [2011a] determined the individual terms of the ML heat budget for considerable larger regions (about 5° latitude and 9° longitude). Their box 5, representative for a region including 0°E,0°N, shows a considerable larger residual term of $80Wm^{-2}$ compared to our findings, which they associated with the diapycnal heat flux. Note, though that the box extends until 6°W, where the diapycnal heat flux may still be elevated compared to 0°E,0°N. In addition, their estimate of the net surface heat flux within this box ranges from $50-120Wm^{-2}$, clearly above the estimates at 0°E,0°N (fig.6.6). Thus, for their study a larger cooling by oceanic processes is required.

6.4. 23°W,0°N

At the western edge of the cold tongue (23°W), in the central basin of the equatorial Atlantic, the main features of the circulation are rather similar to the ones described at 10°W. Variability in the net atmospheric forcing at this location is comparable to the findings at 10°W. As described for the other equatorial locations, the ML is warmed by the atmospheric forcing as well as the contribution of eddies and cooled by subsurface processes and the meridional eddy advection. Remarkable is that the zonal heat advection cools the ML 23°W (fig.6.4a).

Figure 6.4.: a) Seasonal variability of individual terms contributing to the ML heat budget at 23°W,0°N. Not displayed in this figure are the rather constant contributions of the sensible heat flux (assessed with the COARE algorithm) and the outgoing longwave radiation (from *da Silva et al.* [1994]), which though have been included in the sum of all contributing terms in b) In b) the sum of all contributing terms of the ML heat budget are compared to the observed heat storage. The individual contributions are displayed as indicated in the legend.

In the beginning of the year, during the **absence of the ACT** (January to April), the ML balance is dominated by atmospheric forcing and the eddy advection, which already contributes a warming of $50\,Wm^{-2}$ during this cold tongue phase. *von Schuckmann et al.* [2008] report TIWs in the central basin at 23°W to occur most frequently in boreal summer and autumn. Hence, it is not quite clear, which process should elevate the eddy advection during this timeperiod (fig. 6.4a).

During the **development phase of the ACT** (May to August) as described for 10°W the net surface heat flux counteractingly increases. On the contrary to 10°W, the increase in the net surface heat flux is due to the increasing incoming solar radiation, the latent heat flux remains rather constant throughout the year. Subsurface cooling is equally provided by the diapycnal heat flux and zonal heat advection of about $60\,Wm^{-2}$. In addition, entrainment contributes about 20 Wm^{-2} during this phase. The diapycnal heat flux still contributes a cooling similar to the other two locations. Zonal heat advection is considerably stronger compared to the other locations. This is due to the combination of three factors: stronger westwards velocities, associated with the nSEC, stronger zonal temperature gradient at the edge of the ACT, and deeper MLDs.

Similar to 10°W,0°N eddy advection associated with TIWs moderates the cooling effects (fig. 6.4a).

Within the **mature phase of the ACT** (August to the end of the year) the net surface heat flux further increases. Eddy advection due to TIWs still contributes significant additional warming of about 50 Wm^{-2} during this period. Cooling provided by zonal heat advection decreases at the beginning of the mature phase, due to the reduction in surface velocities associated with the nSEC but re-intensifying towards the end of the year (as does the nSEC). Due to a lack of data, the diapycnal heat flux has not been inferred from microstructure observations during this period. However, chapter 5 has identified the summer months June/July as the season of highest mixing activity during the entire equatorial ACT. Hence, the contribution of the diapycnal heat flux at this location will probably also reduce towards the end of the year. Recent observations have assessed the diapycnal heat flux at the base of the ML at 23°W on the equator during November with 8 Wm^{-2} (S. Thomsen, pers. communication), confirming this suggestion. As for the other equatorial ML budgets the meridional heat advection increases within this phase, nevertheless its magnitude is reduced compared to 10°W because of generally lower meridional velocities and a decreased meridional temperature gradient. The lower meridional velocities could be associated with a reduced meridional wind component in the central compared to the eastern equatorial Atlantic. Entrainment cools the ML throughout the year (fig. 6.4a)

Comparison of the sum of the individual terms contributing to the ML heat budget and the observed heat storage reveals a large residual of 50-120 Wm^{-2} throughout the year, but the contribution of the diapycnal heat flux was omitted. Similar residuals (80 Wm^{-2}) have been reported from the central equatorial Pacific [*Wang and McPhaden*, 1999] as well as from the western equatorial ACT [*Wade et al.*, 2011a].

Integrating the resolved seasonal variability of the diapycnal heat flux into the sum of terms reduces the residual in summer by a factor of 2. However, a large residual remains. Either the estimates of the diapycnal heat flux obtained within the framework of this study underestimate the diapycnal heat flux at this location or other terms of the heat balance are attributed with large errors. Note though, that a large discrepancy throughout the year is found for all available surface velocity products. Further investigations of the individual contributions to the ML heat budget at this location seems pending. Nevertheless, the cooling provided by the diapycnal heat flux during summer is an important contributor in cooling SSTs during ACT development.

6.5. 10°W,10°S

Investigation of the mean circulation of the tropical Atlantic revealed fundamental differences between the equatorial and the southern ACT region (chapter 2). The net surface heat fluxes revealed a cooling instead of warming during cold tongue development in contrast to the equatorial ACT region. In general, surface velocities are rather weak at this location compared to the equatorial region (chapter 2) and can not be associated with distinct current features. Nevertheless, the considerable larger MLD increases the magnitude of the advection terms. As mentioned, the atmospheric forcing at this location acts as a warming or cooling term depending

6. Mixed layer heat budget

on the season. Additional warming at this location is provided by the eddy advection and the meridional advection, additional cooling constitues of entrainment and zonal advection.
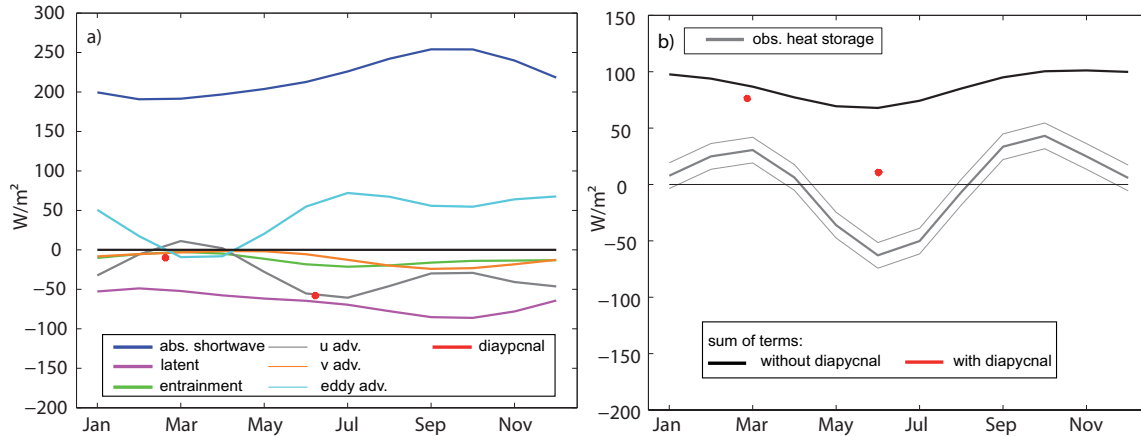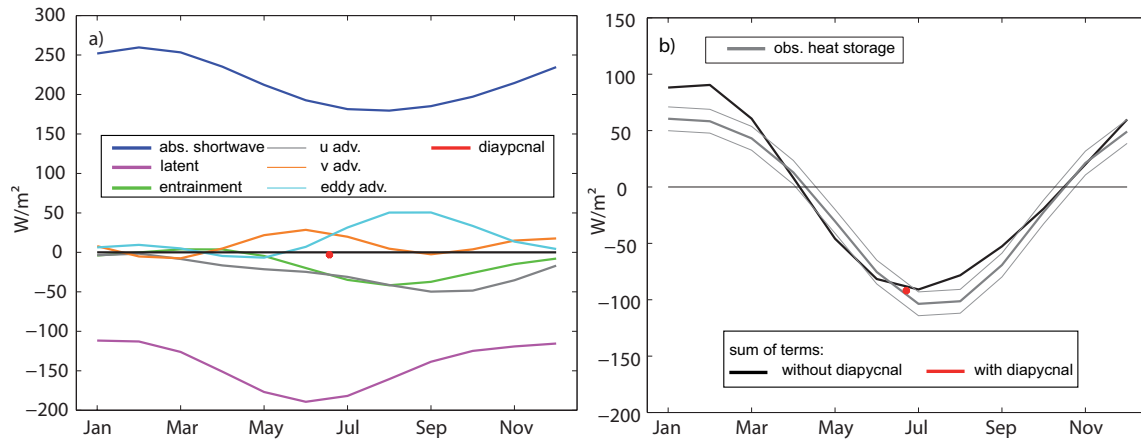

Figure 6.5.: a) Seasonal variability of individual terms contributing to the ML heat budget at 10°W,10°S. Not displayed in this figure are the rather constant contributions of the sensible heat flux (assessed with the COARE algorithm) and the outgoing longwave radiation (from *da Silva et al.* [1994]), which though have been included in the sum of all contributing terms in b) In b) the sum of all contributing terms of the ML heat budget are compared to the observed heat storage. The individual contributions are displayed as indicated in the legend.

During the **absence of the ACT** (January to April) the ML heat budget is determined by the atmospheric forcing (fig.6.5a).

During the **development of the ACT** (May and August) net surface heat fluxes strongly reduce due to the strong increase of the latent heat flux associated with increased winds as well as a reduction in the incoming solar radiation. The net surface heat flux itself now acts to cool the ML. Surface currents within the southern ACT are dominated by the Ekman flow. As the trades have a south-easterly direction, the resulting surface velocities are from the northeast. Increased surface velocities lead to an increase for all advection terms as well as the entrainment during this time period. The diapycnal heat flux inferred from microstructure observations during this period provides a neglegible contribution to the cooling. The contribution of the advection terms and entrainment balances, leaving the cooling of the ML and hence SSTs during ACT development to the atmospheric forcing.

During the **mature phase of the ACT** (August to the end of the year) the incoming solar radiation increases. This is due to the increase in incoming solar radiation and a reduction of the latent heat flux due to decreasing winds. In addition, the decreasing winds lead to a reduction in surface velocities and hence decrease the contribution of advection and entrainment. A warming of the SSTs is caused by the atmospheric forcing.

The sum of contributing terms closely follows the evolution of the observed heat storage at this location. The residual at this location is neglegible in agreement with the estimates of *Foltz et al.* [2003]. This fits with the fact that the diapycnal heat flux at this location was estimated neglegible during the main mixing season of the ACT. The decrease in SSTs at this location

during ACT development is mainly governed by the atmospheric forcing.

6.6. Summary and discussion

The mixed layer heat budget has been estimated at four characteristic sites within the ACT region: in the western, central and eastern equatorial as well as the southern ACT region. The main balances within the seasonal cycle during the absence, development and mature phase of the ACT were described. Individual contributions of the atmosphere and the ocean to the ML heat budget in the equatorial ACT region revealed similarity between the three equatorial locations and fundamental differences between the equatorial and southern ACT region. Within the entire equatorial ACT the diapycnal heat flux dominates the cooling of SSTs during ACT development, whereas in the southern ACT the cooling is provided by atmospheric forcing. The cooling via the diapycnal heat flux acts to decelerate the warming of SSTs during the mature phase of the ACT within the equatorial region.
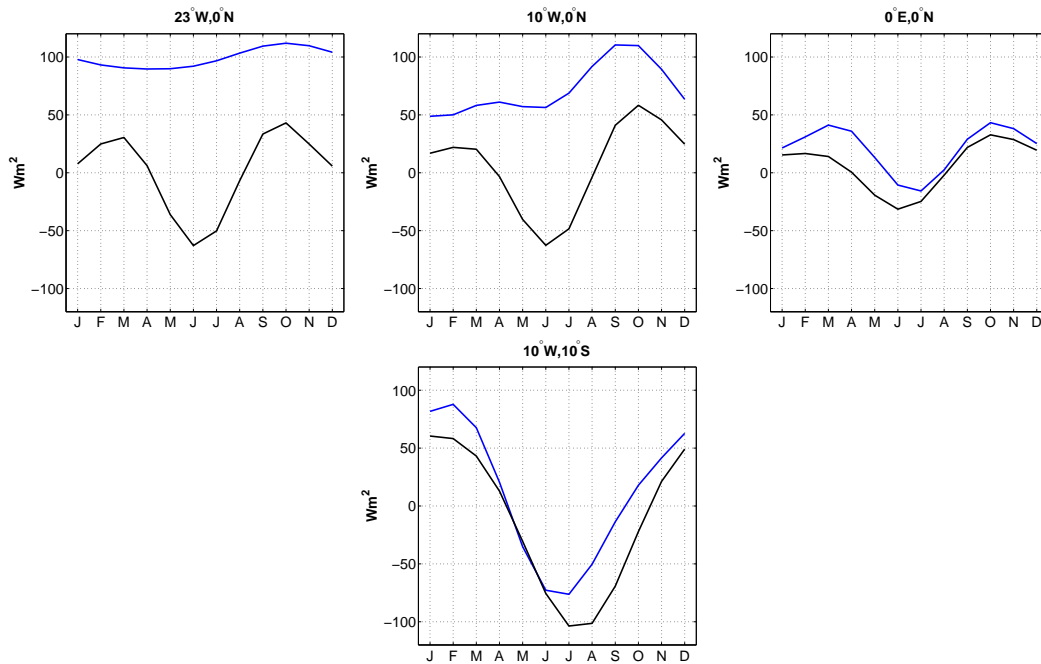
Figure 6.6.: Comparison of seasonal cycles of the net surface heat flux (blue) and the observed heat storage (black) for the different ACT regions investigated above. All terms are estimated from PIRATA buoy observations.

During the **absence of the ACT** (January to April), the ML heat balance at all locations within the ACT is mainly dominated by atmospheric forcing, slightly warming SSTs.
During the **development of the ACT** from May to August the ML heat balance is dominated within the equatorial ACT region by the warming of the atmosphere and eddy advection and cooling by subsurface processes. Of the subsurface processes the diapycnal heat flux at the base of the ML is the dominant cooling term within the entire equatorial ACT. Eddy advection moderates the cooling within the equatorial belt. However, the cooling exceeds and SSTs decrease.

6. Mixed layer heat budget

Within the southern ACT region the cooling of SSTs during ACT development is due to the atmospheric forcing.

During the **mature phase of the ACT** (August to the end of the year) the atmospheric forcing increases throughout the ACT region. Warming by eddy advection is still observed, but reduces. In the equatorial belt the cooling by the diapycnal heat flux decreases in favor of heat advection terms, which become more important in cooling SST towards the end of the year. Nevertheless, this additional cooling by heat advection terms and the successive reduction in the diapycnal heat flux is slowly exceeded by the warming terms, resulting in the increase in SSTs. Within the southern ACT the increase in SSTs is dominated by atmospheric forcing.

The importance of subsurface processes and advection terms in the equatorial ACT region for cooling of SSTs is also apparent from fig. 6.6. The residual between the net surface heat flux and the observed heat storage requires additional cooling terms. Within the southern region, SST variability is explained by the atmospheric forcing during ACT development. Towards the east within the equatorial ACT region the discrepancy between the net surface heat flux and the observed heat storage diminishes. Likewise the magnitude of the diapycnal heat flux is reduced from the western, equatorial ACT towards the east. This strikes the fact that despite its reduction in magnitude, the diapycnal heat flux is also in the eastern, equatorial ACT the important additional cooling required to reduce SSTs.

The large residual at 23°W,0°N between the sum of contributing terms and the observed heat storage remains unexplained. *Foltz et al.* [2003] determined a residual of only maximum 50 Wm^{-2} at this location. Within summer their residual is strongly reduced due to the strong cooling by the zonal heat advection on the order of about 120 Wm^{-2}. In this investigation no comparably high zonal heat advection is found with any of the surface velocity products (fig.6.1b). *Peter et al.* [2006] also report the discrepancy between their modelling study of the ML heat balance within the ACT and *Foltz et al.* [2003] estimates concerning the zonal heat advection. Zonal surface velocities at this location have been associated with the nSEC. Hence, it seems plausible that the zonal heat advection should be imprinted by a semi-annual cycle in accordance to the nSEC variability. This is supported by the findings of this study. Note, in addition the combination of the strong zonal heat advection of 120 Wm^{-2} in July of *Foltz et al.* [2003] in combination with the assessed diapycnal heat flux of about 60 Wm^{-2} would cool the ML excessively. Further investigation of the contribution of the individual terms to the ML heat budget at this location are required.

Despite of 23°W,0°N the ML heat budgets within the equatorial ACT region could be closed within the uncertainties, at least during the periods where the diapycnal heat flux was estimated. This suggests that the observed mixing processes are at least to some degree representative for the respective regions and seasons. However, supplementary information on the contribution of the diapycnal heat flux to the ML heat budget is required during the periods unresolved by this study. This requires either further observations and/or the assessment of magnitude and variability of the diapycnal heat flux via parametrization schemes. The latter approach will be further investigated within the following chapter.

7. Parametrization

In the introduction the need for reliable parametrizations of turbulent terms to be incorporated in ocean models was highlighted. As was pointed out, different parametrization schemes have been developed by different authors for various regions of the oceans, several of them for the surface boundary layer of the ocean, which is subject to strong interactions with the atmosphere [*Gaspar et al.*, 1990; *Large et al.*, 1994]. Parametrizations for the ocean interior have been divided into schemes for the open ocean [*Henyey et al.*, 1986; *Gregg*, 1989; *Polzin et al.*, 1995; *Large et al.*, 1994], shelf [e.g. *MacKinnon and Gregg*, 2003] and the equatorial regions [*Pacanowski and Philander*, 1981; *Peters et al.*, 1988; *Large et al.*, 1994; *Zaron and Moum*, 2009].

In the upper layer of the equatorial region turbulent mixing is associated with shear instabilities generated by the vertical shear of the large-scale background flow. Hence within this region parametrization schemes are often related to the gradient Richardson number ($Ri = N^2/S^2$). The relationship of turbulence parameters and Ri has been suggested from laboratory as well as analytical studies [see *Zaron and Moum*, 2009]. In chapter 5 the correlation of the fraction of critical Fr (1/Ri) and dissipation rates was found (fig.5.10). Enhanced mixing activity in the equatorial thermocline has been usually associated with Ri smaller than 0.25 [e.g. *Peters et al.*, 1988], which is based on theoretical considerations, evaluating the so called Taylor-Goldstein equation in search for instable processes. *Canuto et al.* [2008] found energy transfer from the large scale background flow towards turbulence also taking place at higher Ri. However, parametrization schemes for the equatorial thermocline are often based on a direct functional dependence of dissipation rates (ϵ) or eddy diffusivities (K) on Ri^{-1} as single parameter: increasing turbulent parameters for decreasing Ri. These rather simple parametrizations are more pragmatic than the result of a consistent theory. Nevertheless, their simplicity is tempting and facilitates their implemention in numerical models. Thus, they have been widely accepted. The KPP parametrization [*Large et al.*, 1994] has been implemented in many major community Ocean General Circulation Models (OGCMs). Within the following sections existing parametrizations schemes are tested against the observational data presented in this study (section 7.2). Further, our observations are used as base for an own parametrization with parameters N and S (section 7.2). Finally, this alternative parametrization is compared to the existing ones with independent data collected at PIRATA moorings, particularly focusing on resulting diapycnal heat flux (section 7.3).

7.1. Existing parametrization schemes

Some of the following parametrization schemes were especially developed for the equatorial ocean by either tuning models of the equatorial ocean (*Pacanowski and Philander* [1981] (section 7.1.1))
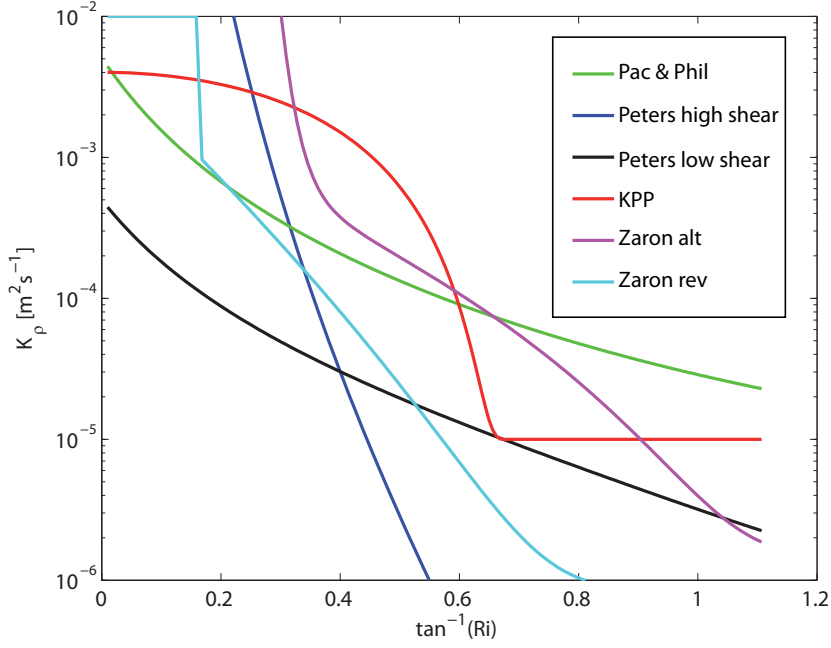
Figure 7.1.: Visualisation of the K-Ri dependence of the existing parametrization schemes. Names in legend refer to subsections 7.1.1 to 7.1.4. The parametrizations of *Zaron and Moum* [2009] are scaled with a constant parameter for κ_0 for simplicity.

or by comparison with observations from the equatorial Pacific (*Peters et al.* [1988](section 7.1.2) and *Zaron and Moum* [2009] (section 7.1.4)). Others claim universality for various ocean regions (*Large et al.* [1994] (7.1.3)). The K-Ri dependence of the existing parametrizations are displayed in fig.7.1.

7.1.1. Pacanowski and Philander, 1981

In previous models before 1981 for the equatorial oceans, constant values for eddy viscosity (ν) and K were used. This lead to a too diffuse thermocline, as the magnitude of the ν and K were adjusted to appropriate values for the EUC, where mixing is strong. In addition, the eastward shoaling of the EUC and the thermocline was not detectable. Therefore, *Pacanowski and Philander* [1981] tuned their model against observations with Ri-dependant relations, which dated back to *Munk and Anderson* [1948] and *Robinson* [1966]:

$$\nu = \frac{\nu_0}{(1 + \alpha Ri)^n} + \nu_b \tag{7.1}$$

and

$$K = \frac{\nu}{(1 + \alpha Ri)} + K_b, \tag{7.2}$$

where ν_0, α, n, ν_b and K_b are constant parameters. These constant parameters were tuned to fit the modelled thermocline and EUC to observations. The model was tested against varying magnitudes of background mixing (K_b) and the response to eastward and westward wind forcing. In addition it was found that the representation of the EUC and the thermocline in terms of

the eastward shoaling was strongly improved by more realistic net surface heat fluxes via its effect on N^2. The optimum parameter set was found as $\nu_b = 1 \cdot 10^{-4} m^2 s^{-1}$, $K_b = 1 \cdot 10^{-5} m^2 s^{-1}$, $n = 2$, $\alpha = 5$ and $\nu_0 = 50 \cdot 10^{-4} m^2 s^{-1}$.

7.1.2. Peters, 1988

In a study by *Peters et al.* [1988] estimates of ϵ and turbulent dissipation rates for temperature (χ) from microstructure observations were used to infer eddy diffusivities using equation 3.1 and equation 3.2. These estimates together with the observed large-scale parameters S^2 and N^2, providing estimates of Ri, were used to determine a relation of K on Ri alone. The parametrization was based on the average profiles obtained from a 4.5 day time series acquired at a single location in the equatorial Pacific (140°W,0°N) during the Tropic Heat Experiment. *Peters et al.* [1988] found a significantly different dependence of K on Ri for the upper shear zone of the EUC, which they defined as between 23 and 81m depth, and the deeper layer, where Ri is in general larger. They decided to fit the upper shear zone and the deeper layers separately. The dramatic increase in K they observed within the upper shear zone lead them to fit a K-Ri dependence of the form

$$K = aRi^b \qquad [m^2 s^{-1}]. \tag{7.3}$$

They note though that this dramatic increase in K for $Ri < 0.4$ in the upper shear zone was not found in data during a later mission at the same location [*Peters et al.*, 1987]. For the deeper layers they fitted a functional dependence for K on Ri as in *Pacanowski and Philander* [1981]. For the upper shear zone the parameters for K_ρ best fit the data for $a = 1.1 \cdot 10^{-8}$ and $b = -9.2$. For the deeper layers they found that the parameter choice of *Pacanowski and Philander* [1981] clearly overestimated their inferred eddy diffusivities K. *Peters et al.* [1988]'s fit for the deeper layers resulted in

$$K = \frac{5 \cdot 10^{-4}}{(1 + 5Ri)^{2.5}} + 1 \cdot 10^{-6} \qquad [m^2 s^{-1}]. \tag{7.4}$$

7.1.3. KPP Parametrization (Large,1994)

The KPP parametrization claims universality for the global ocean. It includes a parametrization scheme for turbulent parameters within the surface boundary layer, which is connected to a parametrization scheme for the ocean interior. Within this study only the parametrization scheme for the ocean interior is investigated. This ocean interior part of KPP is designed as a superposition of internal wave breaking, double diffusive processes as well as instabilities caused by resolved vertical shear of horizontal large-scale velocity. *Large et al.* [1994] suggest a parametrization for the local vertical diffusivities for each of these processes ($K_{internal}$, K_{double}, K_{shear}), which are added to form the total interior diffusivity K.

Eddy diffusivities caused by shear instabilities are assumed to be dependent on Ri, increasing

in magnitude when Ri is below some critical value Ri_c. The K-Ri dependence was defined as

$$K_{shear}/K_0 = \begin{cases} 1, & Ri < 0 \\ [1 - (Ri/Ri_c)^2]^p, & 0 \leq Ri \leq Ri_c \\ 0 & \text{otherwise.} \end{cases} \quad (7.5)$$

In the absence of double diffusive processes the total interior diffusivity K is given by $K_{shear} + K_{internal}$, where $K_{internal}$ was chosen constant. In a follow-up publication these constants were readjusted by tuning a high resolution model (large eddy simulation (LES)) to observations of upper-ocean temperature and mixed layer depth on varying timescales from diurnal to inter-annual [*Large and Gent*, 1999]. The readjusted set of constants reads $K_{internal} = 0.1 \cdot 10^{-4} m^2 s^{-1}$, $K_0 = 40 \cdot 10^{-4} m^2 s^{-1}$, $Ri_c = 0.8$ and $p = 3$. The chosen parametrization scheme is per definition more steplike than the one of *Pacanowski and Philander* [1981] and *Peters et al.* [1988] (fig.7.1).

7.1.4. Zaron and Moum, 2009

Zaron and Moum [2009] argued that despite some evidence for the dependence of turbulent parameters on Ri, this simple dependence would be insufficient by physical as well as dimensional reasoning: The physical argument is that different flow states can exist for the same value of Ri, which should then result in different values of K, impossible to achieve with a simple functional dependence. The dimensional reasoning relies on the Buckingham pi theorem: there are not enough dimensional groups in N^2, S^2 and K_h to provide for a simple relation $K_h(Ri)$, which would be invariant to dimensional units. These arguments lead *Zaron and Moum* [2009] to the proposal of an alternative parametrization of the form $K_h = \kappa_0 \cdot \phi_h(Ri)$. The term $\kappa_0 = |\mathbf{V}|^2/S$ scales the functional dependence of K on Ri ($|\mathbf{V}|$ is regarded as the norm of the velocity vector), whereas ϕ_h retains the functional dependence on Ri. They propose two alternative new parametrizations for ϕ_h. The first one is fitted to the derived values of K_h (ϕ_h^{alt}), while the second fits derived diapycnal heat fluxes (ϕ_h^{rev}). The parametrizations are defined as

$$\phi_h^{alt} = a(\frac{Ri_1}{Ri - Ri_1})^\alpha + be^{-\beta Ri} + c \quad (7.6)$$

and

$$\phi_h^{rev} = \begin{cases} \phi_h^{max} & \text{if } Ri \leq Ri_2 \\ \Delta\phi_h e^{-\gamma(Ri - Ri_2)} + \phi_h^w & \text{otherwise} \end{cases} \quad (7.7)$$

The constant coefficients for their equations are given by $a = 8 \cdot 10^{-7}, b = 2 \cdot 10^{-4}, c = 1.5 \cdot 10^{-7}, \alpha = 5, \beta = 4.3, Ri_1 = 0.25$ for ϕ_h^{alt} and $\phi_h^{max} = 1 \cdot 10^{-3}, \Delta\phi_h = 9.8 \cdot 10^{-5}, \phi_h^w = 8.4 \cdot 10^{-8}, \gamma = 9.86$ and $Ri_2 = 0.168$ for ϕ_h^{rev}. Note, that the value for β in their publication reads -4.3, which leads to unrealistic eddy diffusivities.
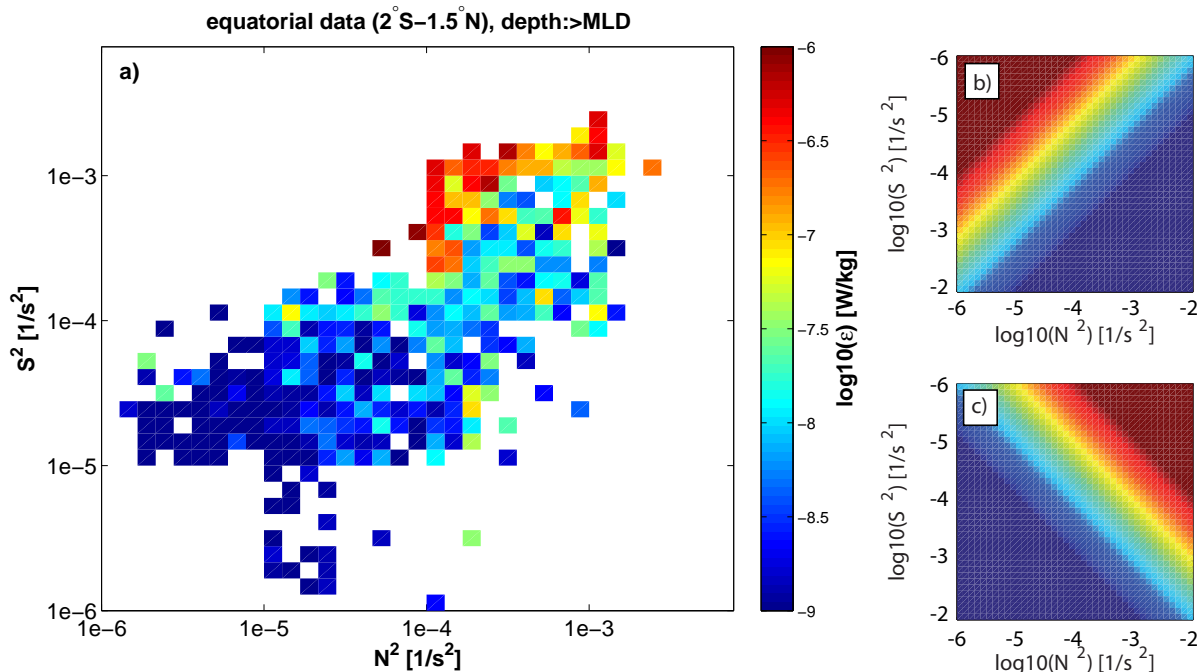
Figure 7.2.: a) Observed dissipation rates (ϵ) from the equatorial ACT region binned into loga-
rithmic $N^2 - S^2$-space. b) Predicted dissipation rates for the observed large-scale
conditions N^2 and S^2 assuming a functional dependence of the form $\epsilon = 1 \cdot 10^{-8} Ri^{-1}$.
c) Same as b), but assuming a functional dependence of the form $\epsilon = N^2 \cdot S^2$.

7.2. ϵ vs. shear and stratification

In previous studies data sets have been used to tune constant coefficients for K-Ri dependencies,
which have been acquired at a single location during several days or weeks. These local data
sets may not exhibit the full range of possible realisations of the $K - Ri$ dependence. On
the contrary, the data set presented in this study consists of spatially scattered short term
observations: microstructure observations and observations of large-scale parameters as shear
and stratification from various locations and different seasons from the equatorial ACT region.
Therefore, the present data set seems to provide a good data base to test the performance of
the different parametrization schemes.

The existing parametrization schemes (section 7.1) all relate the eddy diffusivities K to the
Ri number. Microstructure data, as presented within this study, is first used to estimate the
turbulent dissipation rate ϵ. Deriving K from ϵ via equation 3.1 has to be, as pointed out
previously, regarded with caution. However, as existing parametrization schemes are formulated
for K and ϵ is observed, equation 3.1 has to be implemented in one way or the other for
comparative purposes. In this study, it was decided to investigate the N and S scaling of ϵ. This
allows upcoming studies to directly compare the estimates of ϵ without invoking equation 3.1.
Therefore, the existing parametrizations for K are transformed to ϵ invoking equation 3.1. Note
that at least the studies of *Peters et al.* [1988]; *Zaron and Moum* [2009] explicitly point out the
use of equation 3.1 to convert their estimates of dissipation rates to eddy diffusivities, hence a

reconversion seems permitted.

Some of the existing parametrization schemes for the interior ocean only claim applicability within the equatorial region [*Peters et al.*, 1988] as they are explicitly only fitted to observations from this region. Within the following investigation only data between 2°S and 2°N below the mixed layer are considered. The methodology used in the following for a first step comparison is visual inspection of logarithmically binned data (fig. 7.2). For this purpose ϵ is averaged in logarithmic bins of N^2 and S^2. Shear was calculated from 10 minute averages of velocity obtained with different vessel mounted ADCPs. A different vertical resolution of horizontal velocity leads to differing values for calculated shear [*Moum et al.*, 1992]. The different vessel mounted ADCPs had a resolution of 4m or 8m respectively. To homogenise these shear profiles, data recorded with a bin size of 4m were treated with a Bartlett filter (regarding the processing of ADCP signals) of 8m bin length to match the resolution of the other instruments. Subsequently shear profiles were averaged over one hour (typical duration of a CTD station, where temperature and salinity profiles for the N^2 estimates were obtained). For consistency N^2 and ϵ were also treated with a 8m Bartlett filter. Note though, if N^2 and ϵ are not treated with the filter results do not change significantly. The entire data set of ϵ in logarithmic bins of N^2 and S^2 is shown in fig. 7.2. To illustrate a possible functional dependence of ϵ on Ri, $\epsilon = 1 \cdot 10^{-7} Ri^{-1}$ is displayed in fig. 7.2b. As an alternative an open ocean type scaling [*Gregg*, 1989; *Polzin et al.*, 1995; *Fischer*, 2011] of the form $\epsilon = N^{\alpha_1} \cdot S^{\alpha_2}$ is shown (fig.7.2c, $\alpha_1 = \alpha_2 = 2$ chosen arbitrarily).

As mentioned previously, the idea behind a $K - Ri$ dependence is based on the fact that turbulent mixing within the upper shear layer is driven by shear instabilities. As has been shown in chapter 4 Fr $(1/Ri)$ are large within this layer. Below the EUC core though, Fr numbers have been observed considerably smaller usually indicating stable conditions. Hence, turbulent mixing might by driven by other dynamics, e.g. internal wave breaking. *Peters et al.* [1988] divided their data set for fitting parametrizations in the upper and lower shear layer due to the apparent different dependence of K on Ri within these layers. Our observations (fig. 7.2) support this division, as high N^2, high S^2 observations that originate mostly in the upper shear layer resemble the Ri type dependence, while low N^2, low S^2 observations that originate mostly in the lower shear layer rather resemble the interior ocean type dependence. Therefore in the following the comparison of observed and parametrized dissipation rates for the existing parametrization schemes will be divided into the upper shear layer (MLD to MLD+20m) and deeper layer (MLD+40m to MLD+130m). This choice insures a clear distinction between the two regimes. Note, that the chosen depth range of the upper shear layer is reduced compared to the study of *Peters et al.* [1988], which is due to the different locations of the EUC core (centered at about 60m in this study and about 110m in the study of *Peters et al.* [1988]).

Peters et al. [1988] suggested a different functional dependence of K on Ri in the deeper layer than compared to the upper shear zone. Nevertheless they used a Ri dependence to parametrize K within the deeper layers. In the analysis presented below the inferred dissipation rates will also be compared to an internal wave parametrization within the deeper layer.
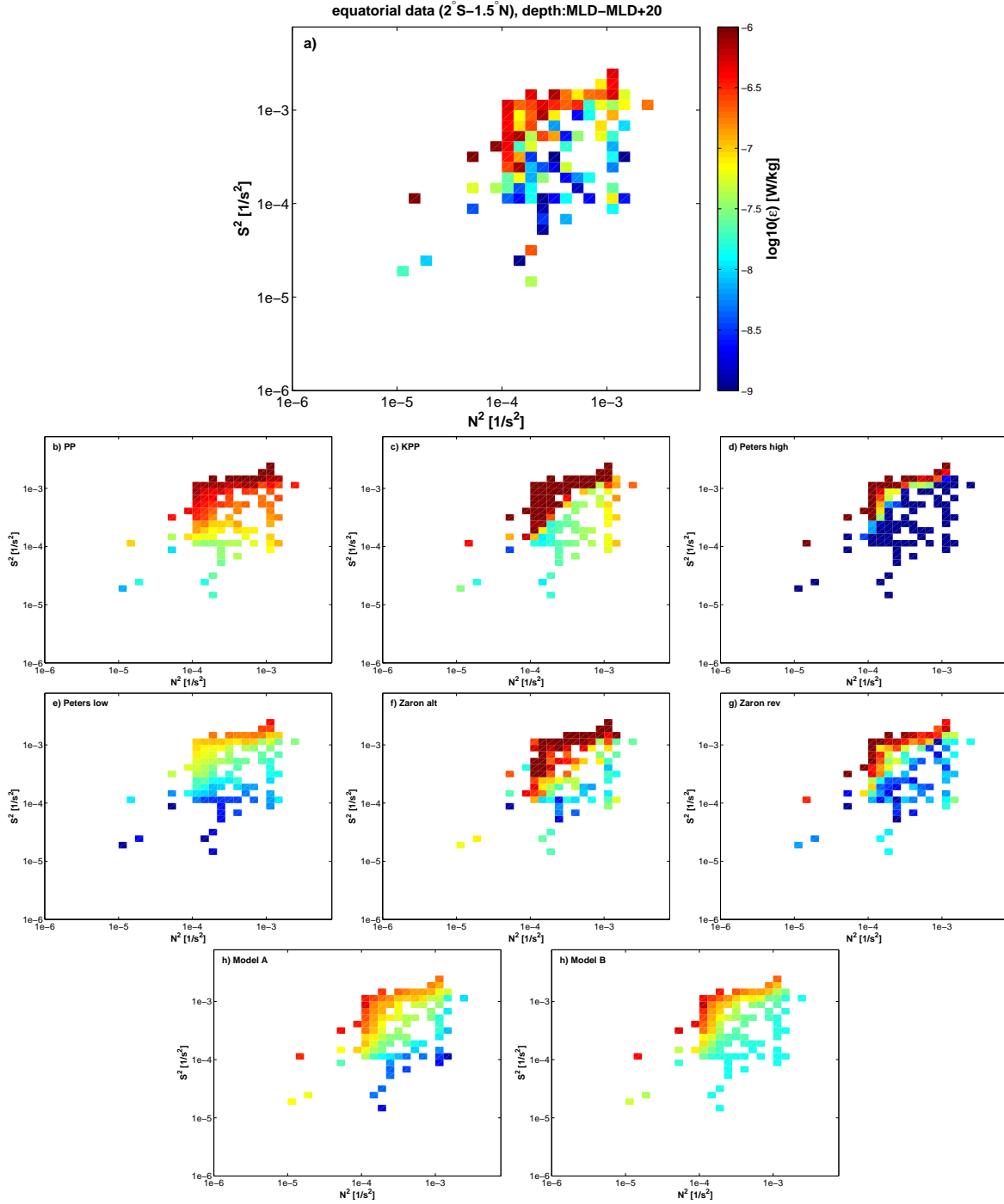
Figure 7.3.: a) Observations of the logarithmically binned ϵ in the upper shear layer and ϵ as predicted from the different parametrization schemes inferred from the N^2, S^2 observations: b) Pacanowski Philander (PP), c) KPP, d) Peters high shear zone formulation (Peters high), e) Peters lower shear zone formulation (Peters low), f) Zaron's alternative parametrization (ϕ_h^{alt}) (Zaron alt), g) Zaron's revised parametrization (ϕ_h^{rev}) (Zaron rev), h) Model A and i) Model B.

coefficient	lower limit	upper limit
$a = 4 \cdot 10^{-8}$	$3.1 \cdot 10^{-8}$	$4.5 \cdot 10^{-8}$
$b = -1.2$	-1.2	-1.2
$c = 2.5 \cdot 10^{-6}$	$8.4 \cdot 10^{-7}$	$8.3 \cdot 10^{-6}$
$d = 3.1$	2	4.3
$e = 1.45 \cdot 10^{-8}$	$8 \cdot 10^{-9}$	$2.3 \cdot 10^{-8}$
$f = 7.5 \cdot 10^{-7}$	$4 \cdot 10^{-7}$	$1.2 \cdot 10^{-6}$
$g = 0.53$	0.39	0.66
$h = 0.71$	0.55	0.9

Table 7.1.: 95% confidence limits for coefficients of model A (a-b) and model B (c-e) for the upper shear zone as well as model C (f-h; introduced in section 7.2.2) for the lower shear zone fitted to the observations of this study as indicated in the text.

7.2.1. Upper shear layer

The binned representations of the parametrized dissipation rates in the upper shear layer suggest some of the parametrizations being more plausible than others (fig.7.3). From visual inspection, the extremely step like functional form of KPP (fig.7.3c), the Peters parametrization for the high shear zone (fig.7.3d) and Zaron's alternative parametrization (fig.7.3f) seem not compatible with the dissipation rates inferred from microstructure observations (fig.7.3a).

Two additional parametrizations of ϵ were obtained here from fitting the observed ϵ to the Ri. The first parametrization (referred to as model A) resembles the most simple dependence of ϵ on Ri of the form $\epsilon = aRi^b$ as proposed by *Peters et al.* [1988] for the upper shear zone. The second scaling (referred to as model B) corresponds to *Peters et al.* [1988]'s scaling for the lower shear zone, in accordance to the form used in *Pacanowski and Philander* [1981]: $\epsilon = \frac{c}{(1+5 \cdot Ri)^d} + e$. In order to find the appropriate coefficients a, b, c, d, e a least squares fit was performed. Therefore, the cost function $\sum_i \left(log_{10}(o_i) - log_{10}(p_i)\right)^2$ was minimized for the individual models taking the logarithm of observations (o) and parametrization (p) to account for their logarithmic scaling. The best fit is obtained for $a = 4 \cdot 10^{-8}$ and $b = -1.2$ for model A and for $c = 2.5 \cdot 10^{-6}$, $d = 3.1$, $e = 1.45 \cdot 10^{-8}$ for model B. 95% confidence limits for the coefficients $a - e$ are obtained via bootstrapping and summarized in table 7.1.

Visual inspection of the binned distributions of ϵ gave an impression, whether some parametrization schemes seem more plausible than another one. *Peters et al.* [1988] parametrization for the low shear zone (Peters low), *Zaron and Moum* [2009]'s revised parametrization (Zaron rev) as well as the models of this study seem more plausible than *Peters et al.* [1988] parametrization for the high shear zone (Peters high), the parametrization of *Pacanowski and Philander* [1981] (PP) and KPP as well as *Zaron and Moum* [2009]'s alternative parametrization (Zaron alt). However, in order to rank the performance of the different parametrizations in representing the observations of this study, different statistical criteria are considered. At first the correlation coefficient (r) between the observations and the various parametrizations of ϵ is regarded. The correlation coefficient can be calculated for data of any kind, regardless of their distribution function. When examining the significance of the correlation coefficient a significance test should be considered:

To decide whether the correlation is significant from zero a criterion has to be established whether to accept or reject a null hypothesis of the form: "H_0: the correlation between observations and parametrization is zero". The significance test for the correlation coefficient, referred to as the t-test, requires the variables (observations and parametrization) to be normally distributed. ϵ is usually found not strictly log-normally distributed, but often reported nearly log-normally distributed [*Osborn*, 1978; *Gregg*, 1989, 1998]. Hence, the t-test was performed as an additional guidance factor: The t-value is defined as $t = r\sqrt{\frac{n-2}{1-r^2}}$, with r the correlation coefficient and n the number of degrees of freedom and is supposed to be t-distributed. A significance level of $\alpha = 0.05$ corresponds for data of the upper shear layer to a critical value of $t_{crit.} = 1.97$. Hence, if $t > t_{crit.}$ H_0 has to be rejected. An alternative to the Pearson correlation, which often only termed the correlation, is proposed for variables of unknown distributions referred to as the Spearman rank correlation coefficient. In this case the variables are ranked in descending order and the correlation of these ranks (rx,ry) is calculated via

$$r_s = 1 - 6\frac{\sum\limits_{i=1}^{n}(rx_i - ry_i)^2}{n(n^2 - 1)}. \tag{7.8}$$

The significance of this correlation coefficient can then be obtained by comparing the resulting value of r_s to the critical value (dependant on the number of observations), which are given in tables (e.g. *Ramsey* [1989]; *Conover* [2001]). For the number of observations in the upper shear layer the critical value of $r_{s-crit.} = 0.16$ at a significance level of $\alpha = 0.05$. As an additional measure of the performance of the parametrizations in question the standard error (s_e) between observations and parametrized values is calculated as

$$s_e = \sqrt{\frac{\sum\limits_{i=1}^{n}(log_{10}(o_i) - log_{10}(p_i))^2}{n - 2}}. \tag{7.9}$$

Again the logarithm of observations and parametrized values is taken to account for their near logarithmic distribution.

The results of the statistical analysis agree well with the results from the N-S binned plots (fig.7.3). Highest correlation (r) is not surprisingly found for the proposed models A and B as these were fitted against the observations. Zaron rev shows similar high correlation. PP, KPP, Peters high and Peters low and show similar correlations on the order of 0.45, whereas Zaron alt shows lowest correlation coefficients. All pass the t test of significance. The rank correlation coefficient r_s shows a similar distribution among the parametrization schemes as r. The standard error (s_e) is smallest for the two models of this study, Zaron rev and Peters low. Note, that model A and model B produce nearly identical results in the statistical analysis presented above. In the following therefore only the simple model A is further considered, as it requires less fitted constant coefficients. Nevertheless, all further investigations lead to identical results regardless if model A or model B is used.

Parametrization	r	t	r_s	s_e
PP	0.44	6.6	0.46	1.3
KPP	0.49	7.5	0.47	1.5
Peters high	0.47	7.2	0.54	4.5
Peters low	0.45	6.7	0.46	0.87
Zaron alt	0.37	5	0.4	1.7
Zaron rev	0.52	8.2	0.53	0.96
Model A	0.53	7.5	0.53	0.88
Model B	0.53	8.2	0.53	0.85

Table 7.2.: Statistical parameters such as correlation coefficient (r), the critical t value (t), the Spearman rank correlation coefficient (r_s) as well as the standard error (s_e) for the parametrization of ϵ in the upper shear layer for the different schemes. Highlighted in red are the parametrizations, which have comparably high standard error. Highlighted in green are parametrizations with an overall good combination of statistical parameters.

7.2.2. Deep layers

As was pointed out in section 7.2, dissipation rates in the deeper layers do not seem to follow the same Ri dependence as was observed for the upper shear layer. Hence, it may be not surprising that most of the existing Ri-dependent parametrization schemes obtained from fitting the upper shear layer can not adequately reproduce the observations of dissipation rates in the deeper layers. Ri-dependent schemes adequate for the upper shear zone tend to overpredict dissipation rates especially within low stratification regions: KPP, Peters high and Zarons formulations (fig.7.4). In addition, dissipation rates from high S^2 and N^2 regions of the deeper layers are often overestimated by all existing parametrization schemes. As the observed dissipation rates of the deeper layers seemed to rather follow an open ocean kind of scaling on N and S instead of a Ri (fig.7.2), the dissipation rates of the deeper layers are best fitted to the functional form $\epsilon = f N^g S^h$ (referred to as model C) with a least squares fit and tuning parameters f,g,h constant. The best fit was obtained for $f = 7.5 \cdot 10^{-7}$, $g = 0.53$, $h = 0.71$. 95% confidence limits for these parameters are given in table 7.1. Statistical parameters in use to rank the performance of the parametrization schemes are the same as described for the upper shear zone, here the critical t value is $t_{crit} = 1.95$. The critical value for the Spearman rank correlation has to be approximated as described in *Conover* [2001] and is estimated as $r_{s-crit} = 0.03$.

Highest correlation of 0.5 is obtained for the model C of this study. Peters low and PP is still correlated on the order of 0.35. All other parametrization show extremely low correlations. Zaron rev and Peters high do not pass the t-test of significance. The rank correlation gives similar results. The standard error is lowest for the model of this study and Peters low, for the other parametrizations the s_e is rather high.

7.3. Parametrized timeseries of ϵ and J_h

Zaron and Moum [2009] mention that most of the parametrization schemes have been tuned
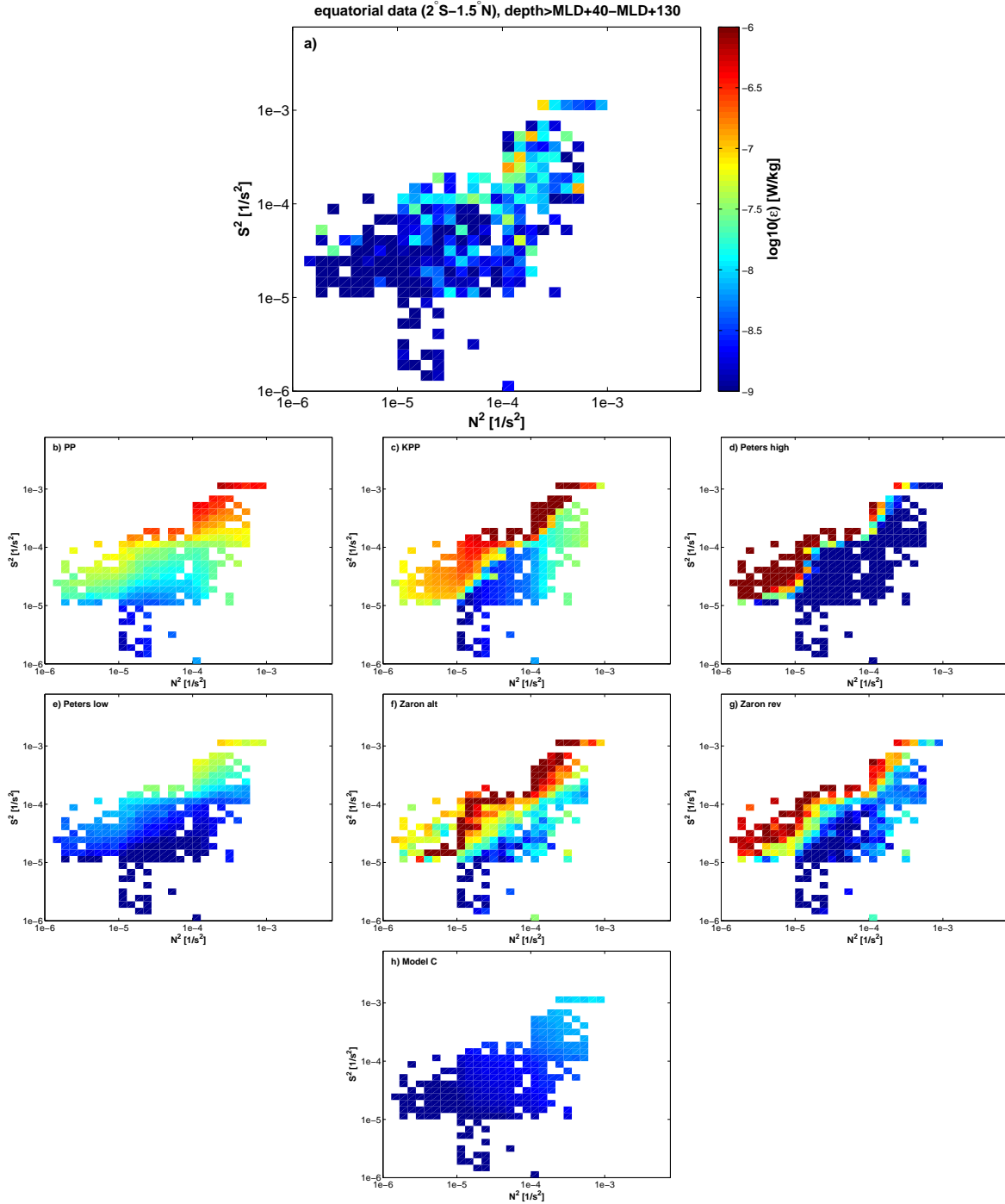
Figure 7.4.: a) Observations of the logarithmically binned ϵ in the deeper layer (MLD+40m to MLD+130m) and ϵ as predicted from the different parametrization schemes inferred from the N^2, S^2 observations: b) Pacanowski Philander (PP), c) KPP, d) Peters high shear zone formulation (Peters high), e) Peters lower shear zone formulation (Peters low), f) Zaron's alternative parametrization (ϕ_h^{alt}) (Zaron alt), g) Zaron's revised parametrization (ϕ_h^{rev}) (Zaron rev), h) Model A and i) Model B.

to best fit dissipation rates or eddy diffusivities. They claim that even though the ability of parametrizations representing these quantities may be rather high, they can still fail to correct-

7. Parametrization

Parametrization	r	t	r_s	s_e
PP	0.36	12	0.32	1.33
KPP	0.14	5	0.08	1.57
Peters high	0.1	0.18	-0.17	>100
Peters low	0.34	11	0.3	0.7
Zaron alt	0.1	3.2	0.13	2
Zaron rev	0.05	0	0	1.42
Model C	0.5	18	0.54	0.5

Table 7.3.: Same as table 7.2, but for the deeper layers

ly represent the diapycnal heat flux especially below the ML: they find that KPP overpredicts the diapycnal heat flux below the ML by a factor of 4 for their data set. As pointed out previously numerical models crucially depend on the parametrization of turbulent fluxes. A large overestimation of the diapycnal heat flux as reported by *Zaron and Moum* [2009] could e.g. severely imbalance the ML heat budget (chapter 6). Therefore in the following the skill of the discussed parametrization schemes in parametrizing the diapycnal heat flux out of the ML will be investigated, this time performed with an independent data set of shear and stratification observations obtained from the PIRATA moorings at 10°W,0°N (section 7.3.1) and 23°W,0°N (section 7.3.2). This will allow a fair comparison of literature parametrizations and the ones fitted to our microstructure observations.

With the formulation for dissipation rates as a function of observed large-scale shear and stratification at hand, timeseries of ϵ at PIRATA locations can be constructed, based on timeseries of velocity, temperature and salinity. This setting is found for the PIRATA buoys, where subsurface velocity, temperature and salinity are available extending the analysis to time-depth space.

7.3.1. 10°W,0°N

Time-depth series of ϵ are constructed for all available parametrizations based on the shear and stratification data from the PIRATA mooring described in chapter 4 (fig.4.4). The parametrized dissipation rates for the model of this study combining the different functional forms for the upper (model A) and lower (model C) shear layer, as well as the dissipation rates for the most commonly used KPP parametrization are shown (fig.7.5). Note, for the model of this study the parametrization for the upper shear layer was extended until MLD+40 to improve the transition between the different parametrization for the upper and lower shear zone. KPP obviously produces generally 10-fold higher dissipation rates than the model of this study, maximum values reaching $1 \cdot 10^{-5} W kg^{-1}$ (KPP) and $1 \cdot 10^{-6} W kg^{-1}$ (this model) respectively. For both timeseries dissipation rates rapidly decay just above the EUC core depth and highlight the upper shear zone as the zone of most active mixing. The parametrized ϵ of this study exhibits some seasonal variations for dissipation rates below the ML. In 2007 and 2009 during boreal summer (about June-September) dissipation rates are elevated and to a lesser extent also in November/December. During 2008 no seasonal variation can be detected. A seasonal variation for dissipation rates below the ML from KPP can not be assessed as explicitly, however dissipation rates are very high throughout the timeseries. For the average profiles of ϵ over the

entire time period the large discrepancy of a factor of 10 between the model of this study and KPP is confirmed (fig.7.5c). Compared to the average profile for the equatorial region based on microstructure observations as presented in fig.5.1a the average parametrized ϵ with the model of this study inferred from PIRATA observations is closer to the observations than KPP.

In the following the parametrized diapycnal heat flux at the base of the ML will be investigated. For this step the direct formulations of K as a function of Ri for the existing parametrization schemes could be used. The parametrized dissipation rates (for the model of this study) or eddy diffusivities (for the existing parametrization schemes) are used to infer the diapycnal heat flux via equation 3.12. The main focus investigating this quantity will be laid on the correct representation of the general magnitude of J_h at the base of the ML and possible seasonal variations in terms of a boreal summer maximum.
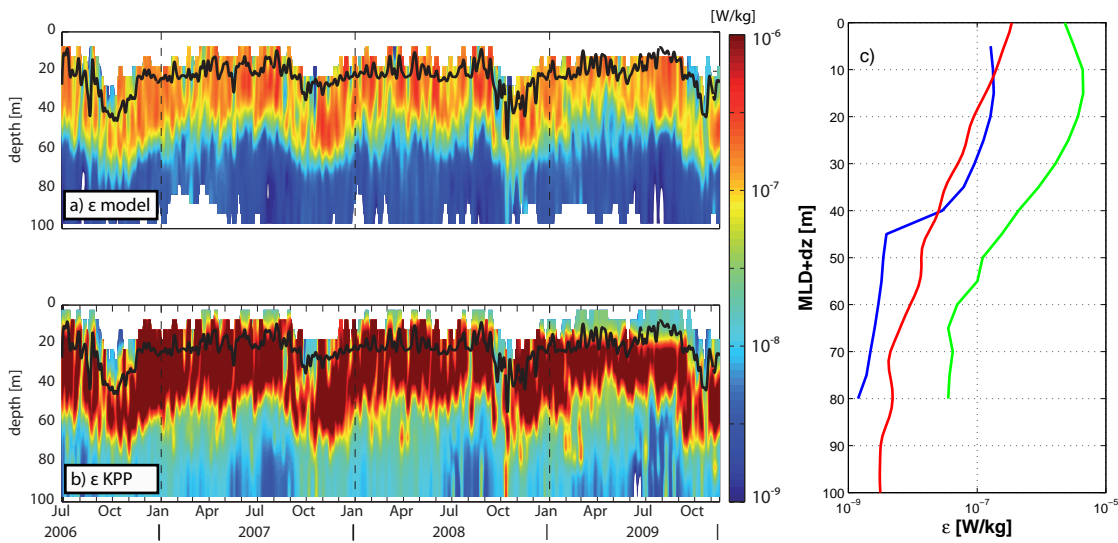

Figure 7.5.: Time-depth series of the parametrized ϵ for a) the model of this study and b) KPP. c) Average profiles of dissipation rates in adjusted vertical coordinates of MLD+dz for the model of this study (blue), the KPP parametrization (green) and the observations of equatorial dissipation rates as presented in fig.5.1a (red). The black line in a) and b) denotes the MLD.

In section 5.3 the diapycnal heat flux out of the ML inferred from microstructure observations is characterized by this quantity in a rather narrow layer from MLD+5 to MLD+15. Thus, diapycnal heat fluxes for the parametrized time-depth series are also averaged over this layer for every time step. The general magnitude of J_h at the mixed layer base at this location was inferred in the range of 40-90 Wm^{-2} from microstructure observations (section 5.3). In addition, highest mixing activity throughout the equatorial ACT region was observed during boreal summer. Parametrized fluxes should exhibit these main features.

The timeseries of monthly averaged diapycnal heat fluxes out of the ML constructed via the different parametrization schemes show a wide range of scales (fig.7.6). Note that Peters high and Zaron alt are not included as they overshoot the range of 2000 Wm^{-2}. Peters high parametrization results in diapycnal heat fluxes out of the ML of over 100000 Wm^{-2}, highly unrealistic,

whereas Peters low provides the lower end of scales with diapycnal heat fluxes out of the ML ranging between 10 and 60 Wm^{-2}. The majority of parametrizations clearly overshoots the 0-100 Wm^{-2} range that was obtained from shipboard observations. Only Peters low and the model of this study are limited to this range. In addition, most of these extremely elevated heat fluxes do not reveal any seasonality - their monthly magnitude seems fortuitous. For the four lowest proposed estimates: Peters low, the model of this study, PP, and Zaron rev, a peak in the diapycnal heat fluxes can be detected during boreal summer (June-August) at least for the years 2007 and 2009.

Concentrating on the two lowest and most plausible proposed estimates of the diapycnal heat flux out of the ML and the years 2007 and 2009 a variation in magnitude within the year is more (less) pronounced for the parametrization of this study (Peters low) with boreal summer peaks of up to 70-80 (30-40) Wm^{-2} and the remainder of the year ranging between 20-40 (10-20) Wm^{-2}. A timeseries of only 3 years can not assess a robust seasonal signal. However, the 3 available years were averaged and compared to the assessed seasonal variability of the diapycnal heat fluxes out of the ML at this location based on microstructure observations. The general magnitude of the diapycnal heat flux is best captured with the parametrization of this study. Peters low underestimates the diapycnal heat fluxes inferred from observations (fig.7.7). In addition, during boreal summer elevated heat fluxes are observed and parametrized. The averaged seasonal evolution of the parametrized diapycnal heat flux suggests a second peak in magnitude in November and December. A similar second increase during this period was found in the modelling study of *Jouanno et al.* [2011], but is not resolved in the estimates from the microstructure surveys (fig.7.7). It is not clear however, if this is a robust seasonal signal.
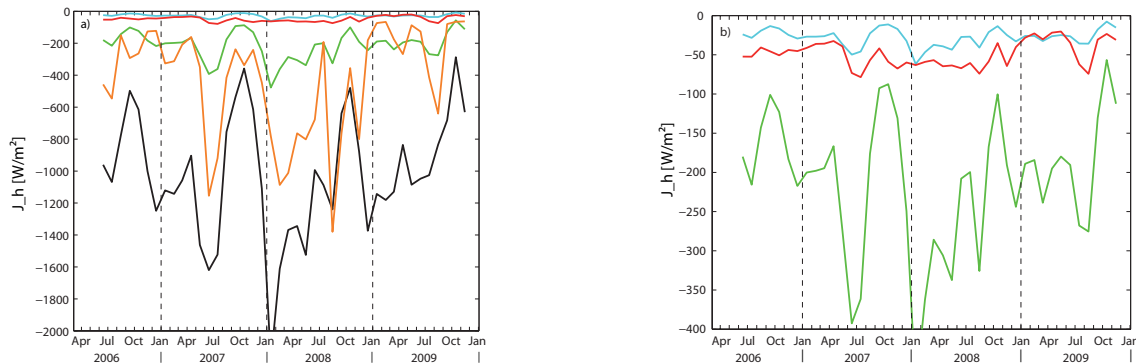

Figure 7.6.: a) Monthly mean values for the parametrized diapycnal heat fluxes out of the ML based on shear and stratification data from the PIRATA mooring at 10°W,0°N for the different parametrizations: PP (green), KPP (black), Peters low (cyan), Zaron rev (orange) and the model of this study (red), b) zoomed-in for heat fluxes lower $400Wm^{-2}$.

As the diapycnal heat flux out of the ML at 10°W,0°N constructed from shear and stratification data of the PIRATA buoy observations via the parametrization scheme of this study seems to produce plausible estimates of dissipation rates and diapycnal heat fluxes out of the ML (fig.7.5a,c, 7.7), its average seasonal cycle will be integrated into the estimates of the ML heat budget, which has been discussed previously (section 6.2). Despite the generally lower diapy-
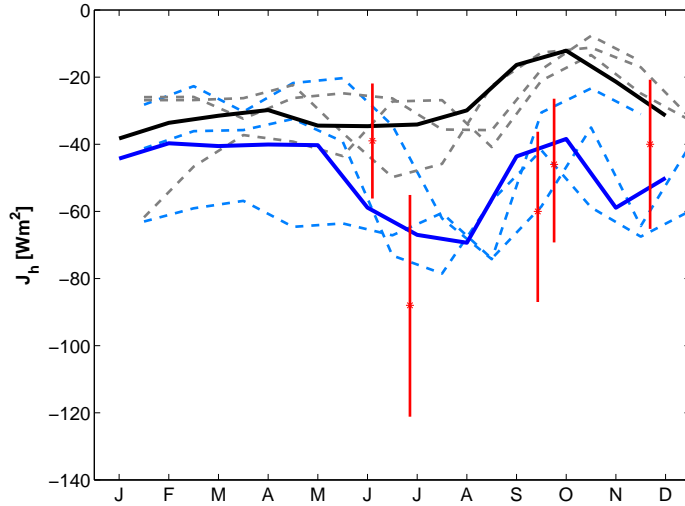
Figure 7.7.: Monthly averages of parametrized diapycnal heat fluxes for the Peters low (das-
hed grey lines) parametrization and the model of this study (dashed blue lines) at
10°W,0°N together with their average (Peters low - heavy black line; model of this
study - heavy blue line) and the estimates of the diapycnal heat fluxes in the equa-
torial region at 10°W based on observations (red stars) and their associated error
estimates.

Figure 7.8.: a) Seasonal variability of individual terms contributing to the ML heat budget at
10°W,0°N as fig.6.2a, but including the parametrized diapycnal heat flux. The in-
dividual contributions are displayed as indicated in the legend. In b) the sum of
all contributing terms of the ML heat budget are compared to the observed heat
storage as in fig.6.2b, but including parametrized diapycnal heat flux instead of the
estimate based on observations.

cnal heat fluxes obtained from the parametrization compared to the observations during boreal
summer, the diapycnal heat flux is still recognized as the dominant cooling term during ACT
development (fig.7.8a). The timeseries provides an entire annual cycle to be included in the sum
of individual terms and the budget can be nearly closed for the entire year within the uncer-
tainties (fig.7.8b). A slight residual from May to July is found between the sum of contributing
terms and the observed heat storage. Hence, the parametrization of this study seems to provide a

7. Parametrization

plausible estimate of the diapycnal heat flux out of the ML based only on large-scale background observations obtained from the PIRATA buoy.

7.3.2. 23°W,0°N
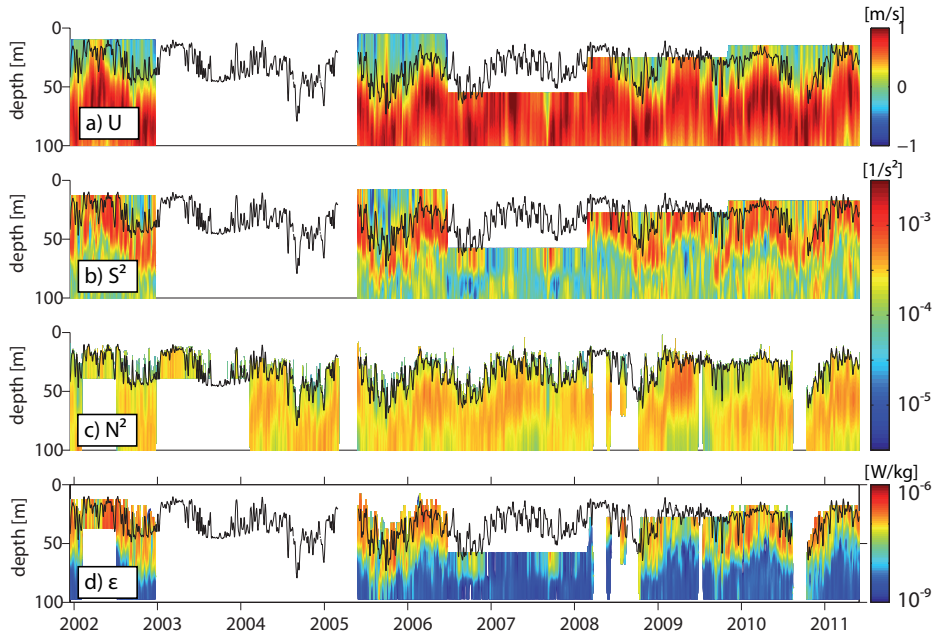
Figure 7.9.: Time-depth series between 2002 and 2011 of a) zonal velocity, b) shear, c) stratification measured by the PIRATA buoy at 23°W,0°N and d) the parametrized dissipation rate obtained with the model of this study. The black line denotes MLD.
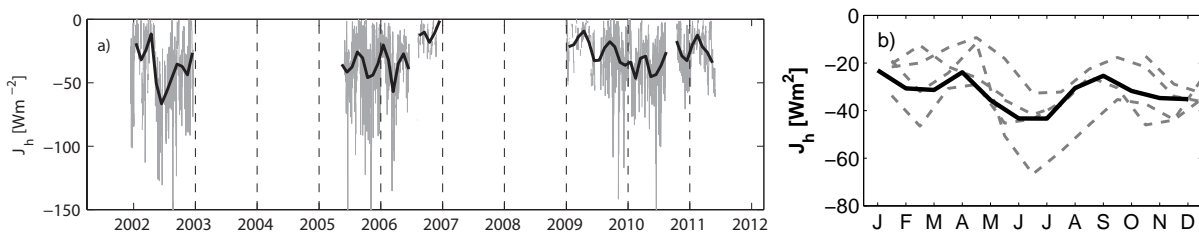
Figure 7.10.: a) Timeseries of the daily (grey line) and monthly averaged (heavy black line) parametrized diapycnal heat flux out of the ML at 23°W,0°N; b) average seasonal cycle of the diapycnal heat flux in a) with monthly averages (dashed grey lines) and average seasonal cycle (heavy black line).

The investigation of the ML heat budget at 23°W,0°N (section 6.4) revealed a large discrepancy between the sum of individual terms and the observed heat storage throughout the year, which contradicts previous results of *Foltz et al.* [2003]. Unfortunately, microstructure observations at this longitude presented in this study are sparse and could not provide the missing diapycnal heat flux required in either of the budget estimations. In the following, the parametrization of this study will be tested for shear and stratification observations of the PIRATA buoy at 23°W,0°N
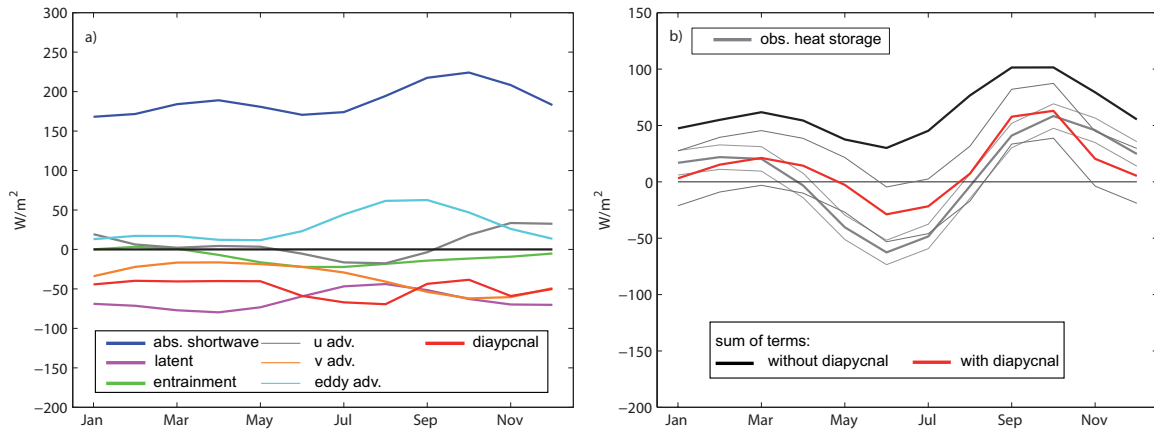
Figure 7.11.: a) Seasonal variability of individual terms contributing to the ML heat budget at 23°W,0°N as fig.6.4a, but including the parametrized diapycnal heat flux. The individual contributions are displayed as indicated in the legend. In b) the sum of all contributing terms of the ML heat budget are compared to the observed heat storage as in fig.6.4b, but including parametrized diapycnal heat flux instead of the estimate based on observations.

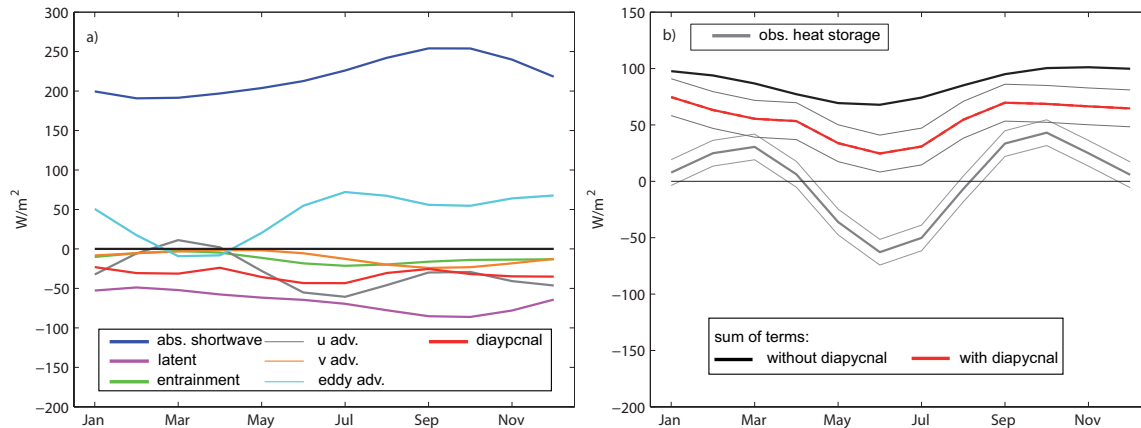in order to gain more insight in possible magnitude and seasonal variation of the diapycnal heat flux out of the ML at this location. This also provides a supplementary, independent test for the parametrization scheme.

In general, the construction of the time-depth field of dissipation rates at 23°W,0°N based on shear and stratification data is the same as at 10°W,0°N. Bi-daily ADCP velocity observations are available from 2002-2011 with considerable gaps within the timeseries (fig.7.9a). Subsurface temperature from the PIRATA mooring is available at 10 minute resolution from 2002 to mid October 2010, which is combined with daily resolution data as described for the buoy at 10°W,0°N. Salinity is available hourly until mid June 2009, with a one year gap, which is filled and extended with daily data.

Strong similarities concerning the magnitude and seasonal development of the different variables (zonal velocity, shear and stratification) are found between 23°W,0°N and 10°W,0°N. Maximum zonal velocities associated with the EUC core are found slightly deeper within the water column compared to 10°W,0°N, nevertheless the seasonal vertical migration of the core accompanied by the vertical movement of the MLD is similar as at 10°W,0°N. Westward surface velocities associated with the nSEC can not be observed equally pronounced as at 10°W,0°N, which might be partly explained by the different ADCP settings. At 23°W the reliable bins start deeper in the water column. Shear levels generally seem to be slightly reduced in magnitude compared to 10°W, which could maybe be related to insufficient resolution of the instrument at 23°W lacking information on the westwards surface flow. An alternative explanation could be, that due to the deeper EUC core, the depth range of varying velocities is expanded, leading to lower shear levels. These lower shear levels at 23°W on the equator compared to 10°W observed by the PIRATA moorings were already noted by *Jouanno et al.* [2011]. However, shear levels are highest in the layer just below the ML throughout the year. A slight reduction towards autumn

can be detected. Stratification seems in general also lower than further east, as has been discussed in chapter 4. Maximum values coincide with highest shear levels within the thermocline layer as was reported for 10°W. A reduction towards autumn can be detected, but less pronounced than at 10°W. Note, that huge data gaps exist for both, the ADCP observations as well as the temperature and salinity records.

The resulting parametrized dissipation rates for the model of this study are in general reduced in magnitude by a factor of 1.5-2 compared to their counterparts at 10°W. The average profile over the entire timeperiod is nearly identical with the average equatorial dissipation rate profile inferred from microstructure observations (red curve in fig.7.5c). The general magnitude of the diapycnal heat flux at the base of the ML during the year is slightly reduced to the findings at 10°W. During boreal summer diapycnal heat fluxes seem elevated compared to the remainder of the year. The parametrized fluxes are in rather good agreement with the diapycnal heat fluxes inferred from microstructure observations during the appropriate seasons at this location as presented in section 5.3. Thus, re-investigating the contribution of the diapycnal heat flux to the mixed layer heat budget with parametrized diapycnal heat fluxes does not change the large residual at 23°W between the sum of contributing terms and the observed heat storage (fig.7.11b). The residual remains unexplained and further investigations have to clarify the contributions of the individual heat flux terms.

7.4. Summary and discussion

Most of the existing parametrization schemes used for the equatorial thermocline overestimate the magnitude of the diapycnal heat flux out of the ML. The heterogeneous data set of this study was used to evaluate the existing Ri-dependent parametrization schemes for their skill in assessing observed dissipation rates from observations of large-scale background parameters (shear and stratification). The evaluation included an own simple N-S parametrization fitted separately to dissipation rates observed within the upper shear zone of the EUC and the deeper layer.

Visual inspection of dissipation rates averaged in logarithmic bins of shear and stratification as well as the analysis of statistical parameters have revealed the model of this study to produce the most plausible estimates for the upper shear layer. This is not quite as surprising as it was fitted to the observations. Zaron rev and Peters low follow, while the other parametrizations have larger deficiencies. Within the deeper layers clearly better results are obtained for the model of this study. The other parametrization schemes show significantly lower correlations. However, the scaling of this study fitted to the deeper layers, is not Ri-dependent, but closer to the parametrizations for the open ocean. This supports the presumption that turbulent mixing within the deeper layers is due to internal wave breaking instead of shear instabilities caused by the large-scale background flow, because shear levels have significantly reduced within this layer (chapter 4). Correlation coefficients for the statistical analysis do not exceed 0.6, which may appear rather low. Nevertheless, turbulent parameters are highly variable and the correlation coefficients were calculated for individual observations.

The skill of the parametrization schemes in assessing the magnitude of dissipation rates and the diapycnal heat flux at the base of the ML was tested with independent data sets of shear and stratification obtained from the PIRATA moorings at 10°W,0°N and 23°W,0°N. Differences between the diapycnal heat fluxes assessed from the shipboard measurements and via the parametrization schemes are to be expected due to the different spatial sampling. As discussed previously the latitudinal range between 2°S and 2°N is subject to additional shear due to the nSEC and TIWs at these locations (chapter 4), which are not necessarily captured in their whole extent by the mooring. In addition, the lower resolution of temperature and especially salinity from the mooring compared to the ship sections probably leads to differing estimates of N^2.

The general magnitude of parametrized dissipation rates inferred from independent observations of shear and stratification of the PIRATA moorings agree well with the observations from shipboard measurements. The KPP parametrization has been found to overestimate dissipation rates by a factor of about 10. Parametrized diapycnal heat flux at the base of the ML mostly overestimate the magnitude inferred from shipboard observations (40-90 Wm^{-2}). The only parametrization schemes limited to this range are Peters low and the model of this study. However, Peters low estimates are too low.

Including the parametrized diapycnal heat fluxes for the model of this study in the ML heat budgets at 10°W,°N and 23°W,0°N leads to similar results as discussed in chapter 6 for the shipboard observations. The advantage of the plausible estimates via parametrization is that a complete seasonal curve is provided. Furthermore, no additional measurements are required, if all terms of the ML heat budget can be estimated from the PIRATA buoy measurements only. Note though, especially for 10°W the seasonal cycle is obtained with a timeseries of only 3 years. A longer timerseries would be necessary to improve the estimate.

As the parametrization of this study provides much more plausible estimates of the diapycnal heat flux at the base of the ML within the equatorial ACT region than e.g. KPP, its use should improve the representation of the turbulent flux within a numerical model at this location.

8. Synthesis

An important region of strong seasonal and inter-annual SST variability is the Atlantic Cold Tongue (ACT) region. The aim of this study was to investigate the regional as well as seasonal variability of turbulent mixing within the ACT region with a focus on the contribution of diapycnal heat flux on the heat budget of the mixed layer (ML). For this purpose the first substantial data base of microstructure observations in the tropical Atlantic was evaluated. Microstructure data, in this case observations of small scale velocity shear from 8 cruises into and at different stages of ACT development, were analyzed. This unique data set was used to assess for the first time not only the magnitude, but the regional and seasonal variability of mixing related parameters in the ACT region. In combination with observations of large scale background parameters (from CTD, vmADCP, ARGO, PIRATA, climatological products) the driving mechanisms for mixing intensity and its variability were derived. The contribution of the inferred diapycnal heat fluxes to the ML heat budget was investigated at four characteristic locations within the ACT to gain insight in its role in cooling SSTs.

Investigation of the background conditions observed directly during the cruises as well as assessed seasonal cycles of the background state via climatological products revealed fundamental differences between the western equatorial, the eastern equatorial and the southern part of the ACT region. Net surface heat fluxes in the equatorial ACT region tend to heat the surface mixed layer throughout the year. Within the western equatorial ACT region a net surface heat flux maximum is observed during summer, counteracting the development of the cold tongue. Towards the eastern equatorial ACT the atmospheric surface heating during summer is reduced. In the southern ACT region net surface heat fluxes act to cool the ML during cold tongue development. In addition to variability in the atmospheric forcing, the differences in ocean currents are responsible for differences between the sampled regions: Highly energetic zonal currents flowing in opposite directions, namely the nSEC at the surface and the subsurface EUC have a substantial impact on the equatorial ACT region, but diminishing towards the east due to diminishing strength and vertical extent of the current system. Superimposed on the equatorial current system are strong intra-seasonal velocity fluctuations associated with TIWs, which are most pronounced in the western equatorial ACT region. It was found that these intra-seasonal fluctuations are strongest during boreal summer and autumn, while in the southern ACT region neither strong current features nor strong intra-seasonal fluctuations are observed.

The variability of the atmospheric forcing and the current system within the ACT region leads to fundamental differences in the background conditions for turbulent mixing in terms of shear and stratification. Shear levels of horizontal velocities within the equatorial ACT region are elevated between the surface mixed layer and the core of the EUC. Despite the mentioned reduction in strength for the zonal currents, shear levels at 2°E are still of comparable magnitude to

	23°W,0°N	10°W,0°N	0°E/2°E,0°N	6°E,0°N	10°W,10°S
strength EUC/nSEC system	++	++	+	-	o
shoaling of EUC	-	+	++	o	o
TIW presence	+	+	-	-	-
elevated shear	+	++	+	-	-
elevated strat.	-	-	+	++	-
occurrence crit. Fr	o	++	+	-	-
elevated turbulent mixing	++	++	+	-	-
major cooling terms in ML heat budget during ACT development	diapycnal heat flux zonal heat advection	diapycnal heat flux	diapycnal heat flux	o	atmospheric forcing

Table 8.1.: Summary of the regional variability of important features as described within the text for the different ACT regions. + denotes feature present, - not present, o not assessed due to data lack or absence of the feature.

10°W. This is probably due to the shoaling of the EUC, narrowing the depth extent of varying velocities and hence keeping shear at a significant level. However, the depth extent of elevated shear decreases. As far east as 6°E, where the EUC looses signature and is rather a transient feature, shear levels are strongly reduced. A reduction of shear towards autumn is observed in the equatorial ACT region. Here the zonal shear component is dependent on nSEC strength and the core depth of the EUC. The variability of the zonal shear component dominates the variability in the total shear component. The meridional shear component was observed rather constant in summer and autumn and was associated with the presence of TIWs. Within the southern ACT region shear levels are strongly reduced compared to the equatorial region due to the strongly reduced velocities. Stratification is strongest below the surface mixed layer within the main thermocline. On the contrary to shear, stratification below the ML increases from west to east in the equatorial ACT region mainly due to the strong salinity gradient in the eastern Gulf of Guinea. For the southern ACT region a similar distribution is observed below the ML. Similar to shear, stratification within the western equatorial ACT region decreased towards autumn.

The possibility of shear instabilities to develop is often expressed with the gradient Ri or Fr number, relating large scale shear to stratification. Critical Fr numbers are most frequently observed within the western equatorial ACT region and in the second half of the year. Within the eastern ACT region they are observed only during summer. They do not occur within the southern ACT region. During summer and fall the fraction of critical Fr numbers decreases by a factor of up to 2, when the meridional shear component was omitted from the calculations. This suggests TIW crucially influencing background conditions for turbulent mixing within this region.

The regional and seasonal variability of turbulent mixing corresponds to the variability in observed background conditions:

8. Synthesis

1. Turbulent dissipation rates are significantly elevated in the equatorial ACT region compared to the southern ACT by a factor of up to 10.

2. Dissipation rates are enhanced in the western equatorial ACT region compared to the eastern region during all sampled ACT stages (early summer to mid November).

3. Of the sampled seasons highest mixing activity throughout the equatorial ACT region is found in summer.

4. In the western equatorial ACT region dissipation rates are elevated and penetrate deeper into the stratified water column in particular during the presence of TIWs

Inferred heat losses of the ML due to diapycnal mixing were highest within the western ACT region, varying between 90 Wm^{-2} in summer, about 50 Wm^{-2} in autumn and 40 Wm^{-2} towards the end of the year (November). Reduced mixing towards the east resulted in maximum 25 Wm^{-2} heat loss in the eastern equatorial ACT region during summer, reducing here even to only 5 Wm^{-2} towards the end of the year. No seasonal variability and diapycnal heat fluxes of about 10 Wm^{-2} were found for the southern ACT region.

Considering the inferred diapycnal heat fluxes at the ML base in the ML layer heat budget, revealed significant differences between the equatorial and southern ACT region. Within the equatorial ACT regions the diapycnal heat flux at the base of the ML is the dominant cooling term during the development of the cold tongue. In addition, its considerable magnitude during the mature phase of the cold tongue delays the increase in SSTs forced by the net surface heat fluxes and eddy advection. During both periods elevated turbulent mixing was associated with the presence of TIWs. It is therefore suggested that these waves play a crucial role in the development and maintenance of the ACT. Apart from 23°W, where the contribution of the individual terms to the ML heat budget needs further clarification, the mixed layer heat budgets could be closed within the uncertainties.

An overview about the regional variability of the current system, resulting background conditions for turbulent mixing, mixing intensity and the dominating cooling terms of the ML heat budget during ACT development for the investigated ACT regions as described above are summarized in tab. 8.1.

Obtaining microstructure data sets as the one analyzed in the framework of this study is cost-worthy and timeconsuming. Hence, reliable parametrization schemes relating mixing intensity to the large-scale background parameters would enlarge information on the variability of mixing related parameters without supplementary costs. In addition parametrization schemes are required in numerical modelling. The similarity of the variability in large scale background shear and stratification and the regional and seasonal variability of mixing intensity suggested that parametrization may be possible. The data set of this study revealed large discrepancies in the skill of existing parametrization schemes in assessing the magnitude of turbulent mixing and the diapycnal heat fluxes out of the ML within the equatorial ACT. A simple parametrization scheme was fitted to the underlying data set and tested against an independent data set of shear and stratification. This simple scheme reproduces the magnitude of the diapycnal heat

flux out of the mixed layer adequately and should provide improved estimates of this quantity in a numerical model.

The results of this study revealed substantial regional and seasonal variability of turbulent mixing within the ACT region. In addition this study highlights the crucial importance of the diapycnal heat flux at the mixed layer base in cooling SSTs during cold tongue development.

A. Calculation of confidence limits for ϵ, K_ρ and J_h

The influence of instrument noise level on average quantities was estimated using the same method as applied by *Gregg* [1989]. Dissipation rate estimates ranging at the noise level of the instruments (below $1 \cdot 10^{-9} W kg^{-1}$) are set to the constant value of $1 \cdot 10^{-10} W kg^{-1}$. In depth layers where these conditional averages diverge from the standard arithmetic average noise is dominating (fig.5.1a). Depth intervals, where dissipation rates are dominated by noise are indicated as dashed lines in averages for the inferred variables eddy diffusivities (K_ρ) and diapycnal heat fluxes (J_h) (fig.5.1b,c).

The average seasonal profiles of ϵ, K_ρ and J_h are calculated on a 4m depth grid including values from an interval of $\pm 3m$. All contributing profiles are previously resorted to the vertical coordinate $MLD + \Delta z$. The 95% confidence limits for e are than derived in every depth bin by a bootstrap method [*Efron*, 1979], separate day and night averaging before providing the final average is included in the bootstrap method.

The confidence limits for the eddy diffusivity K_ρ were derived performing Gaussian error propagation similar to the procedure described in *Ferrari and Polzin* [2005] via

$$C_{95}(K_\rho) = K_\rho [(\frac{\Delta\Gamma}{\Gamma})^2 + (\frac{C_{95}(\epsilon)}{\epsilon})^2 + (\frac{\Delta N^2}{N^2})^2]^{1/2} \tag{A.1}$$

and accordingly the confidence limits for the diapycnal heat flux J_h via

$$C_{95}(J_h) = J_h [(\frac{C_{95}(K_\rho)}{K_\rho})^2 + (\frac{\Delta\Theta_z}{\Theta_z}))^2]^{1/2} \tag{A.2}$$

as described in *Schafstall et al.* [2010], where Δ denotes the absolute uncertainties for the various average variables. $\Delta\Gamma$ is set to the constant value of 0.04 [*St Laurent and Schmitt*, 1999], $C_{95}(\epsilon)$ are the 95% confidence limits for ϵ derived via the bootstrap method and ΔN^2 as well $\Delta\Theta_z$ are the standard errors for N^2 and Θ_z (vertical temperature gradient) in a depth interval defined as the standard deviation divided by the square root of the number of measurements.

The confidence limits for the diapycnal heat flux out of the ML are shown in e.g. in fig.6.2 are derived via the same principle as described for the profiles, in this case all values falling between MLD+5 and MLD+15 are included. Note that these error estimates are solely statistical and do not include uncertainties due to measurement errors.

B. Submitted manuscript

Seasonal and regional variability of upper ocean diapycnal heat flux in the Atlantic Cold Tongue

Rebecca Hummels[1], Marcus Dengler[1], Bernard Bourlès[2]

[1] Leibniz-Institut für Meereswissenschaften (IFM-GEOMAR), Kiel, Germany
[2] IRD, LEGOS, CRHOB, Cotonou, Benin

Abstract SST variability within the Atlantic cold tongue (ACT) region is of climatic relevance for the surrounding continents. A multi cruise data set of microstructure observations is used to infer regional as well as seasonal variability of upper ocean mixing and diapycnal heat flux within the ACT region. The variability in mixing intensity is related to the variability in large scale background conditions, which were additionally observed during the cruises. The observations indicate fundamental differences in background conditions in terms of shear and stratification below the mixed layer (ML) for the western and eastern equatorial ACT region causing critical Froude numbers (Fr) to be more frequently observed in the western equatorial ACT. The distribution of critical Fr occurrence below the ML reflects the regional and seasonal variability of mixing intensity. Turbulent dissipation rates (ϵ) at the equator (2°N-2°S) are strongly increased in the upper thermocline compared to off-equatorial locations. In addition, e is elevated in the western equatorial ACT compared to the east from May to November, whereas boreal summer appears as the season of highest mixing intensities throughout the equatorial ACT region, coinciding with ACT development. Diapycnal heat fluxes at the base of the ML in the western equatorial ACT region inferred from ϵ and stratification range from a maximum of 90 Wm^{-2} in boreal summer to 55 Wm^{-2} in September and 40 Wm^{-2} in November. In the eastern equatorial ACT region maximum values of about 25 Wm^{-2} were estimated during boreal summer reducing to about 5 Wm^{-2} towards the end of the year. Outside the equatorial region, inferred diapycnal heat fluxes are comparably low rarely exceeding 10 Wm^{-2}. Integrating the obtained heat flux estimates in the ML heat budget at 10W on the equator accentuates the diapycnal heat flux as the largest ML cooling term during boreal summer and early autumn. Critical to the enhanced diapycnal heat flux in the western equatorial ACT region is elevated meridional velocity shear in the upper thermocline. It is thus suggested that TIWs are crucial contributors to mixing in the upper equatorial thermocline and to the development and maintenance of the ACT from boreal summer to mid-autumn.

1. Introduction

An important role of the oceans in our climate system is the transport and storage of heat. Oceanic regions of strong heat flux divergence are reflected in high net surface heat flux. The Atlantic cold tongue (ACT, Fig. B.1) represents one of the most intense regions of heat gain in the oceans [e.g. *Josey et al.*, 1999]. Inter annual variability of sea surface temperature (SST) in the ACT (Fig. B.1b) is strongly linked to variability of the Atlantic Marine Inter Tropical Convergence Zone (AMI) complex [e.g. *Kushnir et al.*, 2006; *Chang et al.*, 2006; *Brandt et al.*, 2011a]. Anomalies in position and intensity of the AMI on these time scales most notably impact variability of rainfall over northeast Brazil and the coastal regions surrounding the Gulf of Guinea. Furthermore, inter-annual ACT variability influences the onset and strength of the West African Monsoon [e.g. *Wagner and Silva*, 1994; *Marin et al.*, 2009; *Caniaux et al.*, 2011; *Brandt et al.*, 2011].

The ACT region itself exhibits a most striking seasonal SST cycle. From mid-May to mid-July SST decreases by about 6°C and stays at a cold level throughout September. In November it gradually recovers to warm levels reached towards the end of the year (Fig.B.1c). The strongest imprint of the seasonal SST cycle is centered around 10W [e.g. *Jouanno et al.*, 2011].

Up to now, the mechanisms driving the seasonal and inter-annual SST variability within the ACT region have not been fully revealed. Attempts to provide a complete description of the seasonal cycle of the mixed layer (ML) heat balance from observations have yet been unsuccessful in closing the heat budget. *Foltz et al.* [2003] obtained a residual heat gain of the ML of the order of 50 Wm^{-2} during boreal spring and early summer in the central basin (23°W), and of the order of 100 Wm^{-2} from late boreal spring to late autumn in the center of the ACT at 10W. Similar residual heat gains in the ACT region were obtained in a recent study, using ARGO floats, by *Wade et al.* [2011a]. High-resolution general ocean circulation models suggest that the ML heat content in the ACT region is mainly controlled by airsea heat exchange, vertical processes at the base of the ML, and lateral advection of heat due to Tropical Instability Waves (TIWs) [*Peter et al.*, 2006; *Jouanno et al.*, 2011]. TIWs result from instabilities of the equatorial currents [*Philander*, 1976]. Of the different vertical processes, turbulent diapycnal heat flux due to mechanical mixing in the stratified vertically-sheared equatorial current system was found to dominate mixed layer cooling [*Jouanno et al.*, 2011].

The importance of diapycnal mixing across the base of the ML and in the stratified water column for the ML heat budget in the equatorial Pacific and Atlantic oceans has long been recognized [e.g. *Gregg et al.*, 1985; *Chang*, 1994; *Wang and McPhaden*, 1999]. Results from several extensive observational programs in the equatorial Pacific and model studies have greatly improved understanding of mixing processes that are responsible for strong turbulence occurring in the upper equatorial thermocline [*Gregg et al.*, 1985; *Moum and Caldwell*, 1985; *Peters et al.*, 1988; *Moum et al.*, 1989; *Peters et al.*, 1994; *Lien et al.*, 1995; *Skyllingstad and Denbo*, 1995; *Wang and Müller*, 2002; *Moum et al.*, 2009]. Common to all studies is that the vertically-sheared background current system in the tropics, in particular the shear between the eastward Equatorial Undercurrent (EUC) and the surrounding westward flows is the main source of energy for turbulence production. Baroclinic inertial-gravity waves [*Peters et al.*, 1991], Kelvin waves [*Lien et al.*, 1995], and TIWs [e.g. *Moum et al.*, 2009] superimpose on the background current system and additionally add to vertical shear of horizontal velocity in the upper ocean, thereby nudging the flow towards Kelvin-Helmholtz instability.

Within the zones of high vertical shear, strong bursts of turbulence occur that sometimes extend down from the surface mixed layer well into the upper thermocline particularly during night time [e.g. *Gregg et al.*, 1985]. Repeated microstructure measurement programs were carried out in the central equatorial Pacific at 140°W in the western flank of the cold tongue [*Peters et al.*, 1988; *Moum et al.*, 1989; *Peters et al.*, 1994; *Lien et al.*, 1995; *Moum et al.*, 2009]. They revealed that these bursts, termed deep-cycle turbulence due to their daily cycle, extend several tens of meters below the base of the surface mixed layer and last for a few hours. Asso-
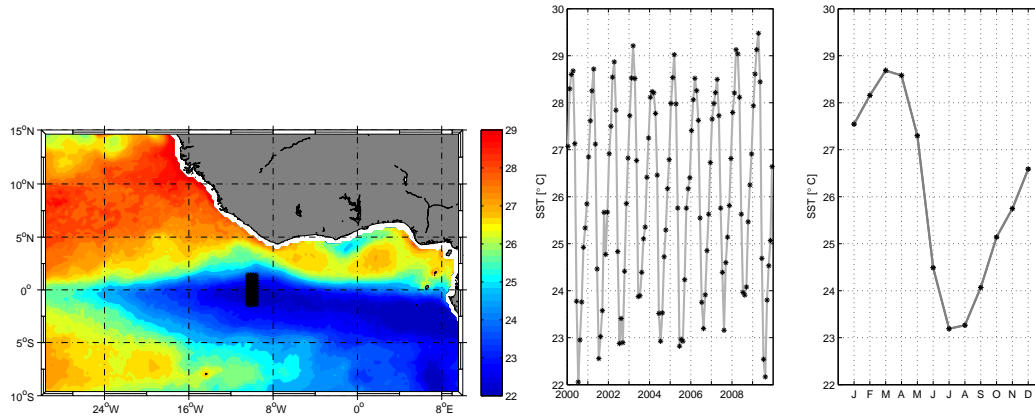
Figure B.1.: Satellite-SST distribution during July 2001 showing the spatial extent of the equatorial cold tongue (Black stars mark area of averaging for Fig. 1b and 1c), b) Monthly SST averages for the box marked in a) showing year-to-year variability at 10°W,0°N from 2000-2009, c) average (2000-2009) seasonal evolution of SST.

ciated dissipation rates of turbulent kinetic energy within these bursts are strongly elevated and in the range of 1-10·$10^{-6} Wkg^{-1}$. Diapycnal heat flux determined from microstructure data averaged over several days to weeks was found to be in the order of 40 Wm^{-2} to 100 Wm^{-2} when deep-cycle turbulence was present [*Peters et al.*, 1988; *Moum et al.*, 1989; *Lien et al.*, 1995]. During those periods night time heat fluxes usually exceed day time heat fluxes by more than an order of magnitude [e.g. *Peters et al.*, 1988]. When deep-cycle turbulence was weak or absent, average diapycnal heat flux reduced to 10 Wm^{-2} to 30 Wm^{-2} [*Peters et al.*, 1994; *Lien et al.*, 1995]. The observed variability in strength of deep-cycle turbulence or its absence is attributed to variable background conditions of shear and stratification, and to a lesser extent to variable surface winds and net surface heat flux. High resolution models additionally suggest that the location of elevated shear in the water column is important for the occurrence of the strong turbulent bursts across and below the mixed layer [*Wang and Müller*, 2002].

Most recent turbulence observations from the central equatorial Pacific using microstructure probes [*Moum et al.*, 2009] and a Lagrangian float [*Lien et al.*, 2008] revealed a deep-reaching and strongly elevated deep-diurnal cycle and related vigorous mixing in the upper equatorial thermocline occurring in the presence of a TIW. Average diapycnal heat fluxes of 200 and 400 Wm^{-2} were estimated from those measurements over a period of 7 and 15 days respectively. *Moum et al.* [2009] suggested two factors responsible for the enhanced turbulence: additional shear due to the meridional velocity of the TIW above the EUC core and a near doubling of the kinetic energy in the equatorial region due to the presence of the wave. These observations support earlier model results by *Menkes et al.* [2006] and *Jochum and Murtugudde* [2006], which suggested that the warming of the cold tongue due to lateral heat flux by TIWs is nearly compensated by increased diapycnal heat flux during the presence of the TIW at the equator.

In the Atlantic, elevated mixing levels in the upper shear zone of the EUC have also been observed [*Crawford and Osborn*, 1979]. However, a detailed investigation of the seasonal variability of mixing processes and diapycnal heat fluxes has not been performed in the cold tongue regions of either ocean. In this study we investigate the contribution of diapycnal heat flux to the ML layer heat budget of the ACT. In contrast to former process-oriented studies in the equatorial Pacific, integral estimates of mixing parameters representative for different seasons and regions in the eastern tropical Atlantic are provided. Using observed background parameters, processes involved in shaping mixing intensity for the different seasons and regions are

identified.

The study was carried out within the frame work of CLIVARs Tropical Atlantic Climate Experiment (TACE) which aims at advancing understanding of coupled ocean-atmosphere processes and improving climate prediction for the Tropical Atlantic region. Currently, the ACT is still ill represented in coupled climate models as the sea surface temperature in this region is biased warm in the models [*Richter and Xie*, 2008] hampering predictive skills, in particular for intra seasonal precipitation forecasting. Apart from advancing understanding of a key processes that control SST in the ACT, the results presented below may be used as guidance to constrain mixing parametrizations in the coupled climate models as has previously been attempted [e.g. *Jungclaus et al.*, 2006].

The data set used for this study consists of microstructure shear and temperature profiles as well as larger scale velocity data and hydrography from a multi-cruise program carried out predominately between 2005 and 2008 in different seasons and regions of the central and eastern equatorial Atlantic (section 2). In section 3, the observed seasonal and regional differences in background conditions are discussed. These background conditions are related to the variability of dissipation rates of turbulent kinetic energy and turbulent eddy diffusivities in section 4. Finally, seasonal and regional variability of diapycnal heat fluxes are discussed and their contribution to the heat budget of the ML is assessed by estimating individual terms of the budget in the center of the cold tongue in section 5. We conclude with a summary and discussion in Section 6.

2. Data and Methods

Data sets consisting of a suite of shipboard observations from a multi-cruise program, buoy data from the Prediction and Research moored Array in the Tropical Atlantic [PIRATA; *Bourlès et al.*, 2008] ATLAS buoy network, satellite derived products and surface velocity climatologies are used.

2.1 Shipboard Observations

The shipboard observations were collected on eight cruises to the ACT region and the eastern equatorial Atlantic (Tab. B.1). Five of these cruises (EGEE2 to EGEE6) were carried out in the scientific framework of the French EGEE project ("Etude de la circulation océanique et des échanges océan-atmosphère dans le Golfe de Guinée") that was the oceanic component of AMMA [African Monsoon Multidisciplinary Analysis; refer to *Redelsperger et al.*, 2006] and were conducted from Cotonou, Benin between 2005 and 2007 [*Bourlès et al.*, 2007]. Two cruises (EGEE3 and EGEE5) were scheduled to coincide with the West African Monsoon onset and the development of ACT in boreal spring and early summer (end of May to July), while another two cruises (EGEE2 and EGEE6) were carried out during the mature phase of the monsoon (September-October), when the cold tongue is still well developed. Finally, one cruise (EGEE4) was conducted in the second half of November while the cold tongue was disintegrated.

Several meridional transects were repeatedly occupied during the EGEE cruises. A primary focus was given to a section along 10°W that had been occupied previously during several other programs and by PIRATA service cruises and to a section along 3°E (Fig. B.2). In addition, data sets from two cruises to the western part of the ACT carried out in June 2006 and March 2008 were available. These cruises were part of the Verbundprojekt Nordatlantik focusing on tropical climate variability. The measurement program was conducted on a meridional section along 23°W and the 10°W section was additionally occupied during the June 2006 cruise. Furthermore, a station program was carried out on two zonal sections along the equator and along 2°N between 23°W and 10°W (Fig. B.2). Finally, data from a cruise by N/O Le Noroit (December 1994) was also analyzed that was collected in the regions about and between the Romanche (RFZ) and Chain Fracture Zones. Specifically, two cross-equatorial sections from 1°N to 0.75°S at about 13°W are used (Fig. B.2).

The cruise data presented here is a subset of the above observational programs and consists of microstructure shear and temperature profiles using loosely-tethered or free-fall instruments, conductivity-temperature-depth (CTD) profiles and near-continuously sampled profiles of upper-ocean horizontal velocity recorded with the vessel-mounted acoustic Doppler current profilers
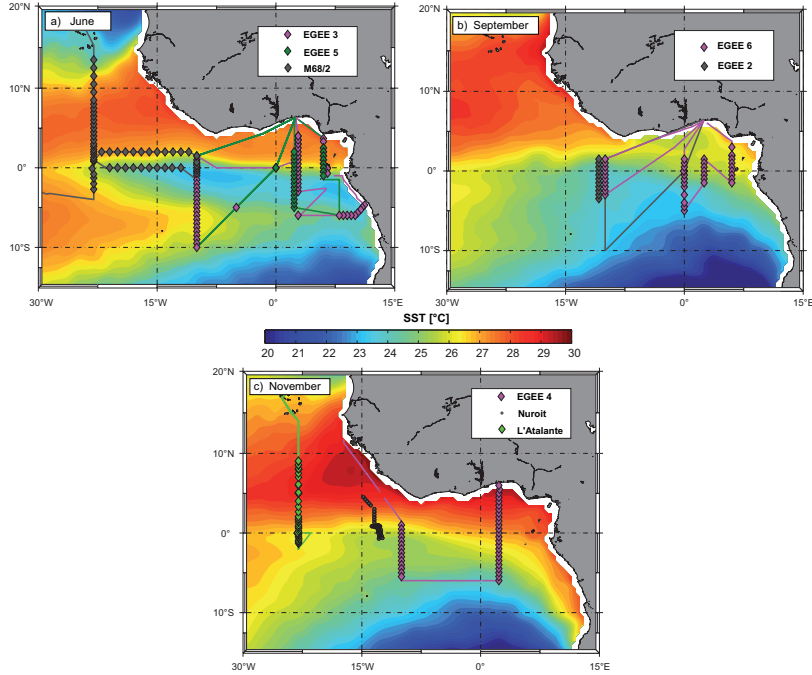
Figure B.2.: Cruise tracks and SST during different cruise seasons (upper left: June; upper right: September; lower: November). Monthly SSTs are averaged over years 2005-2007 and diamonds mark positions of microstructure stations.

(vmADCP). Microstructure data was collected using different microstructure profilers (MSS90L and MSS90D) manufactured by Sea&Sun Technology in cooperation with ISW-Wassermesstechnik. All profilers were equipped with two shear sensors (airfoil), a fast temperature sensor (FP07), an acceleration sensor, tilt sensors and standard CTD sensors. For a detailed description of the instruments the reader is referred to *Prandke and Stips* [1998]. The profilers were adjusted to descent at 0.5-0.6 ms^{-1}. Noise levels of turbulent dissipation rates from the microstructure profilers are better than $1 \cdot 10^{-9} W kg^{-1}$ for the MSS90L and better than $5 \cdot 10^{-10} W kg^{-1}$ for MSS90D [*Prandke and Stips*, 1998; *Schafstall et al.*, 2010]. During the cruise in December 1994, microstructure data was acquired with the High Resolution Profiler [HRP, *Schmitt et al.*, 1988] a free-falling internally recording instrument. The HRP samples velocity shear with two airfoil probes and temperature microstructure, as well measuring finescale temperature, conductivity and horizontal velocity. Dissipation noise levels from this instrument are of order $1 \cdot 10^{-11} W kg^{-1}$ [see *Polzin and Montgomery*, 1996].

In addition to the microstructure measurements separately acquired CTD profiles were routinely measured at each station using a Seabird 911 system attached to a rosette of 12 (N/O L'Antea) or 24 (on all other vessels) Niskin bottles. Water samples were used for calibration purposes as well as for analysis of biogeochemical parameters including nutrients. Water samples for calibration of the Seabird conductivity sensors were analyzed on board using Guildline salinometers. Final accuracy of salinity derived from CTD measurements was in general better than 0.003. On all but the December 1995 cruise, continuous velocity data were recorded by vmADCPs. The systems and configurations used during the individual cruises differed. The frequency of the ADCP was either 150 kHz (N/O Le Suroit) or 75 kHz on all other vessels. N/O LAtalante was additionally equipped with a 300 kHz ADCP and FS Meteor had an additional 38kHz ADCP installed that were simultaneously collecting data on both vessels. Bin sizes also varied between 4 m (300kH L'Atalante) and 8 m for all other ADCPs. Standard techniques [e.g. *Fischer et al.*, 2003] were used during data post-processing.

2.2 Other data

In addition to the shipboard observations described above, vmADCP and CTD data from 7 PIRATA service cruises along the 10°W section are used. These data that have been collected between 10°S and 1.5°N from 1999 to 2009 during different seasons of the year are used to describe the background conditions for mixing processes. They were obtained from the PIRATA web site at (www.ifremer.fr/ird/pirata/pirata_cruises.php). The velocity and hydrographic sections are described and analyzed in detail by *Kolodziejczyk et al.* [2009].

For the calculation of individual terms of the mixed layer heat budget at 10°W, SST, incoming solar radiation, subsurface temperature profiles, air temperature, relative humidity, wind speed and rainfall from the PIRATA mooring at 0°N, 10°W were used (1997-2009). Near-surface velocities are constructed with the YoMaHa'07 [*Lebedev et al.*, 2007] data set, where surface velocities are obtained from the ARGO float surface trajectories. Long wave radiation is taken from the *da Silva et al.* [1994] surface marine atlas. Finally, averaged mixed layer depth of the mixed layer climatology of *de Boyer Motegut et al.* [2004] and SST of the climatology of *Reynolds and Smith* [1994] were used.

For determining seasonal cycles of SST and wind stress, satellite products are used. SST distributions were obtained from microwave sensors aboard the Tropical Rainfall Measuring Mission satellite. 3-day or monthly average distributions were taken from www.ssmi.com/tmi/. Wind stress data were obtained from the Seawinds scatterometer onboard the Quickscat satellite of the NASA. Here, the CERSAT product was chosen (www.cersat.ifremer.fr). Additional information about the seasonal variability of the net surface heat fluxes are taken from the *da Silva et al.* [1994] surface marine atlas and surface velocities are described with the drifter climatology of *Lumpkin and Garaffo* [2005].

2.3 Sampling Strategy

In this study the regional and seasonal variability of turbulent mixing in the ACT region is investigated. Thus in contrast to previous microstructure measurement programs in the equatorial Pacific that often sampled at a single location for a period of several days to several weeks [e.g. *Moum et al.*, 1989; *Peters et al.*, 1988; *Lien et al.*, 1995; *Moum et al.*, 2009], the sampling strategy pursued here was to profile at several locations during a single cruise. This was accomplished by integrating microstructure profiling into the CTD station program during all cruises except for the 1994 cruise (Tab. B.1). At least 3 but up to 20 microstructure profiles were collected at a single station from the surface to between 150m and 300m depth. In addition several stations were occupied for 24 hours or longer while microstructure data was collected continuously, in particular during boreal summer 2006 (Tab. B.1). In total, 783 profiles were collected on 224 stations (Tab. B.1) from the surface to between 150 and 250m depth.

2.4 Microstructure data processing

Dissipation rates of turbulent kinetic energy (ϵ) were determined from the airfoil shear data recorded at the sampling rate of 1024 Hz via the variance method. Shear wavenumber spectra are integrated assuming isotropic turbulence:

$$\epsilon = 7.5\nu \int_{k_{min}}^{k_{max}} E_{du'/dz}(k)dk, \qquad \text{(B.1)}$$

ν being the dynamic viscosity of seawater. Shear spectra $E_{du'/dz}$ were calculated from one-second ensembles (1024 values) corresponding to a vertical interval of 0.5-0.6m and integrated between a lower = 3 cpm and an upper wavenumber, which varied between 14 cpm and 30 cpm depending on the Kolmogorow wavenumber. Unresolved shear variance due to the limit wavenumber band used in the integration was accounted for by fitting the shear spectra to the universal Nasmyth spectrum using the function provided by *Wolk et al.* [2002]. Additionally, corrections for the loss of variance due to finite sensor tip of the air foil probes were applied. For further details on the processing algorithm see *Schafstall et al.* [2010].

Turbulent eddy diffusivities for mass were estimated from dissipation rates of turbulent kinetic energy (ϵ) using the dissipation method of *Osborn* [1980]: $K_\rho = \Gamma \epsilon N^{-2}$. Here, Γ is mixing efficiency and N^2 buoyancy frequency. Energy arguments require $\Gamma = 0.2$ [*Osborn*, 1980], which is commonly used [e.g. *Peters et al.*, 1988; *Lien et al.*, 2008; *Moum*

Schedule	Vessel and cruise ID	Sections	Number of Stations	Number of Profiles
11/20/-12/06/1994	N/O Le Nuroit[1]	13°W	15	15
09/02/-09/19/2005	N/O Le Suroit EGEE2	10°W	8	25
05/29-06/22/2006	N/O L'Atalante EGEE3	10°W (eq/s)	15/6	45/18
		2°E(eq/s)	8/2	43/12
		6°E	5	15
		24h10°W0°N	8	24
		24h10°W6°S	8	23
		24h10°W10°S	8	24
		other	19	101
06/09-07/08/2006	FS Meteor M68/2	23°W	8	39
		10°W	7	21
		0°N	11	32
		2°N	13	40
11/17-12/02/2006	N/O L'Antea EGEE4	10°W(eq/s)	7/5	21/15
		2°E(eq/s)	8/5	24/15
06/07-06/14/2007	N/O L'Antea EGEE5	2°E	8	24
		6°E	6	17
09/03-09/24/2007	N/O L'Antea EGEE6	10°W(eq/s)	8/2	24/6
		0°E(eq/s)	9/4	29/8
		2°E	7	21
		6°E	7	21
02/26-03/10/2008	N/O L'Antea IFMGEOMAR 4	23°W	16	78
			$\sum$224	$\sum$ 783

Table B.1.: Spatial and temporal distribution of microstructure profiles available to this study. Usually at least three microstructure casts were collected at each station. Numbers separated by slashes separate number of stations and profiles collected within 2° of the equator (eq) and number of profiles collected south of 2°S (s) along the respective sections. Each of those ensembles was used to infer diapycnal heat fluxes (see section ?).

[1] Microstructure data was collected with the high resolution profiler [*Schmitt et al.*, 1988] and only one profile was sampled at each station.

et al., 2009, etc.]. More recent numerical simulations *Smyth et al.* [2001] showed that Γ can sometimes exceed 0.2 dependent on the evolutionary stage of a turbulent overturn. *Shih et al.* [2005] found in their numerical study a dependence of Γ on the turbulent activity parameter $I = \epsilon/(\nu N^2)$. For an intermediate turbulent regime characterized by 7<I<100, they find Γ=0.2 the best estimate, which holds for more than 65% of the data set in use. Thus here, Γ is set to the constant value of 0.2 that additionally facilitates comparison of the results to previous studies [e.g. *Moum et al.*, 1989; *Lien et al.*, 2008; *Moum et al.*, 2009].

Buoyancy frequency was calculated from least squared fits to salinity and temperature using a depth interval of up to 30m or less close to the mixed layer to avoid biases in stratification. Estimates of the diapycnal heat flux ($J_h = -\rho c_p K_H \frac{\partial T}{\partial z}$, where ρ, c_p and T are the density, heat capacity and temperature of sea water respectively) requires information about the eddy diffusivity of heat K_H. By examining the transport equation of temperature variances, *Osborn and Cox* [1972] related K_H to the dissipation rate of temperature variance χ. Microscale scale temperature gradients can be mea-

sured with fast thermistors such as an FP07 and are used to determine χ. However, processing of the small scale temperature gradient inhibits several uncertainties due to e.g. the universal functional form of the temperature variance spectrum used to correct for unresolved variance (Batchelor or Kraichnan), the functional form of the thermistor response (proposed are single [*Lueck and Mudge*, 1997] or double pole [*Gregg and Meagher*, 1980] filter), and an often unknown response time of the thermistor. The latter has been found to depend on the profiler velocity [e.g. *Gregg and Meagher*, 1980], and on the thickness of the glass coating [*Nash and Moum*, 2002] that varies for each individual sensor and which is thought to be more significant [*Nash et al.*, 1999]. We implemented an algorithm estimating the individual response time, which failed to give a consistent result due to the other various uncertainties. In addition, at high profiler speeds of 0.6 ms^{-1}, only about 10% of the variance of the temperature gradient can be actually resolved for values of $\chi > 1 \cdot 10^{-6} K^2 s^{-1}$, which has been noted previously [*Nash et al.*, 1999; *Gregg*, 1999]. The sum of uncertainties challenges the belief in reliable estimates of χ in this configuration. In regions, where

stratification is dominated by temperature, which is highly accurate within the equatorial thermocline, K_H should equal K_ρ [e.g. *Peters et al.*, 1988]. In the following the diapycnal heat flux is therefore calculated via $J_h = -\rho c_p K_\rho \frac{\partial T}{\partial z}$.

This study focuses on heat fluxes out of the mixed layer which requires accurately resolving these fluxes in the transition zone between the base of the mixed layer and the stratified region below. Profiles of the diapycnal heat flux are highly divergent in the vertical, showing maximum values at the base of the mixed layer and, rapidly decrease below [e.g. *Lien et al.*, 2008]. Hence, the amount of heat being extracted from the ML into the interior ocean is characterized by the diapycnal heat flux in a rather narrow layer. In order to compare these values, the diapycnal heat fluxes in the interval ML depth +5m to ML depth +15m are averaged, insuring values from within the ML to be excluded. The ML depth was generally calculated using the temperature threshold criterion with $dT = 0.2°C$, although inspection of the individual temperature profiles led to corrections in some cases.

2.5 Heat budget calculations

To assess the relative importance of the diapycnal heat fluxes on the ML heat budget, the individual terms of the budget are estimated. The heat balance equation for the ML can be expressed as

$$h\frac{\partial T}{\partial t} + h(\mathbf{v}\cdot\nabla T + \overline{\mathbf{v'}\cdot\nabla T'}) + (T-T_{-h})w_{entrain} = \frac{q_{net}-q_{-h}}{\rho c_p}$$
(B.2)

where h represents the MLD, $\mathbf{v}$ and T are the velocity and temperature averaged from the surface until the depth h, whereas $\mathbf{v'}$ and T' are the deviations from the time mean, q_{net} stands for the net surface heat flux and q_{-h} for the net heat loss of the mixed layer. Here, q_{-h} is determined from the combination of the penetrative shortwave radiation and the diapycnal heat flux at the base of the ML [according to *Foltz et al.*, 2003]. The terms represent from left to right local heat storage, horizontal advection (divided into a mean and eddy term), entrainment and the combination of net atmospheric heating and vertical turbulent diffusion at the base of the ML. Advective contributions due to baroclinic currents and temperature gradients in the mixed layer

(the vertical temperature/velocity covariance) were neglected as they were found to be small [*Swenson and Hansen*, 1999]. The evaluation of the individual terms closely follows the procedures described by *Foltz et al.* [2003]. Seasonal cycles of different variables are obtained from daily PIRATA data, averaged on every given day of the year and subsequently formed to a monthly average. The penetrative fraction of the shortwave radiation dependent on the MLD and the optical transparency of water is calculated via a simple e-folding decay following *Wang and McPhaden* [1999] leaving the shortwave radiation absorbed in the ML to be estimated as $Q_{abs} = (1 - 0.45e^{-h/25m})$. Latent and sensible heat fluxes are obtained with the COARE algorithm [*Fairall et al.*, 2003]. Horizontal advection is determined by multiplying the monthly velocities (YoMaHa07) with climatological long term SST gradients [*Reynolds and Smith*, 1994]. The eddy term of horizontal advection is estimated indirectly via the residual between horizontal advection and horizontal advection estimated as $h(\mathbf{v}\cdot\nabla T) = h(\frac{dT}{dt} - \frac{\partial T}{\partial t})$ [*Swenson and Hansen*, 1999]. The total time derivative is obtained from drifter SSTs [*Lumpkin and Garaffo*, 2005], whereas the local derivative is estimated from the climatological SST [*Reynolds and Smith*, 1994]. The entrainment velocity can be expressed as $w_{entrain} = \frac{\partial h}{\partial t} + \nabla \cdot h\mathbf{v}$ [*Stevenson and Niiler*, 1983] estimating the local time derivative of the MLD from PIRATA temperatures and the divergence term by combining the mixed layer climatology with the surface velocities.

3. Background conditions

The circulation in the upper tropical Atlantic consists of energetic surface and subsurface zonal currents. Within the region of the ACT surface westward flow associated with the South Equatorial Current (SEC) occurs in two current branches. The northern SEC (nSEC) is located between the equator and 4°N while the central SEC (cSEC) is situated between 6°S and 2°S (Fig. B.3a) [e.g. *Molinari*, 1982; *Kolodziejczyk et al.*, 2009; *Brandt et al.*, 2010]. Between the westward flows, the eastwards EUC can be found between 2°S and 2°N with maximum velocities of $1 ms^{-1}$ in the upper stratified ocean between 4°S and about 2°N (Fig. B.3b) su-
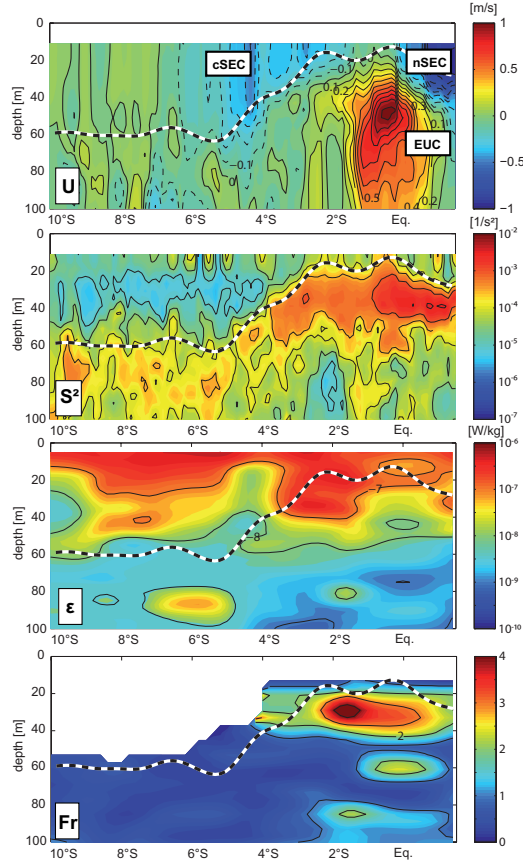
Figure B.3.: a) Zonal velocity, b) shear, c) turbulent dissipation rate ϵ and d) Fr numbers along 10°W during EGEE3 (June 2006). The black and white line denotes MLD.

staining elevated mixing levels (Fig. B.3c). Hence, elevated shear levels and enhanced mixing levels in the ACT region below the ML are not only confined to the equator but are pronounced within a wider latitudinal extent ranging from about 4°S to 2°N.

In the following, the regional as well as seasonal variability of large scale background conditions such as surface forcing, the current system, the MLDs shear, and stratification representative for the ACT region are discussed.

3.1 Net surface heat flux and winds

As pointed out in the introduction the tropical Atlantic is characterized by positive net surface heat fluxes throughout the year ranging from 20-150 Wm^{-2} between 2°N and 2°S (Fig. B.4a). The seasonal variability in the net surface heat flux is caused by variations in the incoming shortwave radiation and the latent heat flux, while the sensible and outgoing long wave heat fluxes remain rather constant throughout the year. In the central basin (30°W-

5°W) net surface heat flux is dominated by a semi-annual cycle with a first peak in February/March and a second occurring from July to September. As discussed previously [e.g. *Marin et al.*, 2009], this second peak, caused by a reduction of the latent heat flux due to decreasing surface winds, acts against the development of the cold tongue by warming the upper ocean at a rate of 100-120 Wm^{-2}. The net heat flux in the eastern part of the ACT (east of 5°W) strongly differs in amplitude and variability compared to the western one. Here, net surface heat fluxes are reduced and between 20 and 90 Wm^{-2} and exhibit a minimum from May to August. This minimum is due to reduced short wave radiation and increased latent heat flux.

The general atmospheric circulation is dominated by the easterly trade winds surrounding the ITCZ, which shifts meridionally during the year imprinting a semiannual cycle on the wind stress within the equatorial band (Fig. B.4b). Resulting magnitu-
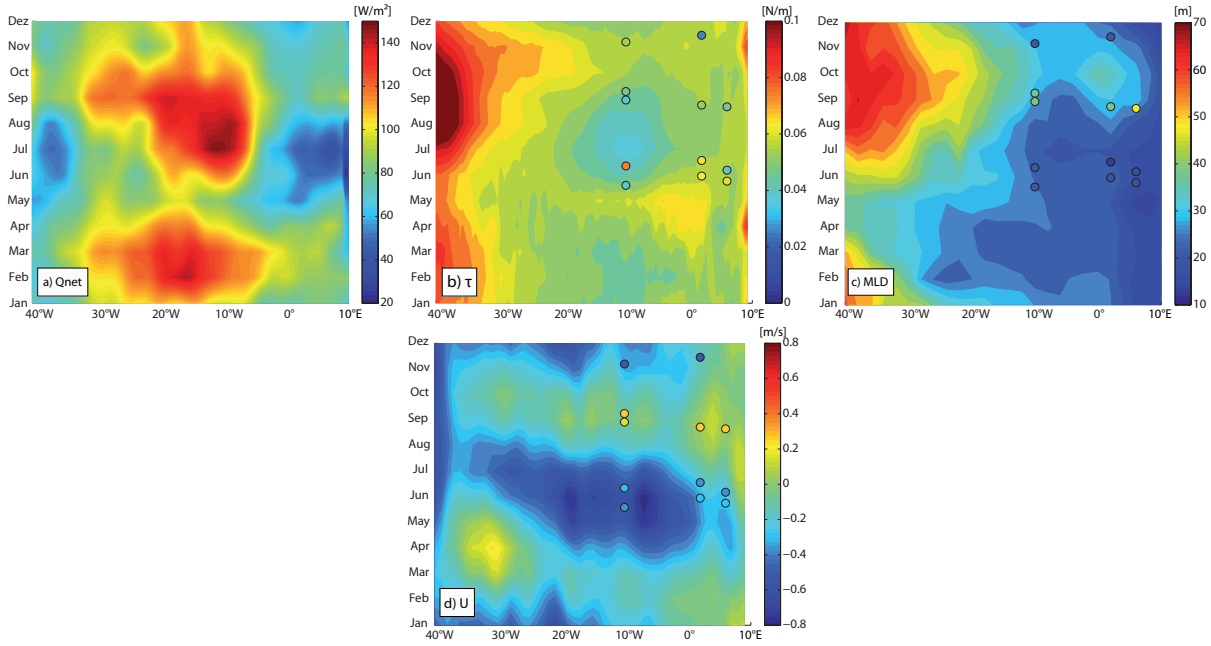
Figure B.4.: Seasonal evolution of large scale parameters in the Atlantic averaged over 2°N-2°S: a) net surface heat flux [*da Silva et al.*, 1994], b) windstress (Quickscat), c) mixed layer depth [*de Boyer Motegut et al.*, 2004], d) zonal surface velocities [*Lumpkin and Garaffo*, 2005]. In circles section averaged observations from the cruises are shown for comparison.
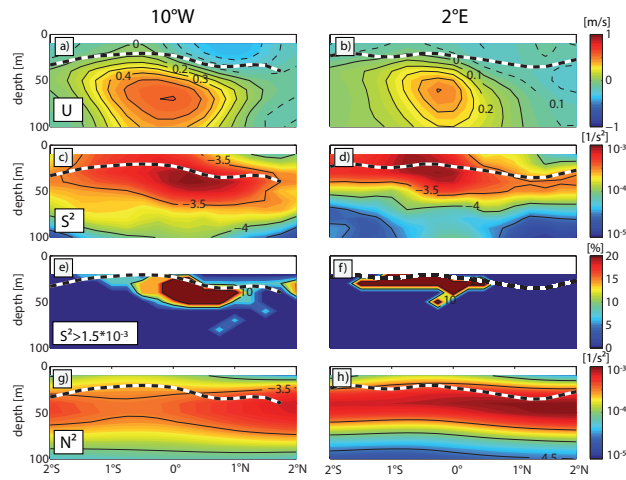

Figure B.5.: Mean sections of zonal velocity (a,b), shear (c,d), percentage of shear exceeding $1.5 \cdot 10^{-3} s^{-2}$ (e,f), and stratification (g,h) along 10°W (1st column) and 2°E (2nd column). The average section at 10°W is compiled from 13 cruises, whereas the 2°E average was compiled from 4 cruises (Tab. B.1). The black and white line denotes average MLDs.

de and phase of this semiannual cycle vary throug-   hout the basin. In the central basin wind stress in-

tensifications are found in April/May and in October/November. The latter wind stress maximum has been reported to cause a second cooling of the ACT in late autumn [*Okumura and Xie*, 2006, Fig. 1b]. Superimposed on this seasonal variability are intra-seasonal wind bursts, which can elevate the wind stress locally and contribute to temporal variability of cold tongue development [*Marin et al.*, 2009]. *Yu et al.* [2011] find spectral peaks in zonal as well as meridional winds at intra-seasonal periods, among which the 40-60-day peak is evident across most of the equatorial basin.

3.2 Mixed layer depth

In general, MLDs are shallower in the eastern equatorial Atlantic than in the west. This zonal MLD gradient is most pronounced between 40°W and 10°W during boreal summer and autumn. East of 20°W from about 2°N to 4°S (Fig. B.3a) and within the Gulf of Guinea, MLDs of only 10-30m are present throughout most of the year. Within the equatorial belt (2°N-2°S) a seasonal cycle in the magnitude of the MLDs is observed with maximum values occurring in autumn. During this period, mixed layers of 40m were reported for 0°,10°W [*Foltz et al.*, 2003], while climatologies suggest MLs to be slightly shallower (Fig. B.4c, *de Boyer Motegut et al.* [2004]).

3.3 Currents and variability

Surface flow

The variability associated with the wind driven SEC is strongest in the central basin, extending until about 0°E into the Gulf of Guinea [*Lumpkin and Garaffo*, 2005] with maximum westward velocities of up to 0.8 ms^{-1}. The seasonal variation corresponds to the semi-annual variation in the wind stress: A strong SEC in boreal spring/summer accelerated shortly after the trade wind intensification in April/May and a reduced SEC in autumn after the relaxation of the wind stress (Fig. B.4). The second increase in wind stress in late autumn is weaker and accordingly, the second SEC maximum, as first reported by *Richardson and McKee* [1984] is reduced in comparison to the boreal summer maximum.

Subsurface

A well-known feature of the subsurface flow is the weakening and shoaling of the EUC from west to east [*Stramma and Schott*, 1999; *Bourlès et al.*, 2002; *Kolodziejczyk et al.*, 2009; *Brandt et al.*, 2011]. In the center of the basin at 23°W, the EUC is still rather strong, and exhibits velocities above 0.8ms^{-1} at its core [*Brandt et al.*, 2011]. In the Gulf of Guinea, however, zonal velocities associated with the EUC are reduced and reach 0.6ms^{-1} at 10°W (Fig. B.5a) [*Kolodziejczyk et al.*, 2009; *Brandt et al.*, 2011]. Maximum eastward velocity of the EUC at 2°E (Fig. B.5b), compiled from four EGEE cruises (3-6, Tab. B.1), is only about 0.5ms^{-1} and its meridional extent is much reduced being confined to between 1°N and 1°S. In addition, the vertical extent of the EUC also diminishes towards the east. In the eastern Gulf of Guinea (6°E), the EUC appears to be a transient feature: During August 2000 an eastward subsurface current was not present between 2°N and 2°S [*Bourlès et al.*, 2002]. Additionally, the depth of the EUC core is modulated seasonally, deepening in autumn in accordance with the MLD and thermocline movements. However, the EUC strength in terms of maximum velocities does not seem to follow a distinct seasonal cycle [*Arhan et al.*, 2006; *Brandt et al.*, 2008; *Kolodziejczyk et al.*, 2009].

Intra-seasonal variations

In addition to seasonal variability of the current system, intra-seasonal equatorial waves are known to impact variability of the equatorial circulation. *Düing et al.* [1975] were the first to report that the tropical Atlantic Ocean is traversed by baroclinic intra-seasonal waves, e.g. TIWs. On the equator, these waves have typical periods of 20-40 days and zonal wave lengths of 600-1200 km. They are most active in boreal summer and fall [e.g. *von Schuckmann et al.*, 2008] and have been observed in the western and central equatorial Atlantic [*Athie and Marin*, 2008]. Accordingly, at least the western part of the Atlantic cold tongue is subject to intra-seasonal variability of the velocity field induced by TIWs. On the equator, TIWs are associated with elevated meridional velocities of up to 1 ms^{-1} (Fig. B.6b) [e.g. *Weisberg and Weingartner*, 1988]. Shipboard ADCP sections from 10°W indicate that in the center of the cold tongue they are characterized by highly baroclinic velocity structures. Typically, meridional velocities are most pronounced just below the mi-
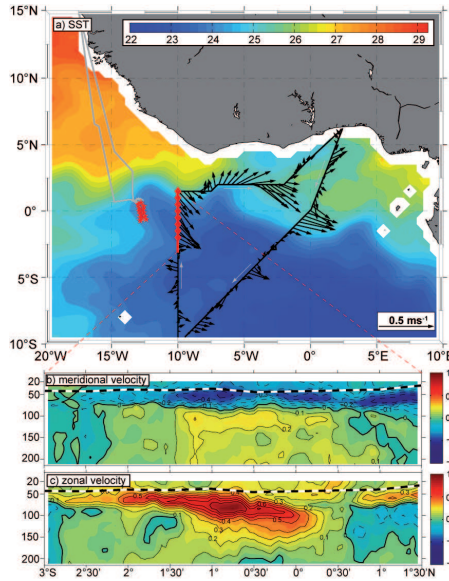
Figure B.6.: Example of the impact of intra-seasonal fluctuations on a) SST, b) meridional velocity, c) zonal velocity as observed during EGEE2 (September 2005) along 10°W.

xed layer at 50-60m depth (Fig. B.6b), while below the EUC core, meridional velocities change sign and weaken. Similar baroclinic structures of TIWs have also been observed in the equatorial Pacific [e.g *Kennan and Flament*, 2000; *Moum et al.*, 2009].

In the Gulf of Guinea east of 10°W [*Athie and Marin*, 2008] reported the dominance of intra-seasonal signals with periods of 10-20 days which they interpreted as equatorially mixed-Rossby-gravity waves having large zonal scales and no apparent zonal propagation.

3.4 Background shear and stratification
Shear

Shipboard ADCP sections indicate average shear variance $S^2 = (\partial U/\partial z)^2 + (\partial V/\partial z)^2$ to be elevated in the equatorial region from 2°N to 2°S (Fig. B.3b, Fig. B.5c,d). Highest shear levels are found between the surface ML and the core of the EUC which is located at 80m at 10°W and 23°W and at about 60m at 2°E. Thus, due to the shoaling of EUC from west to east, the region of elevated shear levels diminishes in depth extent accordingly (Fig. B.5c, d). Regardless of the reduction of EUC strength and the simultaneous weakening of the westward surface flow towards the east, average shear levels are of similar magnitude at 10°W and 2°E and elevated levels of shear variance ($> 1.5 \cdot 10^{-3} s^{-2}$) are frequently

observed at both locations. However, upper-ocean shear levels determined from moored ADCPs from the equator at 23°W and 10°W indicate a lower shear variance above the EUC core at 23°W compared to 10°W [*Jouanno et al.*, 2011].

In addition to spatial variability, there is pronounced seasonal variability of shear in the upper water column. A climatological seasonal cycle of shear variance averaged from 2°N to 2°S along 10°W was constructed from 13 shipboard ADCP sections (Fig. B.7a). Here, only ADCP data recorded using 8m bin sizes were used and shear variances were calculated from vertical derivatives of hourly-averaged horizontal velocities. Shear variance is highest in boreal spring and early summer, reducing in September during the ceasing of the westward surface velocities and whiles the EUC core is deepening. In November shear levels again intensify.

Separating contributions of zonal and meridional shear indicates that zonal shear (Fig. B.7b) is strongest during March to August, when the SEC shows its maximum velocities. The second SEC intensification in November/December is also reflected in a re-enhancement of zonal shear. Meridional shear shows maximum values in boreal summer and autumn (Fig. B.7c). During this time period, TIWs are pronounced in the equatorial band and inspec-
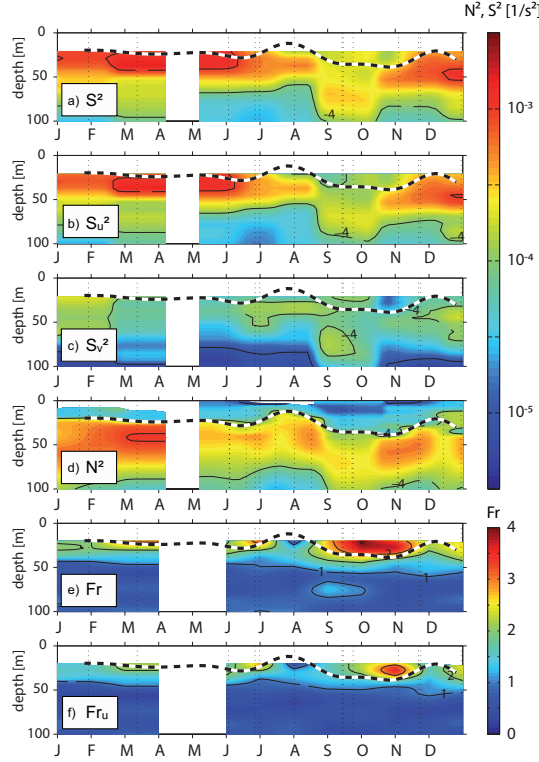
Figure B.7.: Seasonal evolution of section averaged shear (a) and its zonal (b) as well as meridional (c) component, stratification (d) and Froude number (e,f) constructed from available PIRATA cruise data along 10°W between 2°S and 2°N. The different shear sections arise from $S^2 = (du/dz)^2 + (dv/dz)^2$ and $S_u^2 = (du/dz)^2$ as well as accordingly $Fr = S^2/N^2$ and $Fr_u = S_u^2/N^2$.

tions of the individual velocity sections in combination with satellite SST data (e.g. Fig. B.6) indicate that meridional velocity shear is dominated by contributions of these waves. In autumn and between 2°N and 2°S, meridional shear variance $(\partial V/\partial z)^2$ contributes about 33% to total shear variance S^2 while in boreal summer it contributes about 25%. However, profile velocity time series from directly on the equator (not shown) suggest lower contributions of meridional shear: about 20% during boreal autumn and 12% during summer. This suggests that TIWs enhance shear levels throughout the region between 2°N and 2°S, but their relative contributions to S^2 directly at the equator is reduced. Regional and seasonal variability of shear variance in the layer right below the surface ML (Fig. B.8a) is more pronounced than in the deeper regions. Shear levels at 10°W and 2°E are of similar magnitude and reduced in boreal autumn compared to summer. At 6°E, the vessel mounted velocity data from

3 cruises indicate strongly reduced shear levels. It should be noted that enhanced shear variance below the ML is not only associated with the EUC but that elevated levels are also found poleward of the EUC region, particularly north of the equator in the vicinity of the nSEC (Fig. B.3).

Stratification

Stratification, often characterized by the Brunt-Väisälä-Frequency ($N^2 = \frac{g}{\rho_0}\frac{\partial \rho}{\partial z}$), is determined by the vertical density gradient. Hence, the typical vertical distribution of N^2 shows low values within the surface ML of only around $5 \cdot 10^{-5} s^{-2}$ on average, increasing to maximum values of up to $1 \cdot 10^{-3} s^{-2}$ within the main thermocline associated with a depth range of 40-70m in the eastern equatorial Atlantic. In contrast to shear, stratification within the ACT region below the ML increases from west to east (Fig. B.5g,h, Fig. B.8b). A likely explanation for this behavior is associated with the large scale salinity distribution [e.g. *Jouanno et al.*, 2011]. East
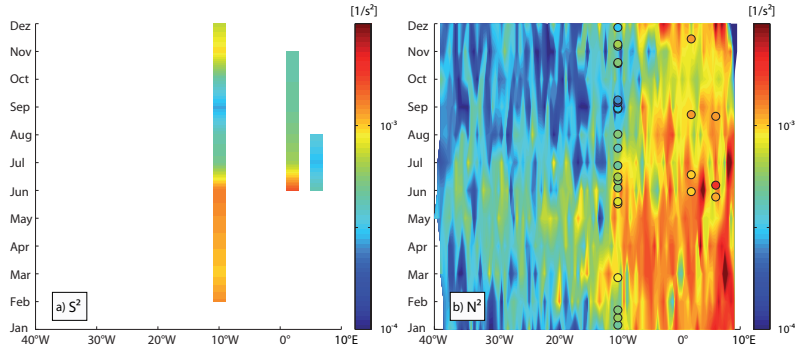
Figure B.8.: Seasonal evolution of shear below the ML constructed from available cruise data (a) and stratification below the MLD (b) constructed from ARGO float data, in circles the section averaged values observed on our cruises are shown for comparison.

of 10°W surface waters are fresher due to enhanced precipitation in the Gulf of Guinea and fresh water discharges from the Niger and Congo rivers. The stronger stratification in the upper ocean is thus due to the strong increase of salinity of up to 3 in the upper 20-30m of the thermocline. The depth extent of elevated stratification, however, diminishes towards the east (Fig. B.5).

At 10°W, the seasonal variability of stratification between 2°N and 2°S constructed from the ship sections (Fig. B.7d) shows a similar temporal evolution compared to shear variance. Stratification is strongest from January to April, while lowest values are observed in autumn. Similar to shear, stratification is strongest between the surface ML and the EUC core. Note that stratification is in general observed to be lower than shear in the western equatorial ACT region, indicating an average Richardson number of less than unity there. However, stratification exceeds shear in the eastern equatorial ACT region.

3.5 Froude numbers
Although energy transfer from the background flow to turbulence may also occur at higher gradient Richardson numbers $Ri = N^2/S^2$ [e.g. *Canuto et al.*, 2008], vigorous mixing in the equatorial thermocline is usually associated with Ri-numbers smaller than 0.25 [e.g. *Peters et al.*, 1988], i.e. gradient Froude numbers ($Fr = 1/Ri$) larger than 4. As suggested by the meridional sections of shear variance, the occurrence of elevated Fr numbers are not only restricted to the equator, but are found in the region

between 2°N and 2°S (e.g. Fig. B.3d).
Average Fr numbers determined from the seasonal distributions of shear and stratification levels from 10°W averaged between 2°S and 2°N, show values above one in the upper 50m of the water column throughout most of the year (Fig. B.7e). However, higher average Fr numbers of above 2 below the ML are evident during the second half of the year. This suggests that Kelvin-Helmholtz instability and thus elevated mixing is more likely to occur in the upper stratified ocean from late boreal summer to early winter. As shear variance reduces from below the ML towards the EUC core while stratification increases, Fr numbers rapidly decrease below 50m depth. Average meridional velocity shear significantly contributes to the seasonal Fr distribution, particularly during the second half of the year. Fr numbers determined from zonal shear only hardly exceed values greater than 1 during this period (Fig. B.7f).

Focusing on the layer just below the ML and extracting Fr numbers separately for every individual station yields the following results:

1. Fr numbers pass the critical threshold of 4 rather frequently in the western ACT region (10°W) between 2°S and 2°N (up to 35%, Fig. B.9) while in the eastern ACT region the Froude number threshold is only rarely exceeded.

2. The threshold is reached more frequently from July to November (10-35%), whereas in the beginning of the year, lower Fr numbers
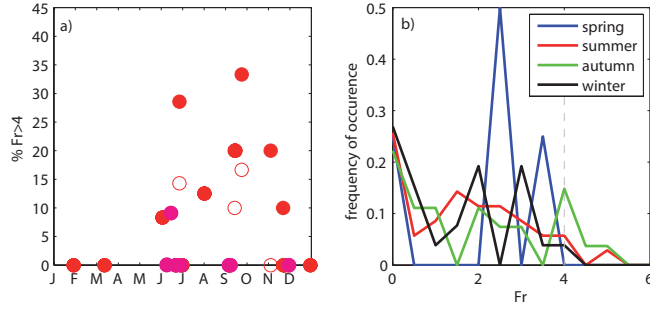
Figure B.9.: Seasonal evolution of Froude numbers derived from available cruise data: a) the percentage of Fr (filled circles) and Fr_u (empty circles) crossing the threshold of 4 at 10°W (red) and at 2 & 6°E between 2°S and 2°N b) distribution of Fr numbers at 10°W between 2°S and 2°N for the different seasons.

are observed (Fig. B.9a,b).

3. The percentage of Fr numbers exceeding the threshold of 4 is significantly reduced (by up to a factor of about 2), when meridional shear contributions are omitted from the calculations, highlighting the importance of meridional shear for instabilities to develop.

As discussed above for shear, it is suggested that TIWs (e.g. Fig. B.6) significantly contribute to elevated meridional shear in the upper 50m of the water column in the western ACT region during the second half of the year, in particular from June to October. As has been shown for the equatorial Pacific [*Moum et al.*, 2009], the data presented here suggests that TIWs contribute to the elevated frequency of occurrence of critical Fr numbers in the western ACT region.

4. Diapycnal mixing

Here, the microstructure data collected during 8 cruises in the equatorial ACT region (Tab. B.1) is discussed. In general, the background conditions encountered during those cruises agree well with the climatological background conditions described in section 3 above (Fig. B.4-B.8). An exception were enhanced winds encountered during the Meteor cruise from June 25 to July 5, which were due to the occurrence of an intra-seasonal wind burst causing westerly wind stress above climatology [*Marin et al.*, 2009].

4.1. Dissipation rates

To date and except for the analysis presented below, results from microstructure measurements in the equatorial Atlantic were solely reported by *Crawford and Osborn* [1979]. Their data, consisting of 8 profiles obtained from different locations in the central equatorial Atlantic during July 1974, showed elevated turbulence levels in the upper shear layer of the EUC between the surface ML and the main thermocline. Typical values of turbulent dissipation rates below the ML in their study were on the order of $3 \cdot 10^{-7} W kg^{-1}$.

As described in section 2, the 785 microstructure profiles available for this study were predominately collected during repeated surveys from different seasons along 3 meridional sections: 10°W, 2°E, and 6°E (Tab. B.1, Fig. B.2). In general, profiles of turbulent dissipation rates calculated from the data collected away from the equator (latitudes > 3) rarely exhibit elevated levels in the upper thermocline (Fig. B.10). In fact, (arithmetically-) averaged dissipation rates from this region decrease from the ML to a few meters into the upper thermocline by an order of magnitude and are indistinguishable from the instruments noise level ($< 1 \cdot 10^{-9} W kg^{-1}$) below 80 m below the ML. In contrary, however, dissipation rates from below the ML within 2 of the equator frequently show patches of elevated turbulence (Fig. B.10, B.11). Here, average dissipation rates at the base of the ML are about $4 \cdot 10^{-7} W kg^{-1}$ (with lower and upper 95% confidence limits of $3.2 \cdot 10^{-7}$ and $4.4 \cdot 10^{-7} W kg^{-1}$, denoted by [] in the following, respectively. Note that these confidence limits are only based on statistical evaluations as explained in Appendix A) and gradually decrease
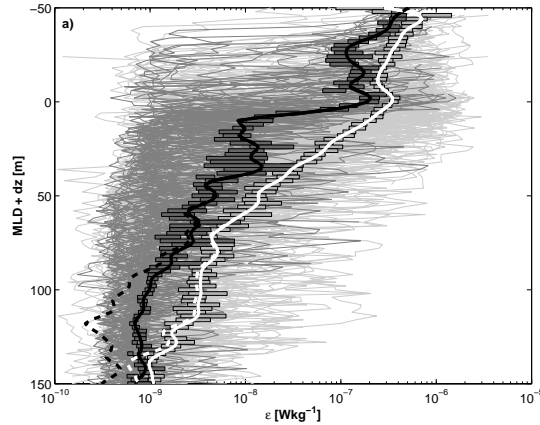
Figure B.10.: Individual profiles of dissipation rates of turbulent kinetic energy from the equatorial Atlantic (2°N-2°S, 23°W-6°E) (thin grey lines) compared to profiles away from the equator (> 3° N/S) (thin dark grey lines) together with their average profiles (heavy white and black respectively). 95% uncertainties for the averages (horizontal bars) were calculated using the boot strap method (see Appendix A). Dashed lines indicate effect of the noise level of the instrument (Appendix A).

to $1 \cdot 10^{-9} Wkg^{-1}$ at a depth of 130 m below the ML. Above this depth, average dissipation rates are hardly affected by the instruments noise level (Fig. B.10). In the layer from the ML to 30 m below, turbulent dissipation rates are elevated in the equatorial region by up to an order of magnitude compared to the off equatorial rates. Turbulence in the mixed layer is also enhanced by at least a factor of 2 compared to off-equatorial locations. As for the equatorial Pacific mixed layer [*Moum et al.*, 1989], this indicates that turbulence here is not only driven by air-sea buoyancy fluxes because they are of same order at and away from the equator. In particular, a recent detailed investigation of the TKE budget of the mixed layer showed the importance of shear production as well as vertical diffusion of TKE within the mixed layer [*Wade et al.*, 2011b]. In the following, the discussion will focus on the data collected within the equatorial band.

Particularly notable in the data from within 2 of the equator were vertically coherent dissipation rate maxima of $0.5 - 3 \cdot 10^{-6} Wkg^{-1}$ that extended from the mixed layer into the thermocline to up to 50m depth (Fig. B.11a-c). These maxima were particularly pronounced at 10W and to a lesser extend at 2°E. Usually, they persisted during the sampling period of one to two hours at an individual station, indicating longer decay time scales. They were most common at 10°W during boreal summer (Fig. B.11a) where they were observed to extended 20 to 30 m into the stratified water column. At 2°E and 6°E, depth penetration of the coherent maxima into the thermocline was significantly reduced and they were typically observed to extend only into the upper 5 to 10 m of the stratified waters.

The vertical and temporal distributions of these vertically coherent maxima of turbulent dissipation rates at 10°W agree well with observations from the central equatorial Pacific at 140°W [e.g. *Gregg et al.*, 1985; *Moum et al.*, 1989; *Peters et al.*, 1994; *Lien et al.*, 1995]. Similarly to our observations, strong burst of turbulence extending from the mixed layer into the Pacific thermocline were frequently observed. However, many of the Pacific microstructure data sets indicate that the strong coherent bursts of turbulence predominately occur during night time. This process, termed deep-cycle turbulence involves night time convection in the mixed layer, elevated vertical shear of horizontal velocity in and below the ML and internal waves [e.g. *Moum et al.*, 1992; *Peters et al.*, 1994; *Wang and Müller*, 2002] and is confined to the upper 20 to 30 m of the thermocline. When active, night-time dissipation rates in that layer in the Pacific exceed day
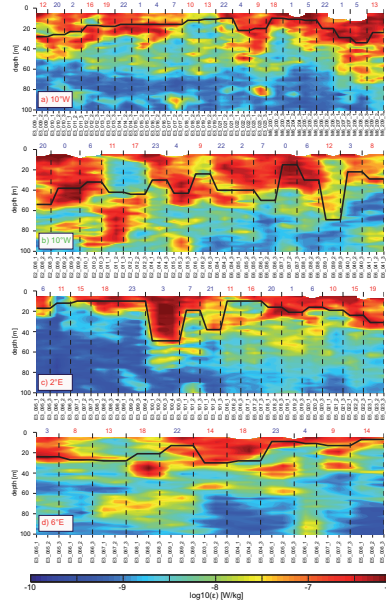
Figure B.11.: Contoured profiles of dissipation rates of turbulent kinetic energy from within 2° of the equator from different latitudes and seasons: (a) June/July 10°W, (b) September 10°W, (c) June 2°E and (d) June 6°E. Vertical dashed lines mark changes of sampling position. Profiles at single position were usually repeated after about 20 minutes. Red and blue numbers above the plots indicate local sampling time.

time values by an order of magnitude [e.g. *Peters et al.*, 1988, 1994]. Although the depth penetration of the coherent turbulent bursts in the western ACT region is similar to the Pacific observations, night time dissipation rates in a 20 m layer below the ML determined from all data collected between 23°W and 10°W are on average only elevated by a factor of 3 compared to day time values. Moreover, in the eastern ACT region east of 2°E differences in day and night time dissipation rates are not detectable. Nevertheless, average dissipation rates from the equatorial region are of similar magnitude compared to the observations from the equatorial Pacific [e.g. *Peters et al.*, 1988; *Moum et al.*, 1992; *Lien et al.*, 1995]. In contrary to the Pacific observations, elevated coherent bursts of turbulence in the Atlantic also occur during day time (Fig. B.11) and contribute to the elevated average dissipation rates just below the ML (Fig. B.10).

At 10°W, two deeper maxima of turbulent dissipation rates $(0.5-1\cdot10^{-6}Wkg^{-1})$ were observed that did not connect with ML turbulence and extended to up 80m depth (Fig. B.11a,b). Both occurrences were observed just above the EUC core in the region

close to the equator. During both September cruises, a TIW was present at the sampling site contributing additional vertical shear in the upper water column (Fig. B.9). It is thus likely that the enhanced dissipation rates below the ML (Fig. B.11b), in particular the deeper maxima, are related to the presence of the instability waves. In the 10°W boreal summer data, the low mixing region between 60 and 80m depth (Fig. B.11a) reflects the core depth of the EUC, while below this region, i.e. in the lower shear zone of the EUC, occasional mixing events were observed. Within those events, however, dissipation rates rarely exceeded $1\cdot10^{-7}Wkg^{-1}$. Similar deeper turbulent patches were also observed in the eastern ACT region (Fig. B.11c,d). At 6°E in particular, these patches cannot be due to shear instability of the background EUC/SEC system as those currents are particularly weak in the easternmost part of the Gulf of Guinea.

To quantify seasonal variability of the mixing levels for the different ACT regions, average dissipation rate profiles and uncertainties were calculated for different month of the year (Fig. B.12). To avoid biases due to possible diurnal variations, dissipati-
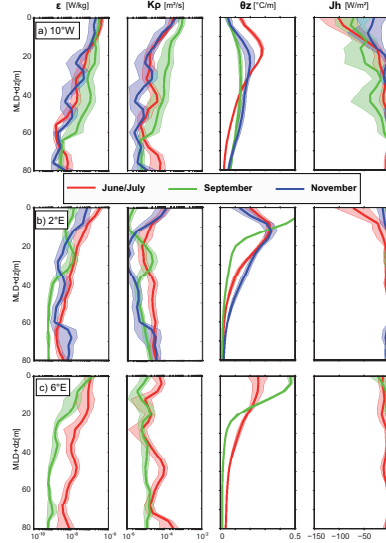
Figure B.12.: Average seasonal profiles of dissipation rate (ϵ), eddy diffusivity (K_ρ), temperature gradient (dT/dz) and diapycnal heat flux (J_h) on sections 10°W (a), 2°E (b) and 6°E, together with their confidence limits (see Appendix) in vertical coordinates of MLD+Δz.

on rates were averaged separately for day and night before final averaging. Maximum average dissipation rates just below the ML are $2 - 4 \cdot 10^{-7} W kg^{-1}$ [$8.4 \cdot 10^{-8}$; $5.6 \cdot 10^{-7} W kg^{-1}$] at 10°W in June, September and November. Here, dissipation rates decrease by two orders of magnitude from below the base of ML to the EUC core at 80m depth. In the September average that includes data from two cruises (Sep. 2005 and Sep. 2007) dissipation rates stay on a rather uniform level until about 60m below the ML, abruptly decreasing towards the EUC core. It is suggested that the enhanced dissipation rates between 20 and 60 m below the ML are associated with the presence of the TIWs at the sampling site, contributing additional vertical shear in the upper thermocline. This deeper penetration of elevated dissipation rates during the presence of a TIW was also observed in the Pacific [*Moum et al.*, 2009]. In the eastern ACT region at 2°E, highest dissipation rates below the ML are found in June, significantly reducing in September and November. In general, the decay of average dissipation rates at 2°E and 6°E in the vertical occurs more rapidly than at 10°W. At 2°E average dissipation rates below the ML are two orders of magnitude lower in September.

In summary, average dissipation rates in the upper thermocline at the equator ($\pm 2°$) are an order of magnitude larger than at off-equatorial locations and are also lower in the eastern equatorial ACT compared to the west. In the western equatorial ACT region, dissipation rates in the upper thermocline are of similar magnitude from June until November, while in the eastern Gulf of Guinea (2°E and 6°E) dissipation rates in June clearly exceed September and November values.

4.2. Turbulent Eddy Diffusivities

Turbulent eddy diffusivities (K_ρ) increase with increasing dissipation rates and decreasing stratification (section B2.4). Here, station-average diffusivities were calculated from station average dissipation rates and average buoyancy profiles that were subsequently averaged into ensembles as detailed below. Error treatment is explained in the appendix. The observed variability of these two parameters in the upper equatorial thermocline results in a range of eddy diffusivities. As for turbulent dissipation rates, average equatorial eddy diffusivities below the ML are about a factor 10 larger than those from away from the equator, in particular between 10 and 30m below the ML (Fig. B.13). Average equatorial diffusivities reach $2.5 \cdot 10^{-4} m^2 s^{-1}$
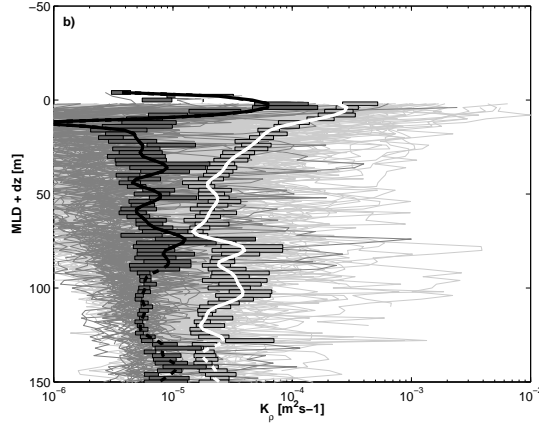
Figure B.13.: Individual profiles of eddy diffusivity from the equatorial Atlantic (2°N-2°S, 23°W-6°E) (thin grey lines) compared to profiles away from the equator ($> 3°$ N/S) (thin dark grey lines) together with their average profiles (heavy white and black respectively). 95% uncertainties for the averages (horizontal bars) were calculated using the boot strap method (see Appendix A). Dashed lines indicate effect of the noise level of the instrument on ϵ (Appendix A).

(with upper and lower 95% confidence limits being $2 \cdot 10^{-4}$ and $5 \cdot 10^{-4} m^2 s^{-1}$ respectively, see Appendix A and denoted by [] in the following), just below the ML, almost linearly decreasing to $2 \cdot 10^{-5} m^2 s^{-1}$ $[1.4 \cdot 10^{-5}; 2.3 \cdot 10^{-5} m^2 s^{-1}]$ at 50m below the ML and then stay at about this level in the deeper water column up to 150m below the ML (Fig. B.13). In contrary, average off equatorial diffusivities decrease from $6 \cdot 10^{-5} m^2 s^{-1}$ $[5 \cdot 10^{-5}; 1.3 \cdot 10^{-4} m^2 s^{-1}]$ at the depth of the ML to around $5 \cdot 10^{-6} m^2 s^{-1}$ $[4 \cdot 10^{-6}; 8.3 \cdot 10^{-6} m^2 s^{-1}]$ at 10m below the ML and stay at this level until 80m below the ML although the vertical distribution of stratification is rather similar in the equatorial and off-equatorial regions. Deeper values were not determined as instrumental noise dominated the dissipation rate measurements. Similarly, diffusivities in the ML were not determined due to marginal stability of stratification.

Monthly averaged diffusivities from the different regions in the ACT indicate maximum eddy diffusivities below the ML at 10°W (Fig. B.12). While average vertical distributions of K_ρ at this longitude from June and November are rather similar in magnitude, September values are enhanced by about a factor two. This is due to reduced upper ocean stratification during this period (Fig. B.7). In the eastern equatorial ACT region, average eddy diffusivities are elevated only in the upper few meters below the ML where values do not exceed $1 \cdot 10^{-4} m^2 s^{-1}$. From 10m to 80m below the ML eastern equatorial diffusivities rarely reach above $1 \cdot 10^{-5} m^2 s^{-1}$.

4.3 Diapycnal heat fluxes

Vertical distributions of the diapycnal heat flux (J_h) have previously been inferred from microstructure observations for the equatorial Pacific. There, diapycnal heat flux profiles showed a strongly vertically-divergent flux of heat in the upper stratified ocean indicating that due to turbulence, heat from the ML is redistributed to the upper 100m of the thermocline [e.g *Gregg et al.*, 1985; *Peters et al.*, 1988; *Lien et al.*, 1995]. Similar to the equatorial Pacific, the vertical distribution of equatorial diapycnal heat fluxes inferred from microstructure observations in the ACT exhibits only negative values in the upper thermocline with maximum magnitude at the base of the ML (Fig. B.14). However, considerable regional as well as seasonal variability in the ACT region is evident concerning the maximum magnitude of J_h as well as the depth interval over which it decays. Within the equatorial region, average diapycnal heat fluxes are of 55 Wm^{-2} just below MLD (with lower and upper 95% confidence limits of 44 and 60 Wm^{-2} respectively, see
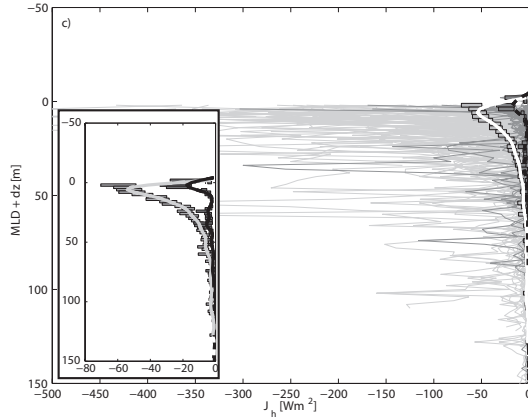
Figure B.14.: Individual profiles of diapycnal heat flux from the equatorial Atlantic (2°N-2°S, 23°W-6°E) (thin grey lines) compared to profiles away from the equator (> 3° N/S) (thin dark grey lines) together with their average profiles (heavy white and black respectively). 95% uncertainties for the averages (horizontal bars) were calculated using the boot strap method (see Appendix A). Dashed lines indicate effect of the noise level of the instrument on ϵ (Appendix A)

Appendix A, and are indicated by [] in the following), decaying to below 5 Wm^{-2} at 60m below the ML. The average heat flux profile from the off-equatorial region indicates maximum values of only 17 Wm^{-2} [15; 33 Wm^{-2}] just below the ML, decreasing to below 5 Wm^{-2} at a depth of 10m below the ML (Fig. B.14).

In general, average diapycnal heat fluxes in western equatorial ACT region exceed those inferred for the eastern equatorial ACT region (Fig. B.12). In the western part at 10°W, average values of J_h reach 90 Wm^{-2} [62; 124 Wm^{-2}] just below the ML in June/July and are reducing to 7 Wm^{-2} [4; 10Wm^{-2}] 30m below the ML. In September the average heat flux inferred from the data from two cruises were 75 Wm^{-2} [50; 100 Wm^{-2}] just below the ML, somewhat lower than in boreal summer. However, the heat flux is less vertically-divergent compared to the summer average. Values of about 10 Wm^{-2} are still inferred at a depth of 60m below the ML. Although eddy diffusivity is highest in September (Fig. B.12), the reduced temperature gradient during this period leads to smaller maximum values of J_h below the base of the ML during this period. The J_h profile inferred from the data collected during one cruise at 10°W in November suggests lower average diapycnal fluxes during late autumn. Maximum values

just below the ML are below 40 Wm^{-2}.

In the eastern ACT region at 2°E average profiles of J_h are strongly reduced compared to 10°W during all seasons (Fig. B.12). Highest average maximum values below the ML are also observed in boreal summer, but only reach about 50 Wm^{-2} [30; 70 Wm^{-2}] decaying rapidly within the upper 20m of the thermocline. In September and November J_h is further reduced, with values of 5 Wm^{-2} [3; 10 Wm^{-2}] and 13 Wm^{-2} [2; 23 Wm^{-2}] just below the ML respectively. At 6°E J_h does not exceed 10 Wm^{-2}. Although temperature gradients at 2°E and 6°E are more pronounced, eddy diffusivities are not as elevated as those determined to the west, resulting in the lower values of J_h.

To quantify heat loss of the mixed layer due to turbulence from the data of all cruises, station averages of turbulent heat flux in the interval 5m to 15m below the ML base were computed from the individual station data and then averaged in regional ensembles. For the equatorial region, stations between 2°S and 2°N were averaged, while for outside of the equatorial region stations were combined as indicated in Fig. B.15. Number of profiles and stations used for individual ensembles are indicated in Tab. B.1. Day and night averages were computed prior to ensemble averaging to avoid biases due to enhanced
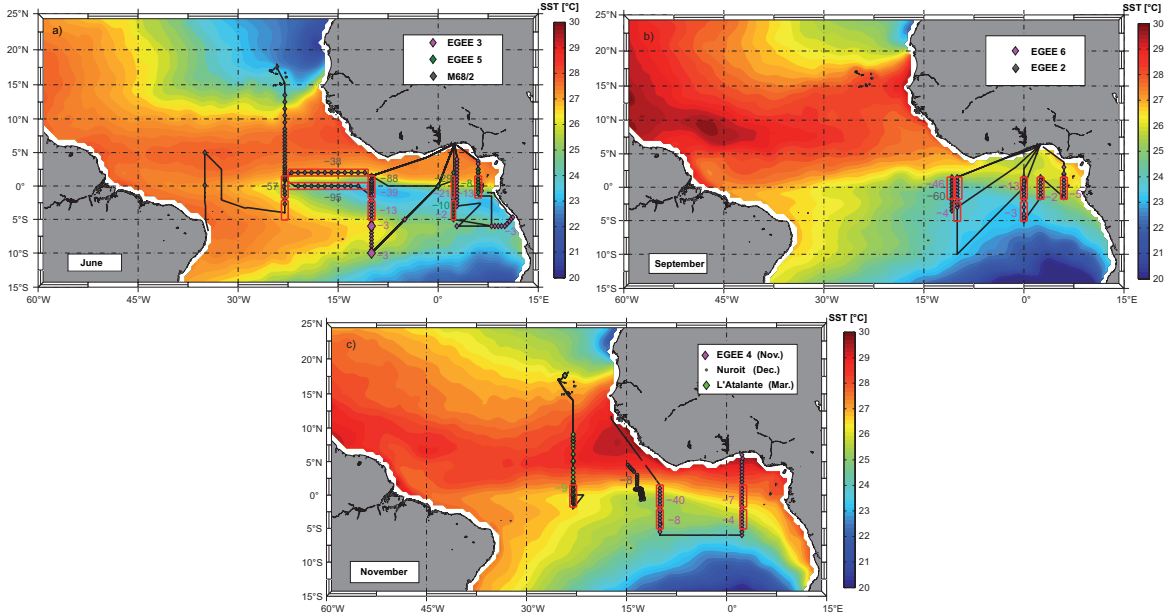
Figure B.15.: Spatial and temporal variability of the section averaged diapycnal heat flux out of the ML. Maps show SST averaged for the indicated months over the years 2005-2007.

night time mixing. It should be stated that due to the vertically-divergent diapycnal heat fluxes, the average between 5m and 15m below the ML is somewhat smaller than the maximum diapycnal heat flux. For example, the average off-equatorial heat flux out of the ML would be about $4\ Wm^{-2}$, while the maximum is $17\ Wm^{-2}$ (Fig. B.14).

The results of this approach lead to a relatively coherent picture of the seasonal and regional diapycnal ML heat loss (Fig. B.15). Most elevated ML heat flux divergences are found in the western equatorial ACT region during boreal summer between 23°W and 10°W. Between mid-June and end of July (cruise M68/2) inferred ML heat flux divergences at 10°W were 89 Wm^{-2}) while along the equator between 23°W and 10°W 95 Wm^{-2} were inferred (Fig. B.15). Somewhat lower but still elevated values of 57 Wm^{-2} were determined between 2°N and 2°S at 23°W. During the same period, a ML heat loss of 38 Wm^{-2} was determined between 23°W and 10°W at 2°N above the SEC, indicating that significant mixing also occurs in a region where elevated shear is solely due to the northern branch of the SEC. In very early summer (end of May), however, when light winds were still present at the equator and the

ITCZ had not jet progressed northward, lower ML heat losses of only 39 Wm^{-2} were inferred between 2°N and 2°S at 10°W (Fig. B.15a). Similar values at the same location (2°N-2°S, 10°W) were also inferred in November (39 Wm^{-2}) while in September ML heat losses of 48 and 60 Wm^{-2} were calculated. In the eastern equatorial ACT region at 2°E highest heat fluxes of around 25 Wm^{-2} were inferred in June, reducing to 13 Wm^{-2} in September and 17 Wm^{-2} in November. Further to the east at 6°E, maximum equatorial heat loss was again inferred in June but yielded 13 Wm^{-2} only, while in September even lower values (5 Wm^{-2}) were determined. It should be noted that this data set does not indicate an enhancement of the diapycnal heat fluxes in November compared to early boreal autumn as has recently been suggested by a model study for the ACT region [*Jouanno et al.*, 2011].

A very different picture is obtained for the region away from the equator. Although there are less microstructure profiles available for the region away from equator compared to the equatorial region (Tab. B.1), none of the ensemble averages indicate a ML heat loss of more than (15 Wm^{-2}). Furthermore, no regional as well as seasonal differences in

the diapycnal heat flux divergences can be determined for this region. For completeness, all available section averages from Tab. B.1 are included in Fig. B.15.

In summary, the seasonal variability of the diapycnal heat flux out of the ML results in some general findings:

1. During all seasons diapycnal heat fluxes out of the ML are higher in the equatorial region compared to the regions poleward.

2. Within the equatorial region, the western part of the ACT (23°W and 10°W) shows elevated values compared to the eastern part (0°E, 2°E, 6°E).

3. Seasonally, boreal summer is the season of highest diapycnal heat fluxes out of the ML throughout the ACT region.

5. Mixed layer heat budget

The diapycnal heat flux presented in the previous section suggests elevated fluxes within the equatorial region. To put the obtained values into context to other ML heat fluxes a heat budget is presented. The seasonal variability of the diapycnal heat flux is best resolved at 10°W. In the following contributions to the ML heat budget at this location will be discussed. The calculation of the individual terms of the budget is described in section B2.5.

Foltz et al. [2003] investigated the different contributions to the seasonal ML heat budget climatology at various PIRATA buoy locations in the Atlantic Ocean. Lacking information on the magnitude of diapycnal heat flux, this contribution was estimated as the residual between the observed heat storage and the sum of all other terms of the budget. Note that the residual also includes all possible errors arising from the large uncertainties of the parametrizations and from the approximation inherent to the calculations of individual terms. At 10°W they found a large residual of up to 100 Wm^{-2} during boreal summer. At other locations outside the ACT region, e.g. at 35°W,0°N the residual is negligible as was found for the southern edge of the ACT region at 10°W,6°S and 10°W,10°S. In agreement to these findings, the inferred diapycnal heat fluxes from the region south of the equatorial region presented

above indicated reduced levels of diapycnal ML heat loss (only 3 Wm^{-2}) compared to the equatorial ACT region.

In addition to the unavailable diapycnal ML heat loss estimates, *Foltz et al.* [2003] attributed the main error sources and uncertainties contributing to the residual to 1) low-biased meridional velocity-divergence-induced entrainment due to the coarse resolution of the drifter climatology and 2) low-biased latent heat flux due to limited data coverage. *Foltz et al.* [2003] only used one full year of data, during which the relative humidity was anomalously high, resulting in low latent heat fluxes. In order to minimize these main error sources and thereby isolating the contribution of the diapycnal heat flux at 10°W, the different terms contributing to the ML budget at 10°W,0°N were estimated taking a more recent and higher resolved surface velocity climatology (YoMaHa07 data) and a longer time period of PIRATA buoy measurements (1997-2009).

Changing the drifter resolution mainly affects the entrainment term as anticipated by *Foltz et al.* [2003] and has a visible effect on the heat content. Nevertheless, this effect only accounts for changes of about 10 Wm^{-2} of the residual (Fig. B.16). Calculating the individual terms of the ML heat budget based on the longer time period has a major effect on the latent heat flux term as suggested by *Foltz et al.* [2003], affecting the residual by about 17 Wm^{-2} between May and July. In addition, the estimated absorbed shortwave radiation here is lower than the value used by *Foltz et al.* [2003], which has not been anticipated.

When comparing the improved estimates of the individual terms of the mixed layer heat budget to monthly averages of the inferred diapycnal heat flux when available (Fig. B.16a) shows that during the boreal summer months, the diapycnal heat flux divergence provides the largest cooling term. During this period, latent heat flux is at a seasonal minimum. In September, diapycnal heat flux divergence, latent heat and cooling due to meridional advection of heat are of similar magnitude while in November, meridional advection and latent heat dominate the cooling of the mixed layer.

The sum of all heat flux estimates and the changes in heat storage agree well during the period when
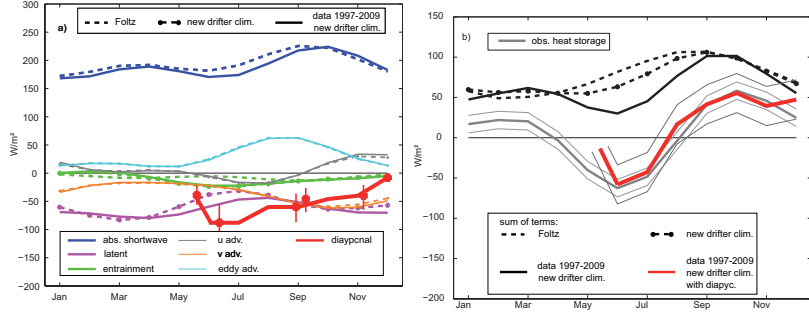
Figure B.16.: Individual terms of the ML heat budget at 10°W,0°N: dashed lines are reproduction of *Foltz et al.* [2003] estimates with coarse drifter resolution, and data from 1997-2002; dashed-dotted lines with higher drifter resolution, but data also from 1997-2002; solid lines with higher drifter resolution and data from 1997-2009; the red bars denote confidence limits for the average diapycnal heat flux below the ML, (b) black lines represent the sum of all terms contributing to the heat budget except turbulent heat flux (line styles are assigned to the same set up as in a)), red line sum of all terms including diapycnal heat flux.

diapycnal fluxes are available (Fig. B.16b). From May to November the changes in heat storage and the sum of all fluxes are well within the uncertainties of the estimates. Both show a net cooling of the ML from May to mid-august of about 50 Wm^{-2} and a warming from mid August to mid-November. Due to the lack of data from January to mid-May, the seasonal cycle of diapycnal fluxes is not fully resolved. However, the occurrence of elevated Fr numbers (Fig. B.9) during this part of the season is much reduced suggesting a reduced diapycnal heat flux compared to the values obtained for boreal summer and autumn.

In the eastern region of the ACT the net surface heat flux during the cold tongue season is considerably lower than in the western region, requiring a lower cooling term to produce the observed reduction in SSTs. This is qualitatively in agreement with the inferred diapycnal heat flux of maximum 25 Wm^{-2} during boreal summer in this region.

6. Summary and discussion

This study was carried out to investigate seasonal and regional variability of mixing related parameters (dissipation rates ϵ, eddy diffusivities K_ρ, diapycnal heat fluxes J_h), within the ACT region, their connection to large-scale background parameters and the contribution of the diapycnal heat flux to the ML heat budget. We use a unique data

set consisting of microstructure shear profiles, CTD and ship-board velocity measurements from eight cruises to the ACT region carried out between 2005 and 2008. The major result of this study is that the diapycnal heat flux strongly contributes to the cooling of the ML in the western ACT during boreal summer and autumn.

In general, we find close correspondence between the seasonal and regional variability of background shear and stratification levels and ensemble mixing intensities, eddy diffusivities and diapycnal heat flux. Shear levels were found to be strongly elevated in the equatorial region (2°N-2°S) at 10°W and 2°E while lower values are found eastward of this longitude. However, stratification below the ML strongly increases from the western ACT region to the eastern ACT region reducing the likelihood of shear instabilities to occur in the eastern part. In the center of the ACT (10°W) the occurrence of critical Fr numbers is increased particularly during the second half of the year. During this period, the meridional shear component is often elevated. Turbulent dissipation rates at the equator are strongly increased in the upper thermocline compared to off-equatorial locations. The major findings concerning their seasonal and regional variability are:

1. Dissipation rates are elevated in the western equatorial ACT region in comparison to the

eastern equatorial ACT region;

2. In the whole equatorial ACT, most intense mixing is observed in boreal summer;

3. In the western equatorial ACT region, mixing is enhanced during boreal summer and autumn, in particular when TIWs are present.

In the whole equatorial ACT region, diapycnal heat flux in the upper thermocline is elevated. In the equatorial region at 10°W, where diapycnal heat flux was found to peak, its magnitude ranges from 90 Wm^{-2} in boreal summer to 55 Wm^{-2} in September, and to 40 Wm^{-2} in November. In the eastern ACT region, elevated values of about 25 Wm^{-2} were inferred during boreal summer only, while towards the end of the year diapycnal fluxes are about 5 Wm^{-2}. Integrating the obtained heat flux estimates in the ML heat budget showed that the diapycnal heat flux represents the largest ML cooling term during boreal summer and autumn in the central cold tongue region.

The background settings observed in the equatorial ACT region as well as the range of average dissipation rates, eddy diffusivities and diapycnal heat fluxes are in good agreement with results from previous studies from the equatorial Pacific [e.g *Gregg et al.*, 1985; *Peters et al.*, 1988; *Moum et al.*, 1989; *Lien et al.*, 1995]. A striking difference however is the reduced strength of the deep diurnal cycle in the equatorial ACT region compared to the Pacific. While in data sets from the equatorial Pacific a night time enhancement of dissipation rates below the ML of about an order of magnitude is frequently observed, average night time enhancement in the western equatorial ACT is a factor of 3 only. Moreover, in the eastern equatorial ACT a night time enhancement is not evident.

Observations from the Pacific and model studies indicate that the strong turbulent bursts occurring at night time below the ML are associated with elevated internal wave activity. These internal waves are characterized by frequencies near the local buoyancy frequency and short horizontal wave length ($\sim$ 200m). To date, the connection between the turbulent bursts and the internal waves is not fully clarified. A possible explanation of the night-time enhancement was that these internal waves are ge-

nerated by convectively driven eddies in the ML [e.g. *Gregg et al.*, 1985] or by shear instabilities formed within the ML [*Skyllingstad and Denbo*, 1995]. In this concept, these waves are then thought to radiate into the stratified water column where they trigger local shear instability. However, recent observations [*Moum et al.*, 2011] and linear stability analysis [*Smyth et al.*, 2011] indicates that the properties of these oscillations are consistent with shear instabilities formed locally from the hourly mean structure of currents and stratification, as had been suggested previously [*Mack and Hebert*, 1997; *Sun et al.*, 1998; *Smyth and Moum*, 2002; *Lien et al.*, 2002]. The results presented here show that in the western equatorial ACT deep reaching turbulent patches were also found to occur during day time, ruling out the possibility that the turbulent bursts are solely driven by night-time convection in the ML.

The analysis of the background conditions showed that the percentage of critical Froude numbers strongly depends on the meridional shear component in the western equatorial ACT region in boreal summer and autumn. In particular, Fr number distributions suggest that the probability of shear instabilities to occur in the western equatorial ACT region is enhanced by up to a factor of 2 due to the meridional shear contributions. As indicated by shipboard velocity sections and satellite SST maps, TIWs appear to be a major contributor to these elevated levels of meridional shear. In the tropical Atlantic, TIWs are most active in boreal summer and autumn [e.g. *von Schuckmann et al.*, 2008]. It is thus indicated that the occurrence of TIWs is crucial for sustaining the elevated mixing levels observed in the western equatorial ACT region during the latter part of the year.

In the equatorial Pacific, *Moum et al.* [2009] found a 32 % increase in shear levels due to the presence of a TIW while enhancing the probability of critical Fr numbers by a factor of 4. Moreover, their data analysis showed average values of diapycnal heat fluxes out of the ML of around 400 Wm^{-2} during a 14 day period while a TIW was present at the measurement site. The ensemble averages presented here do not indicate comparably high diapycnal ML heat losses. A possible explanation is the weaker TIW signature
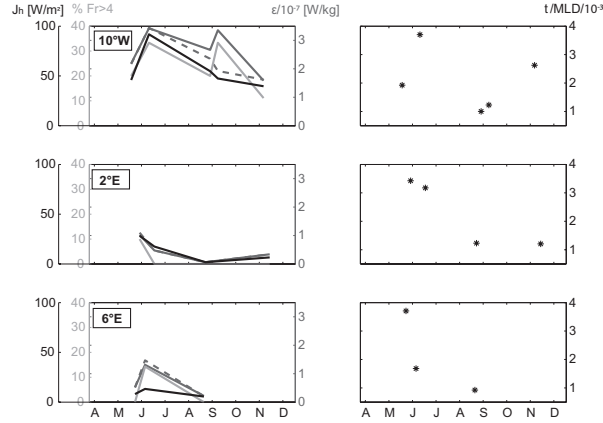
Figure B.17.: Comparison of seasonal evolution of different parameters below the ML on sections 10°W (top), 2°E (middle) and 6°E (bottom). Left column: Light grey line: Percentage of Froude numbers below the ML larger than the threshold of 4. Dark grey line: section averaged dissipation rate below the ML ($\epsilon/10^{-7}$). Dashed grey line: section averaged dissipation rate below the ML accounting for day and night tiacquisitionsons, black line: section averaged diapycnal heat flux below the ML accounting for day and night time acquisitions; Right column: wind stress divided by MLD.

in the western ACT region compared to the TIWs observed in the equatorial Pacific at 140°W. In light of the heat budget presented above for the equator at 10°W, a diapycnal heat flux of $400\ Wm^{-2}$ would lead to a severe imbalance and thus strong cooling of the ML. On the other hand, the role of TIWs was previously sought to supply heat to the ML of the tropical cold tongues predominately by meridional eddy heat flux divergence. Here it is suggested that TIWs also contribute to cooling of the ACT ML by enhancing diapycnal heat fluxes.

Apart from TIWs, other large scale variability such as inertio-gravity waves and Kelvin waves have been reported to contribute to variability of mixing intensities and diapycnal heat flux [e.g. *Peters et al.*, 1991; *Lien et al.*, 1995]. Although these equatorial waves are frequently observed in the region of the ACT [e.g. *Polo et al.*, 2008; *Hormann and Brandt*, 2009] they could not be distinguished from other variability in the data set used here. Nevertheless, the fact that in the seasonal mixed layer balance calculations heat storage closely follows the sum of the heat fluxes when explicitly including diapycnal heat flux estimates suggests that the mixing processes observed during the different measurement campaigns are to some degree representative for the respective seasons.

The finding of elevated diapycnal heat fluxes and its dominant role in the ML heat budget essentially agrees with a recent model study by *Jouanno et al.* [2011]. An eastward reduction of the diapycnal heat fluxes was also diagnosed in their model and highest diapycnal fluxes were also obtained during boreal summer. However, a striking discrepancy between the results presented here and the model results is a second diapycnal heat fluxes maximum of comparable magnitude to the boreal summer maximum in November/December which was diagnosed in the model runs. In the model, mixing is driven primarily by the zonal shear within the surface currents. In late boreal fall the strengthening of the zonal winds lead to a strengthening of the westward SEC and thus to enhanced zonal shear in the upper thermocline of the equator. Although this process could have explained the semi-annual SST cycle previously reported by *Okumura and Xie* [2006], the data presented here do not support a second maximum of diapycnal heat flux in November. In fact, a correlation between zonal wind stress and diapycnal heat flux is not evident at any of the repeat sections occupied within the ACT in this study (Fig. B.17). As noted above, vertical shear of upper-ocean meridio-

nal velocity appears to be the dominant cause for the elevated diapycnal heat fluxes in boreal summer and autumn.

The dominant contribution of the diapycnal heat flux on the ML heat budget highlights the importance of its correct representation in numerical simulations in order to improve biases in the SSTs, which are of relevance to climate predictions. Some hope for an adequaparametrizationion for models that captures enhanced mixing observed in conjunction with the presence of a TIW was recently put forth by *Lien et al.* [2008]. However, the model used by *Jouanno et al.* [2011] failed to reproduce the seasonal variability of the diapycnal heat fluxes although using the mixing paraparametrizationgested by *Lien et al.* [2008]. The observations and analysis presented in this study provide magnitude as well as the regional and seasonal variability of mixing related parameters in the region of the ACT, which can serve as a benchmark against which the performance of numerical simulations can be evaluated. The apparent close relation of Fr distribution shaped by shear and stratification below the ML, and the observed dissipation rates (Fig. B.17) give hope that paraparametrizationemes can be sought estimating mixing variability via observations of large scale background variables. However, the findings of this study need to be confirmed by further observations possibly taken at higher temporal and spatial resolution, whereas gliders seem to be the most promising platform.

C. Other applications for MSS data

The observations of dissipation rates of turbulent kinetic energy (ϵ) and the inferred eddy diffusivities (K_ρ) in the tropical Atlantic during different seasons lead to collaborational work with two other research groups resulting in two different publications:
1) *Wade et al.* [2011b]: A one-dimensional modeling study of the diurnal cycle in the equatorial Atlantic at the PIRATA buoys during the EGEE-3 campaign
2) *Rhein et al.* [2010]: Upwelling and associated heat flux in the equatorial Atlantic inferred from helium isotope disequilibrium

C.1. ϵ for validation of an ocean model: *Wade et al.* [2011b]

In *Wade et al.* [2011b] a one-dimensional modeling study of the diurnal oceanic mixed layer was performed at the station of three PIRATA buoys (10°W,0°N; 10°W,6°S; 10°W,10°S) to analyze the diurnal response of the equatorial Atlantic ocean under different meteorological and oceanic settings at the local scale during the appearance of the ACT. The model could be initialized, forced and validated with high resolution meteorological data, sub-surface profiles obtained with CTD and microstructure probes as well as current observations from vessel mounted ADCPs collected during the 2-days maintenance phase at each buoy.

As was mentioned in the introduction finding expressions for turbulent terms in numerical models remains a challenge. Different approaches estimating the turbulent terms are chosen for different layers (boundary layer, ocean interior) and dynamically dominated regions of the ocean (open ocean, shelf areas, equatorial belt etc.). In the study of *Wade et al.* [2011b] the performance of an improved version of the one-dimensional model developed by *Gaspar et al.* [1990] for boundary layers is investigated. The turbulence closure is based on a parametrization for atmospheric models, which has been adapted to oceanic simulations by *Gaspar et al.* [1990] relating the diffusivity K to the local turbulent kinetic energy e (TKE) via a mixing length scale (l_K) and a calibration constant (c_K). Below the ML the turbulence scheme is improved by adding the parametrizations of *Large et al.* [1994] and *Kantha and Clayson* [1994]. The dissipation rate of TKE is parametrized using the *Kolmogorov* [1942] theory: $\epsilon = c_\epsilon e^{-3/2}/l_\epsilon$, with a calibration constant c_ϵ and a characteristic dissipation length scale (l_ϵ). Hence, the performance of the model can not only be validated against large-scale parameters such as SST, sub-surface profiles of salinity and temperature as well as mixed layer depth, but also against direct observations of ϵ. This is a crucial point in assessing the ability of the model in correctly representing the diurnal cycle. To further analyze the processes controlling the oceans response to the meteorological forcing, modelled heat and TKE budgets of the mixed layer are analyzed in *Wade et al.* [2011b].

In the framework of this study the observed dissipation rates for the comparison with the model were provided. The investigations of this study giving insight into the background conditions within the area, the variability of mixing related parameters as well as the estimation of the individual contributions to the mixed layer heat budget helped to improve and discuss the modelled results.

The performance of the model concerning the evolution of SST, subsurface profiles of temperature and salinity as well as the mixed layer depths shows good agreement with the observations. Note though that the simulated time period is rather short and that the model is forced with high resolution meteorological
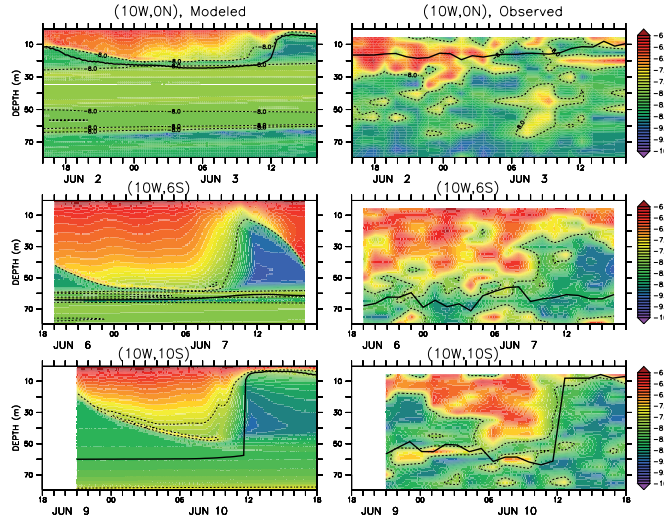
C. Other applications for MSS data

Figure C.1.: Timeseries of vertical profiles of dissipation of turbulent kinetic energy ($\log10(\epsilon)$) at 0°N (top), 6°S (middle) and 10°S (bottom) for the simulation (left) and the observations (right). The mixed layer depth is indicated as the solid black line and the isoline of -8 as dashed line. From *Wade et al.* [2011b].

data. For ϵ the agreement of simulation and observations of dissipation rates within the boundary layer is rather good concerning the night time enhancement of ϵ (fig.C.1). Below the ML the agreement diminishes. The models inability to reproduce small scale mixing patches below the ML as observed at 6°S and 10°S does not challenge the belief in its applicability. The inability to correctly simulate the penetration of enhanced dissipation rates from within the ML into the stratified layer as observed at the equator during night time though give rise to concern, whether the parametrization scheme used below the ML is able to correctly simulate the turbulent processes. Nevertheless, in general the diurnal variation of ϵ is considerably well simulated at all locations. At all locations the simulated heat storage experiences a clear diurnal cycle. For the simulated budget warming is provided by the solar heat flux, whereas in general all other terms cool the ML. Note, that advection terms are not considered with a one-dimensional model, but are considered small on these short timescales. The non-solar heat fluxes cool the ML rather constantly at all locations at a rate of 200-400 Wm^{-2}. Entrainment seems only important at the equator during night time cooling at a rate of about 100 Wm^{-2}. Vertical diffusion at the base of the ML is found an important cooling term on the equator and at 10°S mainly during the afternoon of up to 200-300 Wm^{-2}. It has to be stated that this vertical diffusion term is defined differently than in the ML heat budget estimations described in section 6.1. In *Wade et al.* [2011b] the term consists of the integration of turbulent fluxes over the entire depth extent of the ML, whereas in section 6.1 they are estimated directly at the base of the ML. In addition, this term was estimated as a residue in *Wade et al.* [2011b]. Hence, the results concerning this term are not directly comparable to the estimates described in this study. *Wade et al.* [2011b] find highest fluxes during the afternoon, when dissipation rates are still elevated within extremely shallow mixed layers, which are strongly stratified due to the incoming solar radiation (fig.C.1). In addition, in *Wade et al.* [2011b] a heat gain during night time due to vertical diffusion is evident at the equator, which can not be reported for the estimates of the diapycnal heat flux at the base of the ML from the data set presented in this study. The simulation of the TKE budget highlights the importance of the buoyancy production term in producing TKE during night time south of the equator. At 0°N this term is still important, but overcome by the shear production term, due to the presence of the nSEC, EUC system. However, it is not evident why the shear production term still has large contributions
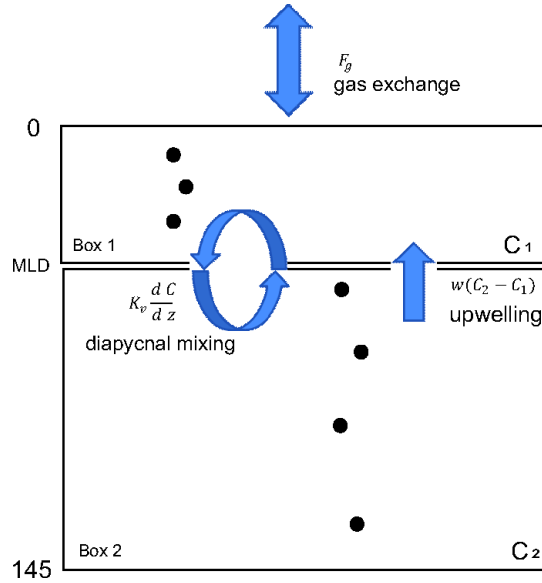
Figure C.2.: Schematic of the one dimensional two layer box model used to infer upwelling velocities from observed disequilibria of helium isotopes. Black dots represent helium samples.

at the 6°S and 10°S, where large scale background shear is observed significantly reduced compared to the equator (chapter 3). When *Osborn* [1980] inferred an expression for K from the TKE balance, they assumed a balance between the production terms of TKE (buoyancy production and production via the interaction with the mean flow) and the dissipation, neglecting other terms including the vertical diffusion of TKE. In the evaluation of *Wade et al.* [2011b] of the contributions to the TKE budget within the ML vertical diffusion of TKE does contribute to the budget. This points towards the inapplicability of the relation $K = \gamma \epsilon / N^2$ [*Osborn*, 1980] at least within the ML.

C.2. K_ρ **constraining a method estimating upwelling:** *Rhein et al.* **[2010]**

One of the processes known to sustain the property exchange from the deeper layers of the ocean and the surface layer is upwelling. The importance of this term for the mixed layer heat balance is still controversially discussed. The small magnitude of upwelling velocities w on the order of $1 \cdot 10^{-5} ms^{-1}$ challenges detection limits for direct observations, hampering estimates of upwelling magnitudes. Hence, these small vertical velocities are predominantly estimated via indirect methods. Outside the equatorial region the widely applied method is calculating w via the wind stress curl. In the equatorial region this method fails due to the vanishing Coriolis parameter. The method described in *Rhein et al.* [2010] uses a one-dimensional two layer box model inferring the upwelling velocities from the observed disequilibria of helium isotopes in the mixed layer.

In general, the surface layer of the ocean is in solubility equilibrium for the noble gas helium with the atmosphere via gas transfer. Nevertheless, in the equatorial band an excess of helium isotopes is observed within the ML compared to the atmospheric boundary layer. The concentrations of the isotopes ^3He and ^4He are commonly reported as an isotopic ratio δ^3He, which is defined as the ratio of ^3He to ^4He in the water sample compared to the ratio in air. The excess of δ^3He within the ML of the tropics originates from δ^3He rich waters from within the ocean interior, where it got released into the ocean predominantly
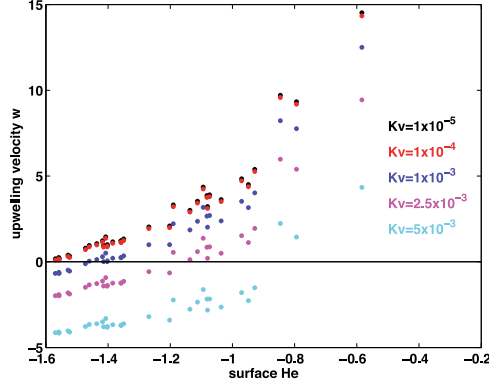
C. Other applications for MSS data

Figure C.3.: Upwelling velocities $w(\cdot 10^{-5})ms^{-1}$ for different helium isotope ratios in the mixed layer. $\delta^3 He$=-1.6% is the equilibrium value. Upwelling was calculated with vertical diffusivities K_v from $1 \cdot 10^{-5}$ to $5 \cdot 10^{-3} m^2 s^{-1}$. Negative w indicate downwelling, positive w indicate upwelling. Helium data are from cruise M68/2. From *Rhein et al.* [2010].

via hydrothermal venting. *Rhein et al.* [2010] have observed horizontal advection playing a minor role in supplying these $\delta^3 He$ rich waters to the ML and therefore solely attribute them to vertical processes such as diapycnal mixing and upwelling. As no temporal trends were observed a steady state balance for a simple one-dimensional 2 box model is considered:

$$0 = F_g + K_v \frac{dC}{dz} + w(C_2 - C_1) \tag{C.1}$$

$C_{1,2}$ are the $\delta^3 He$ ratios within the boxes and dC/dz is the $\delta^3 He$ ratio gradient. Terms on the right hand side represent gas exchange, diapycnal mixing and upwelling (from left to right, see also fig.C.2). The gas exchange rate is determined by the observed helium excess in the ML and the gas transfer velocity. For the diapycnal mixing term information on K_v and the $\delta^3 He$ ratio gradient within the depth range of the thermocline is required. The gradient is obtained by taking the gradient between all measurements averaged 30m above and 30m below the thermocline. The upwelling velocity w can then be obtained with the observed $\delta^3 He$ differences $C_{1,2}$, whereas C_1 is an average over the samples taken within the mixed layer at individual stations. C_2 is taken as the mean of data on all 3 cruises, distinguishing between the equatorial region (1°S-0.5°N), where on all cruises $\delta^3 He$ values were observed lower, and areas further off the equator.

The data set processed within this study was used to provide section mean profiles of K_ρ, which is assumed to equal K_v, for the individual cruises, which could be averaged over the thermocline depth range providing individual K_v estimates to be used in equation C.1. The obtained upwelling velocities w clearly depend on the magnitude of K_v (see fig.C.3) striking the importance for the use of an adequate value in obtaining reliable estimates of w. Note, that if K_v exceeds $1 \cdot 10^{-3} m^2 s^{-1}$ the gas exchange term is overcompensated and even requires downwelling. The occupation with the estimates of the individual contributions to the ML heat budget within the framework of this study led us to the suggestion to attribute the estimated upwelling velocities with entrainment heat fluxes in order to point out their contribution to the heat budget of the ML. In addition, knowledge about the variability of mixing related parameters and the equatorial Atlantic in general obtained within the framework of this study was brought into discussions and further estimations for this publication.

Of the calculated upwelling velocities 48% were smaller than $1 \cdot 10^{-5} ms^{-1}$, 19% were between 1 and

$2 \cdot 10^{-5} ms^{-1}$ and 22% between 2 and $4 \cdot 10^{-5} ms-1$. The mean inferred upwelling velocitities per cruise are $1.4 \cdot 10^{-5} ms-1$ (EGEE2,September 2005), $2.6 \cdot 10^{-5} ms-1$ (M682,June/July2006) and $0.6 \cdot 10^{-5} ms-1$ (EGEE3, May/June 2006), which is at the higher end of published estimates. It has to be mentioned that the estimates represent weekly averages, the time scale being set by the gas exchange time scale needed to equilibrate concentrations between atmosphere and oceanic mixed layer after upwelling has ceased. Other published estimates are often climatological means. In addition it was found, that upwelling velocities are not symmetric about the equator, but are higher south of the equator than to the north. The upwelling velocities w can be used to infer the heat flux due to entrainment for the ML as pointed out in section 6.1. The resulting fluxes per cruise for the equatorial region between 1.5°S and 1.5°N at 10°W are 23 Wm^{-2} (EGEE2), 12 Wm^{-2} for EGEE3 and 138 Wm^{-2} for M68/2 respectively. The two former estimates fit to the entrainment flux at this location estimated in section 6.2. *Rhein et al.* [2010] attribute the high estimate of M68/2 in late June 2006 as a strong short term upwelling event, which can not be resolved with the climatological estimates presented previously. Hence, the estimates presented in *Rhein et al.* [2010] support the idea that vertical advection of cold water due to upwelling is a minor in the heat balance instead being responsible for the formation of the cold tongue as suggested previously [*Weingartner and Weisberg*, 1991b]. For a validation of the obtained variability of upwelling velocities within the measurement area, the comparison of the spatial patterns of upwelling determined from the wind stress curl is obsolete due to the vanishing Coriolis parameter within the equatorial region. As in the equatorial band the biological productivity is determined only by the supply of nutrients, as solar radiation is not a limiting factor, the spatial patterns of estimated upwelling velocities are compared to the spatial patterns of SST and NPP (productivity). Some resemblance of the spatial patterns is obvious encouraging the use of this method. For the comparison with SST though it has to be kept in mind that SSTs are not determined by upwelling alone, but moreover an interplay of terms as discussed in chapter 6.2. Hence, upwelling rates inferred from the assessed linkage between upwelling and weekly SSTs should be regarded with caution.

References

Arhan, M., A. Treguier, B. Bourlès, and S. Michel, Diagnosing the annual cycle of the Equatorial Undercurrent in the Atlantic Ocean from a general circulation model, *Journal of Physical Oceanography*, *36*, 1502–1522, 2006.

Athie, G., and F. Marin, Cross equatorial structure and temporal modulation of intraseasonal variability at the surface in the Tropical Atlantic Ocean, *Journal of Geophysical Research*, *113*, C08020, 2008.

Batchelor, G. K., Small-scale variations of convected quantities like temperaure in turbulent fluid. Part I: Generell discussion and the case of small conductivity, *Journal of Fluid Mechanics*, *5*, 113–133, 1959.

Bonjean, F., and G. S. E. Lagerloef, Diagnostic model and analysis of surface currents in the tropical Pacific Ocean, *Journal of Physical Oceanography*, *32*, 2938–2954, 2002.

Bourlès, B., et al., African Monsoon Multidisciplinary Analysis (AMMA): special measurements in the Tropical Atlantic, *CLIVAR Newsletter Exchanges*, *41(12)*, 7–9, 2007.

Bourlès, B., et al., The Pirata program: history, accomplishments and future directions, *Bulletin of the American Meteoroligical Society*, *89(8)*, 1111–1125, 2008.

Bourlès, B., M. D'Orgeville, G. Eldin, Y. Gouriou, R. Chuchla, Y. DuPenhoat, and S. Arnault, On the evolution of the thermocline and subthermocline eastward currents in the Equatorial Atlantic, *Geophysical Research Letters*, *29*, 32–(1–4), 2002.

Brandt, P., F. A. Schott, C. Provost, A. Kartavtseff, V. Hormann, B. Bourles, and J. Fischer, Circulation in the central equatorial Atlantic: Mean and intraseasonal to seasonal variability, *Geophysical Research Letters*, *33*, L07609, 2006.

Brandt, P., V. Hormann, B. Bourles, J. Fischer, F. A. Schott, L. Stramma, and M. Dengler, Oxygen tongues and zonal currents in the equatorial Atlantic, *Journal of Geophysical Research*, *113*, C04012, 2008.

Brandt, P., V. Hormann, A. Krtzinger, M. Visbeck, G. Krahmann, and L. Stramma, Changes in the Ventilation of the Oxygen Minimum Zone of the Tropical North Atlantic, *Journal of Physical Oceanography*, *40*, 1784–1801, 2010.

Brandt, P., G. Caniaux, B. Bourles, A. Lazar, M. Dengler, A. Funk, V. Hormann, H. Giordani, and F. Marin, Equatorial upper-ocean dynamics and their interaction with the West African monsoon, *Atmospheric Science Letters*, *12*, 24–30, 2011.

Brandt, P., A. Funk, V. Hormann, M. Dengler, R. Greatbatch, and J. Toole, Interannual atmospheric variability forced by the deep equatorial Atlantic Ocean, *Nature*, *473*, 497–U237, 2011a.

Caniaux, G., H. Giordani, J.-L. Redelsperger, F. Guichard, E. Key, and M. Wade, Coupling between the Atlantic cold tongue and the West African monsoon in boreal spring and summer, *Journal of Geophysical Research*, *116*, C04003, 2011.

Canuto, V. M., Y. Cheng, A. M. Howard, and E. N. Essau, Stably stratified flows: A model with no Ri(cr), *Journal of Atmospheric Science*, *65*, 2437–2447, 2008.

Chang, P., Seasonal cycle of sea surface temperature and mixed layer heat budget in the tropical Pacific Ocean, *Geophysical Research Letters*, *20*, 2079–2082, 1994.

Chang, P., et al., Climate fluctuations of tropical coupled systems - The role of ocean dynamics, *Journal of Climate*, *19*, 5122–5174, 2006.

Conover, W. J., *Practical nonparametric statistics*, John Wiley, 3rd edition, 2001.

Crawford, W., and T. Osborn, Microstructure measurements in the Atlantic Equatorial Undercurrent during GATE, *Deep-Sea Research*, *26*, 285–308, 1979.

da Silva, A., A. C. Young, and L. Levitus, Atlas of Surface Marina Data, vol 1, *Algorithms and Procedures, NOAA Atlas NESDIS*, *6*, U.S. Dep. of Commer., Wahington, D.C., 1994.

de Boyer Motegut, C., G. Madec, A. S. Fischer, A. Lazar, and D. Iudicone, Mixed layer depth over the global ocean: an examination of profile data and a profile-based climatology, *Journal of Geophysical Research*, *109*, C12003, 2004.

Düing, W., et al., Meanders and long waves in the equatorial Atlantic, *Nature*, *257*, 280–284, 1975.

Efron, B., 1977 Rietz lecture - bootstrap methods -another look at jackknife, *Annual Statistics?*, *7*, 1–26, 1979.

Fairall, C. W., E. Bradley, J. E. Hare, A. A. Grachev, and J. B. Edson, Bulk parametrization of air-sea fluxes: Updates and verification for the COARE algorithm, *Journal of Climate*, *16*, 571–591, 2003.

Ferrari, R., and K. L. Polzin, Finescale structure of the T-S relation in the eastern North Atlantic, *Journal of Physical Oceanography*, *35(8)*, 1437–1454, 2005.

Fick, A., On liquid diffusion, *Philosophical Magazine and Journal of Science*, *31-39*, 10, 1855.

Fischer, J., P. Brandt, M. Dengler, M. Mller, and D. Symonds, Surveying the upper ocean with the ocean surveyer: A new phased array Doppler current profiler, *Journal of Atmospheric and Oceanic Technology*, *20(5)*, 742–751, 2003.

Fischer, T., Diapycnal diffusivity and transport of matter in the open ocean estimated from underway acoustic profiling and microstructure profiling, Ph.D. thesis, Christian-Albrechts-Universität zu Kiel, 2011.

Foltz, G. R., S. A. Grodsky, J. A. Carton, and M. J. McPhaden, Seasonal mixed layer heat budget of the tropical Atlantic Ocean, *Journal of Geophysical Research*, *108*, 3146–, 2003.

Frantantoni, D. M., W. E. Johns, T. L. Townsend, and H. E. Hurlburt, Low-latitude circulation and mass transport pathways in a model of the tropical Atlantic ocean, *Journal of Physical Oceanography*, *30*, 1944–1966, 2000.

Fringer, O. B., and R. L. Street, The dynamics of breaking progressive interfacial waves, *Journal of Fluid Mechanics*, *494*, 319–353, 2003.

Ganachaud, A., and C. Wunsch, Imporved estimates of global ocean circulation, heat transport and mixing from hydrographic data, *Nature*, *408*, 453–457, 2000.

References

Gargett, A. E., P. J. Hendricks, T. B. Sanford, T. R. Osborn, and A. J. Williams, A composite spectrum of vertical shear in the upper ocean, *Journal of Physical Oceanography*, *11*, 1258–1271, 1981.

Gargett, A. E., T. R. Osborn, and P. W. Nasmyth, Local isotropy and the decay of turbulence in a statified fluid, *Journal of Fluid Mechanics*, *144*, 231–280, 1984a.

Gargett, A. E., T. R. Osborn, and P. W. Nasmyth, Local isotropy and the decay of turbulence in a stratified fluid, *Journal of Fluid Mechanics*, *144*, 231–280, 1984b.

Garrett, C., and W. Munk, Space-Time scales of internal waves, *Geophysical Fluid Dynamics*, *2*, 225–264, 1972.

Garrett, C., and W. Munk, Space-Time scales of internal waves: a progress report, *Journal of Geophysical Research*, *80,3*, 291–297, 1975.

Garrett, C., and W. Munk, Internal waves in the ocean, *Annual Reviews of Fluid mechanics*, *11*, 339–369, 1979.

Gaspar, P., Y. Gregoris, and J.-M. Lefevre, A simple eddy kinetic energy model for simulations of the oceanic vertical mixing: tests at station PAPA and long-term upper ocean study site, *Journal of Geophysical Research*, *95*, 16179–16193, 1990.

Giannini, A., R. Saravanan, and P. Chang, Oceanic forcing of Sahel rainfall on interannual to interdecadal time scales, *Science*, *302*, 1027–1030, 2003.

Gouriou, Y., and G. Reverdin, Isopycnal and diapycnal circulation of the upper equatorial Atlantic ocean in 1983-1984, *Journal of Geophysical Research*, *97(C3)*, 3543–3572, 1992.

Gregg, M. C., Scaling turbulent dissipation in the thermocline, *Journal of Geophysical Research*, *94, No.C7*, 9686–9698, 1989.

Gregg, M. C., Estimation and geography of diapycnal mixing in the ocean, *Physical Processes in Lakes and Oceans*, pp. J.Imberger, Ed., Amer.Geophys. Union, 305–338, 1998.

Gregg, M. C., Uncertanties and Limitations in Measuring ϵ and χ, *Journal of Atmospheric and Oceanic Technology*, *16*, 1483–1490, 1999.

Gregg, M. C., and T. B. Meagher, The dynamic response of glass rod thermistors, *Journal of Geophysical Research*, *85*, 2779–2786, 1980.

Gregg, M. C., H. Peters, J. C. Wesson, N. S. Oakey, and T. J. Shay, Intensive measurements of turbulence and shear in the equatorial undercurrent, *Nature*, *318*, 140–144, 1985.

Gregg, M. C., T. B. Sanford, and D. P. Winkel, Reduced mixing from the breaking of internal waves in equatorial waters, *Nature*, *422*, 513–515, 2003.

Henyey, F. S., J. Wright, and S. M. Flatte, Energy and action flow through the internal wave field: An eikonal approach, *Journal of Geophysical Research-Oceans*, *91(C7)*, 8487–8495, 1986.

Hinze, J. O., *Turbulence*, McGraw-Hill (New York), 1975.

Hormann, V., and P. Brandt, Atlantic equatorial undercurrent and associated cold tongue variability, *Journal of Geophysical Research*, *112*, C06017, 2007.

Hormann, V., and P. Brandt, Upper equatorial Atlantic variability during 2002 and 2005 associated with equatorial Kelvin waves, *Journal of Geophysical Research*, *114*, C03007, 2009.

Jochum, M., and R. Murtugudde, Temperature advection by tropical instability waves, *Journal of Geophysical Research*, *36*, 592–605, 2006.

Josey, S. A., E. C. Kent, and P. K. Taylor, New insights into the ocean heat budget closure problem from analysis of the SOC air-sea flux climatology, *Journal of Climate*, *12*, 2856–2880, 1999.

Jouanno, J., F. Marin, Y. DuPenhoat, J. Sheinbaum, and J.-M. Molines, Seasonal heat balance in the upper 100m of the Equatorial Atlantic Ocean, *Journal of Geophysical Research*, *in press*, C006912, 2011.

Jungclaus, J. H., N. Keenlyside, M. Botzet, H. Haak, J.-J. Luo, M. Latif, J. Marotzke, U. Mikolajewicz, and E. Roeckner, Ocean circulation and tropical variability in the coupled model ECHAM5/MPI-OM, *Journal of Climate*, *19*, 3952–3972, 2006.

Kantha, L. H., and C. A. Clayson, An improved mixed layer model for geophysical applications, *Journal of Geophyscial Research*, *99*, 25235–25266, 1994.

Karstensen, J., and D. Quadfasel, Formation of Southern hemisphere thermocline water: water mass conversion and subduction, *Journal of Physical Oceanography*, *32*, 3020–3038, 2002.

Kennan, S. C., and P. Flament, Observations of a tropical instability vortex, *Journal of Physical Oceanography*, *30*, 2277–2301, 2000.

Kolmogorov, A. N., The local structure of turbulence in an incompressible viscous fluid for very large Reynolds number, *C.R.Acad.Sci. USSR*, *30*, 301–305, 1941.

Kolmogorov, A. N., Equations of turbulent motion of an incompressible fluid, *Isvestiya AN SSSR, Ser.fiz.*, *6, No.1-2*, 56–58, 1942.

Kolodziejczyk, N., B. Bourles, F. Marin, J. Grelet, and R. Chuchla, Seasonal variability of the Euqatorial Undercurrent at 10W as inferred from recent in situ observations, *Journal of Geophysical Research*, *114*, C06014, 2009.

Kraichnan, R. H., Small-scale structure of a scalar field convected by turbulence, *Physics of Fluids*, *11*, 945–953, 1968.

Kushnir, Y., W. A. Robinson, P. Chang, and A. W. Robertson, The physical basis for predicting Atlantic sector seasonal-to-interannual climate variability, *Journal of Climate*, *19*, 5949–5970, 2006.

Large, W. G., and P. R. Gent, Validation of vertical mixing in an equatorial ocean model using large eddy simulations and observations, *Journal of Physical Oceanography*, *29*, 449–464, 1999.

Large, W. G., J. C. McWilliams, and S. C. Doney, Oceanic vertical mixing: a review and a model with a nonlocal boundary layer parametrization, *Review of Geophysics*, *32*, 363–403, 1994.

Lebedev, K., H. Yoshinari, N. A. Maximenko, and P. W. Hacker, YoMaHa'07: Veloctiy data assessed from trajectories of Argo floats at parking level and at the sea surface, *IPRC Technical Note*, *4(2), June 12*, 16p, 2007.

Ledwell, J. R., A. J. Watson, and C. S. Law, Evidence for slow mixing across the pycnocline from an open-ocean tracer-release experiment, *Nature*, *364*, 701–703, 1993.

References

Lien, R. C., D. R. Caldwell, M. C. Gregg, and J. N. Moum, Turbulence variability at the equator in the central Pacific at the beginning of the 1991-1993 El Nino, *Journal of Geophysical Research*, *100*, 6881–6898, 1995.

Lien, R.-C., E. D'Asaro, and M. J. McPhaden, Internal waves and turbulence in the upper central equatorial Pacific: Lagrangian and Eulerian observations, *Journal of Physical Oceanogeaphy*, *32*, 2619–2639, 2002.

Lien, R. C., E. A. D'Asaro, and C. E. Menkes, Modulation of equatorial turbulence by tropical instability waves, *Geophysical Research Letters*, *35*, L24607, 2008.

Liu, Z., A simple model of the mass exchange between the subtropical and tropical ocean, *Journal of Physical Oceanography*, *24*, 1153–1165, 1994.

Lueck, R. G., and T. D. Mudge, Topographically induced mixing around a shallow seamount, *Science*, *276*, 1831–1833, 1997.

Luketina, D. A., and J. Imberger, Determining Turbulent Kinetic Energy Dissipation from Batchelor Curve Fitting, *Journal of Atmospheric and Oceanic Technology*, *18*, 100–113, 2001.

Lumpkin, R., and Z. Garaffo, Evaluating the Decomposition of Tropical Atlantic Drifter Oberservations, *J.Atmos.Oceanic Techn.*, *I 22*, 1403–1415, 2005.

Lumpkin, R., and K. Speer, Global ocean meridional overturning, *Journal of Physical Oceanography*, *37(10)*, 2550–2562, 2007.

Mack, A. P., and D. Hebert, Internal gravity waves in the upper eastern equatorial Pacific: Observations and numerical solutions, *Journal of Geophysical Research*, *102*, 21081–21100, 1997.

MacKinnon, J. A., and M. C. Gregg, Mixing on the late-summer New England shelf - Solibores, shear and stratification, *Journal of Physical Oceanography*, *33*, 1476–1492, 2003.

Malanotte-Rizzoli, P., R. E. Young, K. Hedstrom, H. Arango, and D. B. Haidvogel, Water mass pathways between the subtropical and tropical ocean in a climatological simulation of the North Atlantic ocean circulation, *Dynamics of Atmospheres and Oceans*, *32*, 331–372, 2000.

Marin, F., G. Caniaux, H. Giordani, B. Bourles, Y. Gouriou, and E. Key, Why were sea surface temperatures so different in the eastern equatorial Atlantic in June 2005 and June 2006, *Journal of Physical Oceanography*, *39*, 1416–1431, 2009.

McCreary, J. P., and P. Lu, Interaction betwee the subtropical and equatorial ocean circulations: the subtropical cell, *Journal of Physical Oceanography*, *24(2)*, 466–497, 1994.

Menkes, C., J. G. Vialard, S. Kennan, J.-P. Boulanger, and G. Madec, A modeling study of the impact of tropical instatbility waves on the heat budget of the eastern equatorial Pacific, *Journal of Physical Oceanography*, *36*, 847–865, 2006.

Mercier, H., M. Arhan, and J. R. E. Lutjeharms, Upper-layer circulation in the eastern Equatorial and South Atlantic ocean in January-March 1995, *Deep-Sea Research Part I*, *50*, 863–887, 2003.

Molinari, R., Observations of Eastward Currents in the tropical South Atlantic Ocean 1978-1980, *Journal of Geophysical Research*, *87*, 9707–9714, 1982.

Monin, A. S., and A. M. Yaglom, *Statistical fluid mechanics: Mechanics of Turbulence*, Nauka Press, Moscow, 1965.

Moore, D. W., P. Hisard, J. P. McCreary, J. Merle, J. J. O'Brien, J. Picaut, J. M. Verstraete, and C. Wunsch, Equatorial adjustment in the eastern Atlantic, *Geophysical Research Letters*, *5*, 637–640, 1978.

Moum, J., D. R. Caldwell, and C. Paulson, Mixing in the equatorial surface layer and thermocline, *Journal of Geophysical Research*, *94*, 2005–2021, 1989.

Moum, J. N., and D. R. Caldwell, Local influences on shear flow turbulence in the equatorial ocean, *Science*, *230*, 315–316, 1985.

Moum, J. N., D. Hebert, C. A. Paulson, and D. R. Caldwell, Turbulence and internal waves at the equator. Part I: Statistics from towed thermistors and a microstructure profiler, *Journal of Physical Oceanography*, *22*, 1330–1345, 1992.

Moum, J. N., M. C. Gregg, R. C. Lien, and M. E. Carr, Comparison of Turbulence Kinetic Energy Dissipation Rate Estimates from Two Ocean Microstructure Profilers, *Journal of Atmospheric and Oceanic Technology*, *12*, 346–366, 1995.

Moum, J. N., R. C. Lien, A. Perlin, J. D. Nash, M. C. Gregg, and P. J. Wiles, Sea surface cooling at the Equator by subsurface mixing in tropical instability waves, *Nature Geoscience*, *2*, 761–765, 2009.

Moum, J. N., J. Nash, and W. Smyth, Narrowband oscillations in the upper equatorial ocean. Part I: Interpretation as shear instabilities, *Journal of Physical Oceanography*, *41*, 397–411, 2011.

Munk, W., and C. Wunsch, Abyssal recipes II: energetics of tidal and wind induced mixing, *Deep-Sea Research Part I*, *45*, 1977–2010, 1998.

Munk, W. H., Abyssal recipes, *Deep-Sea Research*, *13*, 707–730, 1966.

Munk, W. H., and E. R. Anderson, Notes on a theory of the thermocline, *Journal of Marine Research*, *7*, 276–271, 1948.

Nash, J. D., and J. Moum, Microstructure estimates of turbulent salinity flux and the dissipation spectrum of salinity, *Journal of Physical Oceanography*, *32*, 2312–2333, 2002.

Nash, J. D., D. Caldwell, M. Zelman, and J. Moum, A thermocouple probe for high speed temperature measurements in the ocean, *Journal of Atmospheric and Oceanic Technology*, *16*, 1474–1482, 1999.

Nasmyth, P., Oceanic Turbulence, Ph.D. thesis, University of British Columbia, 1970.

Oakey, N. S., An instrument to measure oceanic turbulence and microstructure. Bedford Institute of Oceanography, *Report, Ser. B1-R-77*, p. 55pp, 1977.

Oakey, N. S., Determination of the rate of dissipation of turbulent energy from simultaneous temperaure and velocity shear microstructure measurements, *Journal of Physical Oceanography*, *12(3)*, 256–271, 1982.

Okumura, Y., and S.-P. Xie, Some overlooked features of Tropical Atlantic climate leading to a Nino-Like Phenomenon, *Journal of Climate*, *19*, 5859–5874, 2006.

Osborn, N. S., and C. S. Cox, Oceanic fine structure, *Geophysical Fluid Dynamics*, *3*, 321–345, 1972.

References

Osborn, T. R., Measurements of energy dissipation adjacent to an island, *Journal of Geophysical Research*, *83(C6)*, 2939–2957, 1978.

Osborn, T. R., Estimates of the Local-Rate of Vertical Diffusion from Dissipation Measurements, *Journal of Physical Oceanography*, *10*, 83–89, 1980.

Pacanowski, R. C., and S. G. H. Philander, Parametrization of vertical mixing in numerical models of the tropical oceans, *Journal of Physical Oceanography*, *11*, 1443–1451, 1981.

Peter, A., M. L. Henaff, Y. duPenhoat, C. Menkes, F. Marin, J. Vialard, G. Caniaux, and A. Lazar, A model study f the seasonal mixed layer heat budget in the equatorial Atlantic, *Journal of Geophysical Research*, *111*, C06014, 2006.

Peters, H., M. C. Gregg, D. R. Caldwell, and J. N. Moum, Equatorial vertical mixing, *Further progress in Equatorial Oceanography, A report of the U S TOGA Workshop on the Dynamics of the Equatorial Oceans edited by E J Katz and J M Witte*, *Nova University Press, Fort Lauderdale*, 101–120, 1987.

Peters, H., M. C. Gregg, and J. Toole, On the Paarametrization of Equatorial Turbulence, *J.Geophys.Res.*, *93*, 1199–1218, 1988.

Peters, H., M. Gregg, and T. Sanford, Equatorial and off-equatorial fine-scale and large-scale shear variability at 140°W, *Journal of Geophysical Research*, *16*, 913–928, 1991.

Peters, H., M. Gregg, and T. Sanford, The diurnal cycle of the upper equatorial ocean: turbulence, fine-scale shear, and mean shear, *Journal of Geophysical Research*, *99*, 7707–7723, 1994.

Philander, S. G. H., Instabilities of zonal equatorial currents, *Journal of Geophysical Research*, *81*, 3725–3735, 1976.

Polo, I., A. Lazar, B. Rodriguez-Fonseca, and S. Arnault, Oceanic Kelvin waves and tropical Atlantic intra seasonal variability: 1. Kelvin wave characterization, *Journal of Geophysical Research*, *113*, C07009, 2008.

Polzin, K. L., and E. T. Montgomery, Microstructure profiling with the High Resolution Profiler, *Proceedings of Microstructure Sensors Workshop*, *23-25 October*, 109–115, 1996.

Polzin, K. L., J. M. Toole, and R. W. Schmitt, Finescale parametrizations of turbulent dissipation, *Journal of Physical Oceanography*, *25*, 306–328, 1995.

Polzin, K. L., J. M. Toole, G. R. Ledwell, and R. W. Schmitt, Spatial variability of turbulent mixing in the abyssal ocean, *Science*, *276*, 93–96, 1997.

Prandke, H., and A. Stips, Test measurements with an operational microstructure turbulence profiler: Detection limit of dissipation rates, *Aquatic Science*, *60*, 191–209, 1998.

Prandke, H., K. H. K, and A. Stips, MITEC technology development: The microstructure-turbulence measuring system MSS, *EUR 19733 EN*, 2000.

Provost, C., S. Arnault, N. Chouaib, A. Kartavtseff, L. Bunge, and E. Sultan, TOPEX/Poseidon and Jason equatorial sea surface slope anomaly in the Atlantic in 2002: Comparison with wind and current measurements at 23W, *Marine Geodesy*, *27*, 31–45, 2004.

Rahmstorf, S., Ocean circulation and and climate during the past 120,000 years , *Nature*, *419*, 207–214, 2002.

Rahmstorf, S., Thermohaline circulation: the current climate, *Nature*, *421*, 699, 2003.

Ramsey, P. H., Critical values for Spearman's Rank order correlation, *Journal of Educational Statistics*, *14*, 245–253, 1989.

Redelsperger, J., et al., (AMMA): une etude multidisciplinaire de la mousson ouest-africaine, *La Meteorologie*, *54*, 22–32, 2006.

Rehmann, C. R., and J. H. Hwang, Small-Scale Structure of Strongly Stratified Turbulence, *Journal of Physical Oceanography*, *32*, 151–164, 2005.

Reynolds, R. W., and T. M. Smith, Improved global sea surface temperature analyses using optimum interpolation, *Journal of Climate*, *7*, 929–948, 1994.

Rhein, M., M. Dengler, J. Sltenfuss, R. Hummels, S. Httl-Kabus, and B. Bourles, Upwelling and associated heat flux in the equatorial Atlantic inferred from helium isotope disquilibrium, *Journal of Geophysical Research*, *115*, C08021, 2010.

Richardson, P., and T. McKee, Average seasonal variation of the Atlantic equatorial current from ship drift data, *Journal of Physical Oceanography*, *14*, 1226–1238, 1984.

Richter, I., and S.-P. Xie, On the origin if equatorial Atlantic boases in coupled general circulation models, *Climate Dynamics*, *31*, 587–598, 2008.

Robinson, A. R., An investigation into the wind as the cause of the Equatorial Undercurrent, *Journal of Marine Reseach*, *24*, 179–204, 1966.

Ruddick, B., and D. Walsh, Variations in Apparent Mixing Efficiency in the North Atlantic Central Water, *Journal of Physical Oceanography*, *27*, 2589–2605, 1997.

Sandström, J. W., Dynamische versuche mit Meerwasser, *Annals in Hydrodynamic Marina Meterology*, pp. 6–23, 1908.

Schafstall, J., Turbulente Vermischungsprozesse und Zirkulation im Auftriebsgebiet vor Nordwestafrika, Ph.D. thesis, Christian-Albrechts-Universität zu Kiel, 2010.

Schafstall, J., M. Dengler, P. Brandt, and H. Bange, Tidal induced mixing and diapycnal nutrient fluxes in the Mauretanian Upwelling region, *Journal of Geophysical Research*, *115(C10)*, C10014, 2010.

Schmitt, R. W., J. M. Toole, R. L. Koehler, E. C. Mellinger, and K. W. Doherty, The development of a fine-and microstructure profiler, *Journal of Atmospheric and Oceanic Technology*, *5*, 484–500, 1988.

Schott, F., J. McCreary, and G. Johnson, Shallow overturning circulations of the tropical-subtropical oceans, in, *Earth's Climate: The ocean atmosphere interaction*, pp. edited by C.Wang, S.–P.Xie and J.A.Carton, Geophysical Monograph Series 147, AGU, washington, D. C., 2004.

Servain, J., J. Picaut, and J. Merle, Evidence of remote forcing in the equatorial Atlantic, *Journal of Physical Oceanography*, *12*, 457–463, 1982.

Shih, L., J. Koseff, G. Ivey, and J. Ferziger, Parametrization of turbulent fluxes and scales using homogeneous sheared stably stratified turbulence simulations, *Journal of Fluid Mechanics*, *525*, 193–214, 2005.

References

Skyllingstad, E., and D. Denbo, An ocean large-eddy simulation of Langmuir circulations and convection in the surface mixed layer, *Journal of Geophysical Reseach*, *100*, 8501–8522, 1995.

Smyth, W., and J. Moum, Waves and instability in an asymmetrically stratified jet, *Dynamics of Atmosphere and Ocean*, *35*, 265–294, 2002.

Smyth, W., J. Moum, and D. Caldwell, The efficiency of Mixing in Turbulent Patches: Inferenced from Direct Simulations and Microstructure Observations, *Journal of Physical Oceanography*, *31*, 1969–1992, 2001.

Smyth, W., J. Moum, and J. Nash, Narrowband oscillations in the upper equatorial ocean. Part II: Properties of shear instabilities, *Journal of Physical Oceanography*, *41*, 412–428, 2011.

St Laurent, L., and R. W. Schmitt, The contribution of salt fingers to vertical mixing in the North Atlantic Tracer Release Experiment, *Journal of Physical Oceanography*, *29(7)*, 1404–1424, 1999.

Stevenson, J. W., and P. P. Niiler, Upper ocean heat budget during the Hawaii-to-Tahiti shuttle experiment, *Journal of Physical Oceanography*, *13*, 1894–1907, 1983.

Stramma, L., and F. Schott, The mean flow-field of the tropical Atlantic ocean, *Deep-Sea Research Part II-Tropical studies in Oceanography*, *46(1-2)*, 279–303, 1999.

Sun, C., W. Smyth, and J. Moum, Dynamic instability of stratified shear flow in the upper equatorial ocean, *Journal of Geophysical Research*, *103(C5)*, 10323–10337, 1998.

Swenson, M. S., and D. Hansen, Tropical Pacific ocean mixed layer heat budget: The Pacific cold tongue, *Journal of Physical Oceanography*, *29*, 69–81, 1999.

Toggweiler, J. R., and B. Samuels, On the ocean's large-scale circulation near the limit of no vertical mixing, *Journal of Physical Oceanography*, *28*, 1832–1852, 1998.

Torrence, C., and G. P. Compo, A Practical Guide to wavelet analysis, *Bulletin of American Meteorological Society*, *79*, 61–78, 1998.

Townsend, A. A., The Structure of Turbulent Shear Flow, *Cambridge University Press*, p. 429 pp., 1976.

von Schuckmann, K., P. Brandt, and C. Eden, Generation of tropical instability waves in the Atlantic Ocean , *Journal of Geophysical Research*, *113*, C08034, 2008.

Wade, M., G. Caniaux, and Y. duPenhoat, Variability of the mixed layer heat budget in the eastern equatorial Atlantic during 2005-2007 as inferred using Argo floats, *Journal of Geophysical Research*, *116*, C08006, 2011a.

Wade, M., G. Caniaux, Y. DuPenhoat, M. Dengler, H. Giordani, and R. Hummels, A one-dimensional modeling study of the diurnal cycle in the equatorial Atlantic at the PIRATA buoys during the EGEE-3 campaign, *Ocean Dynamics*, *61*, 1–20, 2011b.

Wagner, R. G., and A. M. D. Silva, Surface conditions associated with anomalous rainfall in the Guinea coastal region, *International Journal of Climatology*, *14*, 179–199, 1994.

Wang, D., and P. Müller, Effects of equatorial undercurrent shear on upper-ocean mixing and internal waves, *Journal of Physical Oceanography*, *32*, 1041–1057, 2002.

Wang, W., and M. J. McPhaden, The surface-layer heat balance in the equatorial Pacific ocean. Part I: mean seasonal cycle, *Journal of Physical Oceanography*, *29*, 1812–1831, 1999.

Weingartner, T. J., and R. H. Weisberg, A discription of the annual cycle in sea surface temperature and upper ocean heat in the equatorial Atlantic, *Journal of Physical Oceanography*, *21*, 68–82, 1991b.

Weisberg, R., and T. Weingartner, Instability waves in the equatorial Atlantic Ocean, *Journal of Physical Oceanography*, *18*, 1641–1657, 1988.

Wolk, F., H. Yamazaki, L. Seuront, and R. G. Lueck, A new free fall profiler for measuring biophysical microstructure, *Journal of Atmospheric and Oceanic Technology*, *19(5)*, 780–793, 2002.

Yamazaki, H., and T. Osborn, Dissipation Estimates for Stratified Turbulence, *Journal of Geophysical Research*, *95(C6)*, 9739–9744, 1990.

Yamazaki, H., and T. Osborn, Direct estimation of heat flux in a seasonal thermocline, *Journal of Physical Oceanography*, *23*, 503–516, 1993.

Yu, W., W. Han, E. D. Maloney, D. Cochis, and S.-P. Xie, Observations of eastward propagation of atmospheric intraseasonal oscillations from the Pacific to the Atlantic, *Journal of Geophysical Research*, *116*, D0201, 2011.

Zaron, E. D., and J. N. Moum, A new look at Richardson number mixing schemes for equatorial ocean modeling, *Journal of Physical Oceanography*, *39*, 2652–2664, 2009.

Zhang, D., M. J. PcPhaden, and W. E. Johns, Observational evidence for flow between the subtropical and tropical Atlantic: the Atlantic Tropical Cells, *Journal of Physical Oceanography*, *33*, 1783–1797, 2003.

Acknowledgments

I would like to thank all the people, who have supported me during this study.

Dr. Marcus Dengler, for his dedicated supervision, enormous knowledge of papers and patience with my writing.

All my colleagues at (IFM-)GEOMAR for helpful discussions and support, I especially want to acknowledge the motivational talks with Dr. Johannes Karstensen and Franziska Schwarzkopf, which have helped me "to keep at it".

My proof readers Dr. Johannes Karstensen, Dr. Tim Fischer and Franziska Schwarzkopf.

My colleagues in B11: Sandra, Donata, Michael, Sven, Johannes.

Vincent and Matteo for their continuous support and motivation

My parents for their support of all my study

All my friends, especially the "Muddi connection" and Anna Jesußek for the Skype connection

X for not becoming a premature baby

Erklärung

Hiermit erkläre ich, dass ich die vorliegende Arbeit - abgesehen von der Beratung durch meinen Betreuer - unter Einhaltung der Regeln guter wissenschaftlicher Praxis der DFG sebstständig erarbeitet und verfasst habe. Diese Arbeit hat weder ganz, noch zum Teil, an anderer Stelle im Rahmen eines Prüfungsverfahrens vorgelegen, ist nicht veröffentlicht und auch nicht zur Veröffentlichung eingereicht.

Kiel, 2012

———————————————————

(Rebecca Hummels)